Modelling and Control of Magnetorheological Damper

Real-time implementation and experimental verification

Bhowmik, Subrata; Høgsberg, Jan Becker; Krenk, Steen; Weber, Felix

Publication date:
2012

Document Version
Publisher's PDF, also known as Version of record

Modelling and Control of Magnetorheological Damper:

Real-time implementation and experimental verification

PhD Thesis

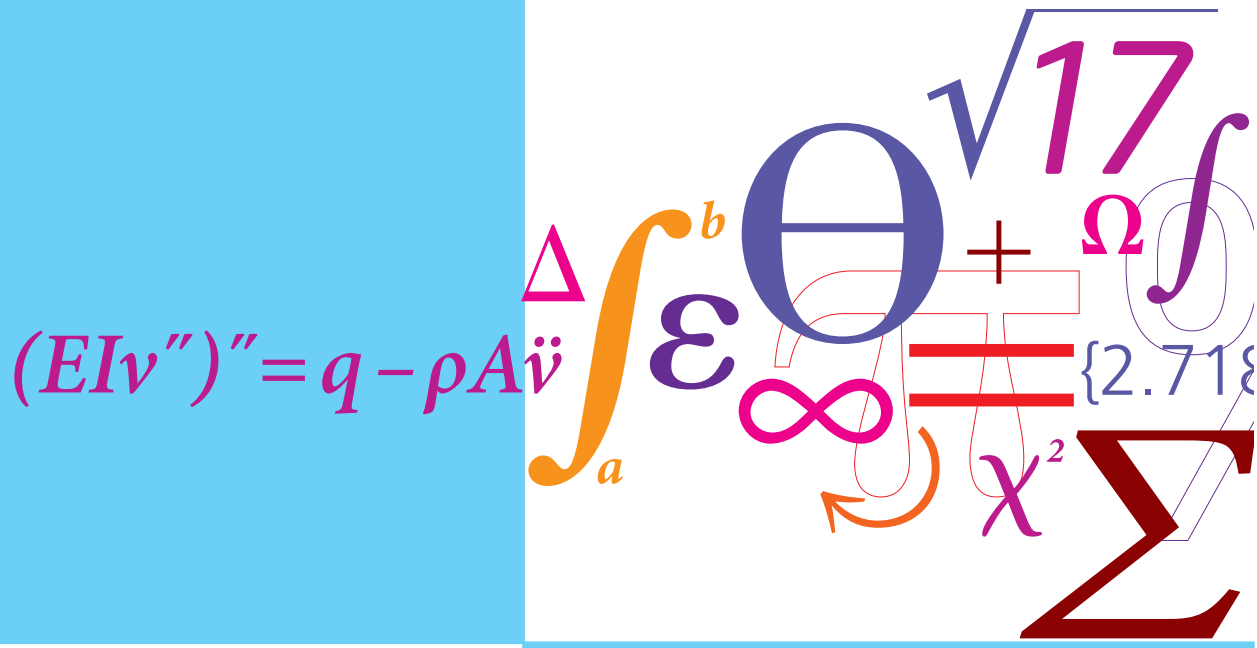

Subrata Bhowmik
DCAMM Special Repport No. S139
October 2011

DTU Mechanical Engineering
Department of Mechanical Engineering

Modelling and Control of Magnetorheological Damper:

Real time implementation and experimental verification

Subrata Bhowmik

Department of Mechanical Engineering
Technical University of Denmark
Lyngby, Denmark
2011

Abstract

This thesis considers two main issues concerning the application of a rotary type magnetorheological (MR) damper for damping of flexible structures. The first is the modelling and identification of the damper property, while the second is the formulation of effective control strategies. The MR damper is identified by both the standard parametric Bouc-Wen model and the non-parametric neural network model from an experimental data set generated by dynamic tests of the MR damper mounted in a hydraulic testing machine. The forward model represents the direct dynamics of the MR damper where velocity and current are used as input and the force as output. The inverse model represents the inverse dynamics of the MR damper where the absolute velocity and absolute force are used as input and the damper current as output. For the inverse model the current output of the network must always be positive, and it is found that the modelling error of the inverse model is significantly reduced when the corresponding input is given in terms of the absolute values of velocity and damper force. This is a new contribution to the inverse modelling techniques for the control of MR dampers. Another new contribution to the modelling of an MR damper is the use of experimental measurement data of a rotary MR damper that requires appropriate filtering. The semi-systematic optimisation procedure proposed in the thesis derives an effective neural network structure, where only velocity and damper force are essential input parameters for the MR damper modelling. Thus, for proper training, the quality of the velocity data is very important. However, direct velocity measurement is not easy. From the displacement data or the acceleration data, velocity can be determined by using simple differentiation or integration, respectively, but these processes add undesirable noise to the velocity. Instead the Kinematic Kalman Filter (KKF) is an effective means for estimation of velocity. The KKF does not directly depend on the system or structural model, as it is the case for the conventional Kalman filter. The KKF fuses the displacement and the acceleration data to get an accurate and robust estimate of the velocity. The simplicity of the network and the application of velocity in terms of KKF is a novel contribution of the thesis to the generation of a training set for neural network modelling of MR dampers.

The development of the control strategies for the MR damper focuses on the introduction of apparent negative stiffness, which basically leads to an increased local motion of the damper and thereby to increased energy dissipation and damping. Optimal viscous damping (VD) is chosen as the benchmark control strategy, used as reference case for assessment of the proposed control methods with negative stiffness. Viscous damping with negative stiffness (VDNS) initially illustrates the effectiveness of the negative stiffness component in structural damping. In a linear control setting negative stiffness requires active control forces, which are not realizable by the purely dissipative MR damper. Thus, these active components are simply clipped in the final control implementation. Since MR dampers behave almost as a friction damper improved damping performance can be obtained by a suitable combination of pure friction and negative damper stiffness. This is realized by amplitude dependent friction damping with negative stiffness (FDNS), where the force level of the friction component is adaptively changed to secure the optimal balance between friction energy dissipation and apparent negative stiffness. This type of control model for semi-active dampers is rate-independent and conveniently described in terms of the desired shape of the associated hysteresis loop or force-displacement trajectory. The final method considered for control of the rotary MR damper is a model reference neural network controller (MRNNC). This novel control approach is designed and trained based on a desired reference damper model, which in this case is the amplitude dependent friction damping with negative stiffness (FDNS). The idea is to train the neural network of the controller by data derived explicitly from the desired shape of the force-displacement loop at pure harmonic motion. In this

idealized representation the optimal relations between friction force level, negative stiffness and response amplitude can often be given explicitly by e.g. maximizing the damping ratio of the targeted vibration mode. Consequently the idea behind this trained neural network is that the optimal properties of the desired hysteresis loop formulation can be extrapolated to more general and non-harmonic response patterns, e.g. narrow-band stochastic response due to wind, wave, traffic or even earthquake excitation.

Numerical and experimental simulations have been conducted to examine the performance of the proposed control strategies. Force tracking by using an inverse neural network of the MR damper is improved by a low-pass filter to reduce the noise in the desired current and a simple switch that truncates negative values of the desired current. The performance of the collocated control schemes for the rotary type semi-active MR damper are initially verified by closed loop dynamic experiments conducted on a 5-storey shear frame structure exposed to harmonic base excitation. The MR damper is mounted on the structure so that it operates on the relative motion between the ground base and the first floor of the shear frame. The shear frame structural model is initially experimentally identified, where mass and stiffness of the model is determined by an inverse modal analysis based on the natural frequencies obtained experimentally. The damping matrix is subsequently determined from the estimated damping ratio obtained by free decay tests. The results in the thesis demonstrate that introducing apparent negative stiffness to the control of the MR damper significantly decreases both the top floor displacement and acceleration amplitudes of the shear frame structure. The structural damping ratios obtained from the response curves of the experiments correspond well to the expected values. This indicates that the mean stiffness and mean energy dissipation of the control forces are predicted fairly accurate.

A final numerical investigation is based on a classic benchmark problem for earthquake protection of a multi storey building. The seismic response of the base-isolated benchmark building with an MR damper installed between the ground and the base is illustrated, and the effectiveness of negative stiffness of the control strategies is verified numerically. Similarly, the response of another wind excited benchmark building installed with MR dampers is demonstrated and the performance shows satisfactory result.

The main contributions to this thesis are the novel modelling approach to the direct and the inverse dynamics of a rotary MR damper from experimental data, the development of model based semi-active control strategies for the MR damper, the effective introduction of negative stiffness in the control of semi-active dampers and the demonstration of effectiveness and closed loop implementation of the control techniques on both a shear frame structure and a numerical benchmark problem.

Preface

This thesis is submitted in partial fulfilment of the Ph.D. degree from the Technical University of Denmark. The study has been conducted from June 2008 to May 2011, partly at the Department of Mechanical Engineering, Technical University of Denmark (DTU), and partly at the Swiss Federal Laboratory for Material Science and Research (EMPA) in Dübendorf, Switzerland. The study has been conducted with Associate Professor Jan Høgsberg (DTU) as main supervisor, and with Professor Dr. Techn. Steen Krenk (DTU) and Dr. Felix Weber (EMPA) as co-supervisors. I owe my deepest gratitude to my supervisors for their excellent guidance and support throughout the entire project.

The Ph.D. project is formulated in association with the DCAMM (Danish Center for Applied Mathematics and Mechanics) Research School and is financed by the Danish Agency for Science, Technology and Innovation via the Grant 09-061788. A significant Part of the research has been carried out at EMPA under the supervision of Dr. Felix Weber, and the collaboration is gratefully acknowledged. Part of the external stay at EMPA has been financed by the Otto Mønsted Foundation.

Finally, I would like to express my most sincere thanks to my parents and close friends for their patience and support.

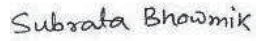

Subrata Bhowmik

Copenhagen, October 2011

Publications

Appended papers

[P1] S. Bhowmik, F. Weber, J. Høgsberg,
Experimental calibration of forward and inverse neural networks for rotary type magnetorheological damper,
(2011), *Submitted for publication.*

[P2] F. Weber, S. Bhowmik, J. Høgsberg,
Design and experimental verification of semi-active control with negative stiffness for MR dampers,
(2011), *Submitted for publication.*

[P3] S. Bhowmik,
Neural Network based semi-active control strategy for structural vibration mitigation with magnetorheological damper,
COMPDYN 2011. Proceedings of the third ECCOMAS Thematic Conference on Computational Methods in Structural Dynamics and Earthquake Engineering, 540–553,
May 25–28, Corfu, Greece, 2011.

[P4] S. Bhowmik, J. Høgsberg,
Semi-active control of magnetorheological dampers with negative stiffness,
SMART 09. Proceedings of the fourth ECCOMAS Thematic Conference on Smart Structures and Materials, 581–590,
July 13–15, Porto, Portugal, 2009.

[P5] S. Bhowmik, J. Høgsberg, F. Weber,
Neural Network modeling of forward and inverse behavior of rotary MR damper,
NSCM-23. Proceedings of the Twenty Third Nordic Seminar on Computational Mechanics, 169–172,
October 21–22, Stockholm, Sweden, 2010.

Contents

Chapter 1

Introduction

Most flexible structures, such as high-rise buildings or bridges, have very little structural damping and are therefore often prone to dynamic excitation, e.g. from wind or seismic loading. Different control mechanisms are used to reduce structural fault and thus prevent failure.

Passive dampers are reliable in the sense that they rely purely on dissipation of incoming energy without any power requirements. Some typical passive installations are tuned mass dampers, see Rasouli et al. [1], or base-isolation systems, see Cho et al. [2] or references herein.

Fully active control systems are able to apply both dissipate and non-dissipative forces to the structure, and when properly designed they yield a significant increase in damping compared to passive dampers. However, active control typically requires a large amount of power and may also introduce instabilities due to time delays or model uncertainties. Examples of active control systems are the active tuned mass dampers [1, 3] or tendon type control [4]. As an alternative to the passive tuned mass dampers, an active tuned mass damper, where an actuator is inserted between the structure and the secondary mass, can be considered as an effective damping device. The design of active tuned mass dampers is typically based on linear quadratic regulator (LQR) theory. Preumont [4] developed and implemented velocity feedback based active control strategies for civil structures. An active control strategy is demonstrated in [5] for application to a flexible structure excited by simulated wind forces for the purpose of minimising along-wind accelerations. A linear quadratic Gaussian (LQG) control strategy based on acceleration feedback is used to reduce the structural response effectively. De and Zheng [6] also applied active control to a tall structure excited by wind where a new active vibration control method which fits non-linear buildings is demonstrated. The control method is based on model identification and structural model linearisation and exerts the control force on the built model according to the force action principle.

Semi-active dampers are often considered to be a desirable compromise between failsafe passive damping and effective active control. They require little power for the operation and are thus able to run for instance on battery power. Besides, they do not add energy to the system, whereby the stability due to the damper is improved because control forces are developed through proper adjustment of damping and stiffness components of controller. The most common types of semi-active dampers for civil engineering applications are variable stiffness dampers [7, 8] and magnetorheological (MR) dampers [9, 10]. A cylindrical type MR damper designed and manufactured by Maurer Söhne GmbH is shown in Figure 1.1.

The characteristics of the MR damper are controlled in terms of the applied current, which almost simultaneously changes the magnetic field and thus the shear viscosity of the damper. A more detailed description of the characteristics and the modelling of MR dampers can be found in for instance [11]. Semi-active MR dampers have been used for both damping and earthquake protection of buildings, see e.g. [12, 13]. One of the most commonly used control strategies for MR dampers is the clipped-optimal control proposed by Dyke et al. [14]. This algorithm consists of a bang-bang (on-off) type of controller that causes the damper to generate a desirable control force, determined by an optimal control algorithm, such as

FIGURE 1.1: A Cylindrical Type Magnetorheological Damper (Courtesy of Maurer Söhne GmbH).

the H2/LQG method. The optimal force is determined by using a full-order observer. This optimal force is clipped by using the Heaviside function to get the desired voltage for the MR damper to implement the semi-active control strategy on the MR damper. Zhu et al. [15] implemented a semi-active control strategy based on the linear quadratic Gaussian (LQG) method in a wind excited structure using the MR damper. Iemura et al. [16] presented both passive and semi-active control strategies for the MR damper for a stay cable bridge and showed the effectiveness of semi-active control strategy over passive control strategy. Other common types of control strategies for MR dampers are based on e.g. Lyapunov functions, the bang-bang theory [10], variable friction damping strategy [17], modulated homogeneous friction damping strategy [18] or sliding mode control [19, 20]. The Lyapunov stability analysis is used for developing control laws where the goal is to choose control inputs for each device that will result in making the derivative of the Lyapunov function as negative as possible. The decentralised bang-bang theory is similar to the Lyapunov approach where the Lyapunov function has been chosen to represent the total vibratory energy in the structure. A modulated homogeneous friction damping approach is proposed because there is strong similarities between the behaviour of a variable friction device and the MR damper [18]. In this control strategy, at each occurrence of a local maximum in the deformation of the device, the normal force applied to the frictional interface is updated to a new value. This method is originally developed for friction dampers but it is modified for the MR damper based on MR damper properties. A detailed comparison of the most common control strategies for MR dampers can be found in [10].

Besides the above-mentioned classical control strategies, several intelligent control algorithms based on soft computing techniques are used for controlling the MR damper. These techniques rely on proper training in the desired behaviour instead of accurate mathematical models. Thus, they are suitable for solving and modelling of highly complex systems, such as damping of a flexible structure by control of a non-linear semi-active damper. Examples of soft computing techniques for damping or control of structures are neural networks [21, 22, 23, 24], fuzzy logic [25, 26], genetic algorithms [27] and various hybrid systems [27, 28].

In this thesis an MR damper in a collocated control setting is used to reduce the vibrational response of a flexible structure, which is verified experimentally on a shear frame structure and numerically on benchmark problems. The effectiveness of negative stiffness in semi-active control design is demonstrated with different control strategies.

In this thesis four main objectives are considered. They are as follows:

- Development of semi-active control strategies for the MR damper.
- Modelling of direct and inverse dynamics of an MR damper and force tracking in closed-loop simulation.
- Closed loop implementation of the semi-active control strategies.
- Implementation of the semi-active control strategies on benchmark problems.

The first part of the thesis presents a framework for design of external dampers for damping of flexible structures. This is based on maximisation of the damping ratio of a critical vibration form and it follows the two-component reduction technique presented by Main and Krenk [29]. This analysis provides analytical expressions for the modal damping ratio, which indicates that effective damping can be obtained by imposing negative stiffness on the damper. Four types of collocated control strategies are considered: (a) pure viscous damping, (b) viscous damping with negative stiffness, (c) amplitude dependent friction damping with negative stiffness and (d) model reference neural controlling. In model reference neural controlling the reference model is considered as an optimal force-displacement hysteresis model of a friction damper with negative stiffness. The shape is primarily identified by Boston et al. [30] by an evolutionary algorithm. The optimal force from the controller is then used for determining the desired current for the MR damper from the inverse MR model, which is another task of the thesis and is discussed in the second part of the thesis. To improve the performance of the controller, the stiffness parts are considered as negative. It has been demonstrated by Iemura et al. [31] that optimal LQR control produces active damper forces for a structure with significant negative stiffness characteristics. In [32, 33] Iemura et al. further developed the strategy with pseudo negative stiffness dampers for seismically isolated structures and stay cables and demonstrated the effectiveness of negative stiffness by numerical simulations. Moreover, for damping of stay cables Li et al. [34] demonstrated a significant improvement due to the introduction of negative stiffness. Høgsberg [35] demonstrated the important role of negative stiffness in controlling of MR dampers for damping of flexible structures. Boston et al. [30] evaluated the optimal closed-form solution for friction damping with negative stiffness applying an MR damper to cable vibration and identified the optimal shape of the force-displacement hysteresis loop. Very recently, Weber et al. [36, 37] demonstrated control strategies considering negative stiffness on cables with an MR damper. However, the efficiency of these techniques is still to be investigated numerically and experimentally by different optimal approaches on building structures because maximum work done in earlier are mainly on benchmark building problem.

The second part of the thesis considers the realisation of the desired control force by an MR damper. The key to accurate tracking of the control force is a representative inverse model of the MR damper, where the applied current is determined via knowledge of the desired force. This part of the thesis presents a non-parametric modelling technique for neural network based system identification of the forward and inverse dynamics of the MR damper. The real MR damper input-output data has been considered as training data for identification of both the forward and the inverse model. The inverse feedforward neural network model is then used for force tracking for closed loop simulation.

The third part of the thesis presents closed loop implementation of the control strategies by use of a rotary MR damper on a five-floor shear frame structure with harmonic base

excitation. The shear frame structural model has been identified experimentally from a free decay test and by modal analysis.

Further in this thesis, two numerical studies based on benchmark problems are presented. One of the numerical studies deals with the performance of the introduced semi-active control schemes and is evaluated on the basis of the response of a base-isolated benchmark structure, introduced by Narasimhan et al. [38, 39], exposed to real earthquake record. For the second numerical study on benchmark problems, the evaluation is based on the response of a 76-floor wind excited tall building introduced by Yang et al. [40]. This building has been scaled and the scaled structure has been used in a wind tunnel test by Samali et al. [41] to generate along-wind and across-wind loading data. The control strategies are primarily based on modal analysis where an approximate solution is obtained as an interpolation between the solutions of the two limiting eigenvalue problems: the undamped eigenvalue problem and the constrained eigenvalue problem in which the MR damper is fully locked in its position. Optimal forces are evaluated for pure viscous, viscous with negative stiffness and friction damping with negative stiffness. All of these control strategies are applied to a flexible structure by an MR damper.

The text is organised as follows. In Chapter 2, a systematic approach to the neural network (NN) modelling of both the forward and the inverse behaviour of a rotary MR damper is discussed. An optimisation procedure demonstrates that accurate training of the NN architecture for the forward damper model is obtained with velocity and current as input states. A similar architecture is then used to train the NN of the inverse MR damper behaviour, but with the absolute values of velocity and force as input states to estimate the current that is always a positive quantity. The forward and inverse models are validated by several measurements at different displacement frequencies and with different constants and half-sinusoidal current records. The validation shows satisfactory results for the forward as well as the inverse model. The validated models are finally used to emulate pure viscous damping. This simulation demonstrates that the main error of the inverse NN based model is due to the modelling errors of the pre-yield behaviour of the MR damper.

Chapter 3 describes an experimental study to determine the system model parameters from test data. The experimental tests were performed using a shaking table. A five-mass shear frame structure has been used for model identification and it is excited by ground acceleration by the shaker. It is assumed that all the mass of the floor is lumped at the center of each floor. The stiffness of the model is determined from the mode shape which is constructed from the frequency transfer function from test data. The damping matrix is determined from the estimated damping ratio from a free decay test. This five-degree-of-freedom structure possesses five natural frequencies corresponding to the number of degrees of freedom. When the structure is subjected to the excitation, resonance is induced if the frequency of excitation is close to each of one of the natural frequencies of the structure. From the frequency response the resonance frequencies are determined. Validation of the model parameters is carried out by independent data sets and shows satisfactory results.

Collocated control strategies for a base excited shear frame building, where a single magnetorheological (MR) damper has been placed between ground and first floor are initially given in Chapter 4. The calibration of the desired damper force is based on maximisation of the damping ratio of the first vibration mode, and the associated damper current is determined by an inverse MR damper. Four types of collocated control strategies are considered: (a) pure viscous damping, (b) viscous damping with negative stiffness, (c) amplitude dependent friction damping with negative stiffness and (d) model reference neural controlling, which mimics the behaviour of friction damping with negative stiffness. For the last three models, the desired stiffness is considered as negative, apparently softening the structure in the location of the damper, so that the damping of the structure is increased while the transmission of the base excitation to the structure is potentially reduced. The closed-loop simulation is

discussed in detail.

In Chapter 5, closed loop implementation of control laws for vibration mitigation of the base excited five-floor building using a rotary MR damper is discussed. The experimental tests are performed using a shaking table and it is excited by harmonic base acceleration using a shaker. The MR damper is located in between ground and first floor. The inverse MR model is designed on the basis of the velocity of the damper and, moreover, some control laws are dependent on the velocity. Therefore, correct velocity estimation from displacement or acceleration data is very important. The Kinematic Kalman Filter (KKF) is used to estimate the velocity of the damper by fusing displacement and acceleration. A detailed description of the experimental setup and a comparison of the results are presented.

The numerical studies on the implementation of control strategies for vibration reduction for two benchmark problems are discussed in Chapter 6. Both the numerical study deals with the performance of the introduced semi-active control schemes. The first numerical study is evaluated on the basis of the response of a base-isolated benchmark structure exposed to real earthquake record and the second numerical study is evaluated on the basis of the response of a wind excited 76 floor tall building.

In Chapter 7, the conclusions of the presented work are summarised.

Chapter 2

Modelling and Identification of a Rotary MR Damper

Magnetorheological (MR) dampers used for controlled damping of structural vibrations have been given considerable attention during the last decades because they offer a possibility of adapting their semi-active force in real-time to the structural vibrations [42]– [45]. MR dampers are suitable for mitigation of vibrations in large civil engineering structures because they combine large control force ranges, low-power requirements, fast response time and failsafe performance [9]. MR dampers are either operated at zero or constant current, which is called passive-off and passive-on strategies [46] or they are controlled in real-time within a particular feedback loop [46, 47]. In the latter case the structural response is typically measured in the damper position and the MR damper current is controlled in real-time for minimum tracking error with respect to the desired control force. The force tracking task is usually solved by a feedforward model in order to avoid costly force sensors [46, 47, 48] in the real-time implementation. The inputs of the feedforward model are the actual collocated displacement, velocity or acceleration, or any combination of these states, and the actual desired control force. The output is the actual desired current. This feedforward model is also called the inverse model of the MR damper. The desired current is tracked by a current driver that compensates for the coil impedance of the MR damper. Therefore, an MR damper model is required with damper force, displacement, velocity or acceleration as possible input states and the damper current as model output. The forward model of the damper represents the damper itself, while the inverse model is used for e.g. tracking of a desired damper force in closed loop control. Many parametric and non-parametric forward models have been presented in the literature for MR dampers of the classical cylindrical type. Some of the prominent parametric approaches are the Bouc-Wen model, which captures both the pre- and post-yield regions [49, 50], the Dahl model, which basically represents current dependent friction [51, 52], the Bingham model, which describes an elasto-plastic material behaviour with supplemental viscous effects [53] and the LuGre approach, which models the MR fluid particle chains as brushes with sticking and sliding effects against the damper housing [54, 55, 56]. These models have also been extended by additional stiffness, viscous and mass elements to account for the accumulator behaviour, the current dependent viscous force and the inertia of the damper piston and other accelerated parts [57, 58]. The parameters for minimum model error are typically obtained from the test data directly [59, 60] or by a numeric optimisation tool [61, 62, 63]. Once calibrated, these parametric approaches can be used as observers to solve the force tracking problem without feedback from a force sensor [48].

Non-parametric models are mainly based on fitted polynomials [47], genetic algorithms [64], fuzzy logic [65], neural networks [66]– [72] or hybrid approaches [73]. As demonstrated in [66] the neural network approach is able to model the forward MR damper behaviour fairly accurately. Most of the neural networks are trained with simulated input-output data, usually generated by the Bouc-Wen model, as e.g. in [68]. Few neural networks have been trained with measured data [72], containing system noise and knocking effects due to bearing tolerances. This makes the training of the network much more difficult. The neural network architecture is usually found by a trial and error method, and the resulting neural network architecture is therefore not necessarily optimal with respect to the minimisation

of the modelling error.

The present chapter provides a systematic approach to the design and calibration of neural networks of the forward and inverse behaviour of a rotary type MR damper based on measured data. The MR damper behaviour is measured at constant and half-sinusoidal current. The half-sinusoidal current tests are performed because they generate training data very similar to the current records associated with emulated viscous damping. In the first part of this chapter a parametric modified Bouc-Wen model of the rotary type MR damper is developed from experimental data sets. The original Bouc-Wen model has been modified to capture the important characteristics of the MR damper behaviour. But the parametric approach is only suitable to model the forward dynamics of the MR damper, while the inverse dynamics are difficult to obtain and model because of the complicated and highly non-linear properties of the MR damper model. The chapter further on describes a semi-systematic approach to a suboptimal neural network architecture for finding the minimum modelling error. The architecture of the neural networks for both the forward and the inverse MR damper models is presented. The forward and inverse models are validated by measurement data that is independent of the training data, and good accuracy is reported. Finally, the validated inverse and forward models are used in numerical simulations, where pure viscous damping is reproduced in real-time. The detailed methodologies about forward and inverse MR damper modeling using neural network are also discussed in [P1, P5].

2.1 Experimental Setup

The MR damper considered is an MR damper of the rotary type manufactured by Maurer Söhne GmbH with a maximum current limit of 4 A. The damper is shown in Figure 2.1 with the hydraulic test set up. The rotary type MR damper consists of a housing including the MR fluid and the rotating part of the disc. The MR fluid is a suspension of oil with magnetizable particles with average diameter of 5 μm and some additives. The particles and the ferromagnetic parts of the housing and of the disc are magnetized by the magnetic field that is produced by two coils which are installed within the housing at both sides of the disc. The magnetized particles built chains and stick to the disc and to the housing When the disc starts to rotate the particle chains are initially stretched before they start to slide relative to the surfaces of the disc and/or the housing. The particle chains may also break, whereby rupture between particles occurs. The phase where particle chains are elastically stretched is commonly denoted as the pre-yield region of the MR fluid, while the sliding phase is called the post-yield region. The particle chains start to slide when the dry friction force between particles or between particle chains and disc or housing is balanced by the elastic force due to elongation of the particle chains. Since this sticking depends strongly on the magnetization of the MR fluid, and thereby on the MR damper current, the post-yield force of the MR damper typically exhibits a strong current dependency. Because the superposed viscous force is usually rather small and the MR fluid viscosity depends only slightly on the coil current, the applied current primarily controls the friction force of the MR damper, while the viscous force component is mainly governed by the rotating speed of the disc and the inherent viscosity of the MR fluid. In order to be able to control the total MR damper force relative to a desired control force, the coil current must be modulated so that the control force tracking error is acceptable. Due to the non-linear beaviour of the MR damper force, i.e. the non-linear relation between current and sticking force and the non-linear current dependency of the MR fluid viscosity, feedback control only with a force sensor may fail to track the desired force accurately. Figure 2.2(a) shows a close-up of the damper of the rotary type at the Swiss Federal Laboratory of Material Science and Research (EMPA) and the schematic diagram of the damper is shown in Figure 2.2(b). Further details on the damper characteristics can be found in [48, 60] and also in [P1]. The damper force is slightly velocity dependent and the force level is approximately 30 N at 0 A and 300 N

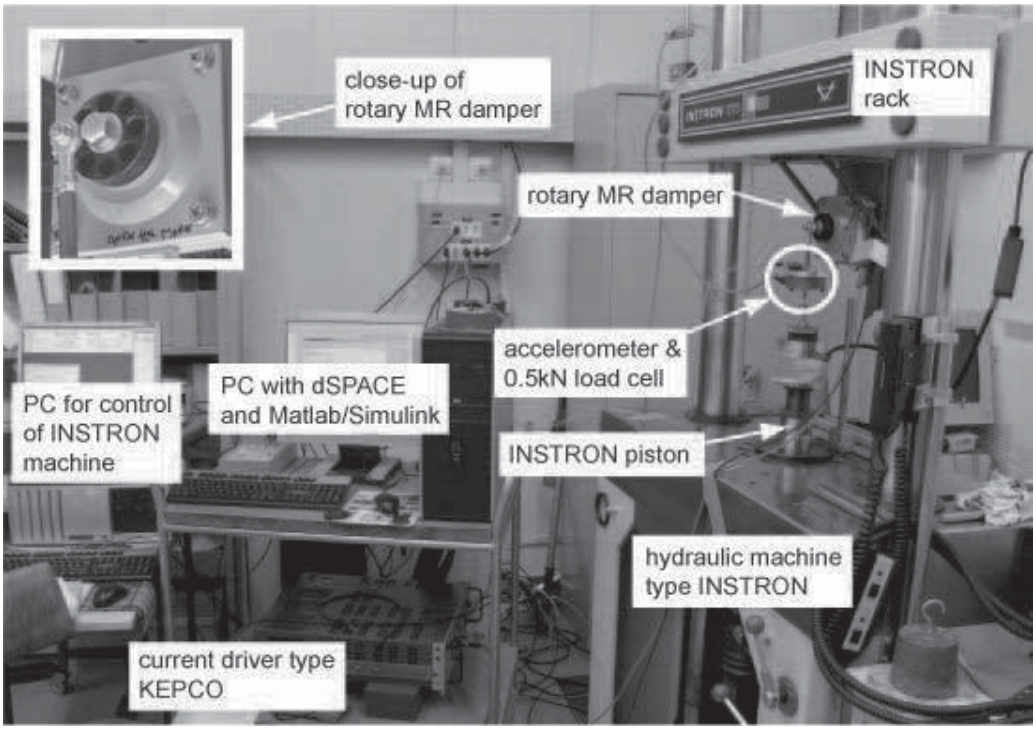

FIGURE 2.1: Hydraulic test set-up with rotary MR damper.

at 4 A. The training and the validation data is obtained from forced displacement tests using a hydraulic testing machine of the INSTRON type, see Figure 2.1. The desired piston displacement is defined in Matlab/dSPACE that outputs the displacement command signal to the INSTRON PC unit. A flow diagram of the experimental setup is shown in Figure 2.3.

The actual displacement is captured directly as output from the INSTRON machine and acquired by the dSPACE system at a sampling frequency of 1000 Hz. The sampling frequency for the force and acceleration measurements are 1000 Hz. The desired MR damper current is also defined in Matlab/dSPACE. The output, i.e. desired current, is tracked using a

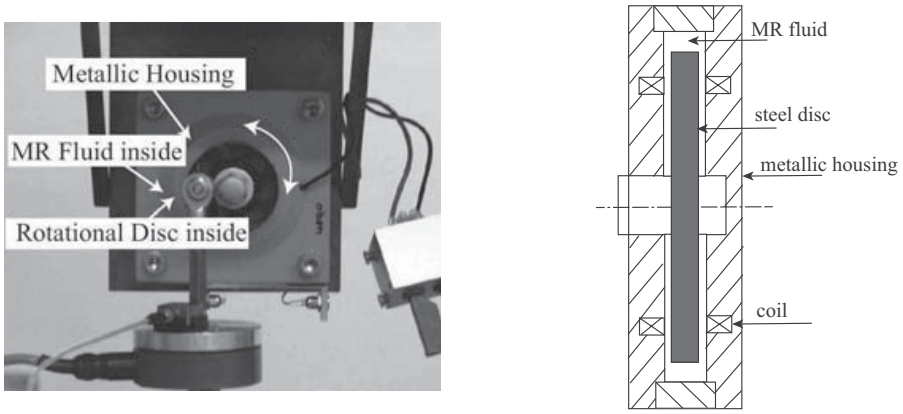

FIGURE 2.2: Rotary MR damper (a) and Schematic view of the damper (b)

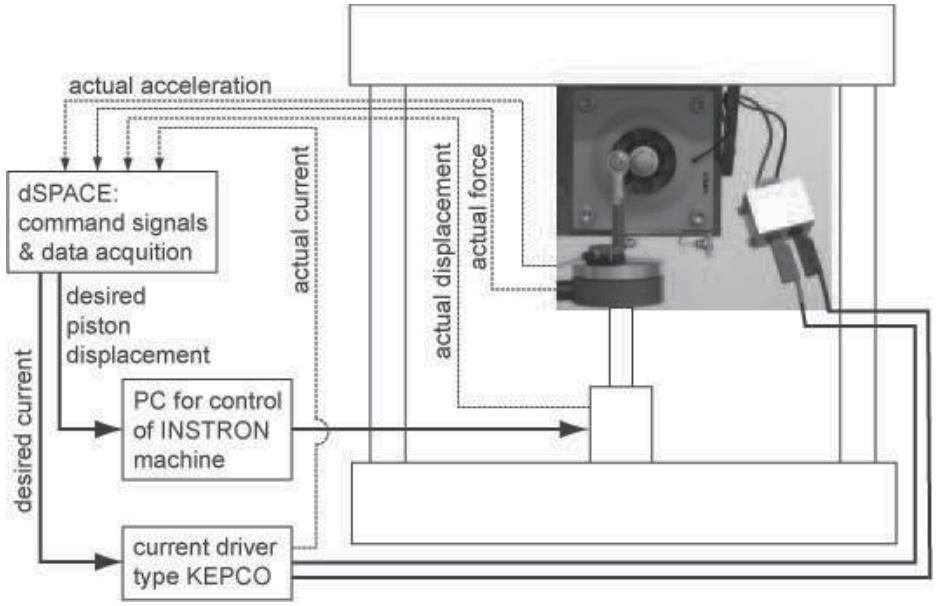

FIGURE 2.3: Schematic of test set-up.

current driver of the KEPCO type. The actual damper current is measured by the KEPCO amplifier and acquired by the dSPACE system. The MR damper force is measured by a 500 N load cell manufactured by PCM, and the acceleration of the piston is also measured in order to use it later, if required, as training data. Furthermore, the acceleration is suitable for detection of the knocking effects due to the finite bearing tolerances of 0.01-0.02 mm of the joints of the damper rod. A summary of the tests conducted is provided in Table 2.1. Each test is performed twice: The first set is used as training data, while the second completely independent set is used to validate the neural network models. Tests 1-10 are performed at constant current, while tests 11-19 are conducted at half-sinusoidal current, which is the mathematically absolute value of current. As seen in Table 2.1 the desired displacement is pure sinusoidal, combining amplitudes of 5 mm and 10 mm, and frequencies range from 0.5 Hz to 2.2 Hz [P1]. The training set and validation data set are separated each other by combining different displacement and current with different amplitude and different frequency. The table only showing some data example. This amplitude range of displacement is based on practical information about the structure which is used for implementing control strategies. The amplitude range contains the maximum amplitude which the structure can sustain before collapse. Moreover, in the frequency range the first resonance frequency of the structure is contained.

2.2 Parametric Model of the MR Damper: Simplified Bouc-Wen Model

The rotational MR damper is modelled using the simplified Bouc-Wen hysteresis model. The parameters of the model have been calibrated from data sets generated by experiments, where the damper has been driven harmonically in a testing machine at various frequency-amplitude combinations of current and displacement. The modified Bouc-Wen model by Spencer et al. [11] was formulated for the cylindrical type MR damper. In the present case this model is slightly simplified, mainly because the cylindrical damper concept has no need for an accumulator chamber, which for many dampers of the cylindrical type introduces an additional stiffness component in the mathematical model. A schematic diagram of the

TABLE 2.1: Measurement data for training of NN and model validation.

training set	validation set	desired displacement	desired current
1a	1b	sine, 5 mm, [0.5, 1.0, 1.27, 1.8, 2.2] Hz	0 A
2a	2b	sine, 5 mm, [0.5, 1.0, 1.27, 1.8, 2.2] Hz	1 A
3a	3b	sine, 5 mm, [0.5, 1.0, 1.27, 1.8, 2.2] Hz	2 A
4a	4b	sine, 5 mm, [0.5, 1.0, 1.27, 1.8, 2.2] Hz	3 A
5a	5b	sine, 5 mm, [0.5, 1.0, 1.27, 1.8, 2.2] Hz	4 A
6a	6b	sine, 10 mm, [0.5, 1.0, 1.27, 1.8, 2.2] Hz	0 A
7a	7b	sine, 10 mm, [0.5, 1.0, 1.27, 1.8, 2.2] Hz	1 A
8a	8b	sine, 10 mm, [0.5, 1.0, 1.27, 1.8, 2.2] Hz	2 A
9a	9b	sine, 10 mm, [0.5, 1.0, 1.27, 1.8, 2.2] Hz	3 A
10a	10b	sine, 10 mm, [0.5, 1.0, 1.27, 1.8, 2.2] Hz	4 A
11a	11b	sine, 5 mm, [0.5, 1.0, 1.27, 1.8, 2.2] Hz	half-sin, 0 A, [0.5, 1.0, 1.27, 1.8, 2.2] Hz
12a	12b	sine, 5 mm, [0.5, 1.0, 1.27, 1.8, 2.2] Hz	half-sin, 1 A, [0.5, 1.0, 1.27, 1.8, 2.2] Hz
13a	13b	sine, 5 mm, [0.5, 1.0, 1.27, 1.8, 2.2] Hz	half-sin, 2 A, [0.5, 1.0, 1.27, 1.8, 2.2] Hz
14a	14b	sine, 5 mm, [0.5, 1.0, 1.27, 1.8, 2.2] Hz	half-sin, 3 A, [0.5, 1.0, 1.27, 1.8, 2.2] Hz
15a	15b	sine, 5 mm, [0.5, 1.0, 1.27, 1.8, 2.2] Hz	half-sin, 4 A, [0.5, 1.0, 1.27, 1.8, 2.2] Hz
16a	16b	sine, 10 mm, [0.5, 1.0, 1.27, 1.8, 2.2] Hz	half-sin, 1 A, [0.5, 1.0, 1.27, 1.8, 2.2] Hz
17a	17b	sine, 10 mm, [0.5, 1.0, 1.27, 1.8, 2.2] Hz	half-sin, 2 A, [0.5, 1.0, 1.27, 1.8, 2.2] Hz
18a	18b	sine, 10 mm, [0.5, 1.0, 1.27, 1.8, 2.2] Hz	half-sin, 3 A, [0.5, 1.0, 1.27, 1.8, 2.2] Hz
19a	19b	sine, 10 mm, [0.5, 1.0, 1.27, 1.8, 2.2] Hz	half-sin, 4 A, [0.5, 1.0, 1.27, 1.8, 2.2] Hz

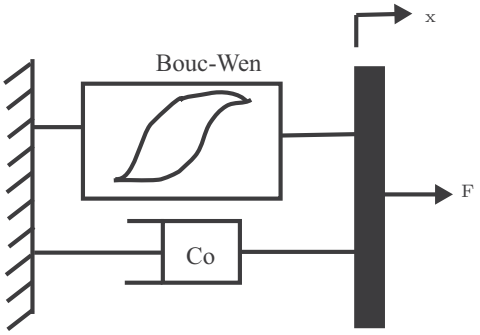

FIGURE 2.4: Bouc-Wen model of MR damper

simplified Bouc-Wen model is shown in Figure 2.4.

The governing equations for the damper force f predicted by the present Bouc-Wen model can be written as follows:

$$f = \alpha z + c_0 \dot{x} \tag{2.1}$$

where the hysteresis effect follows from the evolutionary variable z controlled by the Bouc-

TABLE 2.2: MR damper parameters

α_a	4.038 N/m	η	100 s^{-1}
α_b	1.984 N/m	γ	410 s^{-2}
α_c	7.901 N/m	β	410 s^{-2}
α_d	-0.704 N/m	A	1000
c_{0a}	10 Ns/m	c_{0b}	100 Ns/m

Wen equation

$$\dot{z} = -\gamma|\dot{x}|z|z|^{n-1} - \beta\dot{x}|z|^n + A\dot{x} \tag{2.2}$$

The gain parameters on the hysteresis effect and the viscous effect are in the present case described by cubic and linear functions of the applied current, respectively:

$$\alpha = \alpha_a + \alpha_b u + \alpha_c u^2 + \alpha_d u^3 \quad , \quad c_0 = c_{0a} + c_{0b} u \tag{2.3}$$

The dynamics involved in the MR fluid reaching equilibrium state is represented through first order filter. The applied current u is described with a time delay relative to the desired current I by the following first order filter:

$$\dot{u} = -\eta(u - I) \tag{2.4}$$

A Nelder-Mead direct search simplex method based on multidimensional unconstrained nonlinear optimization is available by the standard MATLAB function *fminsearch*. It is used to estimate the parameters of the modified Bouc-Wen model by minimizing a scalar quadratic cost function of the system variables of the model. It is turns out this is a simple and effective derivative free optimization method. The objective function used for minimization in the direct search method is the RMS value of error between the measured and predicted force values. The parameters of the rotary type MR dampers are derived from measurement data from the real MR damper. Maximum number of iteration is 1000 and the minimum error is 0.01. Convergence is an important issue for this algorithm. Sometimes this algorithm converge on non-stationary point instead of stationary point.This can be solved by restart the algorithm with the final point as the new initial guess. The flow chart for the parametric identification method of rotary type MR damper from experimental data is shown in Figure 2.5. The estimated parameters of the simplified Bouc-Wen model for the rotational MR damper are given in Table 2.2. The value of n is 2.

Typical force-displacement and force-velocity hysteresis loops for the rotational MR damper at different constant current are shown in Figure 2.6. It is visible that the MR damper behaves approximately as a friction damper where the friction force level can be altered by changing the applied damper current. The opening of the force-velocity loops indicates some pre-yield stiffness. The predicted force and the measured force value are compared in time domain. The force-displacement hysteresis diagram for measurement data and predicted data from the Bouc-Wen model are compared. In Figure 2.7(a,c), the comparisons of the measured force data and the predicted force data from the model at constant current 0 A and sinusoidal displacement of 5 mm at two different frequency 0.5 Hz and 1.0 Hz are illustrated. The comparision between force-displacement trajectories for measured and predicted force data at constant current 0 A and sinusoidal displacement of 5 mm at two different frequency 0.5 Hz and 1.0 Hz are also shown in Figure 2.7(b,d). The model validations in time domain and force-displacement trajectories for constant current 2 A and sinusoidal displacement 5 mm, 1.0 Hz are shown in Figure 2.8(a,b)and for sinusoidal current 4 A, 2.0 Hz and sinusoidal displacement 5 mm, 2.0 Hz are shown in Figure 2.8(c,d). The model validations in time

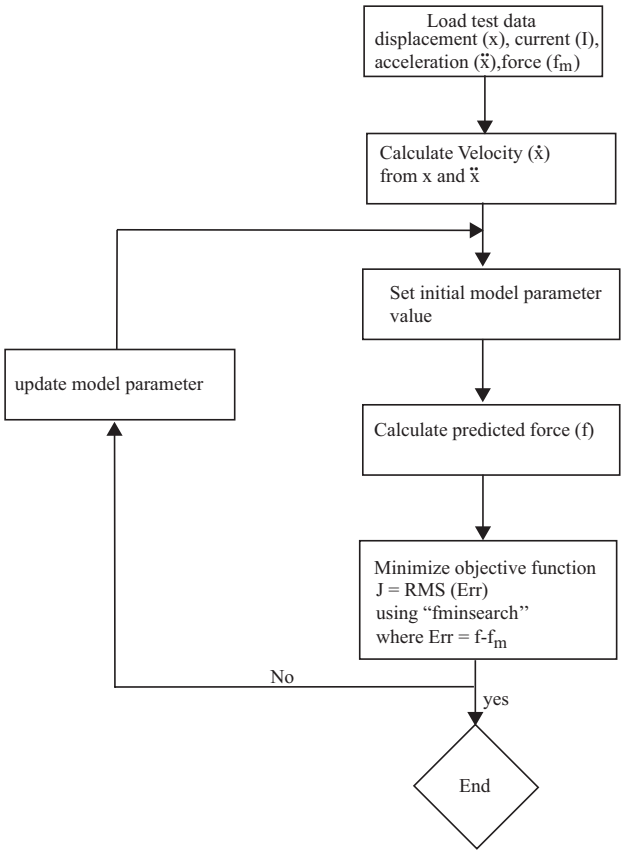

FIGURE 2.5: Parametric identification flow chart.

domain and force-displacement trajectories for sinusoidal current 1 A, 1.0 Hz and sinusoidal displacement 5 mm, 1.0 Hz are shown in Figure 2.9(a,b) and for sinusoidal current 3 A, 1.0 Hz and sinusoidal displacement 5 mm, 1.0 Hz are shown in Figure 2.9(c,d). The measured and predicted forces from model are quite identical, but the Bouc-Wen model has significant limitation in the post yield region because the real rotary damper has high nonlinearity in post yield region which is not properly described by Bouc-Wen model. It is also visible in

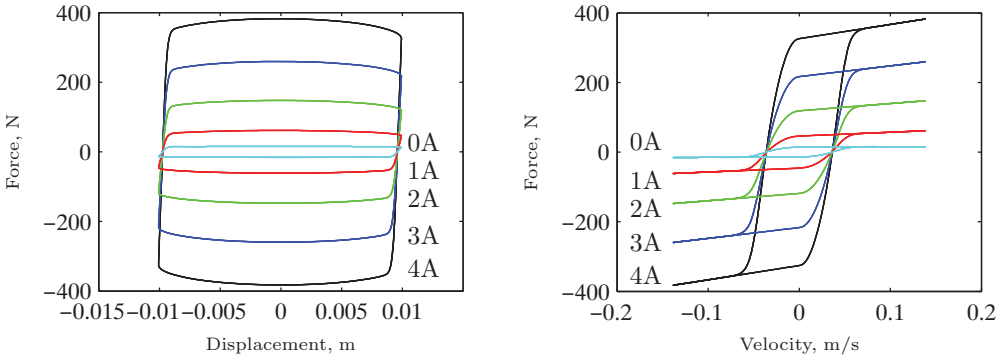

FIGURE 2.6: Force-Displacement (a) Force-Velocity hysteresis loop (b)

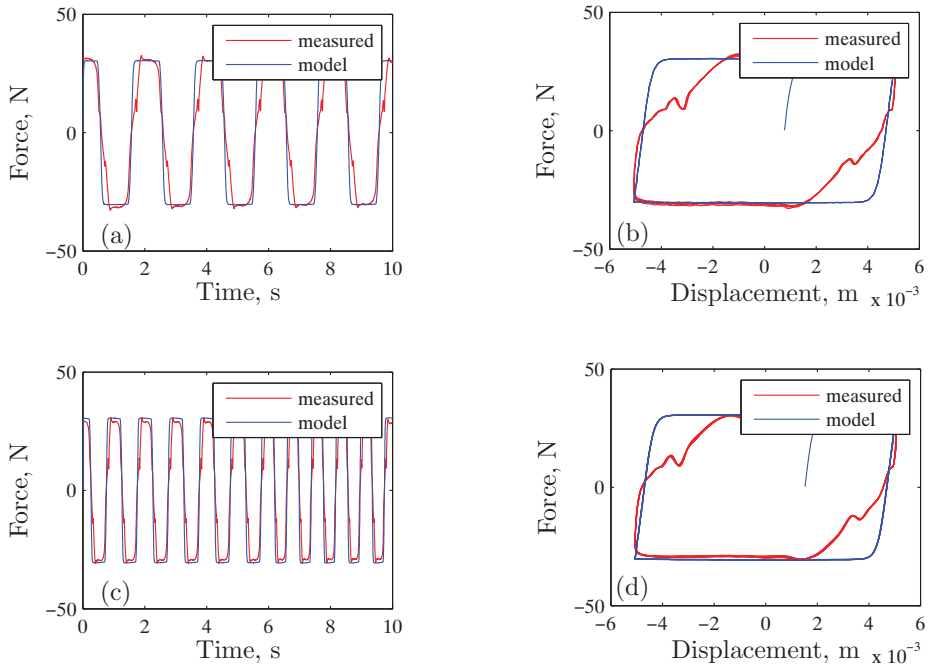

FIGURE 2.7: Model validation at current 0 A, displacement 5 mm, 0.5 Hz (a,b), Model validation at current 0 A, displacement 5 mm, 1.0 Hz (c,d)

the above mentioned figures that there is certain asymmetry in the hysteresis loops of the MR damper obtained from the measurement data. This asymmetry is mainly due to the so-called stribeck effect, which occurs between the pre- and post-yield regions. It is one of the important issues concerning the accurate modelling of rotary type MR dampers. Figure 2.7 shows the damper response at zero current and fairly slow motion with frequencies of 0.5 Hz and 1.0 Hz. In Figure 2.8 the current is increased to 2 A and 4 A, while the frequency is also increased slightly. Furthermore, the 4 A case is for sinusoidal current with frequency 2.0 Hz. Thus, this figure shows the effect of non-constant damper current, and the difference to the passive case is clearly observed. In Figure 2.9 the current is also sinusoidal at low amps and slow motion. In that case the deviation from typical passive behaviour is not as significant. Pinching effect is visible in MR damper hysteresis diagram and this is mainly due to MR fluid flow constriction between disc and the metallic housing in rotational MR damper. The preliminary results for the Bouc-Wen model in Figures 2.7-2.9 show that the rotary MR damper can be represented by the parametric Bouc-Wen model, but due to some limitations it has difficulties representing some of the highly non-linear effects. For this reason the non-parametric approach based on neural network modelling is adopted for a proper and accurate modelling of both the forward and inverse MR damper dynamics.

2.3 Non-Parametric Neural Network Model of MR Damper

This section describes the post processing of the measurement data and the training of the neural network. Section 2.3.1 describes the filtering of the measurement data and how the single test series are combined to get a full training data time history. In Section 2.3.2 the neural network architecture is optimised, while Subsection 2.3.3 presents the identified neural network models used to model both the forward and the inverse MR damper characteristics.

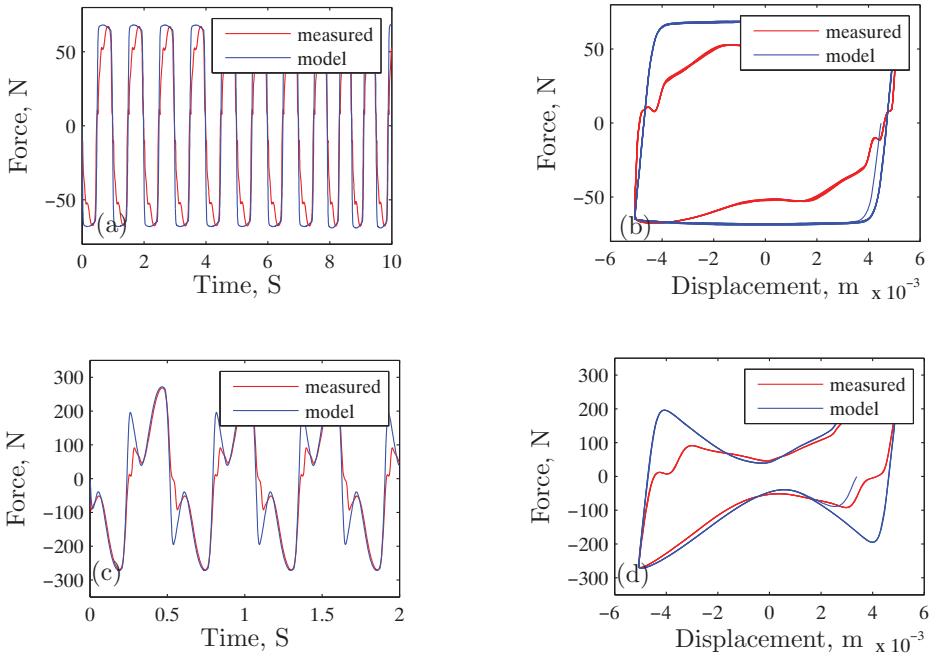

FIGURE 2.8: Model validation at current 2 A, displacement 5 mm, 1.0 Hz (a,b), Model validation at current sin 4 A, 2.0 Hz displacement 5 mm, 2.0 Hz (c,d)

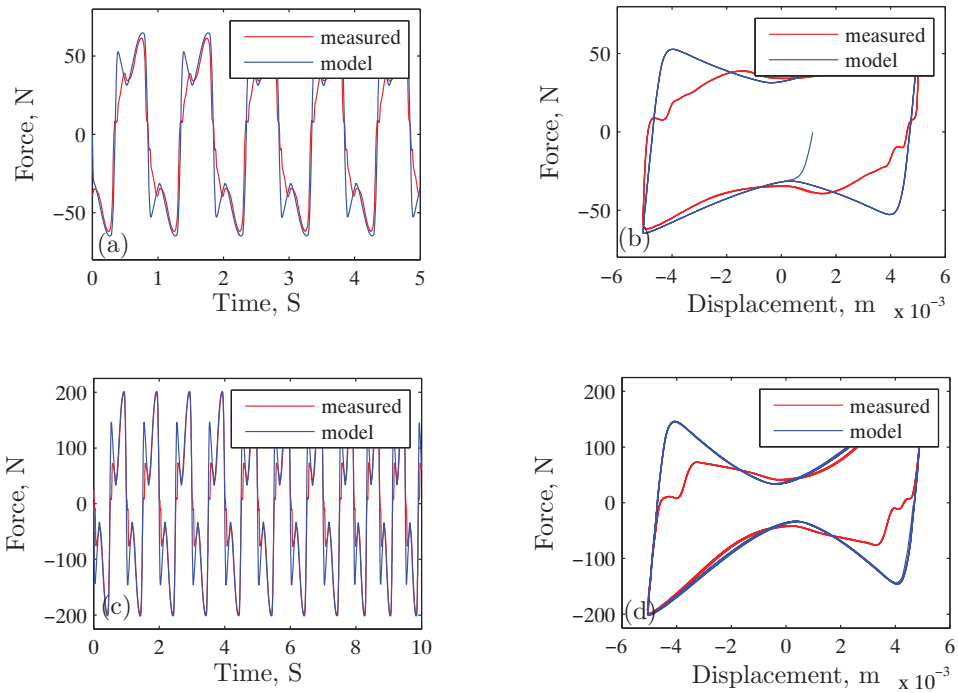

FIGURE 2.9: Model validation at current sin 1 A, 1.0 Hz displacement 5 mm, 1.0 Hz (a,b), Model validation at current sin 3 A, 1.0 Hz displacement 5 mm, 1.0 Hz (c,d)

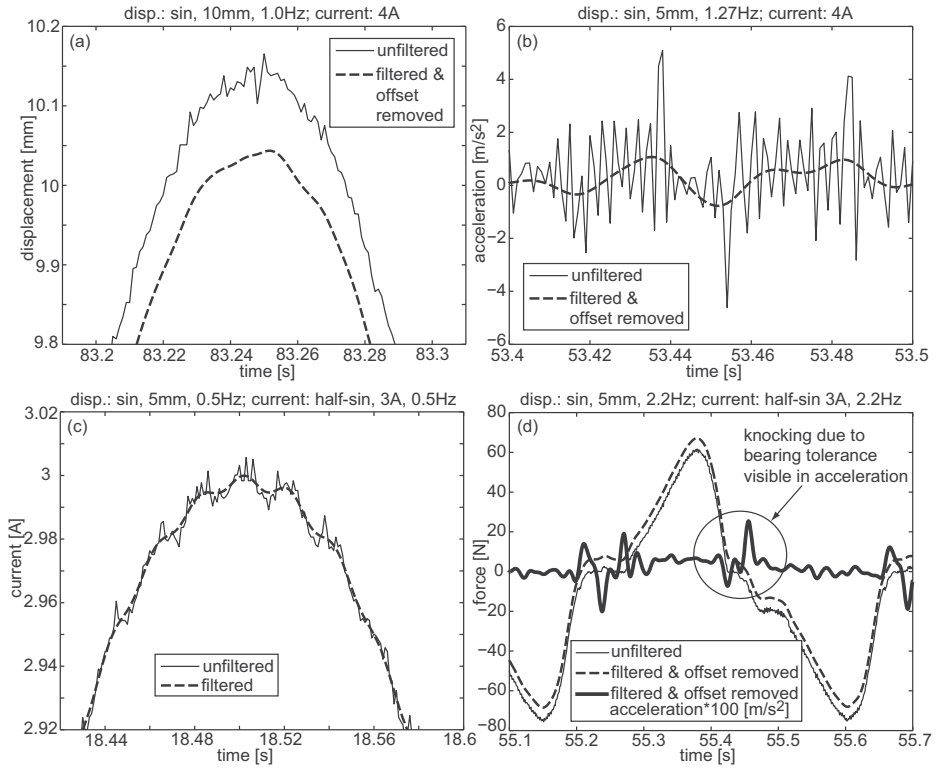

FIGURE 2.10: Filtering of measurement data.

2.3.1 Post Processing of Measurement Data

The measurement data from the rotary MR damper from the test setup contains noise and has also some offset. The measurement data is initially passed through a low-pass filter in order to avoid that the neural network is trained by high-frequency signal components, e.g. due to noise and knocking effects [P1]. These types of external effects typically result in an increasing modelling error in the neural network models. The applied low-pass filter has the following properties:

- Digital Butterworth low-pass filter: It is very efficient for removing high-frequency noise from measurement data.
- Filter order 2: The filter order is kept low so that the main shape and the peak values of the measurement data are not altered.
- Cutoff frequency 100 Hz: The cutoff value is kept higher to remove the high-frequency noise from the measurement data without losing its proper shape.

Any offset in the displacement, acceleration and force signals is removed by simply balancing of positive and negative maxima under steady state conditions. Another possibility of removing offset is a high-pass filter. But in the present case the simple adjustment via the sequence of minima and maxima effectively removes the offset. The effect of the filtering of displacement, acceleration, damper current and the damper force is shown in Figure 2.10. For the displacement and the damper current the high-frequency dithers are carefully removed by the low-pass filter, and the main task is basically to avoid a too significant change in the phase and a reduction in the peak values. This is shown in Figure 2.10(a), where

the displacement amplitude is 10 mm and the frequency is 1.0 Hz, and in Figure 2.10(c), where the damper current is half-sinusoidal with an amplitude of 3 A. The acceleration measurements are very sensitive to the various sources of noise, and the influence of the filter therefore becomes evident in Figure 2.10(b). Figure 2.10(d) shows the damper force, where the main modification is the removal of the offset level. Note that the constant force level at zero crossing is due to the previously mentioned knocking because of finite bearing tolerances. The effect is mainly visible in the acceleration signal, which is also shown in Figure 2.10(d). This effect has a significant influence on the neural network modelling, and a proper filtering is therefore important [P1].

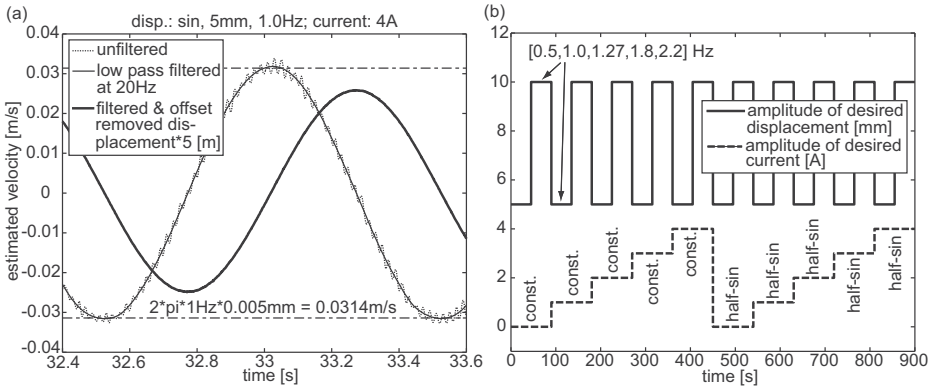

FIGURE 2.11: Estimated velocity (a) and training data time history (b).

The training of the NN also requires the damper velocity $\dot{x}$, which is not directly measured. It is instead estimated at each time instant k by numerical differentiation of the displacement x as

$$\dot{x}(k) = \left(\frac{x(k) - x(k-1)}{t(k) - t(k-1)} \right) \tag{2.5}$$

with initial condition

$$\dot{x}(1) = 0 \tag{2.6}$$

The inherent noise resulting from the numerical differentiation is subsequently removed by the following low-pass filter:

- Digital Butterworth low-pass filter.
- Filter order 2.
- Cutoff frequency at 20 Hz: Strong filtering is needed and a fairly low cutoff frequency is selected.

The so-called Kinematic Kalman filter is another approach to deriving the velocity when displacement and acceleration are available. This will be discussed in Chapter 5. However, for this case numerical differentiation gives sufficient and good training data after some filtering.

Figure 2.11(a) shows the velocity record obtained by differentiation of the sinusoidal displacement at an amplitude of 5 mm and a frequency of 1 Hz. The amplitude of the velocity is 31 mm/s, which agrees well with the analytical value of 31.4 mm/s obtained from a displacement signal at an amplitude of 5 mm and a frequency of 1.0 Hz. The figure also shows the corresponding displacement, and it is observed that the phase shift between displacement and velocity is one quarter of a period. The displacement amplitude in Figure 2.11(a)

is multiplied by 2π. Figure 2.11(a) therefore demonstrates that the method in (2.5,2.6) leads to a velocity signal with the correct amplitude and phase compared to the measured displacement.

After the signal post processing, 10 steady state cycles of the data sets 1-19 in Table 2.1 are isolated and then connected one after each other to get a single continuous time history for displacement, velocity, acceleration, current and force, respectively. The measured displacement data is selected as a sinusoidal signal at two different amplitudes of 5 mm and 10 mm. These amplitude values are selected because the maximum amplitude of the damper displacement is expected to be located in the this range when operating on the shear frame structural model. Each amplitude is combined with five different frequencies in the range from 0.5 Hz to 2.2 Hz, which contains the resonance frequency of the first vibration mode of the shear frame structure. In this way, 10 displacement data sets are produced. And since velocity is obtained by numerical differentiation also 10 velocity data sets are available. The damper current is produced in two ways. A constant current at different constant values from 0 A to 4 A are taken as the initial current input, while half-sinusoidal current records are also applied at five different amplitudes from 0 A to 4 A. Each amplitude is characterized by five different frequencies from 0.5 Hz to 2.2 Hz. The amplitude range is selected between 0 and 4A because these values are the limiting values of the MR damper. Figure 2.11(b) shows the combination logic for the generation of the resulting time histories used for the neural network training and validation. It should be noted that the sets are always connected at zero crossings of the displacement. To have a reasonable amount of data for the training of the neural network, the time histories are finally downsampled from 1000 Hz to 200 Hz. The downsampling is very essential for proper training of neural network architecture.

2.3.2 Feedforward Backpropagation Neural Network Architecture

Two basic types of networks can be differentiated: networks with feedback and networks without feedback. For some networks it is characteristic that for every input vector laid on the network, an output vector is calculated, which can be read from the output neurons. In this case there is no feedback. Hence, only a forward flow of information is present. Networks with this structure are called feedforward networks. Backpropagation is one of the effective tools in feedforward networks. Backpropagation is a systematic approach to the training of multilayer neural networks, and it has a strong mathematical basis. It is a multilayer forward network using the extended gradient-descent based delta learning rule, commonly known as teh backpropagation of errors rule [74, 75]. A generalised multi-layer feedforward backpropagation neural network with one layer of z hidden units is shown in Figures 2.12. The y output unit has w_{oj} bias and the z hidden unit has v_{ok} as bias. The algorithm used to train the neural network architecture is given in Table 2.3.

Backpropagation provides a computationally efficient method for changing the weights in a feedforward network, with differentiable activation function units, to learn a training set of input-output examples. The aim of this network is to train the net to achieve a balance between the ability to respond correctly to the input patterns used for training and the ability to provide food responses to the input that are similar.

Modelling of a given system using the neural network tool requires basically three steps: (a) measurement of the input and output states of the system being considered, (b) choosing the architecture of the particular neural network and (c) training the chosen architecture with the measurement data [P1]. The neural architecture is characterised by:

- The kind of states used as inputs.
- The number of used previous values of input states.

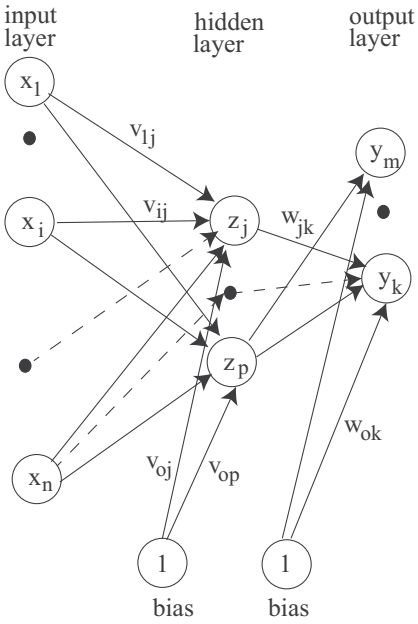

FIGURE 2.12: Feedforward Backpropagation Neural Network

- The number of hidden layers and neurons per layer.

Because of the large variety of modelling parameters, the trial and error method is often applied to find a neural network architecture with acceptable modelling errors. Using the trial and error approach the training yields the best parameters for the chosen neural network architecture, but not necessarily the best neural network architecture with the best parameters. The training algorithm of backpropagation involves four stages, viz.

- Initialization of weight
- Feed forward
- back propagation of errors
- updating of the weights and biases (if there are any)

At the first stage, which is initialization of weights, some small and random values are assigned. At the feedforward stage, each input receives an input signal and transmits this signal to each of the hidden units. Each hidden unit then calculates the activation function and sends its signal to each output unit. The output unit calculates the activation function to form the response of the net for the given input pattern. During the backpropagation of errors, each output unit compares its computed activation with its target value to determine the error associated with this unit for the pattern concerned. Based on the error, the factor is computed and used to distribute the error at the output unit back to all units in the previous layer. Similarly, the factor is computed for each hidden unit. At the final stage, the weight and biases are updated using the factor and the activation.

In the present work, a semi-systematic approach is used to find a neural network architecture close to the optimum. The procedure is illustrated schematically in Figure 2.13. A number of neural networks are trained to model the forward MR damper behaviour with the current records and one, or several, of the time histories for displacement, velocity and acceleration,

respectively, as input states. The number of previous states and the number of hidden layers and neurons are also varied. For all hidden layers the tangent sigmoid function is chosen as transfer function, while a linear transfer function is chosen for the output layer. All trained neural network approaches are based on the Levenberg-Marquardt optimisation method [74, 75], using the $error(k)$ between the target force $f(k)$ and the estimated force $\hat{f}(k)$ by backpropagation. When the training is finished, the neural network architecture is stored and a new neural network architecture is trained for different input properties. After all possible combinations of input data have been used for training of the neural networks architecture, the particular neural network architecture with the smallest modelling error is stored as the best neural networks architecture. This neural networks architecture is then denoted as the suboptimal neural network, because the transfer functions have not been varied. This systematic optimisation strategy shows the following trends:

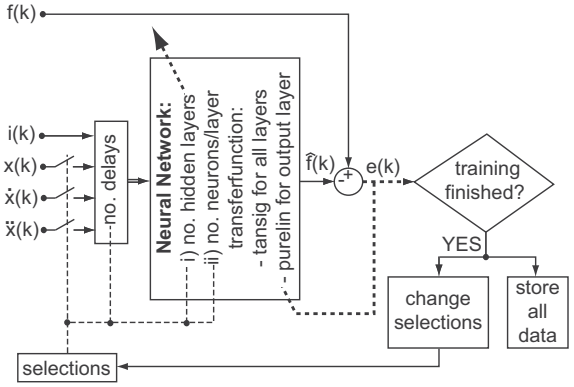

FIGURE 2.13: Procedure to find suboptimal neural networks architecture

- Velocity is a mandatory input besides current. This is also confirmed by the large number of parametric MR damper models that are based on velocity and current as input states.
- Using acceleration as additional input besides velocity and current increases the noise in the estimated force but not the model accuracy.
- Using displacement as additional input besides velocity and current does not decrease the modelling error. This can be explained by the fact that the velocity is determined from displacement (2.5). Another reason is that the rotary MR damper has no accumulator which is known to introduce stiffness and displacement dependence.
- Using displacement and acceleration besides velocity and current as additional inputs does not decrease the modelling error.
- It seems that three previous values, two hidden layers and six neurons per hidden layer provide a suitable compromise between modelling error and computational effort.

2.3.3 Neural Network Model Structure for MR Damper

For efficient operation of the backpropagation network, appropriate selection of the parameters used for the training is necessary.

The initial weights will influence whether the net reaches a global (or only a local) minimum of error and if so how rapidly it converges. If the initial weight is too large the initial input

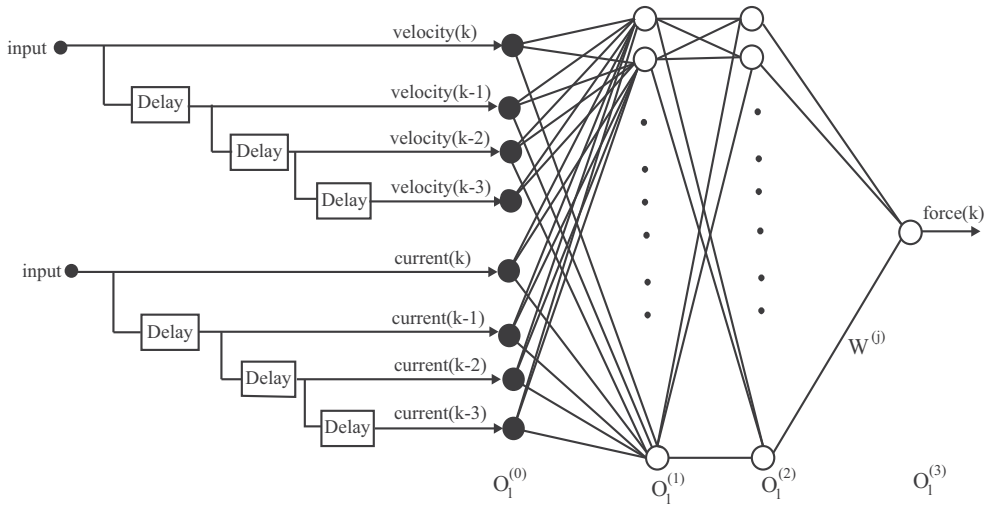

FIGURE 2.14: neural network architectures of forward MR damper model

signals to each hidden or output unit will fall in the saturation region where the derivative of the sigmoid has a very small value. If the initial weights are too small, the net input to a hidden or output unit will approach zero, which then causes extremely slow learning. To get the best result the initial weights are set to random numbers between -0.5 and 0.5 or between -1 to 1.

Selection of learning rate is also very important to efficient neural modelling. A high learning rate leads to rapid learning, but the weights may oscillate, while a lower learning rate leads to slower learning. In order to adopt an optimal learning rate, the learning rate is increased to improve the performance and decrease the error value.

The motivation for applying the backpropagation net is to achieve a balance between memorization and generalization. It is not necessary to continue the training until the error reaches a minimum value. The weight adjustment is based on training patterns. As long as the error for the validation decreases, the training continues. When the error begins to increase, the net is starting to memorise the training patterns, and at this point the training is terminated [P1, P5].

The forward NN architecture that is found to minimize the error of the forward MR damper model is based on velocity and damper current as input states, with three previous values each, and it contains two hidden layers of six neurons each. The architecture of the forward NN and the inverse NN are shown in Figure 2.14 and Figure 2.15, respectively. The transfer function $g^{(j)}$ of the neurone of the two hidden layers are selected as a tangent sigmoid function, while the transfer function of the single output layer, i.e. layer 3, is selected as a linear function. If $N^{(j)}$ is the number of neurons in the j^{th} layer then $N^{(3)} = 1$, since the output layer has only a single signal output. Let $O_l^{(0)}$ be the $R \times 1$ column vector comprising the signal inputs to the 1st hidden layer. In this case R is 8 because of the two input variables: velocity and current, both with a current and three previous values. Let $O_l^{(j)}$ be the $N^{(j)} \times 1$ vector comprising the signal outputs of the j^{th} layer. For the two hidden layers the output are computed in terms of the sigmoid transfer function as

$$O_l^{(j)} = g^{(j)}(W_l^{(j)} O_l^{(j-1)} + b_l^{(j)}) \qquad , \qquad j = 1, 2, 3 \tag{2.7}$$

The matrix $W_l^{(j)}$ contains the weights of the neural connections, while $b_l^{(j)}$ is the bias vector of the j^{th} layer, which is zero in the present application. The final output is $O_l^{(3)}$.

The architecture of the forward NN is shown in Figure 2.16 (a). Thus, the estimated force becomes

$$\hat{f}(k) = NN \begin{bmatrix} \dot{x}(k) & \dot{x}(k-1) & \dot{x}(k-2) & \dot{x}(k-3) \\ i(k) & i(k-1) & i(k-2) & i(k-3) \end{bmatrix} \tag{2.8}$$

where $NN[..]$ represents the neural network function and i is the damper current. Figure 2.16 (b) shows the corresponding neural network for the inverse damper model, which is also based only on velocity besides the damper force as input states. In order to estimate the MR damper current $\hat{i}(k)$ the neural network for the inverse model uses the actual and three previous values of the two input states,

$$\hat{i}(k) = NN \begin{bmatrix} |\dot{x}(k)| & |\dot{x}(k-1)| & |\dot{x}(k-2)| & |\dot{x}(k-3)| \\ |f(k)| & |f(k-1)| & |f(k-2)| & |f(k-3)| \end{bmatrix} \tag{2.9}$$

Irrespective of the sign of velocity and/or force, the damper current is always a positive quantity. Therefore, the neural network architecture is trained using the absolute values of the two input states. This approach helps to avoid the estimated current exhibiting negative spikes when, e.g. tracking a desired viscous damping force. Thus, the modelling error is minimized.

2.4 Model Validation

The model validation is carried out for independent and experimentally determined time records. Sections 2.4.1 and 2.4.2 consider the neural network of the forward and inverse damper model, respectively, while Section 2.4.3 demonstrates that the presented neural model is able to emulate pure viscous damping.

2.4.1 Forward MR Damper Model

The forward MR damper model is validated using the validation data sets 1b-19b listed in Table 2.1. Due to the large amount of validation data, the measured and simulated force displacement trajectories are compared for some selected tests. The selection is made such that the comparison is depicted for all displacement amplitudes, frequencies and currents. Figure 2.17 and 2.18 show the results for constant current, and Figure 2.19 and 2.20 those for half-sinusoidal current. As seen from the figures, the forward MR damper model is able

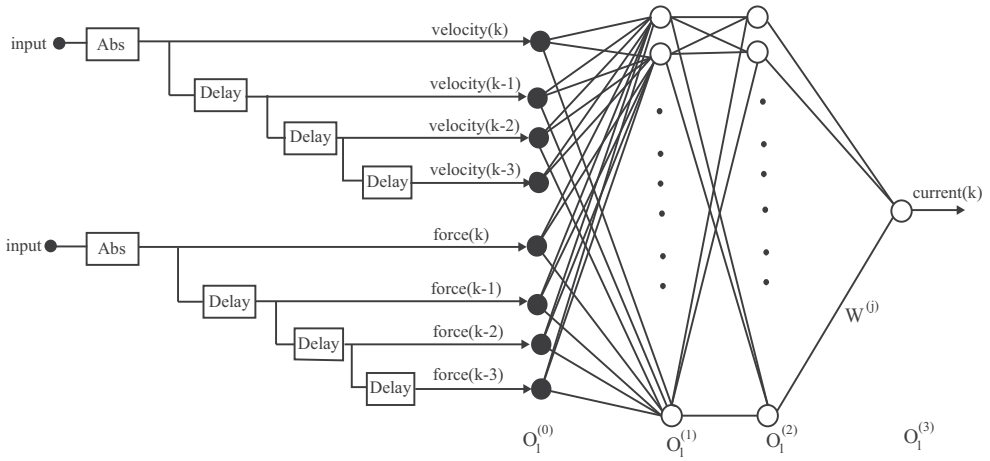

FIGURE 2.15: neural network architectures of inverse MR damper model

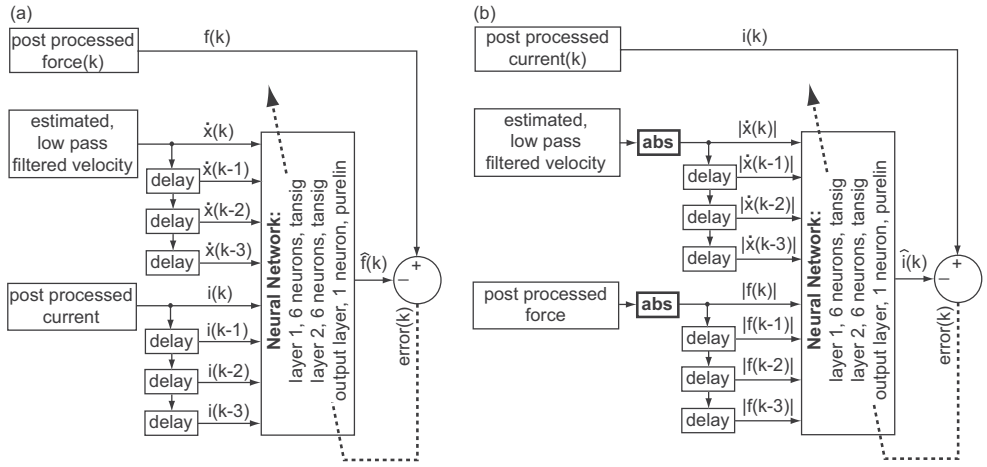

FIGURE 2.16: neural network architectures of forward (a) and inverse (b) MR damper models and their training.

to predict the main characteristics of the MR damper being considered with fairly good accuracy: The strong current dependent yield force is captured well, the slope of the pre-yield region is estimated very accurately in all cases [59, 60] and the force response due to the aggregation and radial migration of particles [56], which is visible by the rather slow force increase after the damper rod turns it direction, is also predicted satisfactorily. It is evident that all of the major damper characteristics are predicted significantly better for the half-sinusoidal current in Figures 2.19 and 2.19 than for the constant current case shown in Figures 2.17, 2.18. The harmonic signal for the current is most effective for the neural network training because the MR damper runs smoothly with harmonic current input at different amplitudes and frequencies.

2.4.2 Inverse MR Damper Model

The inverse MR damper model is also validated using the validation data sets 1b-19b in Table 2.1. The results for constant current, two different displacement amplitudes and four different displacement frequencies are shown in Figures 2.21(a) and (b). The estimated current shows significant spikes that might occur because the neural network architecture has been trained not only with a constant current data but also with half-sinusoidal current data. This is partly verified by the fact that the spikes show the same frequency characteristics as the applied displacement. Similar results have also been reported in [68] and [72]. This property might indicate that the neural network has difficulties estimating a constant target state accurately if the input states change periodically over time. In contrast to the prediction of the constant current, the prediction of the half-sinusoidal current is fairly accurate for different displacement amplitudes, frequencies and current amplitudes, as shown in Figure 2.21(c,d) and in Figures 2.22 and 2.23. Despite the apparent modelling error due to the spikes of the estimated current, these spikes are rather small compared to e.g. the validation results presented in [68].

2.4.3 Emulation of Viscous Damping Using the Validated Model

In this section the forward and inverse models are used to determine how accurately pure viscous damping can be emulated by the rotary MR damper of the present study. Figure 2.24(a) illustrates the flow chart of this simulation study. The velocity of the MR

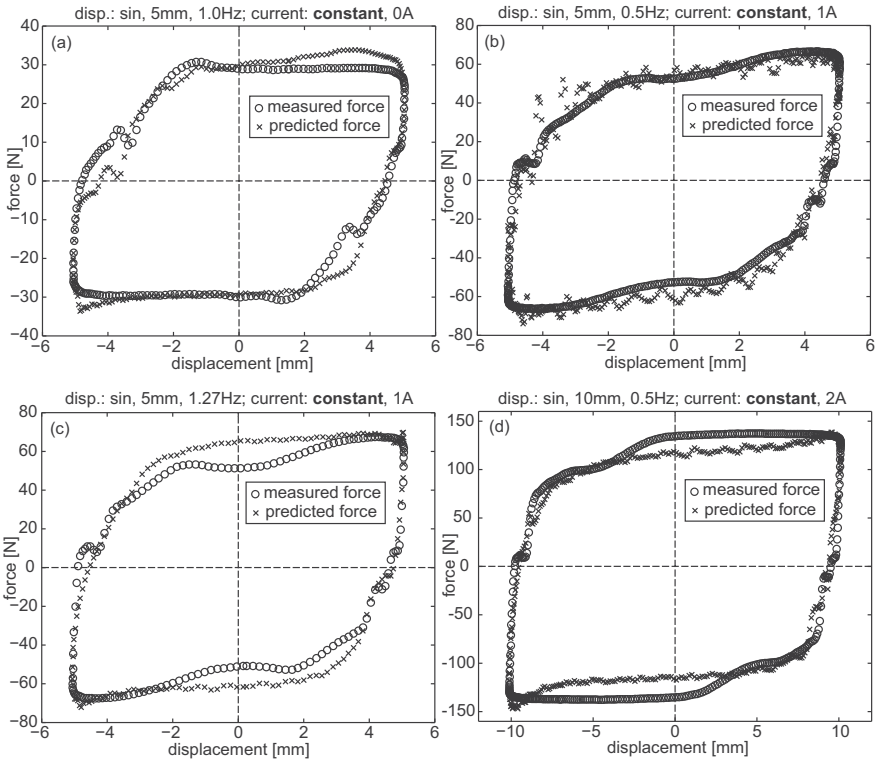

FIGURE 2.17: Validation of forward MR damper model for constant current of 0 A (a), 1 A (b,c) and 2 A (d) and different displacement amplitude and frequencies.

damper is assumed to be pure sinusoidal. This is a reasonable assumption for damping of lightly damped structures, where the structural response is typically dominated by resonance at the frequency of the critical vibration mode and with a slowly varying amplitude envelope. The desired control force is the product of velocity and the viscous coefficient c. The damper velocity and the desired control force are used as the input states for the inverse MR damper model, which then estimates the corresponding damper current that is applied to the MR damper in order to generate a pure viscous force. This force is estimated using the forward MR damper model. If the NN for the inverse and the forward MR damper model are sufficiently accurate the simulated damper force should be comparable to the corresponding pure viscous damper force. The simulation results are shown in Figures 2.24(b-d). The simulated current in Figure 2.24(b) exhibits two significant spikes on top of the approximately half-sinusoidal time history. The first spike should not occur because the desired force decreases to zero. Hence, zero current would be the best choice to track the desired viscous force as precisely as possible. The second current spike occurs when the MR fluid is operated within the pre-yield region. This spike is therefore needed because the actual MR damper force at 0 A within the pre-yield region is smaller than the desired viscous force that increases rapidly at extreme displacement due to the elliptic force displacement trajectory of viscous damping [48]. When the MR fluid is operated in the post-yield region, the current shows approximately a half-sinusoidal behaviour because of the sinusoidal behaviour of the desired force, see Figure 2.22(c). The non-linear relation between yield force and current and the force response due to the migration and aggregation of the particles in the MR fluid [56, 60] are the reasons why the current does not show a pure half-sinusoidal shape. Despite the mediocre estimate of the current at zero velocity and the slightly overestimated current in the pre-yield region, the time history of the damper force

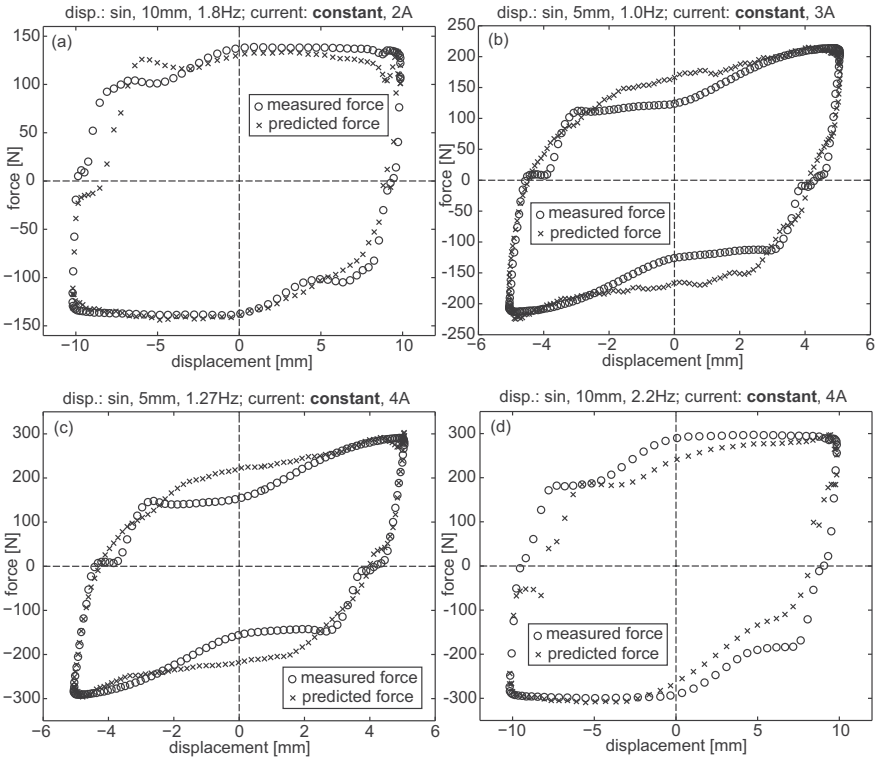

FIGURE 2.18: Validation of forward MR damper model for constant current of 2 A (a), 3 A (b) and 4 A (c, d) and different displacement amplitude and frequencies.

in Figure 2.24 (c) and the force velocity trajectory in Figure 2.24 (d) demonstrate that pure viscous damping is in fact tracked fairly accurately at velocities larger than 0.05 m/s.

2.5 Summary

This chapter has initially demonstrated a modified bouc-wen modelling approach towards rotary type MR damper and later described neural network based modelling of the forward and inverse behaviour of a rotary MR damper using measured data for training and validation. The measured data has been low-pass filtered in order to remove high-frequency signal parts that should not be considered by the neural network during training, and offset values were removed as well. The measured data resulting from two displacement amplitudes, five frequencies and both constant and half-sinusoidal current was combined sequentially to get one time history and downsampled from 1000 Hz to 200 Hz, so that the training data could be handled by the Matlab code for the given neural network architecture. It should be noted that too much training data may create problems in neural network design. An optimisation procedure has been presented for identifying a neural network architecture that minimises the error of the forward model. The procedure was tested with signals of measured displacement, measured velocity and measured acceleration or any combination of these three input states besides the measured current as input for the training. Furthermore, the number of previous values of the input states and the number of hidden layers and neurons have been altered to obtain the best numerical fit. To limit the computational time of this numerical optimisation, the transfer functions for the hidden and output layers were fixed to the tangent sigmoid function and the linear function, respectively. The present procedure

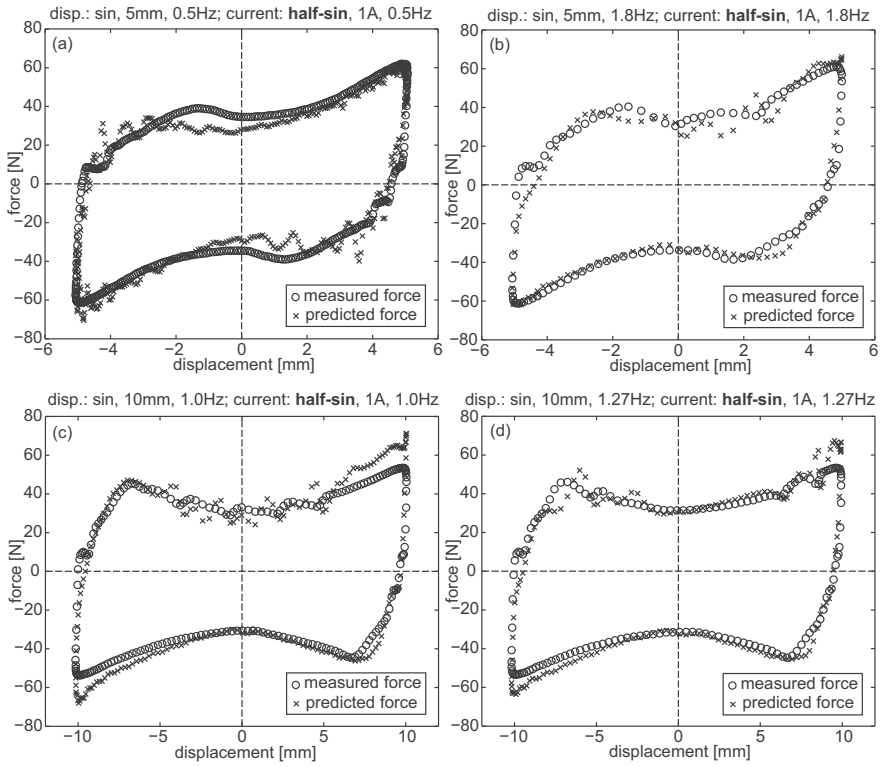

FIGURE 2.19: Validation of forward MR damper model for half-sinusoidal current of 1 A and different displacement amplitude and frequencies.

demonstrated that the modelling error is not decreased significantly:

- if displacement and acceleration are taken as inputs in addition to velocity, and
- if substantially more than three past values of the inputs are taken into account, and
- if substantially more than two hidden layers with more than six neurons are considered.

The same neural network architecture, but with force instead of current, has also been used to model the inverse MR damper behaviour. In this case, the absolute values of velocity and force are used for the training of the neural network that estimates current because current is always a positive quantity. This new approach helps to avoid the output current becoming negative when e.g. tracking a desired viscous force.

The trained forward and inverse MR damper models have been validated with measurement data that is independent of the training data. The validation data comprised also tests at two displacement amplitudes, five frequencies as well as both constant and half-sinusoidal current. The validation shows that the forward model is able to predict the MR damper force with high accuracy. Especially, the force response due to the migration and aggregation of the MR fluid particles is captured well, and the slope of the force displacement trajectory in the pre-yield region is predicted accurately. The validation of the inverse MR damper model shows two particular characteristics. When the measurement data has been obtained from constant current, the predicted current shows significant spikes at the same frequency as the damper displacement, and only the mean value of the predicted current is really accurate. In contrast, the prediction based on the half-sinusoidal current turns out to give very accurate results for all amplitudes and frequencies used in the tests.

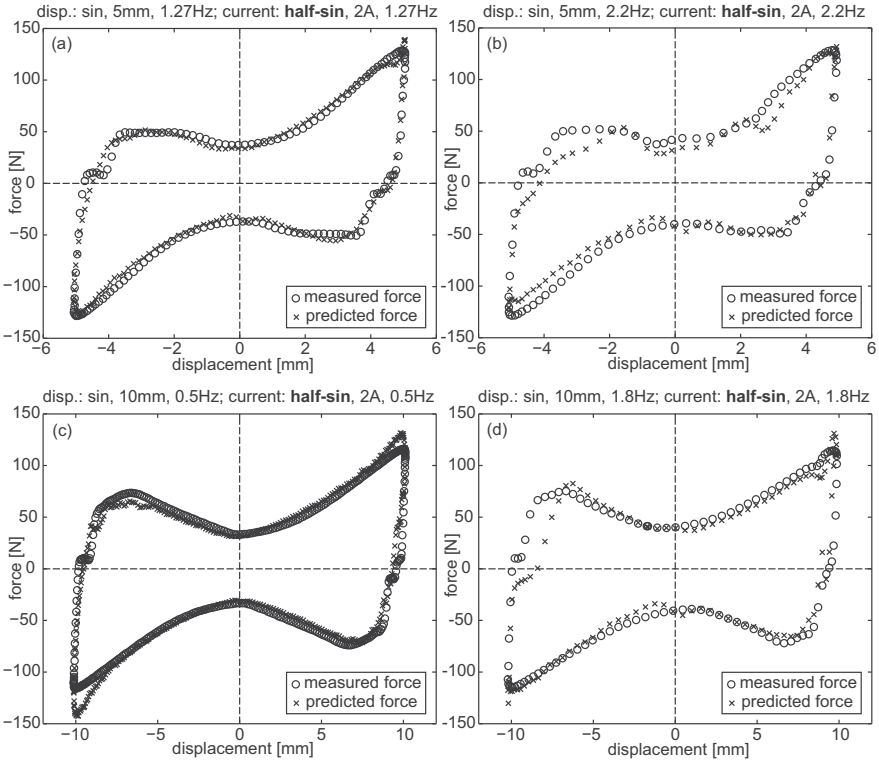

FIGURE 2.20: Validation of forward MR damper model for half-sinusoidal current of 2 A and different displacement amplitude and frequencies.

The validated forward and inverse MR damper models are finally used to simulate the emulation of viscous damping. The simulation shows that the inverse model overestimates the current in the vicinity of zero velocity, i.e. in the pre-yield region, while the output current is quite accurate within the post-yield region. As a result, the force tracking error is fairly large at small damper velocities but considerably small at velocities where the MR damper is not operated in the pre-yield region.

This investigation shows that the neural network technique can be used to model the inverse MR damper behaviour and thus solve the force tracking task directly with a sufficiently small force tracking error.

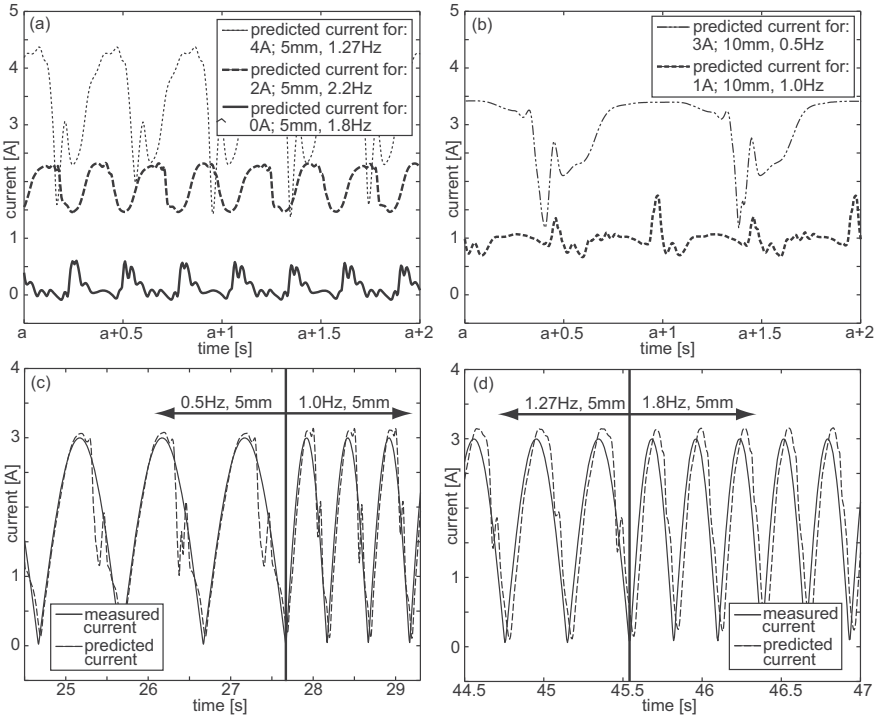

FIGURE 2.21: Validation of inverse MR damper model for constant current (a, b) and half-sinusoidal current at 3 A(c, d).

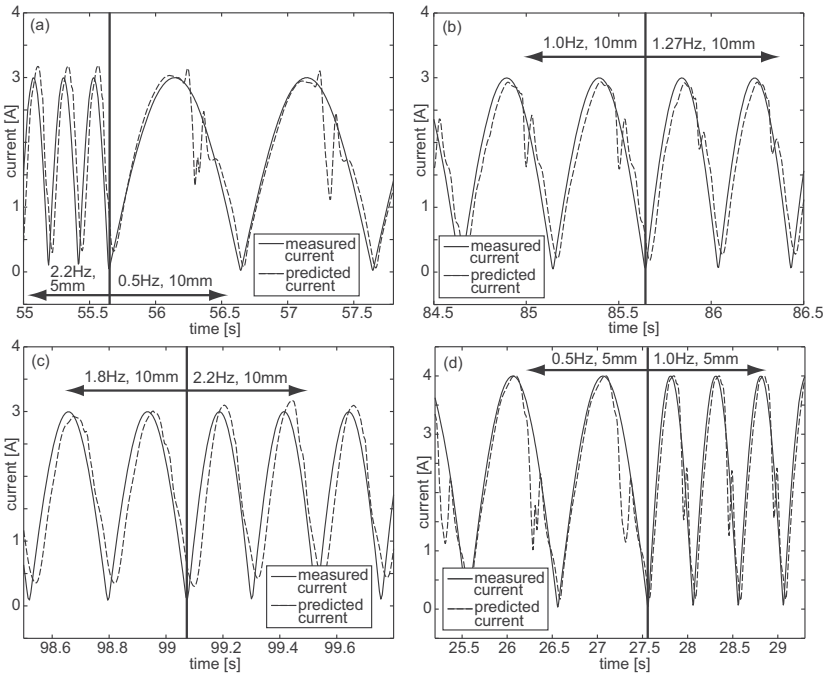

FIGURE 2.22: Validation of inverse MR damper model for half-sinusoidal current at 3 A (a-c) and 4 A(d).

TABLE 2.3: Feed Forward Back Propagation Neural Network Algorithm

Parameters:	
x: Input training vector	
$x = (x_1, ..., x_i, ..., x_n)$	
t: Output target vector	
$t = (t_1, ..., t_i, ..., t_n)$	
δ_k = error at output unit y_k	
δ_j = error at output unit z_j	
α = learning rate	
v_{oj} = bias on hidden unit j	
z_j = hidden unit j	
w_{ok} = bias on output unit k	
y_k = output unit k	
Step 1:	Initialise weights.
Step 2:	Input signal x_i transmits to all units in the next hidden layers.
Step 3:	For each hidden unit $(z_j, j = 1, ..., p)$, its weighted input signal $z_{inj} = v_{oj} + \sum_{i=1}^{n} x_i v_{ij}$ and activation function $Z_j = f(z_{inj})$ this signal transmits to all units in the output layer units.
Step 4:	For each output unit $(y_k, k = 1, ..., m)$, its weighted input signal $y_{ink} = w_{ok} + \sum_{j=1}^{p} z_j w_{jk}$ and activation function $Y_k = f(y_{ink})$
Step 5:	For each output unit $(y_k, k = 1, ..., m)$ which receives a target pattern corresponding to an input pattern, the error information term is calculated as $\delta_k = (t_k - y_k) f(y_{ink})$
Step 6:	For each hidden unit $(z_j, j = 1, ..., n)$ which sums its delta inputs from units in the layer above $\delta_{inj} = \sum_{k=1}^{m} \delta_j w_{jk}$ The error information term is calculated as $\delta_j = \delta_{inj} f(z_{inj})$
Step 7:	updating bias and weights $(j = 0, ..., p)$ for each output unit $(y_k, k = 1, ..., m)$ weight correction term is $\Delta W_{jk} = \alpha \delta_k z_j$ and bias correction term is $\Delta W_{ok} = \alpha \delta_k$. Therefore, $W_{jk}(new) = W_{jk}(old) + \Delta W_{jk}$ $W_{ok}(new) = W_{ok}(old) + \Delta W_{ok}$ Updating bias and weights $(i = 0, ..., n)$ for each hidden unit $(z_j, j = 1, ..., p)$, weight correction term $\Delta V_{ij} = \alpha \delta_j x_i$ bias correction term $\Delta V_{oj} = \alpha \delta_j$ Therefore, $V_{ij}(new) = V_{ij}(old) + \Delta V_{ij}$ $V_{oj}(new) = V_{ok}(old) + \Delta V_{oj}$.
Step 8:	Test the stopping condition, either minimisation of error or number of epoch is met or not. If not do step 2-7 again. Else if stop.

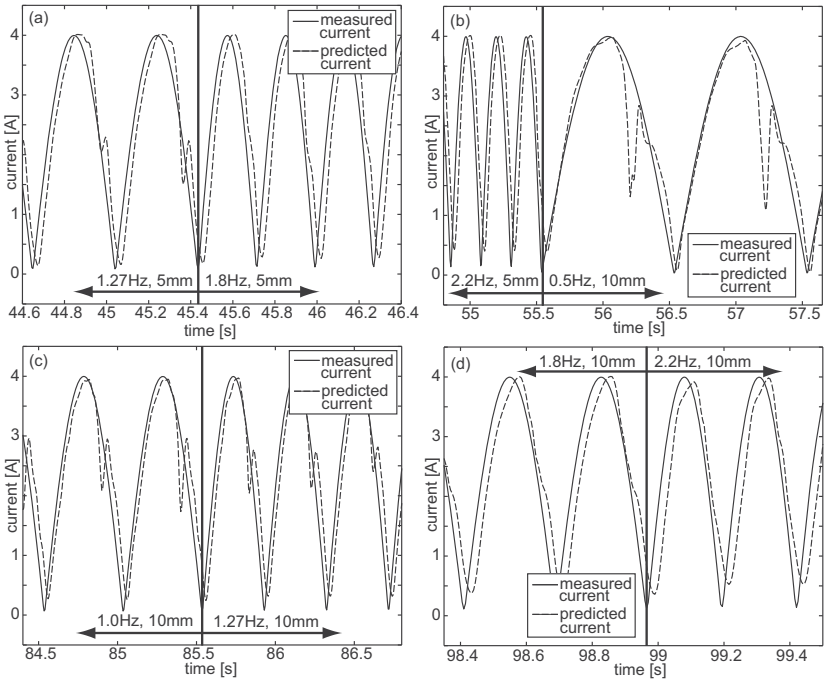

FIGURE 2.23: Validation of inverse MR damper model for half-sinusoidal current at 4 A (a-d).

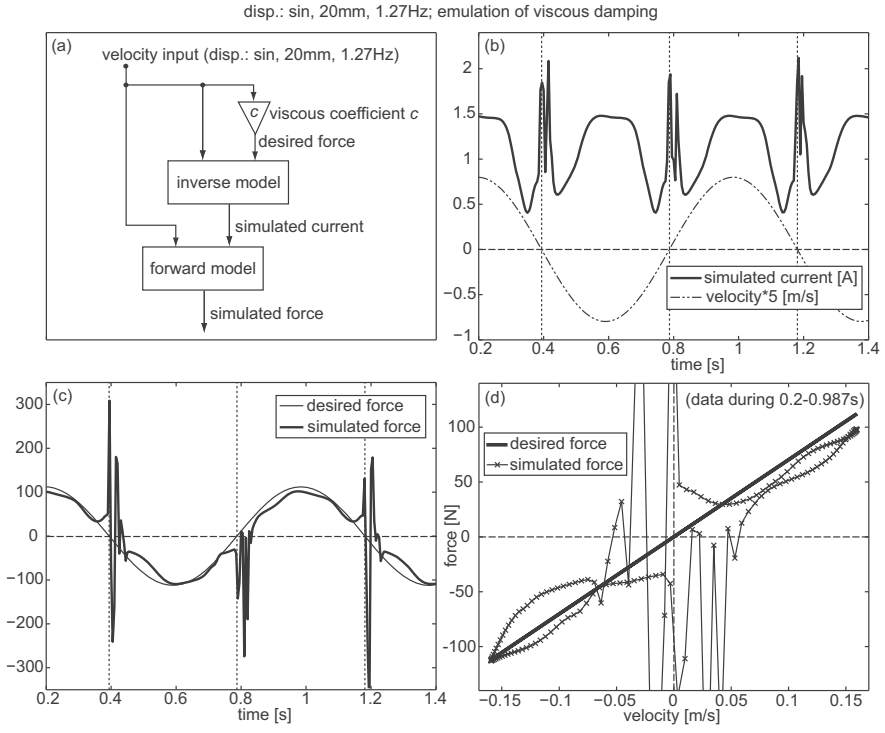

FIGURE 2.24: Simulated emulation of viscous damping: Flow chart (a), simulated MR damper current (b) and simulated MR damper force (c-d).

Chapter 3

Modelling of a Flexible Structure

The present model identification technique uses a parametric approach to determining the parameters of the system model. Parameters may be represented as some kind of physical quantities such as mass matrix, damping matrix and stiffness matrix. This chapter describes an experimental study to determine the system model parameters from test data. The experimental tests are performed using a shaking table. A five-mass shear frame structure has been chosen for model identification and it is excited by ground acceleration by a shaker. It is assumed that all the mass of the floor is lumped at the centre of the mass of the floor. Hence, the sum of the mass of the individual plate and the mass of the four columns are taken as the lumped mass of the individual floor. The stiffness of the model is determined from the mode shape, which is constructed on the basis of the frequency transfer function from the test data. The damping matrix is determined from the estimated damping ratio from a free decay test. These five-degree-of-freedom structures possess five natural frequencies corresponding to the number of degrees of freedom. When the structure is subjected to the excitation, the resonance is induced if the frequency of excitation is close to each of one of the natural frequencies of the structure. From the frequency response the resonance frequencies are determined. Three data sets have been taken from the experimental setup. The first set comprises data from the free decay test, where the five-mass system is initially excited by sinusoidal base acceleration at the resonance frequencies. The excitation is then stopped and the free decay response is used for determining the damping ratio of the vibration mode. The second set comprises data where the system is excited by sine sweep acceleration by the shaker, and it is used for constructing the mode shape as well as for determining the stiffness matrix. The last data set is then used for validation of model parameters.

3.1 Overview of Experimental Setup

This chapter focuses on the parametric identification of the five-mass system subjected to dynamic loading. A three-dimensional, five-floor building frame is used in the experiments. The structure is built in a shear frame configuration in which the building is rigidly attached to the shaking table platform. The parameter of the structure is explored through system identification tests with free and forced vibrations. The ground acceleration is applied by a shaker to the structure. The shaking table is driven horizontally by a hydraulic actuator. The measured ground acceleration is directly found from data acquisition hardware manufactured by OROS. The structure is kept vertically on the shaking table so that the base of the system is fixed to the shaking table. The accelerometers are fixed on each floor to measure the individual floor acceleration. The acceleration signal is taken from the accelerometer and amplified by an amplifier and sent to OROS for processing. The displacements are also measured by laser sensors and used in the OROS data acquisition hardware. All measurements are in volts and conversion into an appropriate unit is done by multiplying measurement data by the corresponding conversion factor of the particular device. The experimental setup of the shaking table is shown in Figure 3.1, and a corresponding schematic diagram of the experimental setup is given in Figure 3.2. Furthermore, the properties of the plates and columns of the shear frame structure are given in Table 3.1.

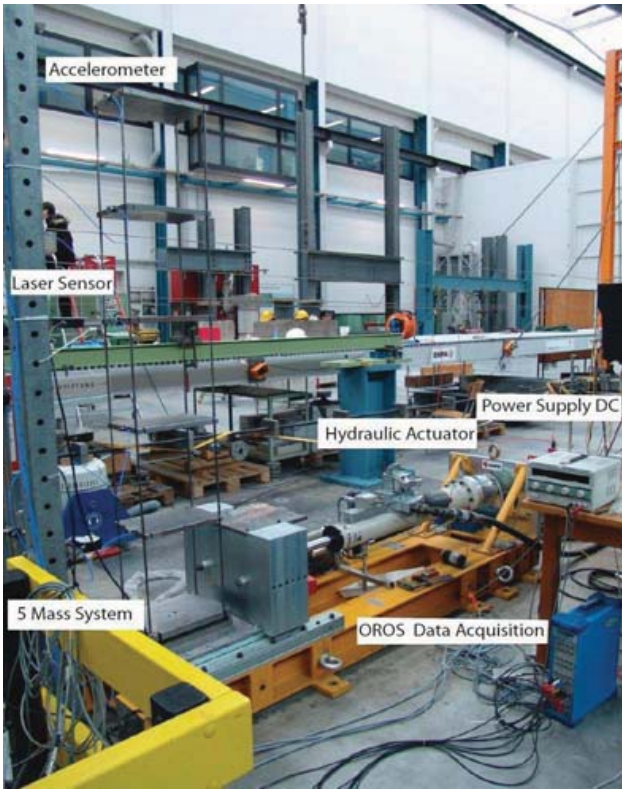

FIGURE 3.1: Experimental Setup without MR Damper.

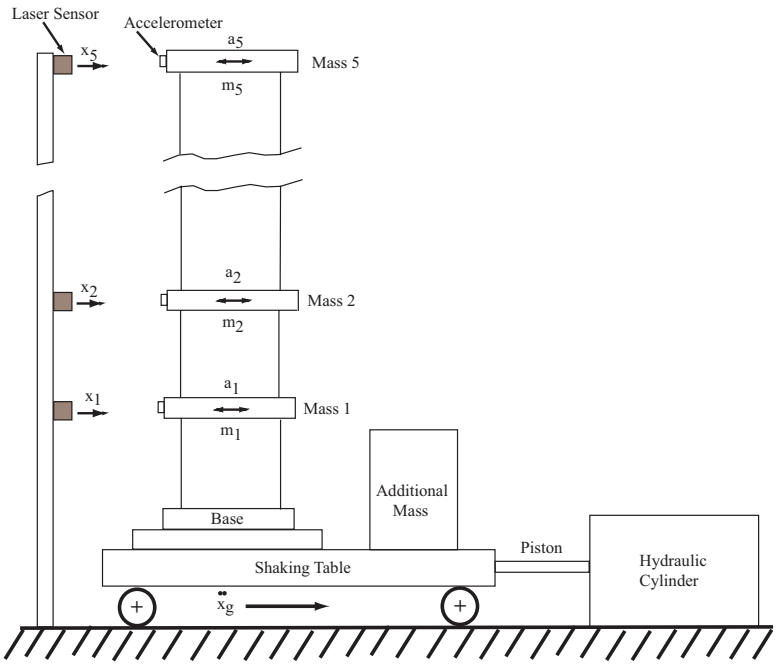

FIGURE 3.2: Schematic diagram of Experimental Setup

Table 3.1: Structural parameters.

Plate	Length	315 mm	E(steel)	$21 \times 10^{10} N/m^2$
(Steel)	Width	215 mm	ρ(steel)	$7.9 \times 10^3 Kg/m^3$
	Thickness	20 mm	σ(steel)	0.3
Column	Length	370 mm	Distance between	two column
(Steel)	Width	10 mm	Longitudinal	300 mm
	Thickness	4 mm	Lateral	175 mm

3.1.1 Measurement Sensors

Accelerometers are used to measure the acceleration of the shaking table as well as for measuring the response of each individual acceleration of the five-floor structure. The accelerometers are of the PCB 3701G3FA3G type and produce an output of 3 volts with a range of 3g. The supply voltage of the accelerometer is 27 V. Laser sensors optoNCDT 2200 are used to measure directly the displacement of the plates. Three laser sensors are available in the lab. They are mounted on a stand which is fixed on the ground. Two sensors are fixed in first and second plate positions. The third is positioned to measure the displacement of the third, fourth or fifth plate, depending on the goal of the test. The laser distance sensor employs triangulation measurement principles so that it projects a beam of visible laser light that creates a spot on a target surface. Reflected light from the surface is viewed from an angle by a digital CMOS line scan camera inside the laser sensor. The displacement of the target is computed from the image pixel data. The supply voltage of the laser sensor is 24 V. This laser can measure an output of 20 mm. The conversion factors for the laser sensors are found by calibration tests and are given in Table 3.2. A photo of one of the accelerometers and the laser sensor is shown in Figure 3.3.

3.1.2 Hydraulic Actuators and Control Unit

The hydraulic control unit is shown in Figure 3.4. The hardware setup is manufactured by Instron. The hydraulic cylinder used in the shaking table is a Schenk hydraulic model. The maximum displacement of hydraulic cylinder is 180 mm. The static force is 40 kN and the dynamic force is 80 times that of the static force.

Table 3.2: Conversion factors for sensor data.

Sensors	Acceleration (PCB 3701G3FA3G)	Displacement (opto NCDT2200)	Force	Ground displacement from OROS
conversion factor	$g(\approx 9.81)$ m/s^2/V	0.0109 m/V	50 N/V	0.018 m/V

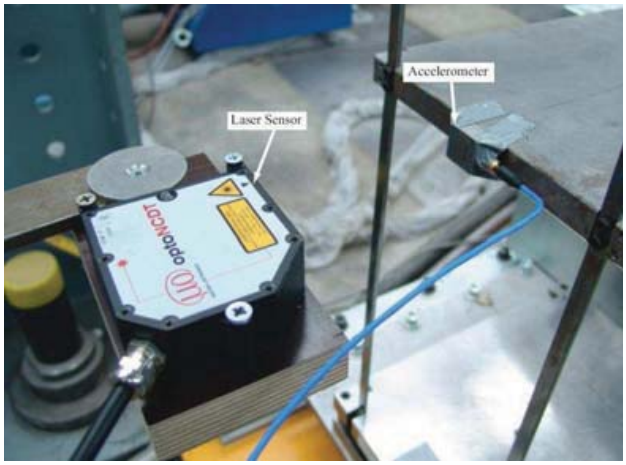

FIGURE 3.3: Laser Sensor and Accelerometer

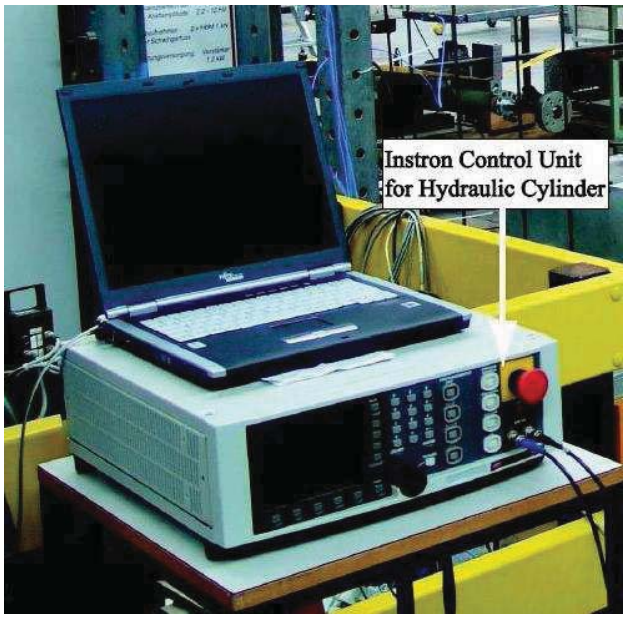

FIGURE 3.4: Hydraulic Control Unit

3.1.3 Filtering

The sensor data from the laser sensor and the accelerometer always has some noise. Thus, before applying the sensor data to modelling, filtering of the signal is necessary. The low-pass reduces the amplitude of the signal parts above the cut-off frequency, while a high-pass filter conversely reduces the signal part below the cut-off frequency. Thus, the low-pass filter is effectively applied to reduce signal and measuring noise, while the high-pass filter can be used to remove any off-set in the data. The two filter types can be combined in a band-pass filter, where frequencies (well) within the band are passed through the filter. For the free vibration decay test the band pass filter is applied and the frequency band is selected at approximately the resonance frequency of the corresponding mode because in the free vibration decay test, only the excited mode is considered. However, for the sine sweep test

the band is selected in between a frequency lower than the first resonance frequency and a frequency higher than the fifth resonance frequency, so that the DC part of the signals and the noise are located at higher frequencies.

For the free decay test for first mode peak detection, the structure is excited using sinusoidal ground displacement with a frequency equal to the first mode resonance frequency. The signal is filtered through a band pass filter where the cutoff frequencies are chosen around the first resonance frequency.

For effective filter design the following points are considered.

- Type of filter: Digital Butterworth band pass filter.
- Selection of filter order.
- Selection of suitable high-pass and low-pass cutoff frequency for band pass filter.

The applied band pass filter properties for acceleration and displacement measurements for the sine sweep test and the free decay test are discussed in the following sections.

3.2 Model Parameter Identification

The method for parameter identification is presented in the following subsections. The structural model has three main parameters: Mass matrix, stiffness matrix and damping matrix. The structural model is considered as a shear frame structure. The mass matrix is formulated on the basis of measuring the lumped mass of each floor, the damping matrix is derived from a free vibration test and the stiffness matrix is calculated from a modal analysis. The damping matrix in a modal coordinate system is constructed by a diagonal matrix where the diagonal elements are the damping coefficients for each mode. The damping coefficient is finally derived from the damping ratios of the individual vibration modes.

The damping ratio is evaluated mainly by the following three methods. First of all, the peaks of the measurement signal are identified and used for constructing the decay profile. The first method is based on linear fitting and the second on a logarithmic fitting algorithm and the third on the average value of the damping ratio of two consecutive peaks. Peaks of the signals are calculated for the entire range of the measurement signal. However, the only range considered is that where the measurement signal decays. The first and the second methods fit the peak values of the signal with linear and logarithmic curves in the region where the measurement signal decays.

The damping ratio may be estimated from the ratio of adjacent local maxima during a free vibration response $u(t)$ at time t and after a period at time $t + T_d$. For logarithmic fitting, the damping ratio is written as

$$\zeta = \frac{\delta}{\sqrt{(4\pi^2 + \delta^2)}} \tag{3.1}$$

where δ is the logarithmic decrement which is as follows

$$\delta = ln\left(\frac{x(t)}{x(t + T_d)}\right) \tag{3.2}$$

The damping ratio is evaluated from the free decay test and thus the damping matrix is formulated. The sine sweep test is conducted next to evaluate the resonance frequencies of all the modes to identify the mode shape from the frequency transfer function of the measurement signal.

TABLE 3.3: Resonance Frequencies.

Mode Number	1	2	3	4	5
Resonance Frequency (Hz)	1.23	3.83	6.13	8.05	9.34
Resonance Frequency (rad/s)	8.0	24.2	38.4	49.9	58.3

3.2.1 Sine Sweep Test

For evaluating the dynamic properties of a structure, a forced vibration test is performed using sinusoidal (harmonic) loading over a range of frequencies that include all modal resonance frequencies. The idea is to excite the structure with harmonic loading over a range of frequencies so that at some frequency the structure experiences resonance. Resonance occurs when the frequency of the excitation is equal to the natural frequency of the structure. At the resonance frequency, the structure experiences its largest response, compared to any other excitation frequency. The measured acceleration data from the sine sweep test using Fast Fourier Transform (FFT) analysis and the five resonance frequencies corresponding to the main five degrees of freedom have been identified approximately. The resonance frequencies for the corresponding five modes are identified from Figure 3.5, which shows the first floor acceleration data in the frequency domain. The resonance frequencies are given in Table 3.3.

For the sine sweep test the band is determined by frequencies lower than the first resonance frequency and higher than the fifth resonance frequency. Hereby, the DC part of the signals and the noise are located at even higher frequencies. For the sinus-sweep test the high-pass and low-pass cutoff frequencies are considered as 0.2 Hz and 14 Hz, respectively, which includes all the modes. The order of the band pass filter is kept low so that the main properties of the measurement signal are unaltered. For the sine sweep test data, the order

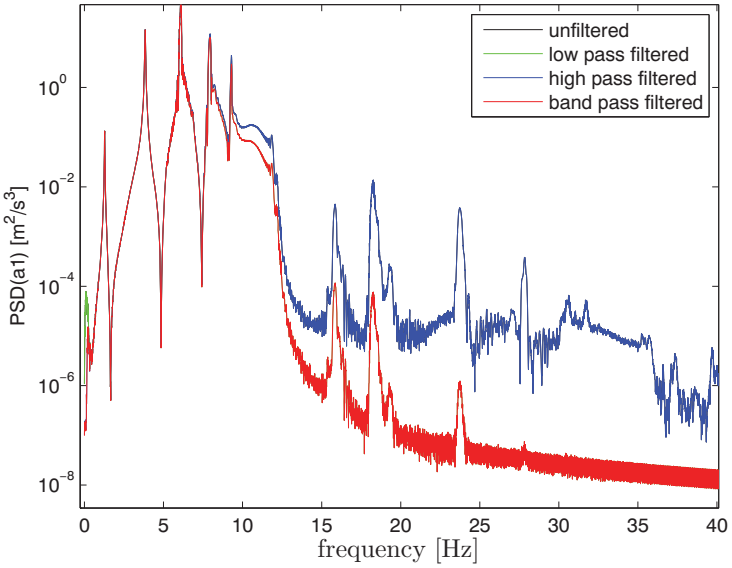

FIGURE 3.5: Filtered and unfiltered acceleration in the frequency domain

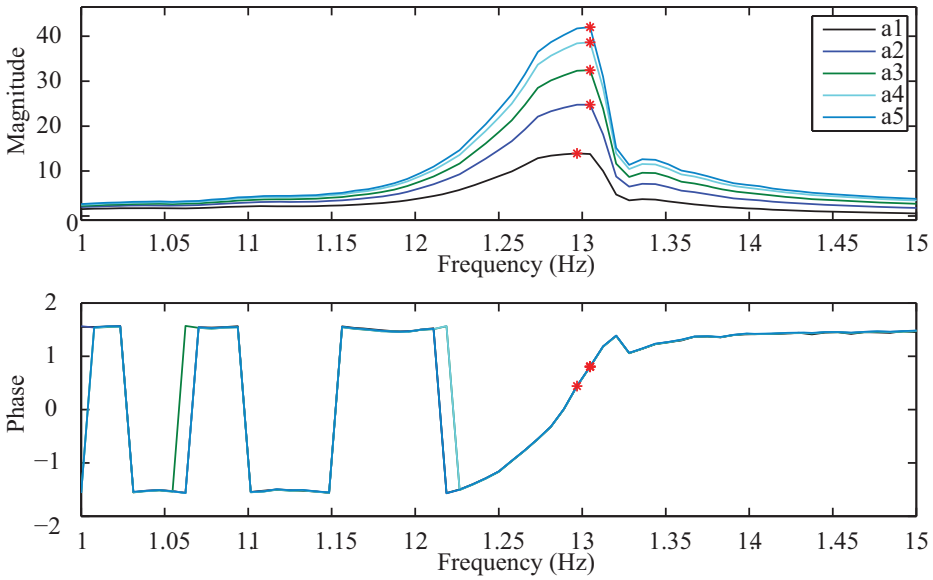

FIGURE 3.6: Magnitude and phase angle from transfer function

is chosen as 3. The five resonance frequencies for the corresponding five modes are also found from first five modal resonance frequency from Figure 3.5. It also shows some other higher frequencies which are mainly arrives due to flexible support. The sine sweep test is conducted to evaluate the mode shape for five different modes and construct a modal matrix and to evaluate the stiffness matrix from the modal matrix. The procedure for stiffness matrix identification is discussed below:

- Estimation of the mass: The mass, m_i, of each floor of the structure is determined. The plate and four columns are lumped together to determine the corresponding mass of the floor. The mass matrix is expressed as

$$\mathbf{M} = \begin{bmatrix} m_1 & & & & \\ & m_2 & & & \\ & & m_3 & & \\ & & & m_4 & \\ & & & & m_5 \end{bmatrix} \tag{3.3}$$

- Identification of the resonance frequency: The resonance frequency is evaluated from the location of the peak in the frequency response diagram. The resonance frequencies for the corresponding five modes are found from the frequency response diagram shown in Figure 3.5.

- Construction of the frequency transfer function: The transfer functions in the frequency domain between the output signals (measured floor acceleration) and the input (ground acceleration) are determined. The relationship between the input ground acceleration (a_g) and output floor acceleration (a_i) is modelled by the linear, time-invariant transfer function T_{gi}. The transfer function is the quotient of the cross power spectral density, $P_{gi}(\omega)$ of a_g and a_i, and the power spectral density, $P_{gg}(\omega)$ of a_g with itself. The frequency transfer function is then expressed as

$$T_{gi}(\omega) = \frac{P_{gi}(\omega)}{P_{gg}(\omega)} \tag{3.4}$$

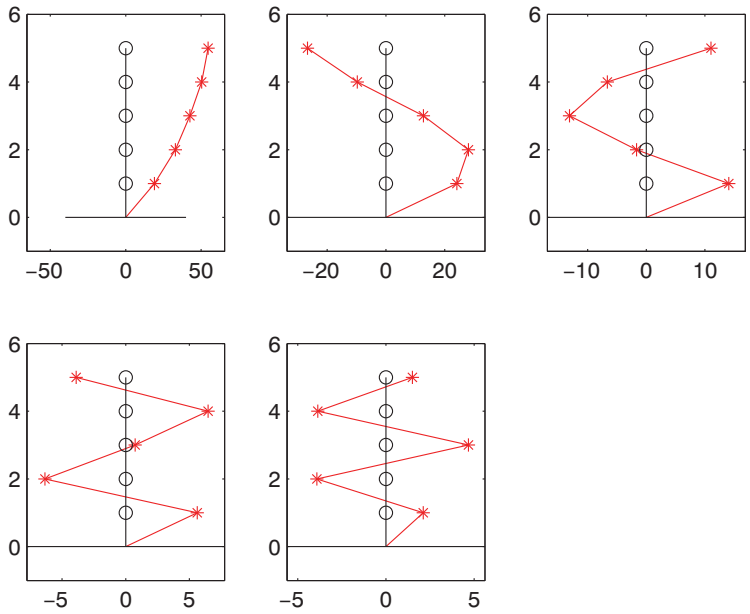

FIGURE 3.7: Mode Shape

- Evaluation of the magnitude and phase from the frequency response of the transfer function: The magnitude and phase are determined from the frequency transfer function for each of the five modes. The magnitude and phase for all floors for the first mode are shown in Figure 3.6. In this diagram, the magnitude and phase are determined from the transfer function constructed between the first floor acceleration and the ground acceleration. Similarly, all other transfer functions have been derived.

- Determination of the maximum magnitude and corresponding phase for all five modes: The magnitude and phase of each of the five floors for all five modes are evaluated. The peak magnitude and the corresponding phase angle for the first mode are shown in Figure 3.6. The frequency at which maximum magnitude is determined is actually represented as the resonance frequency of the corresponding mode. From this diagram the actual resonance frequency for the corresponding mode is also evaluated.

- Construction of the mode shapes for all five modes using the magnitude and phase values: The maximum magnitudes of the five floors for the corresponding modes are considered for construction of the mode shape. The phase at the corresponding frequency where the maximum peak occurs is used to determine the sign of the magnitude for mode shape. Figure 3.7 shows the mode shape diagram for all the five modes.

- Construction of the non-dimensional mode shape: The magnitude of each floor is normalized by dividing the maximum amplitude by the corresponding mode and by dividing the maximum magnitude of the floor at the corresponding floor, so that the dimensionless mode shape is formed and the magnitudes are in between 0 to 1. The non-dimensional mode shape is shown in Figure 3.8. This non-dimensional mode shape is compared with the theoretical mode shape of a shear frame which has one free end. The theoretical mode shape is assumes to be sinusoidal. The comparison is also shown

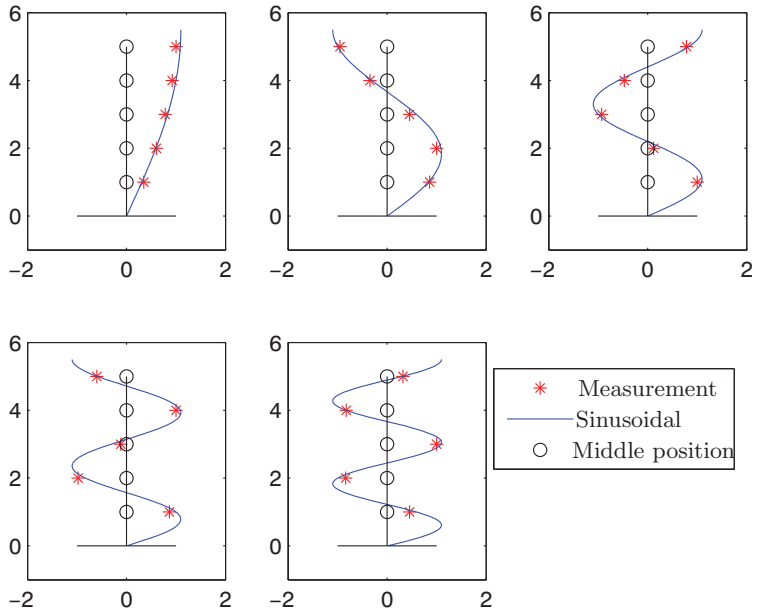

FIGURE 3.8: Mode Shape - Non-dimensional

in Figure 3.8 and the non-dimensional mode shape shows good agreement with the theoretical mode shape.

- Formation of modal matrix: From the mode shape, the modal matrix is formed in modal coordinates

$$\mathbf{U} = \begin{bmatrix} 0.349 & 0.861 & 1.000 & 0.868 & 0.453 \\ 0.604 & 1.000 & 0.117 & -0.979 & -0.838 \\ 0.773 & 0.449 & 0.941 & 0.119 & 1.000 \\ 0.920 & -0.356 & -0.464 & 1.000 & -0.827 \\ 1.000 & -0.952 & 0.789 & -0.596 & 0.319 \end{bmatrix} \tag{3.5}$$

where each column represents the normalised magnitude of each of five nodes at the corresponding mode. The column number represents the mode number.

- Formulation of the stiffness matrix in modal coordinates: The stiffness matrix in modal coordinates $\mathbf{K}_m$ is a diagonal matrix where the the diagonal elements of the matrix are constructed from the mass element and the corresponding modal resonance frequency. The modal stiffness is determined from the following expression

$$k_i = \omega_i^2 \, m_i \tag{3.6}$$

where m_i is the modal mass associated with the mode shape matrix $\mathbf{U}$ and ω_i are the resonance frequencies determined from the peaks in the acceleration spectrum. The stiffness matrix in modal coordinate is calculated as

$$\mathbf{K}_m = \begin{bmatrix} k_1 & & & & \\ & k_2 & & & \\ & & k_3 & & \\ & & & k_4 & \\ & & & & k_5 \end{bmatrix} \tag{3.7}$$

- The diagonal element of the modal matrix $\mathbf{K}_m$ is taken and the stiffness matrix in Cartesian coordinates, $\mathbf{K}$ is found by

$$\mathbf{K} = (\mathbf{U}^{\mathsf{T}})^{-1}\mathbf{K}_m\mathbf{U}^{-1} \tag{3.8}$$

3.2.2 Free Vibration Test

In this section, free vibrations are obtained by initially imposing a harmonic force by a shaker, and when the structure is vibrating at the desired frequency the shaker excitation is then stopped and free vibrations at the desired frequency occur. This free vibration can be analysed based on the concept of the logarithmic decrement. However, for higher modes the free vibration response is not a suitable method due to the inherent ambient noise.

For the free vibration decay test the Butterworth band pass filter is applied and the frequency band is selected around the resonance frequency of the corresponding mode because in the free vibration decay test only the excited mode is considered.

For the free decay test for first mode peak detection, the structure is excited using sinusoidal ground displacement with a frequency equal to the first mode resonance frequency. The signal is filtered through a band pass filter where the cutoff frequencies are chosen around the first resonance frequency. The following properties of the band pass filter are considered.

- A band pass Butterworth filter is used.
- The high-pass cut-off frequency is selected as $\omega_i - \omega_{cut}$ where ω_i is the resonance frequency for the corresponding mode and the margin to the filter limit is $\omega_{cut} = \pi$ rad/s.
- The low-pass part of the filter the cut-off frequency is selected at $\omega_i + \omega_{cut}$.
- The order of the filter is in this case chosen as 5.

The effect of applying the band pass filter to noise reduction is demonstrated in time and in the frequency domain for the 1st floor for free vibration data and is shown in Figure 3.9. The procedure for the damping ratio identification based on free vibration test data is as follows:

- Measurement of peak value in decay zone: The peak of each cycle is identified from the free vibration response when the signal is in decay. Figure 3.10 (a) shows all the peaks detected in the decay envelope.
- Estimation of curve fitting: From the peaks of the data in the decay zone, a curve fitting is estimated using exponential or linear fitting. The curve fitting using exponential and linear fit are shown in Figure 3.10. The exponential fit is working better when compared to linear fit on an average level, while the linear fit is fairly good at the initial part of the free decay.
- Finding the damping ratio : The damping ratio, ζ_i is evaluated from the decay rate of the curve. This done by evaluating the decay rate of the logarithmic and the linear curve fitting. The logarithmic decay is calculated from (3.1). An alternative method for determining the damping ratio is finding the damping ratio between two consecutive peaks, and the computing the final values as the mean value from the individual peak-to-peak values in the decay. Figure 3.10(b) shows the relationship between amplitude and damping ratio from the logarithmic fitting and the point to point estimation. It is found that the average of the point to point damping ratio is almost the same as the

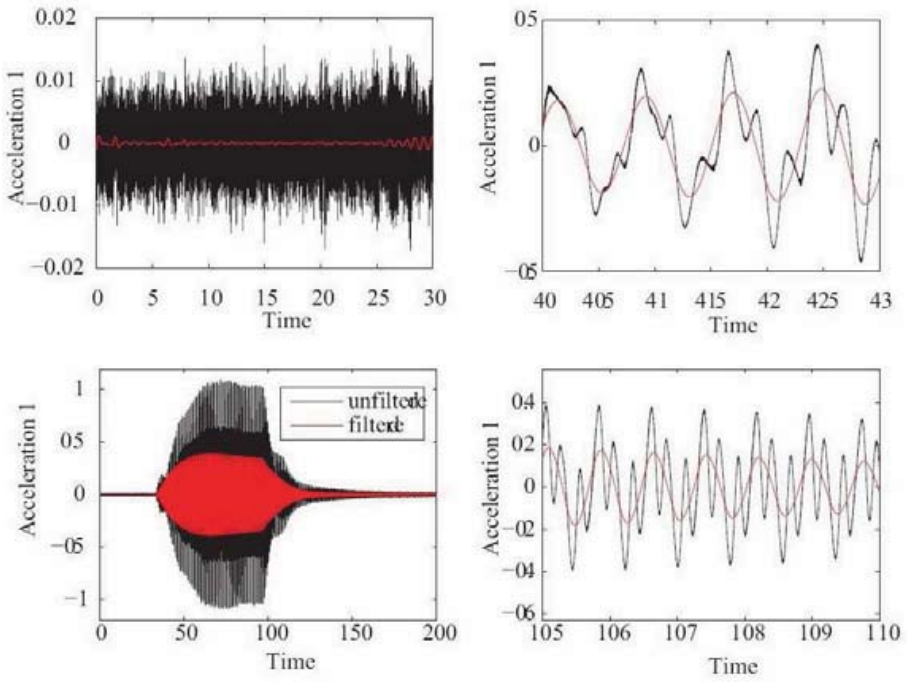

FIGURE 3.9: Filtered and unfiltered acceleration in the time domain

logarithmic estimate. From the decay tests the damping ratios have been estimated for the five vibration forms as

$$\zeta_1 = 0.0030 \quad , \quad \zeta_2 = 0.0024 \quad , \quad \zeta_3 = 0.0020 \quad , \quad \zeta_4 = 0.0015 \quad , \quad \zeta_5 = 0.0010$$

When the structure is in free vibrations the applied loading is zero. In this case the equation of motion is

$$\mathbf{M}\ddot{\mathbf{x}} + \mathbf{C}\dot{\mathbf{x}} + \mathbf{K}\mathbf{x} = 0 \tag{3.9}$$

In modal coordinates the damping matrix C is transformed into a diagonal matrix C_m, when assuming orthogonal damping. The elements in the diagonal are then the

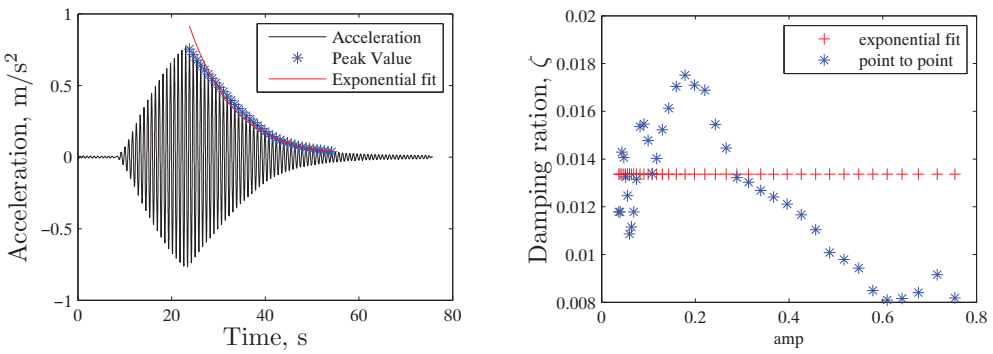

FIGURE 3.10: Peak detection and exponential fitting (a) and damping ratio (b)

viscous damping parameters c_i in modal coordinates.

$$\mathbf{C} = (\mathbf{U}^{\mathrm{T}})^{-1}\mathbf{C}_m\mathbf{U}^{-1} \tag{3.10}$$

The diagonal element of the damping matrix in modal coordinate can then be written in terms of the estimated damping ratio ζ_i as

$$c_i = 2\zeta_i\sqrt{m_i k_i} \tag{3.11}$$

where m_i and k_i are the modal mass and stiffness components for the corresponding modes, which have already been determined via the sine sweep test.

3.3 Equations of Motion

The equation of motion for a shear frame structure with external excitation can be written as

$$\mathbf{M}\ddot{\mathbf{x}} + \mathbf{C}\dot{\mathbf{x}} + \mathbf{K}\mathbf{x} = \mathbf{f}_e \tag{3.12}$$

The degrees of freedom of the model are contained in the vector $\mathbf{x}$, while $\mathbf{M}$, $\mathbf{C}$ and $\mathbf{K}$ are the associated mass, damping and stiffness matrix, respectively. The vector $\mathbf{f}_e$ represents the external loading.

3.3.1 Mass Matrix

For individual plate mass calculation the mass of the plate and the four columns have been taken as a lumped mass and the representative mass of the individual floor is then found as 5.95 kg. The mass matrix in Cartesian coordinates is then determined as

$$\mathbf{M}(i,i) = m_{mass} + 4m_{column} \quad , \quad \mathbf{M}(i,j) = 0 \quad , \quad if \quad i \neq j \tag{3.13}$$

Thus, the matrix matrix is assumed diagonal with identical diagonal elements.

3.3.2 Stiffness Matrix

First, the mode shape vector $\mathbf{u}_i$ and the radial eigenfrequency ω_i of mode i are estimated from the measured transfer functions. The measured mode shapes are normalised to unity at a height of 5.5 floors, where it corresponds to the mode shapes of a sinusoidal function. The comparison is shown in Fig. 3.8. The measured mode shape matrix $\mathbf{U}$ yields the mass matrix in modal coordinates

$$\mathbf{M}_m = \mathbf{U}^T\mathbf{M}\mathbf{U} \tag{3.14}$$

which is found to have predominant diagonal elements. Therefore, the stiffness matrix in modal coordinates $\mathbf{K}_m$ is approximated as follows

$$\mathbf{K}_m(i,i) = {\omega_i}^2\mathbf{M}_m(i,i) \quad , \quad \mathbf{K}_m(i,j) = 0 \quad , \quad if \quad i \neq j \tag{3.15}$$

The back transformation leads to the desired stiffness matrix in Cartesian coordinates,

$$\mathbf{K} = \left(\mathbf{U}^T\right)^{-1}\mathbf{K}_m(\mathbf{U})^{-1} \tag{3.16}$$

which is fully occupied. However, the elements outside the tri-diagonal band are small compared to the main tri-band, which verifies that the present structure can be modelled as a shear frame structure.

3.3.3 Damping Matrix

The damping matrix is determined from free vibration test. The diagonal element of the damping matrix is determined from the corresponding diagonal element of mass and stiffness matrix. The damping ratio ζ_i is found for each corresponding mode. The diagonal element in the damping matrix $\mathbf{C}_m$ in modal coordinates is found from

$$\mathbf{C}_m(i,i) = 2\zeta_i \sqrt{\mathbf{K}_m(i,i)\mathbf{M}_m(i,i)} \tag{3.17}$$

The other elements of the damping matrix are considered as zero. The damping matrix in modal coordinates $\mathbf{C}_m$ is estimated as a diagonal matrix where the diagonal elements are determined from (3.17). The damping matrix in Cartesian coordinates $\mathbf{C}$ is determined from back transformation and expressed as

$$\mathbf{C} = (\mathbf{U}^T)^{-1}\mathbf{C}_m(\mathbf{U})^{-1} \tag{3.18}$$

This matrix is also fully occupied, and is not dominant as much by the tri-diagonal band. This demonstrates the difficulties in the estimation of structural damping.

3.3.4 Model Verification

The equation of motion in (3.12) is formulated in the state space representation and solved in Matlab/Simulink using the measured ground acceleration as excitation and without external damper. The model validation is depicted in Figure 3.11 for two selected accelerations in the time domain and in Figure 3.12 for two other selected accelerations in the frequency domain. The results show a small modelling error in both the time and the frequency domains. The natural frequencies and damping ratios are determined by solving the state-space eigenvalue problem associated with the equation of motion in (3.9). The frequencies are determined as:

$$\omega_1 = 8.0 \quad , \quad \omega_2 = 24.2 \quad , \quad \omega_3 = 38.4 \quad , \quad \omega_4 = 49.9 \quad , \quad \omega_5 = 58.3$$

which agree very well with the experimental frequencies given in Table 3.3. The modal damping ratios are determined as

$$\zeta_1 = 0.0035 \quad , \quad \zeta_2 = 0.0024 \quad , \quad \zeta_3 = 0.0074 \quad , \quad \zeta_4 = 0.0059 \quad , \quad \zeta_5 = 0.0012$$

and they match well with the experimental values provided previously. Thus, the main reason for some deviations in the comparison of experimental and numerical response records is most likely the error in measuring decay in free vibration test.

3.4 Summary

This chapter considers the system modelling of a flexible structure using an experimental procedure and presents validation results from the numerical model. A five-mass shear frame structure has been chosen for the model identification. The stiffness of the model is determined from the mode shapes, which are constructed from a frequency transfer function based on vibration test data. The damping matrix is determined from the estimated damping ratios from a free decay tests. From the frequency response the resonance frequencies are determined, and the validation of the model shows good agreement with the measurement data.

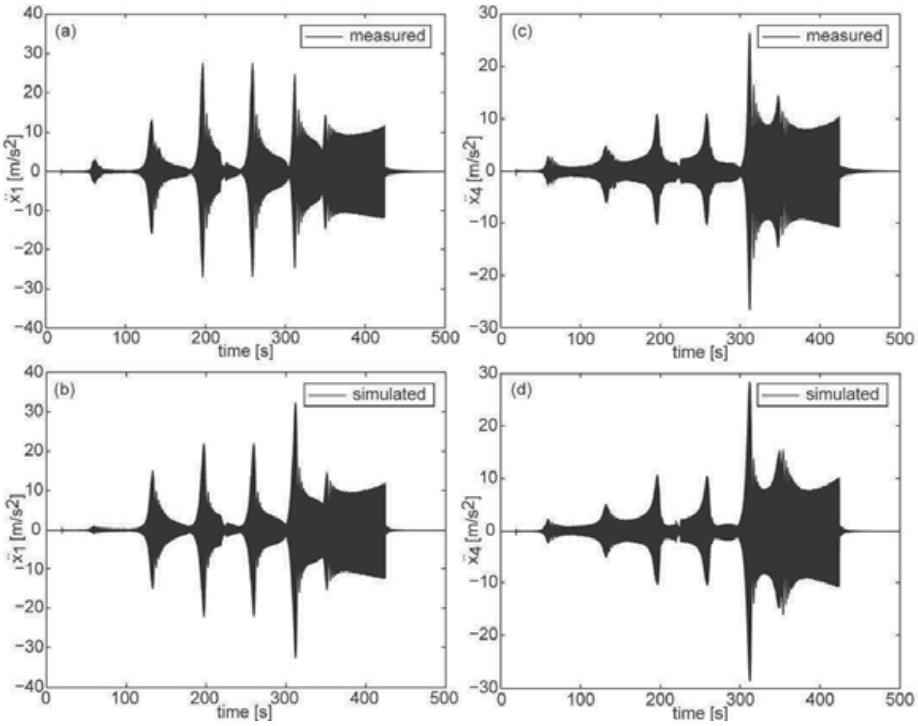

FIGURE 3.11: Validation of shear frame model in time domain.

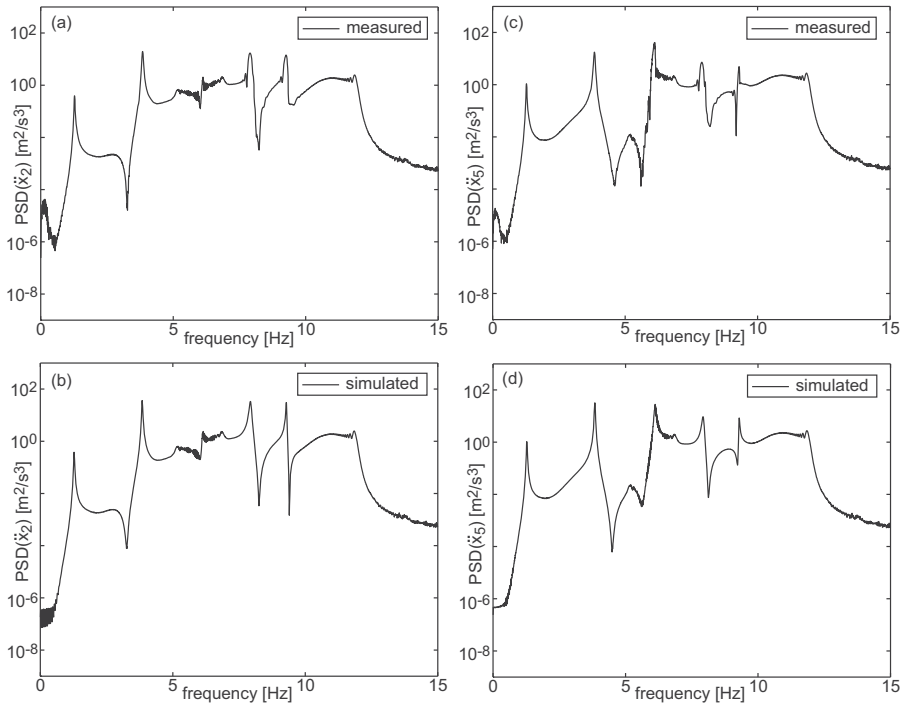

FIGURE 3.12: Validation of shear frame model in frequency domain.

Chapter 4

Control Strategies and Simulation

In civil engineering, the mitigation of structural vibration induced by dynamic loads, such as earthquake or wind loads using appropriate control strategy is one the most challenging task for structural engineers. Several control strategies based on passive, active or semi-active control methods are investigated for finding effective solution to mitigate the structural vibration. In recent year semi active control device like MR damper got considerable attention due to its reliability, adaptability, cost effectiveness and fail safe mechanism.

Passive damping devices are purely dissipative and are not controlled during motion of the damper. They do not have external power requirement and are very stable since they do not add energy but only dissipate it, thus yielding a very robust device [2]. Active dampers can unlike passive dampers be adapted to the dynamic loading. An active damper system consists of of actuators and sensors coupled by active controller, which gives a feedback loop which can be position, velocity, acceleration or force. The active dampers are driven by an external power supply which is a major drawback of using active damper during an earthquake. Active dampers are very stable and robust [5].

Semi-active dampers like MR damper have similarity with active dampers, but they have lower power requirements and also stable as passive control device. In fact, maximum MR dampers can operate on battery power, which is a big advantage during an earthquake. So semi-active control can combine the advantages of active and passive control [9]. The stay cable damping potential due to controlled MR dampers has been investigated by simulation, laboratory and field tests in many research projects [42, 43, 46, 76]. Weber et al. [36, 47, 77] demonstrated different passive and semi-active control strategies on cable bridges. Moreover, the vibration reduction of civil engineering structures such as buildings, bridges and models of these structures with controlled MR dampers has been simulated and tested [79] - [83] and in tuned masses [37] in order to make these passive devices adaptive. Many different clipped active, semi-active and passive control laws for MR dampers have been tested. Clipped optimal control schemes as presented in e.g. [14, 76], clipped viscous damping with negative stiffness as described in e.g. [36], semi-active algorithms [30, 48] and passive control laws such as emulated viscous damping [46], controlled friction damping [30, 32, 42, 84], controlled energy dissipation [47] and passive control [77]. In semi-active control the tracking of a desired force is a main issue and the problem has been solved in various ways. The Heaviside step function approach that requires measuring the actual MR damper force is presented by Dyke et al. [14]. The Bingham model was used to derive the current for given measured damper velocity and desired force [36, 46]. Dahl model is also presented by Aguirre et al. [85] which can also be used as MR damper model. The LuGre friction approach was used to model the MR damper behaviour and the validated model was then used as observer [56, 54, 55]. A mapping approach based on tests of the MR damper connected to the cable is presented in [47], neural network based force tracking approaches have been developed and also fuzzy logic and other methods have been adopted to capture the inverse MR damper dynamics [86] - [95].

In recent years, the structural damping due to the emulation of a negative stiffness force besides the damping force in the MR damper was investigated in several research projects [31,

32, 34]. It is shown in [36] that larger structural damping is achieved because the negative stiffness force increases the motion in the damper, which makes it possible to dissipate two times more energy per cycle in the damper than the optimal viscous damper [96]. It was shown in [97] that clipped optimal control of a cable with semi-active damper results in approximately the same control force as clipped viscous damping with negative stiffness. Consequently, the approach of clipped viscous damping with negative stiffness for semi-active cable damping is a powerful control approach since its realisation requires only measuring the damper displacement, it generates twice as much structural damping as optimal viscous damping and avoids the complex state estimation which is essential for optimal control approach.

This chapter therefore investigates the semi-active damping of a five-degree-of-freedom (5 DOF) shear frame structure with an MR damper. The tested control laws are optimal viscous damping as benchmark, viscous damping with negative stiffness [P4], optimal semi-active damping, i.e. friction damping with negative stiffness [P2] and neural network based reference control strategy [P5]. All four control laws are designed based on a validated shear frame model described in Chapter 3. The force tracking task is solved with a neural network model [P1] that describes the inverse dynamics of the MR damper. Details are discussed in Chapter 2. It is described how the neural network is implemented in simulation using Matlab/Simulink. The structural damping resulting from the above-mentioned control laws is calculated and compared each other for the first excited mode. The comparison shows the effectiveness of negative stiffness. In the closed loop simulation the control approaches has acceptably small force tracking error. This tracking error is mainly due to the MR damper current, which is generated by the neural network, is fairly noisy. It is shown that the neural network approach can be used to track the desired force. A thorough description of the novel neural network approach is given in Chapter 2. The descriptions of the various control strategies and simulation results are discussed in the following sections.

4.1 Damping of Flexible Structures

In dynamic analysis of flexible structures the structural model is typically modelled by finite elements or determined by experimental modal analysis and free vibration test, so that the equation of motion can be written in the form

$$\mathbf{M}\ddot{\mathbf{x}} + \mathbf{C}\dot{\mathbf{x}} + \mathbf{K}\mathbf{x} = -\mathbf{w}f + \mathbf{f}_e \tag{4.1}$$

where the vector $\mathbf{x}$ contains the generalised displacements and a dot denotes time differentiation, and $\mathbf{K}$, $\mathbf{C}$ and $\mathbf{M}$ are the structural stiffness, damping and mass matrix, respectively. The external load is represented by the vector process $\mathbf{f}_e$. Finally, a single damper is acting on the structure, where f represents the damper force and $\mathbf{w}$ is the connectivity vector describing the location of the damper and represented as $\mathbf{w} = [1, 0, ...]^T$ for the present shear frame problem. The base excitation is represented as $\mathbf{f}_e = \mathbf{MI}(-\ddot{x}_g)$ where $\ddot{x}_g$ is the ground acceleration and $\mathbf{I} = [1, 1, ...]^T$ is unity vector. The schematic illustration of the shear frame structure with rotational MR damper is shown in Figure 4.1.

For linear damper models the characteristics of the damper are conveniently formulated in the frequency domain as

$$f(\omega) = H(\omega)x \tag{4.2}$$

where $H(\omega)$ is a frequency dependent damper function. In the frequency domain x is simply the response amplitude of the damper motion. In the next section a system reduction procedure for flexible structures with local dampers is presented. This procedure leads to explicit expressions for the complex-valued natural frequency, which can be used to determine the optimal damper tuning leading to maximum modal damping [P2, P4].

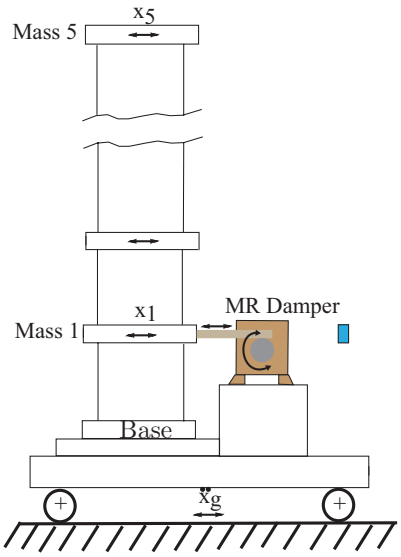

FIGURE 4.1: Schematic diagram of shear frame structure with MR damper.

4.2 Two-Component System Reduction and Modal Damping

The effective damping of the structure is evaluated in terms of its modal damping, where the presence of the external damper generates non-proportional damping with complex-valued natural frequencies and mode shapes. System reduction techniques based on undamped mode shapes require a large number of terms to give satisfactory results. The analysis of the damper modal vibrations is described by the two-component system reduction technique introduced by Main and Krenk [29]. Høgsberg and Krenk [96] have implemented this technique for finding the optimal viscous parameter for cable damping. In this formulation the response of the structure is represented by a linear combination of the two limiting mode shapes for the structure without damper $\mathbf{u}_0$ and for the structure with the damper fully locked $\mathbf{u}_\infty$, respectively. The linear combination can then be written as

$$\mathbf{x} \;=\; \mathbf{u}_0 r_0 + \mathbf{u}_\infty r_\infty \;=\; \mathbf{S}\mathbf{r} \tag{4.3}$$

The first term represents the classical undamped case, while the second term introduces the local effect of the damper described in terms of its ability to lock the structure in its location. The detailed process is also discussed in [P2, P4]. The relative weighting between the two limiting cases is governed by the coordinates of the reduced subspace: $\mathbf{r} = [r_0, r_\infty]^T$. Similarly, the limiting mode shapes are assembled in the modal matrix: $\mathbf{S} = [\mathbf{u}_0, \mathbf{u}_\infty]$. The undamped mode shape is governed by the classical generalised eigenvalue problem:

$$(\mathbf{K} - \omega_0^2 \mathbf{M})\mathbf{u}_0 = 0 \tag{4.4}$$

A smaller eigenvalue problem exists for the case where the damper link is fully locked, defining ω_∞ and $\mathbf{u}_\infty$. The locked mode shape $\mathbf{u}_\infty$ is by construction orthogonal to the connectivity vector which yields the identity $\mathbf{w}^T\mathbf{u}_\infty = 0$. Both limiting mode shapes are real-valued and conveniently normalised to unit modal mass,

$$\mathbf{u}_0^T \mathbf{M}\mathbf{u}_0 = 1 \quad , \quad \mathbf{u}_\infty^T \mathbf{M}\mathbf{u}_\infty = 1 \tag{4.5}$$

Consequently, the limiting natural frequencies are given in terms of the modal stiffness,

$$\mathbf{u}_0^T \mathbf{K}\mathbf{u}_0 = \omega_0^2 \quad , \quad \mathbf{u}_\infty^T \mathbf{K}\mathbf{u}_\infty = \omega_\infty^2 \tag{4.6}$$

The limiting mode shapes and natural frequencies are all real-valued and may be derived directly from the associated generalised eigenvalue problems.

The equations of motion can be described in the reduced two-dimensional subspace by substitution of (4.3) into (4.1) followed by pre-multiplication by the limiting mode-shapes. In the frequency domain the reduced system of equations can be written in the following homogeneous form when free vibrations are considered

$$\begin{bmatrix} \omega_0^2 - \omega^2 + u_0^2 H & \kappa(\omega_0^2 - \omega^2) \\ \kappa(\omega_0^2 - \omega^2) & (\omega_\infty^2 - \omega^2) \end{bmatrix} \begin{bmatrix} r_0 \\ r_\infty \end{bmatrix} = \begin{bmatrix} 0 \\ 0 \end{bmatrix} \tag{4.7}$$

The amplitude of the mode shape in the damper location is $u_0 = \mathbf{w}^T \mathbf{u}_0$ and $\kappa = \mathbf{u}_\infty^T \mathbf{M} \mathbf{u}_0$ represents the coupling between the two limiting mode shapes. Free vibrations require a singular matrix which yields a characteristic equation in ω in e.g. Main and Krenk [29]. This characteristic equation can be rewritten in an explicit, given solution by assuming that the coupling parameter $\kappa \simeq 1$. This solution is conveniently expressed in the following compact form

$$\frac{\omega - \omega_0}{\omega_\infty - \omega_0} \simeq \frac{\mu H}{1 + \mu H} \tag{4.8}$$

In this expression the modal flexibility parameter is given as

$$\mu = \frac{u_0^2}{\omega_\infty^2 - \omega_0^2} \simeq \frac{u_0^2}{2\omega_0(\omega_\infty - \omega_0)} \tag{4.9}$$

The modal damping ratio is determined as the relative imaginary part of the complex valued natural frequency, which can be approximated by $\zeta = \simeq \mathrm{Im}[\omega - \omega_0]/|\omega|$. In the case of response dominated by resonance the magnitude of the structural is approximately inverse proportional to the damping ratio of the dominant mode. Thus, a suitable optimal tuning is based on the maximization of the modal damping ratio with respect to the gain parameter of the particular control strategy. If the approximation $|\omega| \simeq \omega_0$ is introduced the damping ratio can be written as

$$\zeta = \frac{\omega_\infty - \omega_0}{\omega_0} \frac{\mu \mathrm{Im}[H(\omega_0)]}{(1 + \mu \mathrm{Re}[H(\omega_0)])^2 + \mu^2 \mathrm{Im}[H(\omega_0)]^2} \tag{4.10}$$

Optimal calibration of the damper model is based on the maximization of the damping ratio which is related to the stationarity condition $\delta\zeta = 0$. This relation is in the following section used to calibrate the control strategies.

4.3 Control Strategies

The Different control strategies are discussed below. First optimal viscous damping strategy (VD) is demonstrated and later positive (VDPS) and negative stiffness (VDNS) is introduced. It is seen from the expression in (4.10) that the stiffness of the damper $\mathrm{Re}[H(\omega_0)]$ appears in the denominator. It is therefore observed that a potential increase in the damping ratio is associated with a corresponding reduction of damper stiffness and for that reason, the application of negative stiffness improves the damping efficiency for resonant response conditions. Friction damping with negative stiffness (FDNS) is demonstrated and compared with other methods. Finally a neural network based optimal model reference control strategy is discussed and demonstrated by numerical example. Desired force-displacement trajectories for viscous damping, viscous damping with positive and negative stiffness and friction damping with negative stiffness are shown in Figure 4.2.

The schematic diagram closed loop system is shown in Figure 4.3.

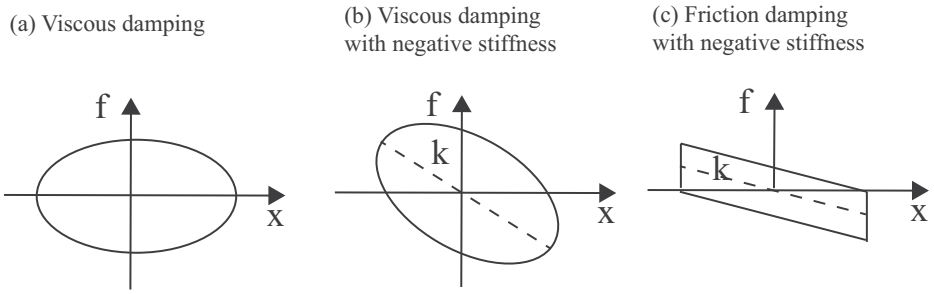

FIGURE 4.2: Desired force displacement trajectories: (a) VD, (b) VDNS, (c) FDNS.

4.3.1 Optimal Viscous Damping

The prototype damper model is the pure viscous model. For this model the damper force is directly proportional to the collocated velocity of the damper motion [P2, P4]. The negative sign in front of f in (4.1) generates viscous damping on the shear frame for $c > 0$.

$$f = c\dot{x} \tag{4.11}$$

where c is the viscous parameter. When compared with the linear frequency representation of the damper force in (4.2), the damper function for the viscous damper is

$$H(\omega) = i\omega c \simeq i\omega_0 c \tag{4.12}$$

The real of this function is zero and the imaginary part is substituted into the expression for the damping ratio (4.10). The optimal viscous parameter is then determined by the condition $d\zeta/dc = 0$, which gives

$$c_{opt} \approx \frac{2(\omega_\infty - \omega_0)}{u_0^2} \tag{4.13}$$

where the approximation $\omega_\infty + \omega_0 \approx 2\omega_0$ has been introduced. The optimal viscous damper is without stiffness and is therefore a suitable benchmark example for damper models with negative stiffness.

4.3.2 Viscous Damping with Negative Stiffness

Viscous damping with negative stiffness model has both frequency dependent stiffness and viscous components [P2, P4]. However, in the present formulation it is assumed that the governing parameters are constant, so that the damper force can be written as

$$f = c\dot{x} + kx \tag{4.14}$$

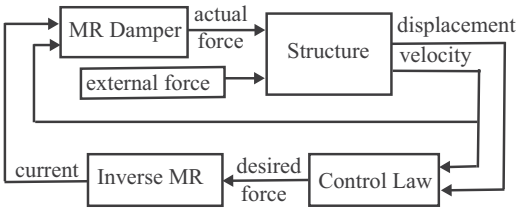

FIGURE 4.3: Closed loop control system.

and the transfer function becomes

$$H = i\omega c + k \tag{4.15}$$

The real and imaginary part of this expression are again substituted into the expression for the damping ratio in (4.10). The damper stiffness k is considered as a system parameter, while the viscous parameter is the control gain. Thus, the optimal viscous parameter is again determined by the condition $d\zeta/dc = 0$, which gives

$$c_{opt} \approx \frac{2(\omega_\infty - \omega_0)}{u_0^2} + \frac{k}{\omega_0} \tag{4.16}$$

where the second term introduces the correction due to damper stiffness. The stiffness term is taken for negative value. The desired force is clipped because unclipped viscous damping with negative stiffness produces active forces, which is highlighted in Figure 4.2 (b) by the dashed trajectory parts. The viscous coefficient in (4.16) must be tuned according to the choice of k. The negative sign in front of f in (4.1) generates positive stiffness on the shear frame if $k > 0$ and negative stiffness on the shear frame if $k < 0$. After clipping, the optimal force for viscous damping with stiffness is expressed as

$$f_{clipp} = \begin{cases} c\dot{x} + kx & : \quad (c\dot{x} + kx)\dot{x} \geq 0 \\ 0 & : \quad c\dot{x} + kx)\dot{x} < 0 \end{cases} \tag{4.17}$$

4.3.3 Amplitude Proportional Friction Damping with Negative Stiffness

The optimal semi-active damping force without clipping that maximises structural damping is the superposition of a friction force controlled in proportion to the damper displacement amplitude and a negative stiffness force balancing the friction at displacement extreme [P2]. The force-displacement trajectory is shown in Figure 4.2 (c). Details of the optimal shape calculation are demonstrated in [30]. Hence, the desired force becomes

$$f = \text{sign}(\dot{x})\alpha X + kx \tag{4.18}$$

where X is the amplitude of the relative damper displacement, α is the proportional gain of the friction force component and $k < 0$. The desired force in (4.18) is a purely dissipative force if

$$\alpha \geq |k| \tag{4.19}$$

Thus, in the case of negative damper stiffness the optimal semi-active balance between the friction force level and the stiffness component is obtained for for

$$k \ = \ -\alpha \qquad , \qquad \alpha > 0 \tag{4.20}$$

This case is illustrated in Figure 4.2(c), where it is seen that the force level exactly reaches zero at reversal. Assuming sinusoidal damper motion, the friction force component of (4.18) i.e. $\text{sign}(\dot{x})\alpha X$, can be transformed into the viscous coefficient of an energy equivalent viscous damper. The equivalent viscous damper is expressed as

$$c_{equiv} = \frac{4\alpha}{\pi\omega} \tag{4.21}$$

The force of the energy equivalent viscous damper with negative stiffness then becomes

$$f_{equiv} = \frac{4\alpha}{\pi\omega}\dot{x} - \alpha x \tag{4.22}$$

In the frequency domain this can be written as

$$f_{equiv}(\omega) = \alpha\Big(i\frac{4}{\pi} - 1\Big)x \tag{4.23}$$

where X is equal to the frequency amplitude x. The equivalent damper function is given as

$$H_{equiv} = \alpha\Big(i\frac{4}{\pi} - 1\Big) \tag{4.24}$$

The damping ratio is found by substitution into (4.10) and the optimal value of the common gain factor α is determined by $d\zeta/d\alpha = 0$. This leads to the expression

$$\alpha_{opt} = \frac{1}{\sqrt{16/\pi^2 + 1}} \frac{(\omega_\infty^2 - \omega_0^2)}{u_0^2} \tag{4.25}$$

4.3.4 Neural Network Based Model Reference Control

This control strategy is developed based on a neural network model identification technique, where the neural network model is trained by a reference damper model [P3]. As demonstrated by Boston et al. [30], the optimal semi-active force is the superposition of a friction force that is controlled in proportion to the damper displacement amplitude and a negative stiffness force. The optimal shape of the force-displacement trajectory identified in [30] is taken as reference model for the neural network model. The hysteresis loop is formed based on the assumption of harmonic displacement, which is used as the input to the proposed neural model, while the damper force based on the desired hysteresis loop is used as the output of the neural controller. The optimal shape of the force-displacement trajectory is shown in Figure 4.4, which corresponds to the friction model with negative stiffness considered previously and shown in Figure 4.2(c). The hysteresis model is inherently non-linear, whereas the calibration formulation in (4.10) requires a linear damper model. Thus, as for the friction damping with negative stiffness an equivalent linear model is assumed to contain a viscous and a stiffness component [P3],

$$f_{equiv} = c\dot{x} + kx \tag{4.26}$$

If x is a sinusoidal signal, the parameters of the linear equivalent model in (4.26) can be determined by equivalence over a full vibration period, see [35]. This yields the following equivalent linear model for the hysteresis loop shown in Figure 4.4.

$$f = \frac{2f_m}{\pi\omega X}\dot{x} - \frac{f_m}{2X}x \tag{4.27}$$

where X again is the amplitude of the damper displacement, k is negative stiffness and fm is the corresponding force of the hysteresis loop at maximum amplitude. In the frequency

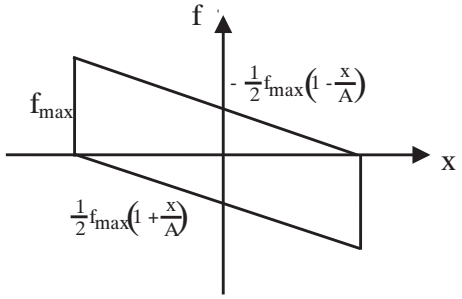

FIGURE 4.4: Force displacement hysteresis plot for FDNS.

domain the model is expressed as

$$f = \frac{f_m}{X}\left(-\frac{1}{2} + i\frac{2}{\pi}\right)x \tag{4.28}$$

Comparison with the frequency representation in (4.2) gives the following expression for the transfer function of the linear equivalent hysteretic damper model:

$$H(\omega) = \frac{f_m}{X}\left(-\frac{1}{2} + i\frac{2}{\pi}\right) \tag{4.29}$$

The force level to amplitude ratio f_m/X represent a proportional gain parameter of this model, similar to α for the friction force with negative stiffness in the previous section. The damping ratio is again found by substitution into (4.10) and the optimal value of the common gain factor is determined stationarity with respect to f_m,

$$f_m^{opt} = 1.24\frac{(\omega_\infty^2 - \omega_0^2)}{u_0^2}\,X \tag{4.30}$$

which shows that the force level must be scaled with the estimated amplitude X. Note that this results corresponds to (4.25) for $f_m = 2\alpha X$.

A four-layer feedforward neural network is adopted which consists of one input, two hidden layers and a single output layer. The displacement and velocity in current state and five preceding values are taken as input and force in current state is output in the proposed neural network. The neural network controller is trained with training data generated at different amplitudes and at different frequencies of both the displacement response and the corresponding force data from the optimal friction model. The trained model is verified with independent data sets and subsequently used in a closed-loop implementation. The training algorithm used in the feedforward backpropagation neural network is the Levenberg-Marquardt (LM) algorithm based on a least-square curve fitting. The design procedure for the feedforward neural network model has been described previously in Table 2.3 in Chapter 2.

4.4 Closed-Loop Simulation

In this section a closed-loop control system is presented. It is used to operate the semi-active MR damper for tracking of the desired force given by different control strategies and then forwarded through an inverse MR damper. The efficiency of the proposed control strategies depends on the proper tuning of control parameters as described in Section 4.3 and subsequently on the ability of the inverse MR damper model to track the desired optimal control force.

4.4.1 Example: Pure Viscous Damping

The viscous damping strategy using MR damper in a closed loop is simulated for a five-floor shear frame structure with harmonic base excitation. The force-velocity and force-displacement hysteresis plots of the damper force and desired force from control laws are compared for the optimal viscous damping strategy and the result is quite satisfactory. The force tracking task by the MR damper is quite well performed. From the force-displacement as well as the force-velocity trajectory for the viscous damper in Figure 4.6, it is visible that the MR damper has a force limit at zero current. Therefore, it is not possible for the MR damper to follow the desired force below the force limit at zero current. Here for this damper, the force limit is 24 N. When viscous damping (VD) is emulated, the force tracking

error is mainly given by the residual force at 0 A and the noise in the current due to the neural network based force tracking as seen from Figures 4.5(a,b). The structural damping of the first excited mode is determined from the top floor displacement. The time history of the top floor displacement and damper displacement is shown in Figures 4.5 and 4.6. The other control concepts are then tested in a simulation at the same excitation amplitude as in Figure 4.5(c,d). The viscous damping strategy is also applied directly to the structure without MR damper and the change in performance is compared.

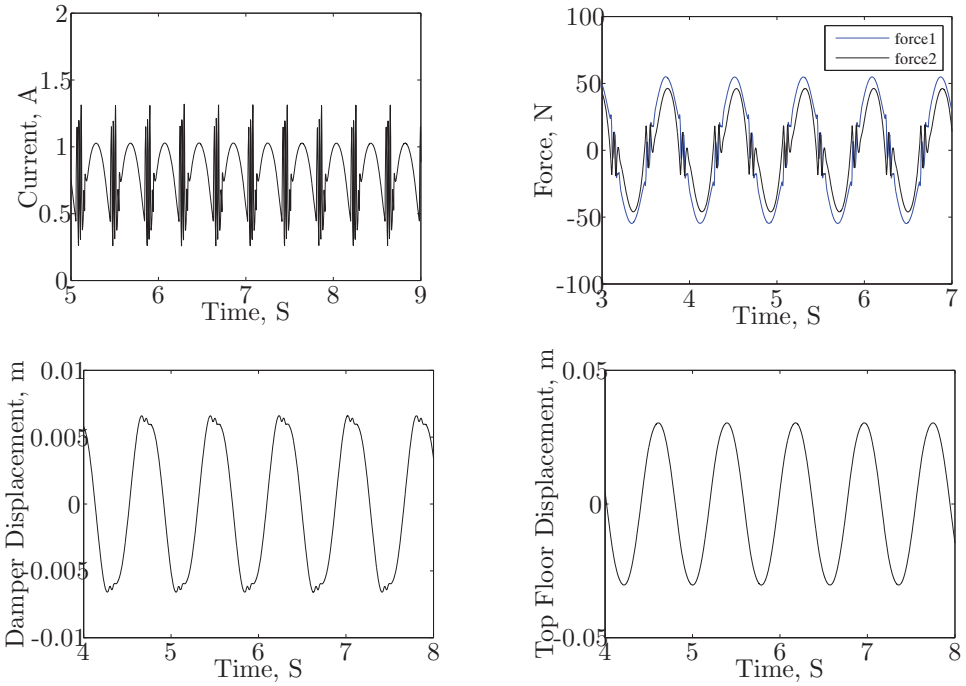

FIGURE 4.5: Current (a), Force comparison (b), Damper displacement (c), Top floor displacement (d) (VD)

4.4.2 Example: Viscous Damping with Negative Stiffness

A negative stiffness component is added to the viscous part and then the optimal viscous parameter is determined. As seen from Figure 4.8, the measured force-displacement trajectory of viscous damping with negative stiffness (VDNS) is spiky. The spikes are triggered by the initial very large increase of the desired force when the MR damper displacement turns its direction. The currents and the force tracking are shown in Figure 4.7. Force displacement and force velocity trajectories for actual and desired forces are shown in Figure 4.8. The time history for top floor and damper displacement is shown in Figure 4.7 , where it is clearly visible that introducing negative stiffness significantly reduces the top floor displacement.

4.4.3 Example: Frictional Damping with Negative Stiffness

Friction damping with negative stiffness is emulated. The actual force-displacement trajectories in the experiment and the simulation are not that noisy as viscous damping with negative stiffness, which shows better structural damping and reduced top floor displacement. The currents and the force tracking are shown in Figure 4.9. The force-displacement

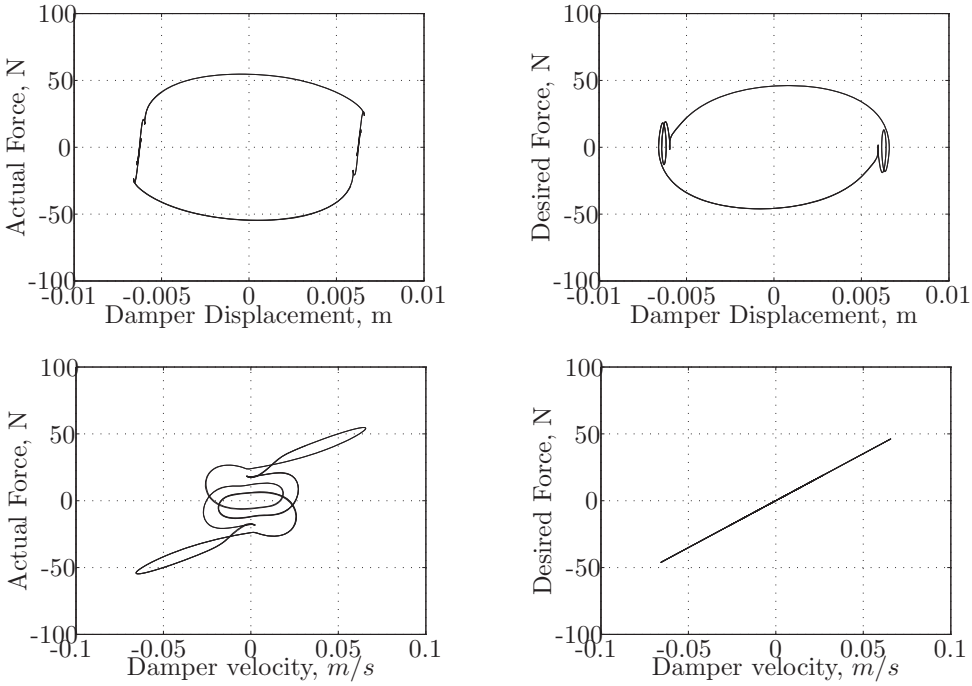

FIGURE 4.6: Force-displacement and force-velocity trajectories (VD)

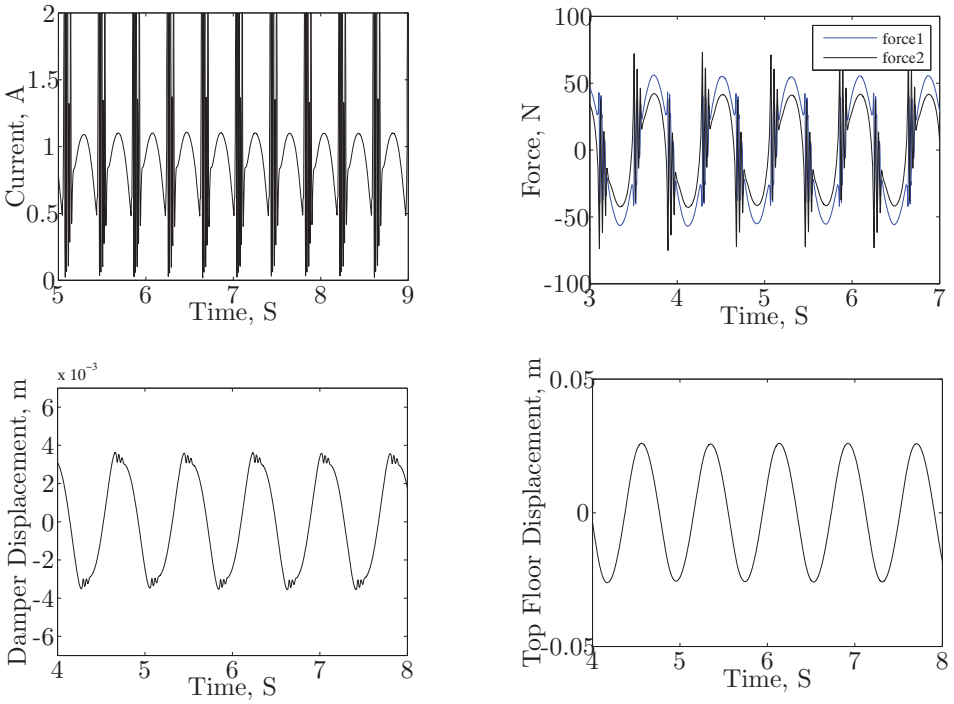

FIGURE 4.7: Current (a), Force comparison (b), Damper displacement (c), Top floor displacement (d) (VDNS)

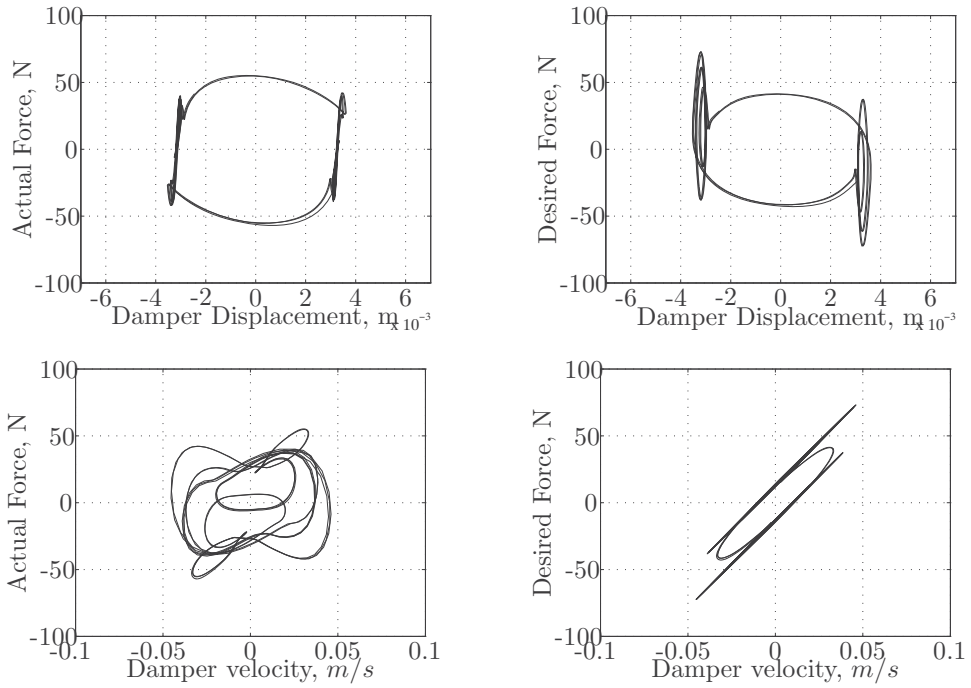

FIGURE 4.8: Force-displacement and force-velocity trajectories (VDNS)

and force-velocity trajectories for actual and desired forces are shown in Figure 4.10. The time history for top floor and damper displacement is shown in Figure 4.9, where it is seen that friction damping with negative stiffness significantly reduces the top floor displacement in comparison with the two other damping strategies discussed earlier.

4.4.4 Example: Neural Network based Model Reference Control

The neural network control (NNC) strategy is applied to structural vibration reduction based on harmonic base excitation using an MR damper in a closed-loop simulation. The time history of damper displacement and top floor displacement is shown in Figure 4.11. The currents and the force tracking are also shown in Figure 4.11. The force-displacement and force-velocity trajectories for actual and desired forces are shown in Figure 4.12. From the time history for top floor and damper displacement, it is seen that the neural network controller can significantly reduce the top floor displacement similarly to friction damping with negative stiffness [P3].

TABLE 4.1: Performance Indices

	VD	VDNS	FDNS	NNC
RMS (x^{max}_{damp})	0.0066 m	0.0038 m	0.0091 m	0.0044 m
RMS (x^{max}_{top})	0.030 m	0.026 m	0.023 m	0.024 m
RMS ($\ddot{x}^{max}_{damp}$)	0.81 m/s^2	0.91 m/s^2	0.80 m/s^2	0.84 m/s^2
RMS ($\ddot{x}^{max}_{top}$)	1.81 m/s^2	1.76 m/s^2	1.76 m/s^2	1.79 m/s^2

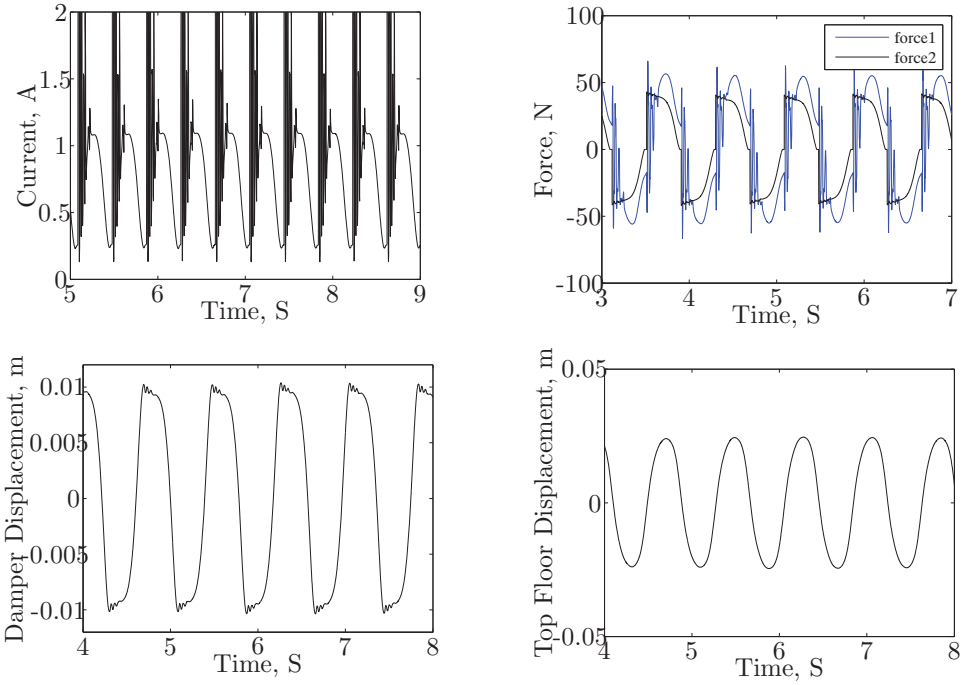

FIGURE 4.9: Current (a), Force comparison (b), Damper displacement (c), Top floor displacement (d) (FDNS)

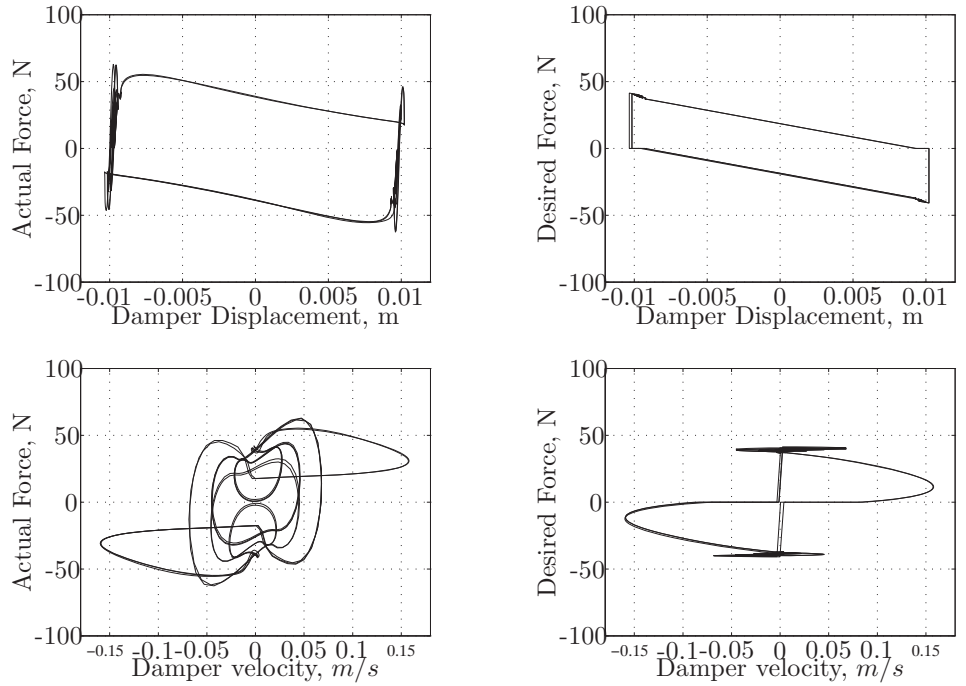

FIGURE 4.10: Force-displacement and force-velocity trajectories (FDNS)

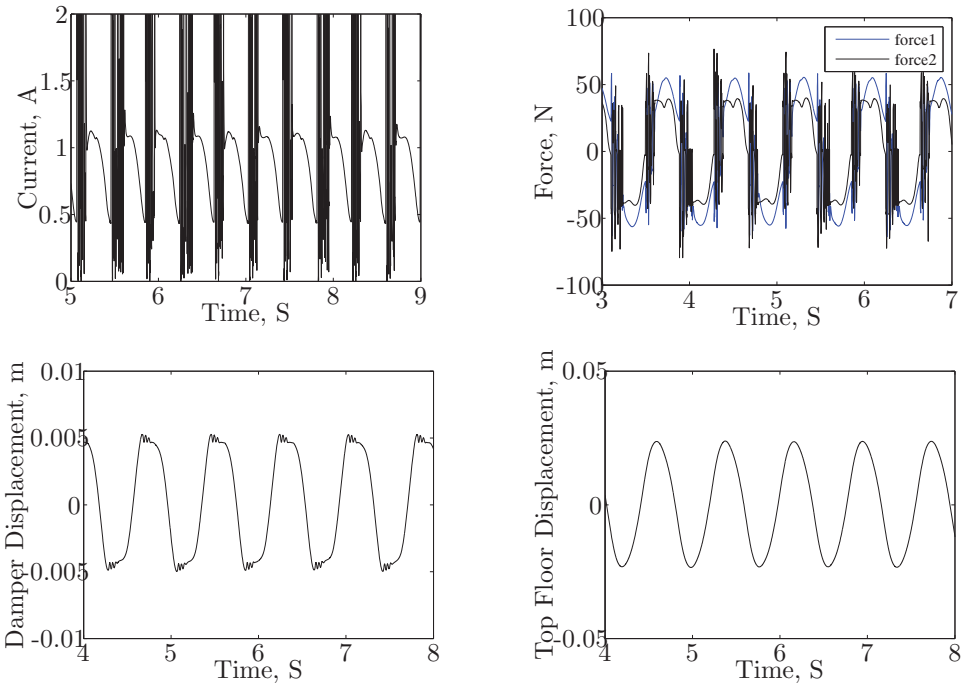

FIGURE 4.11: Current (a), Force comparison (b), Damper displacement (c), Top floor displacement (d) (NNC)

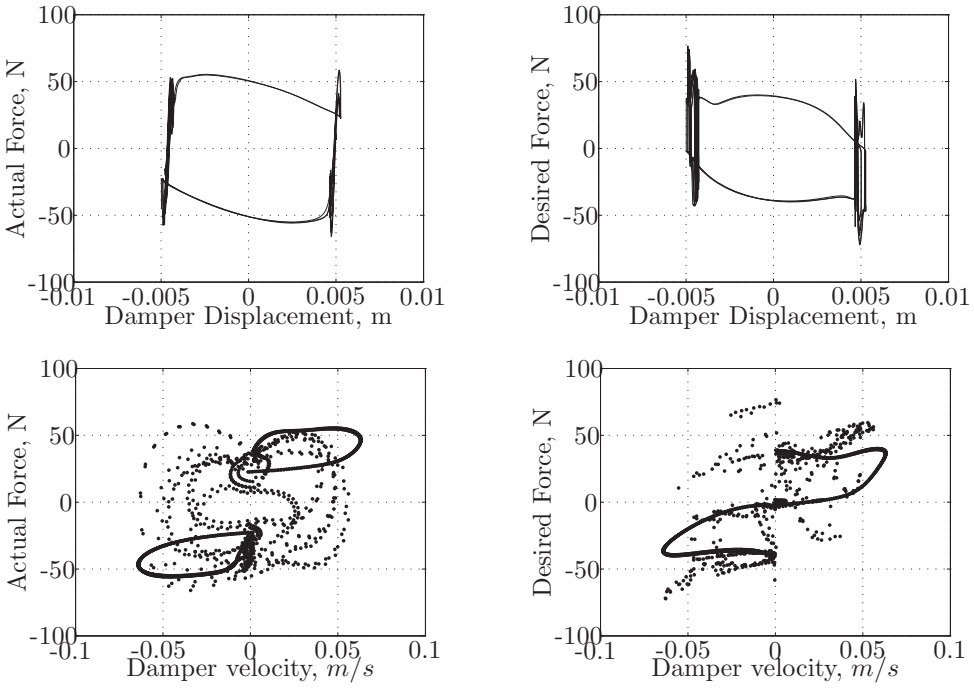

FIGURE 4.12: Force-displacement and force-velocity trajectories (NNC)

4.5 Summary

The damping of a shear frame with five masses with controlled MR damper between ground plate and the first mass was investigated in a simulation. The tested control laws were viscous damping, viscous damping with negative stiffness and optimal semi-active friction damping with negative stiffness and neural network based model reference control. The control laws were designed using a validated model of the shear frame. In the closed-loop simulation, a neural network MR model is used for force tracking. Rms values of the peak displacement and peak acceleration of each cycle for top floor and damper location are taken as performance parameters. From the performance parameters chart in Table 4.1, it is clearly visible that introducing negative stiffness can make significant reduction in damper displacement and also in top floor displacement. The response of the top floor using semi-active neural controller and friction damping with negative stiffness gives quite satisfactory results compared with pure viscous damping and pure viscous damping with negative stiffness. A significant improvement in acceleration is also observed but the acceleration contains some noise.

Chapter 5

Experimental Implementation of Control Strategies

Survival of civil structures from excessive random vibration due to uncontrollable external events - due to natural hazards and otherwise - is very important where vibration control of large flexible structures, such as shear frame buildings, is a great task in closed loop situation. Some success of practical implementation of control laws to attain this goal has been reported in the use of semi-active control devices as for instance magnetorheological dampers [99].

The following sections describe experimental implementation of semi-active control strategies for a shear frame with a controlled magnetorheological (MR) damper mounted between ground and first floor in order to mitigate the fundamental bending mode. Some linear control strategies, for example, optimal viscous damping, clipped viscous damping with negative and positive stiffness and also nonlinear control strategies, for example, optimal friction damping with negative stiffness are implemented. MR damper is a semi-active device and control law can not give direct command to MR damper to produce desired force. For semi active control strategy requires a feed forward mechanism which will produce appropriate current from the desired force value from controller output and feed the current into the MR damper to generate proper force value. This mechanism is also called as force tracking mechanism. The force tracking is solved with a novel neural network model of the MR damper that takes the absolute values of damper velocity and desired force as inputs because the outputted desired current is a positive quantity [P1]. The force tracking is improved by a low-pass filter to reduce the noise in the desired current and a switch that truncates the desired current to zero, if the desired force is smaller than the residual force at 0 A [P2]. The measured and simulated control forces still show a spiky behaviour due to the fairly large sensitivity of the neural network to slightly noisy inputs. However, the measured and simulated structural damping ratios correspond well to the expected values. This indicates that the mean stiffness and mean energy dissipation of the control force mainly determine the structural damping [P2]. Negative stiffness is introduced into the design of control laws. To demonstrate the significance of the negative stiffness, positive stiffness is also introduced with viscous damping. The closed loop implementation of the control laws on real structure also demonstrate the significant improvement in structural damping due to inclusion of negative stiffness [P2].

5.1 Experimental Setup

The experimental setup consists of a hydraulic cylinder driving a shaking table on which a 5 DOF system is mounted. The experimental setup at the EMPA structural laboratory is shown in Figure 5.1. The housing of the MR damper is fixed to the shaking table and the MR damper rod applies the semi-active control force to the first mass of the 5 DOF system. This situation is equivalent to a 5 DOF system with controllable damper that mitigates the relative motion between ground and first floor. The MR damper under consideration is a rotational type with approximately 22 N residual force at 0 A and 300 N at maximum current of 4 A [56].

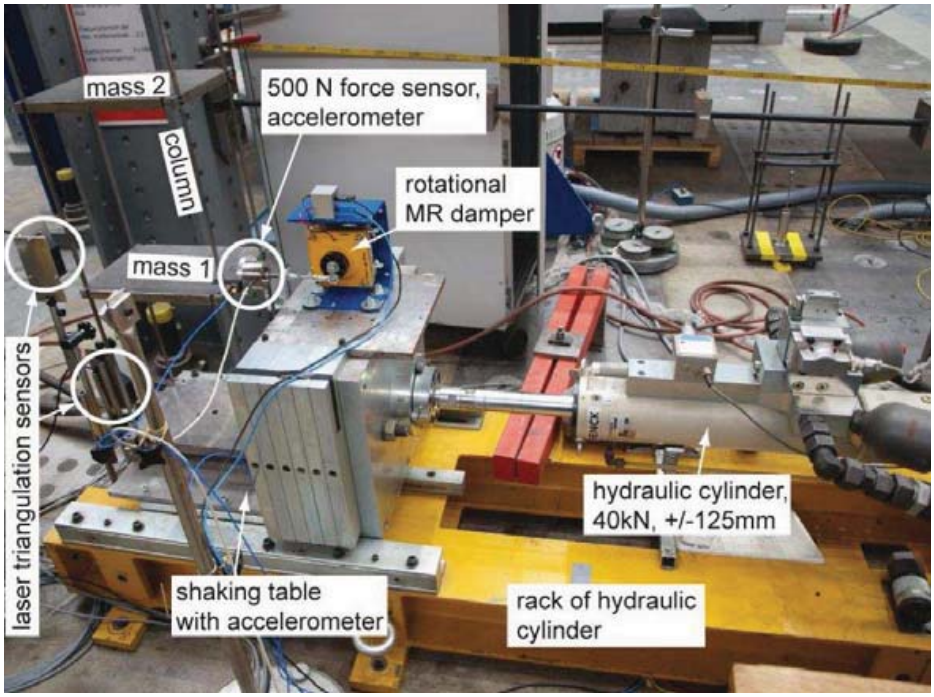

FIGURE 5.1: Filtering of measurement data.

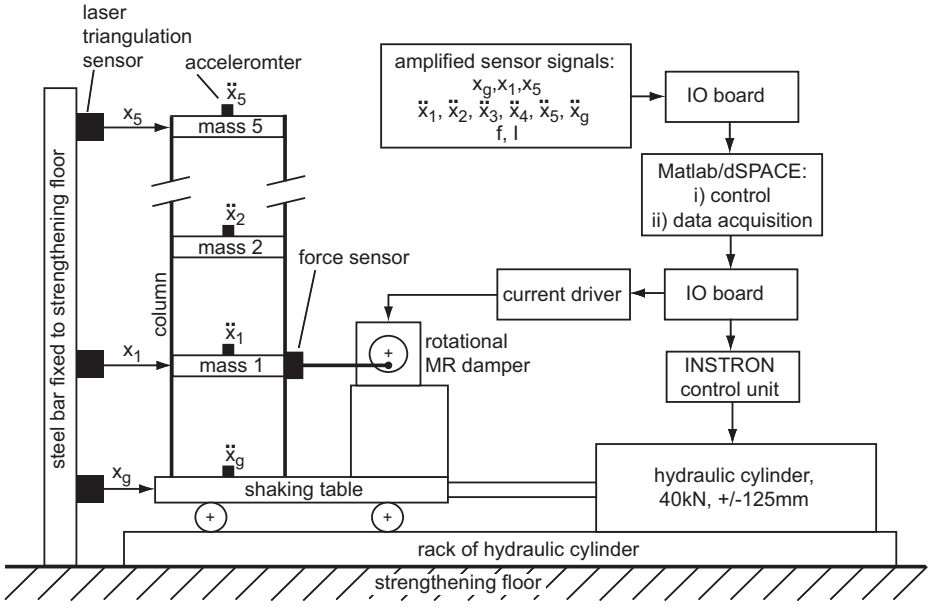

FIGURE 5.2: Schematic of test setup.

The accelerations of all masses and the ground are recorded. The damper rod velocity is estimated by a Kinematic Kalman Filter (KKF) from the relative displacement between base and first mass and from the absolute acceleration of the first mass. The relative displacement derived from the laser sensor at the top mass and the laser sensor at ground represents the tip response of the shear frame. The force sensor between damper rod and first plate is

installed in order to measure the force tracking error but it is not used as force feedback. The schematic of the test setup is shown in Figure 5.2.

The controller is programmed in Matlab/dSPACE which is also used for the data acquisition. The control algorithm outputs the desired control force at a sampling frequency of 500 Hz. A neural network based inverse MR damper model is used to determine the desired current in real-time. The desired current is converted into a command voltage that is outputted by the IO board and is fed to the current driver of type KEPCO that guarantees negligibly small tracking error of the MR damper current. The Matlab/Simulink file of the controller is also used to output the command voltage of the INSTRON control unit that controls the hydraulic cylinder displacement.

5.2 Velocity Estimation Using Kinematic Kalman Filter

The inverse neural network model for the MR damper depends partly on proper velocity measurement to track the desired force. The velocity cannot be measured directly. The only way to measure velocity is taking a differentiation of measured displacement data or taking measured acceleration data into consideration. However, including a differentiator to the system adds noise, while accelerations are inherently noisy and an integrator furthermore introduces a phase delay to the resulting signal. Therefore, a simple but effective method is needed for fusing displacement and acceleration data to derive velocity. The Kinematic Kalman Filter (KKF) is a very effective tool for simple and robust estimation of velocity [98]. KKF does not depend on plant parameters as in model based Kalman filters. If the displacement and acceleration are both measured, the system equation and the KKF estimation model are designed to fuse displacement and acceleration to estimate velocity. The system model for Kinematic Kalman Filter is given as

$$\begin{aligned} \begin{bmatrix} \dot{x}_1 \\ \dot{x}_2 \end{bmatrix} &= \begin{bmatrix} 0 & 1 \\ 0 & 0 \end{bmatrix} \begin{bmatrix} x_1 \\ x_2 \end{bmatrix} + \begin{bmatrix} 0 \\ 1 \end{bmatrix} \begin{bmatrix} a_m + w_a \end{bmatrix} \\ y &= x_m + w_x \end{aligned} \tag{5.1}$$

The output equation can then be represented as

$$y = \begin{bmatrix} 1 & 0 \end{bmatrix} \begin{bmatrix} x_1 \\ x_2 \end{bmatrix} + w_x \tag{5.2}$$

The two-state variables are the displacement $x_1 = x$ and the velocity $x_2 = \dot{x}$ of the system. w_a and w_x are accelerometer measurement noise and displacement measurement noise, respectively. The KKF is obtained as

$$\begin{bmatrix} \dot{\hat{x}}_1 \\ \dot{\hat{x}}_2 \end{bmatrix} = \begin{bmatrix} 0 & 1 \\ 0 & 0 \end{bmatrix} \begin{bmatrix} \hat{x}_1 \\ \hat{x}_2 \end{bmatrix} + \begin{bmatrix} k \\ l \end{bmatrix} \begin{bmatrix} y - \hat{x}_1 \end{bmatrix} \tag{5.3}$$

where k and l are filter gains. From the KKF the predicted displacement is $\hat{x}_1$ and the predicted velocity is $\hat{x}_2$. The advantage of KKF is that it is model parameter independent.

5.3 Closed-Loop Model Design in Matlab/Simulink

As seen from Figure 5.3, the model is extended by a switch and analogue low-pass Butterworth filter. The switch outputs $I_{des}(k) = 0\,\text{A}$ if the absolute value of the desired force $|f_{des}(k)|$ is smaller than the residual force at 0 A of the MR damper under consideration. The application of this practical knowledge reduces the control force tracking error due to modelling errors at small forces. The Butterworth filter with cutoff frequency 60 Hz is included to reduce the noise in the desired current. The noise has mainly two sources:

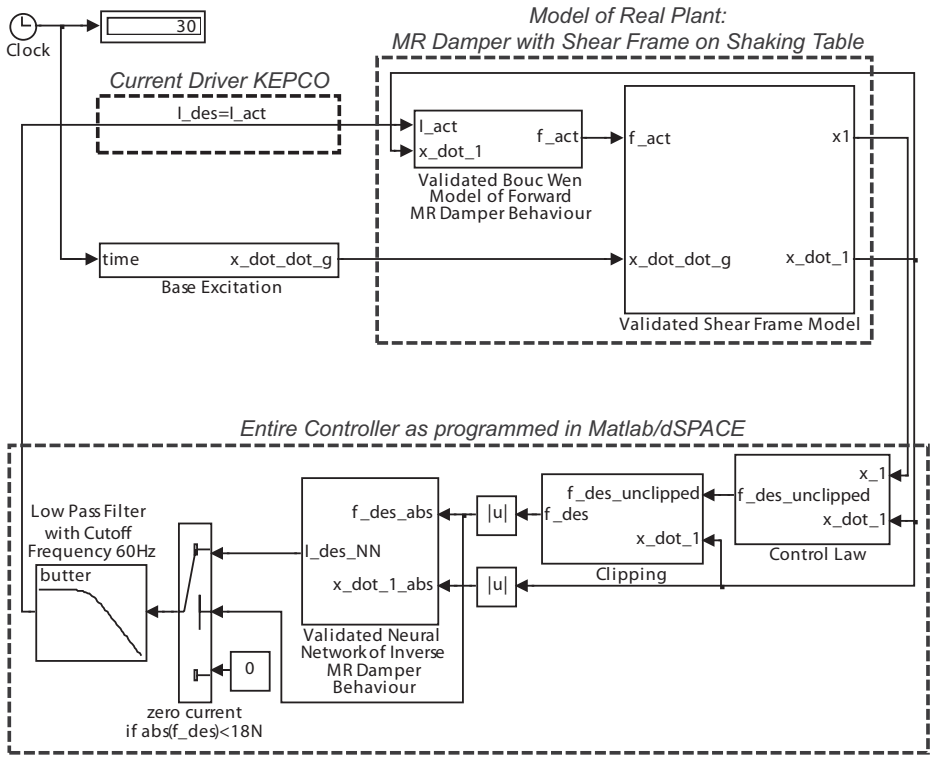

FIGURE 5.3: Matlab/Simulink model of closed loop system.

- One is the high frequencies in the damper velocity that are generated when f_{des} cannot be tracked because f_{des} is larger than the residual force at 0 A. This leads to clamping effects of the shear frame in the damper position. When the force is larger than the residual force value at 0 A, the desired force f_{des} can be tracked and the MR damper starts to work again. The sudden change between locked and smoothly operating MR damper induces the high-frequency signal parts in the damper velocity. This noise source exists in both the simulations and the experiments.
- Another source is the measurement noise, which only exists in the experimental data. The input of the feed forward part are the measured damper velocity $\dot{x}$ and the desired damper force f_{des}, which both include measurement noise and thereby evoke a noisy desired damper current I_{des}.

In order to compare the simulated and measured force tracking and damping of the 5 DOF system, the simulations and the measurements of the closed loop are performed with an identical controller. The controller includes the subsystems control law, clipping, validated neural network of inverse MR damper behaviour, switch and low-pass filter with cut-off Frequency 60Hz as depicted in Figure 5.3 which is programmed in Matlab/ dSPACE. The controller runs at a sampling frequency of 200 Hz, which is the same as used to train the neural network [P1, P2]. The simulation of the closed loop assumes zero current tracking error, i.e. the desired and the actual currents are equal ($I_{des} = I_{act}$). At the test setup, the current driver (KEPCO) is used to guarantee a negligibly small current tracking error, i.e. $I_{des} \approx I_{act}$. The MR damper is simulated with a validated Bouc-Wen model of the MR damper under consideration. The simulated shear frame model is given in Chapter 3. In the simulations, the shear frame structure is excited by the actual measured base acceleration record $\ddot{x}_g = \ddot{x}_g^{meas}$.

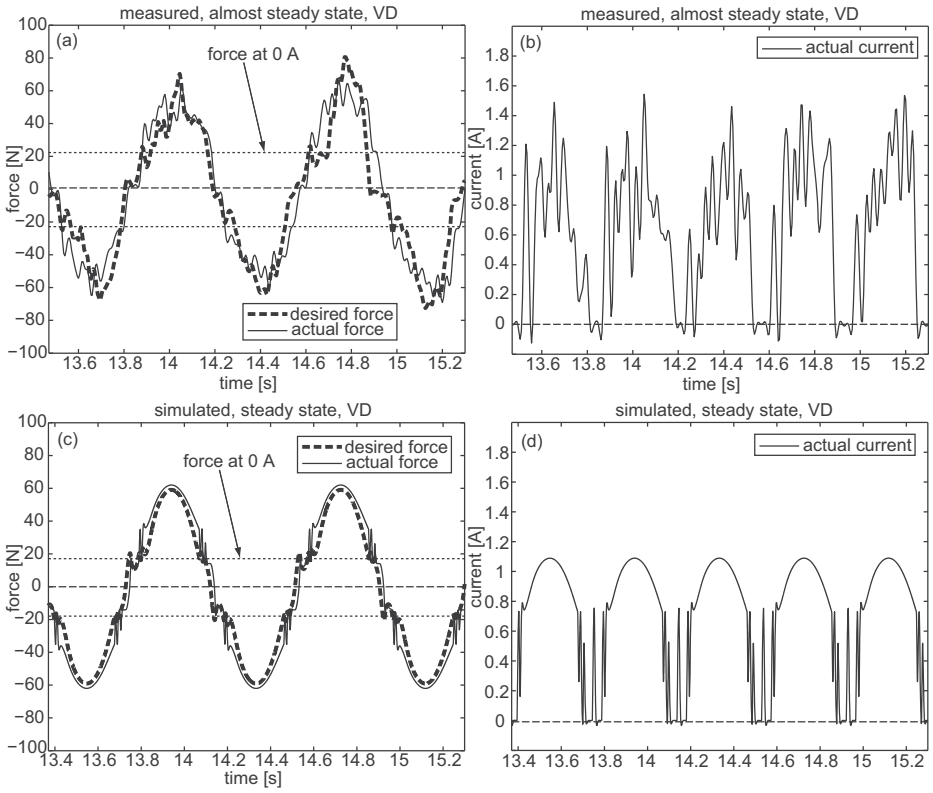

FIGURE 5.4: Measured (a,b) and simulated (c,d) force tracking with NN based MR damper model.

5.4 Force Tracking

The force tracking error is depicted in Figure 5.4 for viscous damping (VD) and the maximum viscous force of approximately 60 N which is a typical value for the first mode of the shear frame under consideration. The force tracking error in the experiment is slightly larger than in the simulation since the measurement noise in the collocated velocity produces a fairly noisy desired force which generates a noisy current as shown in Figure 5.4(b). The actual force is not so noisy as the applied current because the MR damper behaves similarly to a low-pass filter that mitigates these spikes to some extent. It is seen from Figures 5.4(a,c) that the resulting force tracking error in experiment and simulation is acceptably small. Both time histories show the regions of the residual force that constrains the force tracking. Here, zero applied current is the best choice in order to minimise the force tracking error.

5.5 Experimental and Numerical Simulation

Section 5.4 shows the measured and simulated force tracking error due to the inverse neural network approach that is used as model-based feedforward. This section presents the measured and simulated force displacement trajectories, the force-velocity trajectories and the free decay responses of the 5 DOF system resulting from different control concepts: Viscous damping (VD), viscous damping with positive stiffness (VDPS), viscous damping with negative stiffness (VDNS) and friction damping with negative stiffness (FDNS). In order to demonstrate the negative impact of positive stiffness on the damping of the 5 DOF, also clipped viscous damping with positive stiffness is tested. The desired force-displacement

trajectories are shown in Figures 5.5.

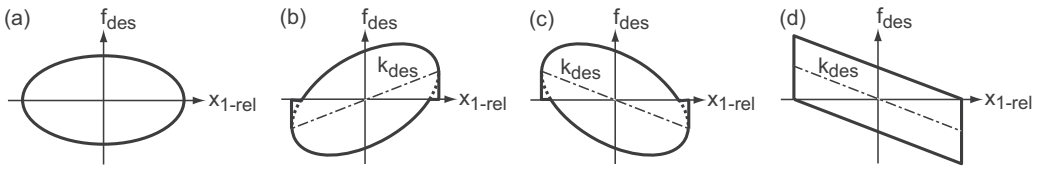

FIGURE 5.5: Desired force displacement trajectories: VD (a), VDPS (b)VDNS (c), FDNS (d).

5.5.1 Pure Viscous Damping

When viscous damping (VD) is emulated, the force tracking error is mainly given by the residual force at 0 A and the noise in the current due to the neural network based force tracking shown in Figure 5.6. The structural damping of the first excited mode is determined from the top floor displacement x_5. Due to the fairly large damper position of 1/11 of the wave length of the first mode, the resulting structural damping is large. Therefore, the number of local peaks with non-zero MR damper current is small which explains the variation of the point-to-point damping ratio shown in Figure 5.7. Thus, the point-to-point damping ratio values are averaged by the exponential fit from which the mean damping ratio $\bar{\zeta}$ is obtained. The values are shown in Table. 5.1. Only the local peaks with non-zero current during their corresponding half period time are taken into consideration for the assessment because these peaks represent the decay response due to controlled damping. The damping of the subsequent peaks is determined by the residual force of the MR damper that cannot be controlled as such. The time history of the displacement during this subsequent part shows an almost triangular shape which indicates predominant friction damping due to the damper ceilings and bearings. As Table. 5.1 shows, the structural damping that is achieved on the real structure is a little bit smaller than the one obtained in the simulation which might be the effect of increased force tracking error on the real structure with the real MR damper.

In addition to the mean damping ratio, the damping performance of the tested control concepts is also assessed by the root mean square (rms) of the steady state response of the tip displacement for constant excitation amplitude (Table 5.1). In order to be able to compare the rms values of the tests and the simulations, the excitation amplitude of base acceleration $\ddot{x}_g$ in the simulation is adjusted such that the $rms(x_5)$ is equal for simulations and experiments associated with viscous damping (VD). The other control concepts are then tested in a simulation at the same excitation amplitude. The rms is determined for:

- The displacement of the top floor, which illustrates the damping performance.
- The displacement of the first floor, which indicates the potential softening due to negative stiffness.
- The acceleration of the top floor, which also identifies the overall damping.
- The acceleration of the first floor, which gives a direct measure for the high-frequency content and thereby the spill-over effect.

The rms values resulting from VD are the benchmark and the rms values due to the other tested control concepts can then be compared to this benchmark. Measured and simulated mean damping ratios and steady state responses are determined for constant excitation

TABLE 5.1: Comparison between Measured and Simulated Performance

control law		VD	Clipped VDPS	Clipped VDNS	FDNS
tuning		c = 650 Nm/s	c = 400 Nm/s	c = 250 Nm/s	α=3000 N/m
			k = +2500 N/m	k = -4000 N/m	
measured					
$\bar{\zeta}$	[%]	11.8	9.0	approx. 22	approx. 26
$rms(x_5)$	[mm]	24.3	23.03	15.5	11.2
$rms(x_1)$	[mm]	6.6	6.7	4.9	3.5
$rms(\ddot{x}_5)$	[mm]	1.81	1.84	1.25	1.02
$rms(\ddot{x}_1)$	[mm]	0.87	1.27	1.02	0.94
simulated					
$\bar{\zeta}$	[%]	13.4	9.6	approx. 30	approx. 30
$rms(x_5)$	[mm]	24.3	35.4	13.8	13.6
$rms(x_1)$	[mm]	6.1	8.8	6.3	5.5
$rms(\ddot{x}_5)$	[mm]	1.60	2.28	0.98	1.16
$rms(\ddot{x}_1)$	[mm]	0.64	0.93	1.40	1.36

amplitude and actual resonance frequency of the excited first mode where the amplitude of $\ddot{x}_g$ is such that the measured $rms(x_5)$ is equal to the simulated $rms(x_5)$.

5.5.2 Viscous Damping with Positive Stiffness

Both the measurements and the simulations of clipped viscous damping with positive stiffness (VDPS) show the typical kink in the force-displacement trajectory due to the clipping, see Figure 5.8(a,c). The measured force follows approximately the desired force except where the tracking is constrained by the residual force at 0 A. As expected from the theory, the positive stiffness evokes smaller damping in the structure than pure VD, see Table 5.1. The decreased damping leads to larger rms values in the simulations. The experiments approximately show the same rms values as for VD. This result can be explained by the increased force tracking error due to the increased residual force when clipped VDPS is emulated. Figure 5.8(a) shows a residual force of approximately 30 N, whereas Fig. 5.7(b) points out a value of approximately 22 N when VD is emulated. In the case of clipped VDPS, the desired force reaches its maximum at displacement extreme. Then, the MR damper current is large which generates large remanent magnetisation in the MR fluid and also in all ferromagnetic damper parts. When the desired force crosses the x-axis in Figure 5.8(a), the desired force is zero and increases with increasing damper displacement step by step. The high remanent magnetisation from the force peak before makes it impossible to track a very small force. It even leads to an increased residual force at 0 A compared to e.g. VD, where the current is lowered step by step when the damper displacement reaches its extreme and the effect of the remanent magnetisation on the residual force at 0 A is thus smaller. The higher residual force in case of clipped VDPS changes the shape of the actual force-displacement trajectory

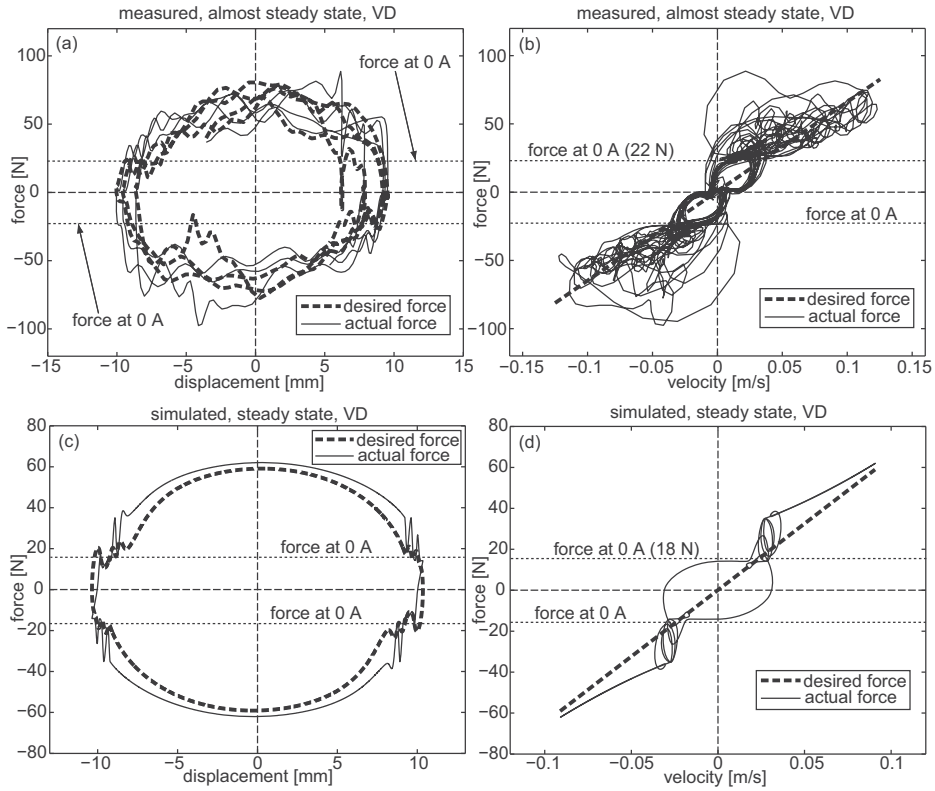

FIGURE 5.6: Measured and simulated control forces due to viscous damping.

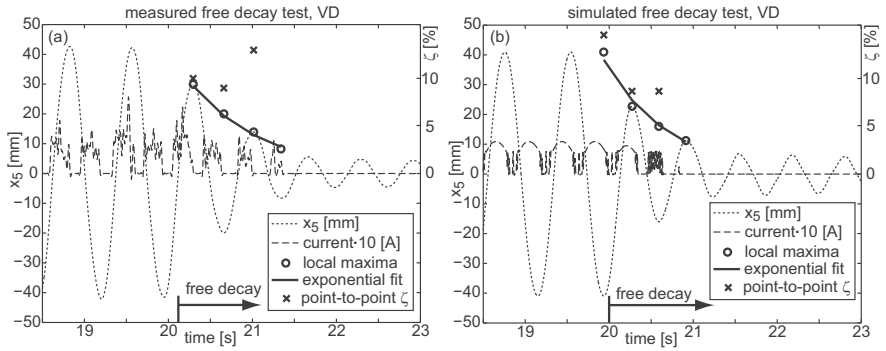

FIGURE 5.7: Measured and simulated free decay tests due to viscous damping.

to almost pure friction damping with negligibly small positive stiffness. The almost non-existent positive stiffness explains why the rms values due to VD and clipped VDPS are so close in the experiments.

5.5.3 Viscous Damping with Negative Stiffness

As is seen from Figure 5.9 (a), the measured force-displacement trajectory of clipped VDNS is very spiky. The spikes are triggered by the initial very large increase of the desired force when the MR damper displacement turns its direction. Then, the model-based feed forward

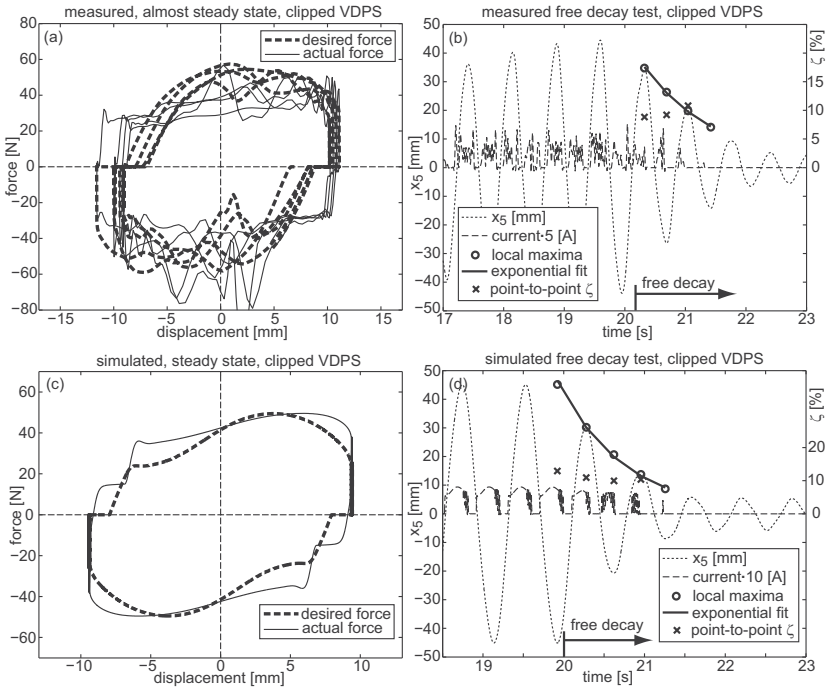

FIGURE 5.8: Measured and simulated clipped viscous damping with positive stiffness.

applies a very high current in order to track the desired force. As a direct result, the MR damper clamps the structure whereby the damper velocity becomes zero. Then, the model-based feedforward outputs zero current which triggers some movement in the MR damper rod. However, since the desired force is still very high, the control again applies a very large current. The large variations of the damper current, when the desired force is high, explain the spiky damper force shown in Figure 5.9(a). The same effect, i.e. the sudden change of the damper force between zero and its large desired value, is also observed in the simulations in Figure 5.9(c), which to some extend verifies the accuracy of the simulations. Figures 5.9(b,d) demonstrate that clipped VDNS leads to extremely large damping. The vibrations decay within one time period to such small values that the desired force is smaller than the residual force at 0 A. At this stage the current is zero and the structural vibrations are determined by the friction of the MR damper ceilings and bearings. The measured and simulated values of displacement in Table 1 are significantly smaller for clipped VDNS compared to VD. This is expected from the increase of the damping comparing VD and clipped VDNS. In contrast, the *rms* of $\ddot{x}_1$ is larger for clipped VDNS than for VD, which is mainly because of the clipping.

5.5.4 Frictional Damping with Negative Stiffness

When FDNS is emulated with $\alpha \geq |k_{des}|$, clipping is not needed in ideal state-state conditions, since the control force remains purely dissipative. As a direct result, the actual force-displacement trajectories in the experiments and simulations are not as noisy as for the clipped VDNS, see e.g. Fig. 5.10(a,c). The lower noise reduces the force tracking error compared to the clipped VDNS, which explains the increased measured structural damping in case of FDNS, see Table. 5.1. As a direct result, all *rms* values are smaller than for clipped VDNS. This clearly indicates that effective semi-active damping is obtained by control schemes that introduce negative stiffness with limited need for clipping of active damper

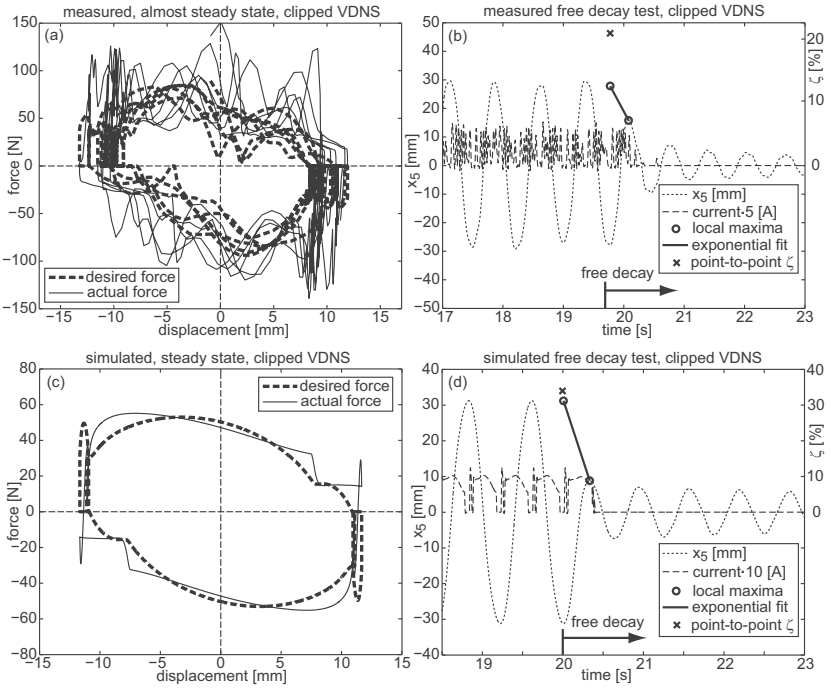

FIGURE 5.9: Measured and simulated clipped viscous damping with negative stiffness.

forces.

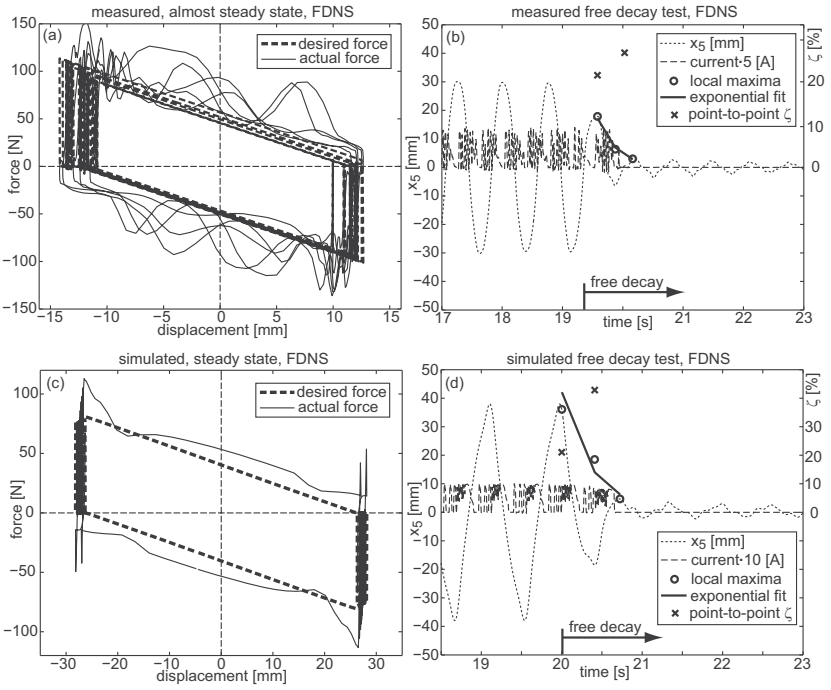

FIGURE 5.10: Measured and simulated friction damping with negative stiffness.

5.6 Summary

The damping of a shear frame with five masses with controlled MR damper between ground plate and first mass was investigated in simulation and experiments. The tested control laws were viscous damping, clipped viscous damping with negative and positive stiffness and optimal semi-active friction damping with negative stiffness. The control laws were designed using a validated model of the shear frame. A novel approach of a validated neural network model of the inverse MR damper behaviour was used to track the desired control force. Since the neural network output, i.e. the desired MR damper current, is very sensitive to measurement noise in the measured damper velocity input, the neural network output was fed through a low-pass filter. In addition, a switch was added to set the outputted desired current to zero if the desired force was smaller than the residual force of the MR damper under consideration. The entire controller included real-time processing of the measured damper displacement and acceleration, real-time calculation of the four tested control laws and real-time calculation of the neural network output and its extensions. The entire controller was implemented in Matlab/dSPACE at a sampling frequency of 500 Hz. Despite the two extensions of the neural network, i.e. the low-pass filter and the switch, the actual MR damper force was still spiky. Nevertheless, the measured structural damping agreed well with the simulated values. This is explained by the fact that the mean stiffness and energy dissipation of the control force which were tracked fairly accurately, except when the desired force was smaller than the residual force at 0 A, mainly determined the resulting structural damping. Thus, the neural network method represents a tool with which the inverse MR damper behaviour can be modelled directly in order to track the desired force in real-time with sufficiently large accuracy without feedback from a force sensor.

Chapter 6

Applications to Benchmark Problems

In recent years, several control strategies have been developed and studied on different buildings for different dynamic loads. Some of the control strategies have been designed and implemented for real structures like cables or building structures or bridges. However, due to experimental limitations, it is hardly possible to implement the control laws on the same building with the same load. Thus, the concept of benchmark problems has come into the picture to compare the various control laws on the same building structure and for the same dynamic load [38, 104]. Based on realistic full-scale buildings, two structural control benchmark problems have been identified for earthquake [38, 39] and wind excitations [40].

For the last decades, several design solutions have been developed and implemented for earthquake mitigation of high-rise buildings. In particular, base-isolation is an effective and robust method for reducing structural response due to earthquake excitation. The base-isolation technique consists of the installation of mechanisms that decouple the structure and its content from the earthquake induced ground motion, especially in the frequency range where the building is most affected. Base-isolation is designed to avoid potential damage in a cost-effective manner to both the structure and its content by reducing inter-floor drifts as well as floor accelerations. Successful base-isolation of a particular structure strongly depends on the choice of isolator devices. The most commonly used types are elastomeric bearings, lead-rubber-bearings and friction pendulum bearings. Details about base-isolation can be found in [100]. Adding supplemental damping to a structure via the base can help reduce the response of the building and especially reduce the base displacement. However, the addition of damping to minimise base displacements may increase both internal deformation and absolute accelerations of the superstructure. The additional damping is provided by installing either passive control devices, active control devices or semi-active control devices on the base-isolated building. The magnetorheological damper is commonly used device for robust semi-active control in connection with base isolation and earthquake excitation. Several semi-active control methods have been investigated for base-isolated structures [101] - [107] and for wind excited structures [108] - [110].

This chapter first describes the implementation of different control strategies for a seismically excited base-isolated building mounted on rubber bearings using MR dampers. Benchmark problems are slightly modified for studying semi-active control strategies for buildings excited to earthquake loadings. The benchmark problem for a base-isolated building is similar to an existing eight-floor building in the earthquake prone Los Angeles region. It is is proposed in [38] and is formulated in association with the ASCE structural control committee. In its basic version it is capable of incorporating three different kinds of base-isolation systems. Moreover, a sample controller design for the benchmark problem is evaluated in [39]. The details of applied control strategies for this benchmark problem have already been discussed in Chapter 4 and also in [P2, P4]. The three types of control strategies are: the pure viscous damping (VD), the viscous damping with negative stiffness (VDNS) and the friction damping with negative stiffness (FDNS). Two MR dampers are acting on the structure at the mass center of the base slab, working in the two planar direction at the base. The parameter calibration of the control strategies are determined by the method following the two-component reduction technique of Main and Krenk [29]. The performance of the control

Table 6.1: Bingham Model Parametrs

f_a	100 kN	f_b	75.0 kN/A
c_a	81.0 kN s/m	c_b	90.0 kN s/m/V

methods is assessed in terms of nine performance indices, which are defined in benchmark problems.

The second part of this chapter describes the implementation of the developed control strategies for a wind excited building. The wind-excited benchmark building is a 76-floor, 306 m tall, concrete office tower, proposed for the city of Melbourne, Australia. The building is tall and slender with a height-to-width ratio of 7.3. Hence, it is wind sensitive, and wind tunnel tests have been conducted for a building model at the University of Sydney. The results of the across-wind data are provided for the analysis of the benchmark problem, and a number of performance criteria are evaluated based on this benchmark problem.

6.1 Magnetorheological Damper: Forward and Inverse Model

For the benchmark problem, two large scale MR damper of 1000 kN are considered. The objective of the benchmark problem is to show effectiveness of negative stiffness on several semi-active control approaches. For that reason a simple MR damper model based on bingham plasticity theory is considered in the benchmark study [13, 35].

The governing equation for the damper force f predicted by the Bingham model is expressed as

$$\mathtt{f} = [f_a + f_b \mathtt{I}] sign[\dot{x}] + [c_a + c_b \mathtt{I}]\dot{x} \tag{6.1}$$

The parameters of the Bingham model are given in Table 6.1. The Bingham model is also used in [P4] for inverse MR damper design. But in this case, neural network based inverse Mr damper is developed based on the methods discussed in [P1]. The Bingham model has two inputs i.e., current and velocity and one output force. The generated force at different constant current level (2 A,4 A, 6 A) is shown in Figure 6.1(a). The training set for NN model here is modified so that it can work with transient behaviour. The training set consists of sinusoidal, triangular, constant step and gaussian white noise (GWN) displacement inputs and also current input. The validation of inverse neural model of the Bingham model for sinusoidal displacement (0.1 m and 3.0 Hz) and sinusoidal current input (5 A and 3.0 Hz) is shown in Figure 6.1(b). The inverse neural network modeling and its training procedure are already discussed in Chapter 2. From Figure 6.1(b), it is visible that the inverse neural network can predict the current accurately though it generates some spiky current due to small modelling error. But this can be removed by proper filtering [P1]. So the validated model is used as feed forward component for force tracking in the control design in both the benchmark problems.

6.2 Seismically Excited Base-Isolated Benchmark Building

The performance of the control strategies are initially evaluated for the base-isolation structure exposed to the El Centro earthquake problem. First the model is introduced and then the performance indices are used to compare the control strategies and evaluated based on the damper performance. The results are also compared to the active LQG sample controller of the benchmark problem.

6.2.1 Structural Model and Evaluation Criteria

The benchmark structure has been developed for the base-isolated benchmark problem defined in [38]. The detailed modelling of the benchmark structure is given in Appendix. A. The base-isolated building has eight floors with an average floor height of 4.04 m, a width of 54.3 m and a length of 82.4 m. The floor plan is L-shaped for the first six floors and rectangularly shaped for the two top floors. The schematic view of the floor plan and the building is presented in Figures 6.2(a,b).

The benchmark building has steel-braced frames with the superstructure bracing located at the building perimeter. The superstructure is supported on a reinforced concrete base slab, and metal decking and a grid of steel beams support all concrete floor slabs. The elevation view with the base isolation system and the control device is shown in Figure 6.2(c). A total number of 92 isolation bearings are used in the present problem, and they are designed as simple linear elastic rubber bearings, whereby a fully linear isolation system can be assumed

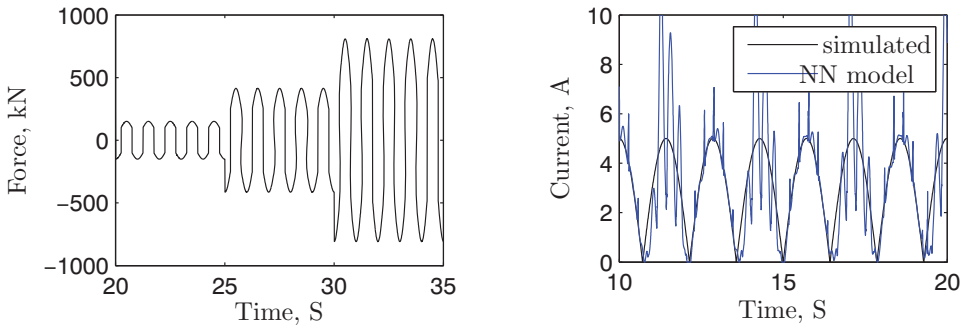

FIGURE 6.1: Force diagram for MR damper (a) and Inverse model validation (b)

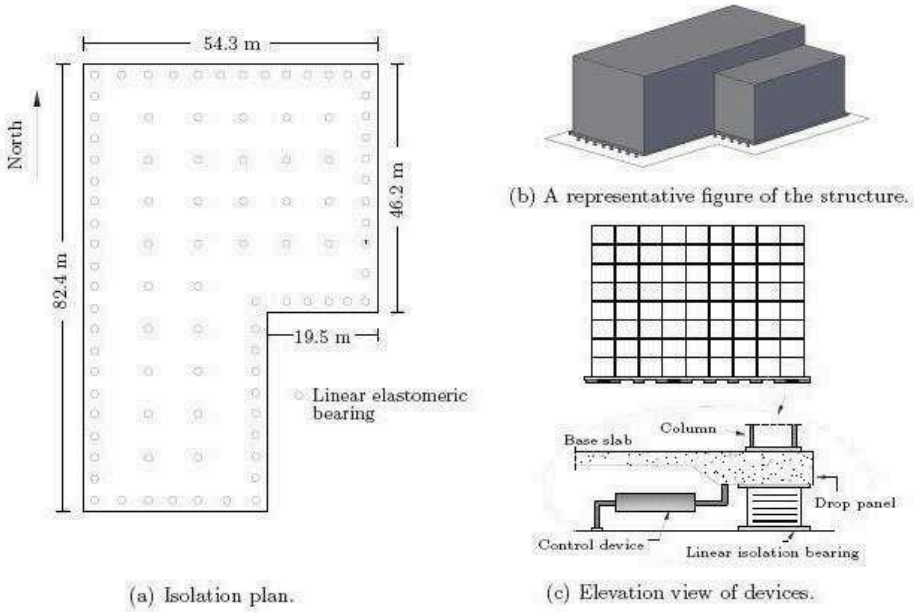

FIGURE 6.2: Schematic diagram of the benchmark building [38].

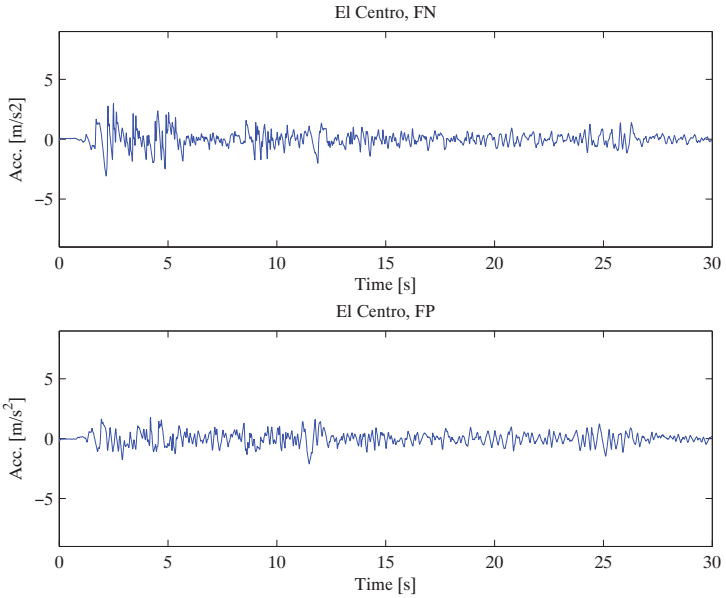

FIGURE 6.3: earthquake acceleration

in the analysis. The superstructure is modelled as a three-dimensional linear elastic system with lateral torsional behaviour, and the floor slabs as well as the base are assumed to be rigid. Each floor plan and the isolation system is modelled using three degrees of freedom located at the center of mass of each floor. They are the two horizontal displacements and the torsional rotation of each slap/floor. Thus, the superstructure itself has a total of 24 DOFs, which yields 24 vibration modes in a fixed-base situation. When including the motion of the base slab, which is supported by the base-isolation system, the total number of DOFs increase to 27. Details of the mathematical modelling of the benchmark structure are discussed in [38]. In the following, when the structure is denoted as uncontrolled it means that no supplemental control devices are attached. This configuration is used as a reference case when evaluating the performance of the control strategies operating on the base-isolation system.

In the performance evaluation criteria the structural response quantities are normalised by their corresponding uncontrolled values. If the uncontrolled values do not exist, e.g. the control force, the values are not normalized. The performance of the controllers is shown in Table 6.3 by the performance indices J_1 to J_9 which are defined in Appendix B. The structural model is discussed in details in Appendix A, and the detailed definition and description of the various performance indices for the evaluation of the proposed control strategies are summarized in Appendix B.

6.2.2 Numerical Simulation

The time domain dynamic analysis has been conducted for the computational structural model developed in MATLAB of a base-isolated benchmark building to investigate the comparative performance of the collocated control laws on the structural response of the benchmark building under El-Centro earthquake ground motion. The two horizontal components of all the earthquakes are designated as fault-normal (F-N) and fault parallel (F-P), as shown in Figure 6.3. The earthquake time history of the El-Centro earthquake record has been considered with a time step of 0.001 s for the first 30 s in the simulation. The

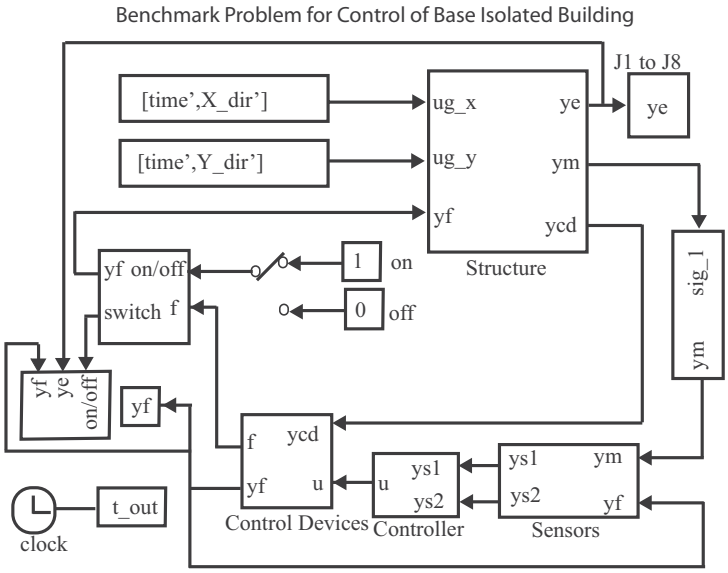

FIGURE 6.4: Original block diagram for benchmark problem

sampling time is very important to be at 1000 Hz because NN based inverse model is developed based on that frequency. The earthquake ground motion is applied bidirectionally to the building in the horizontal plane, in which the fault normal component is applied in the x-direction and the fault parallel component is applied in the y-direction. The vertical component of the excitation has not been considered in the present dynamic analysis of the base-isolated benchmark building. The original benchmark problem has been modelled as in the Matlab/Simulink diagram in Figure 6.4. The original benchmark block diagram has been modified to implement the proposed collocated semi-active control methods. The modified block diagram is shown in Figure 6.5. The location and direction of the two MR dampers is shown in Figure 6.6, where it is seen that they are operating at the center of the mass (COM) of the L-shaped base of the benchmark building.

TABLE 6.2: Evaluation Criteria for Controllers

Earthquake	Criteria	VD	VDNS	FDNS	LQG (active)
El-Centro	J_1	1.31	1.13	1.09	0.93
	J_2	1.19	1.04	0.99	0.92
	J_3	1.13	1.09	1.02	0.82
	J_4	0.95	0.91	0.86	0.82
	J_5	1.17	1.12	1.02	0.85
	J_6	0.67	0.48	0.33	0.12
	J_7	1.21	1.02	0.92	0.78
	J_8	1.15	1.10	1.03	0.72
	J_9	0.91	0.77	0.65	1.89

From the comparison of the J-values it is seen that the friction damper with negative stiffness

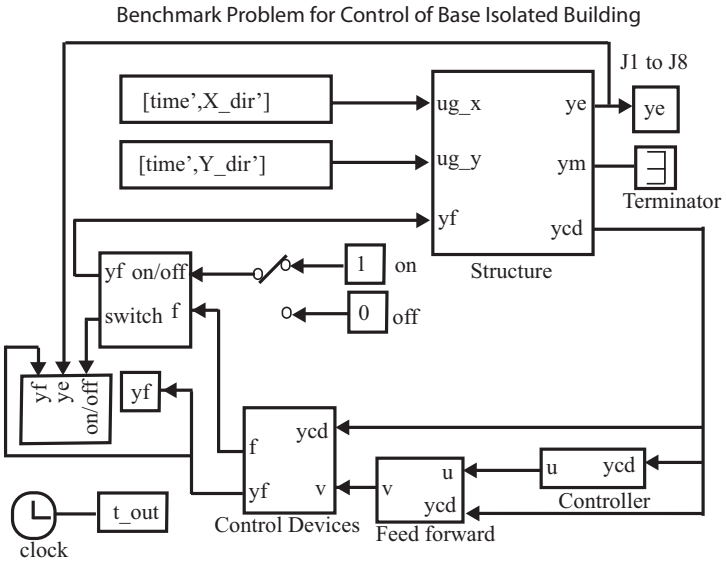

FIGURE 6.5: Modified block diagram for benchmark problem

(FDNS) and the viscous damper with negative stiffness (VDNS) are comparatively better in terms of performance evaluation than the pure viscous damper. For calculating the J value, the response which contains some noise due to spiky current output from inverse neural model, remain unfiltered because the main objective of this benchmark problem is to show effectiveness of the negative stiffness. For the peak base shear (J_1) the performance index is significantly decreasing for viscous damping with negative stiffness and even further reduced for the friction damping with negative stiffness. The peak value of the first floor shear (J_2) is also decreasing for both cases with negative stiffness. The peak base displacement (J_3) is also decreasing for the control strategies with negative stiffness. This is somewhat surprising, because the introduction of apparent negative stiffness should soften the structure locally and thereby allow larger local displacements. The peak inter-storey drift (J_4) is related to

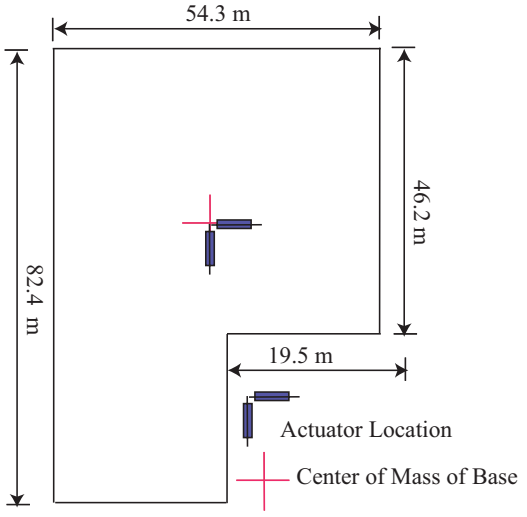

FIGURE 6.6: MR damper distribution at the base

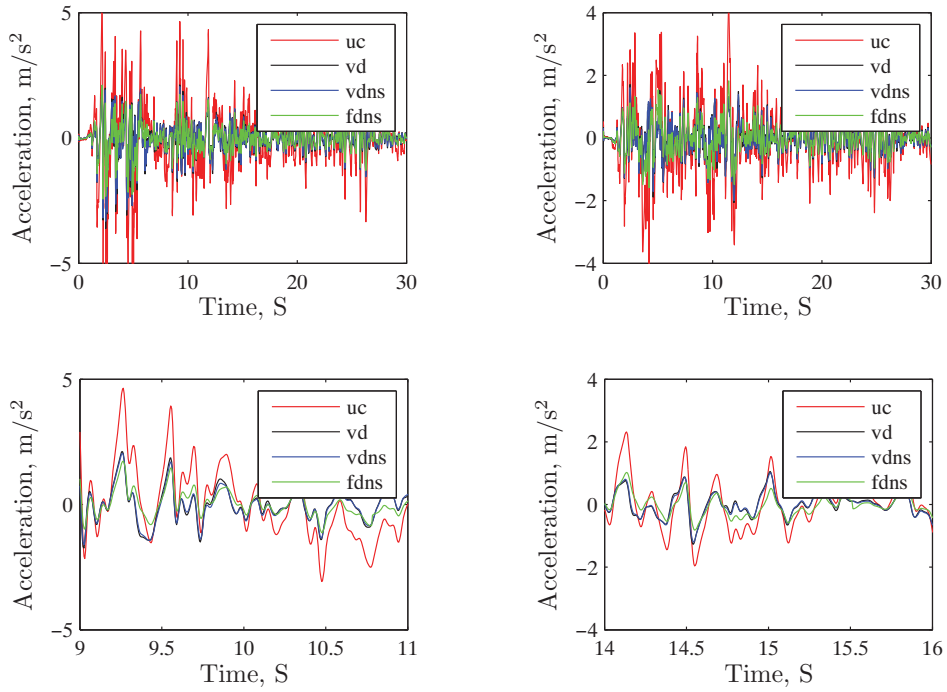

FIGURE 6.7: Top floor acceleration in x-direction (a), Top floor acceleration in y-direction (b),Top floor acceleration in $x$direction (c), Top floor acceleration in y-direction (d)

stresses in the structure and the general condition of the structure. It is seen to decrease for VDNS and FDNS, which again proves the efficiency of the controllers with negative stiffness. The peak absolute floor acceleration (J_5) and peak controller force (J_6) also decrease, which is very important for the selection of an efficient controller. Also the rms values of the base displacement (J_7) and the floor drift (J_8) decrease for the VDNS and FDNS. Finally, the energy absorbed by the damper (J_9) verifies the general trend of the simulations, namely that the introduction of negative stiffness has a beneficial effect on the response reduction and damping of the structure. It is finally observed that the performance of the fully active LQG controller is not reached. LQG controller which is acted as sample controller

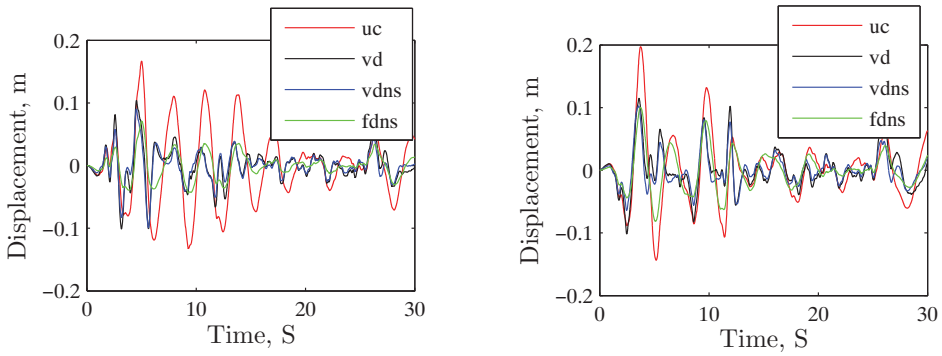

FIGURE 6.8: (a) Top floor displacement in x-direction and (b) Top floor displacement in y-direction

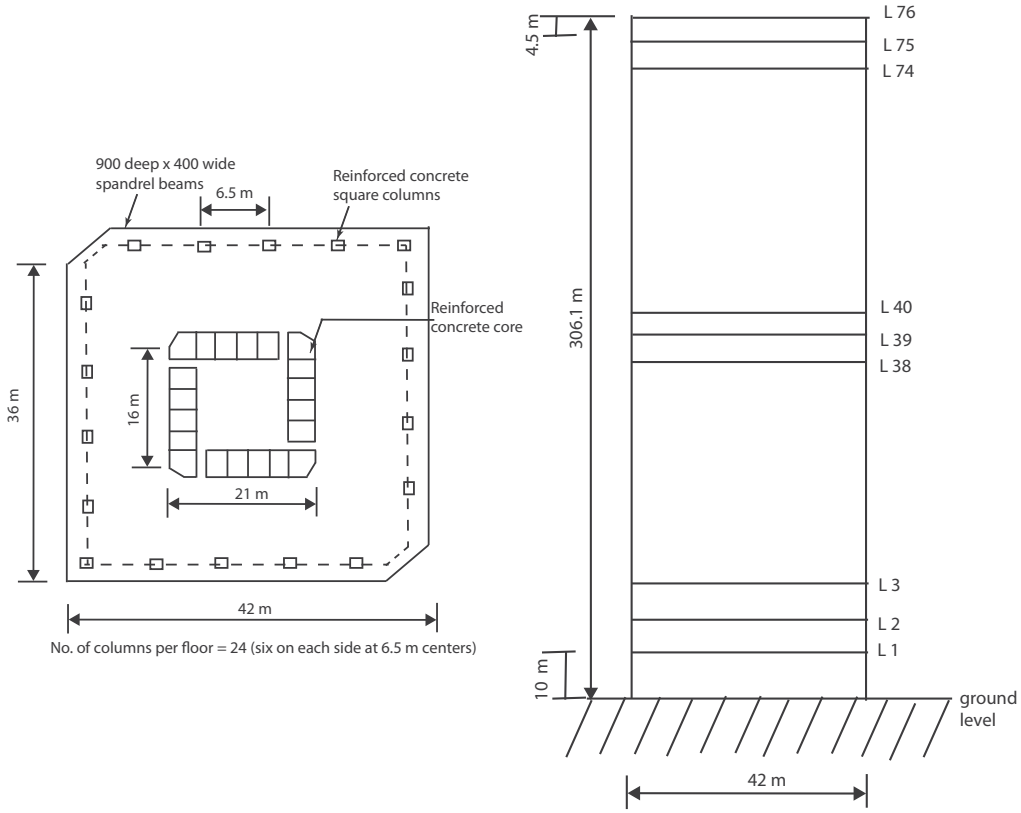

FIGURE 6.9: (a) Plan view and (b) Elevation view of 76-floor building

in benchmark problems are also discussed in Appendix E. However, the friction damping with negative stiffness (FDNS) gives quite better performance over the other methods. The top floor displacement and the top floor accelerations are shown in the Figure 6.7. From these curves it is clearly visible that negative stiffness has a significant influence on the vibration reduction of the structure. The Top-floor displacement in x- and y-direction are shown in Figure 6.8. Also from these results it is found that the friction damping with negative stiffness and the viscous damping with negative stiffness are somewhat better when compared with the pure viscous case.

6.3 Wind-Excited Benchmark Building

While the earthquake benchmark problem in the previous section aims at reducing the transmission of a transient type excitation to the structure, the present wind excitation problem concerns the reduction of a more steady-state response from a distributed stochastic type loading.

6.3.1 Benchmark Structure

The wind-excited benchmark building is considered as a 76-storey, 306 m tall, office tower proposed for the city of Melbourne, Australia. The plan and the elevation sketch of the building structure are shown in Figure 6.9. The building is a typical reinforced concrete building consisting of a concrete core and concrete frames. The mass density of the building

is 300 kg/m^3. The building is quite slender with a height-to-width ratio of $306.1/42 = 7.3$. This means that the structure is quite sensitive to wind excitation. The perimeter dimensions for the central reinforced concrete core is $21 \times 21\,\mathrm{m}^2$. There are 24 columns on the periphery of the building where six columns are distributed on each of the four sides of the building, which are connected to a 900 mm deep and 400 mm wide spandrel beam on each floor. The lightweight floor is constructed by steel beams with a metal deck and a 120 mm slab. The compressive strength of concrete is 60 MPa and the modulus of elasticity is 40 GPa. The sized of the column, the core wall thickness and the floor mass are varying along the height. The building is modelled as a vertical cantilever beam of the simple Bernoulli-Euler type. The finite element model (FEM) model is constructed, where the part of the building between adjacent floors is modelled as classical beam elements of uniform thickness. This results in 76 translational and 76 rotational degrees of freedom. The 76 rotational degrees of freedom have been removed by static condensation, whereby the final model contains 76 degrees of freedom, representing the displacement of each floor in the lateral direction. The mass matrix $\mathbf{M}$ and the stiffness matrix $\mathbf{K}$ are constructed for the FEM model of the building and provided for the analysis by the benchmark problem data. The first five natural frequencies of the model are 0.16 Hz, 0.77 Hz, 1.99 Hz, 3.79 Hz and 6.40 Hz. The damping ratio $\zeta = 0.001$ is assumed for the first five modes to construct the damping matrix $\mathbf{C}$ by Rayleigh's approach. The detailed benchmark model is demonstrated in [40].

6.3.2 Numerical Simulation

The time domain dynamic analysis has been conducted for the numerical structural model developed in MATLAB of the above mentioned benchmark building to investigate the comparative performance of the collocated control laws on the structural response of the benchmark building under wind excitation. Details on the wind loading properties are given in [40]. The wind load time histories have been modified with a time step of 0.001 s for a 900 s wind record for the simulations. The original benchmark problem contains a tuned mass damper (TMD) on the top floor. But in the modified benchmark problem the TMD is removed and the MR damper is installed between ground and first floor. So the benchmark block diagram has been modified to implement the proposed collocated semi-active control methods. The modified block diagram is shown in Figure 6.10.

The performance of the control strategies is based on various performance indices, which are defined in [40] and summarized in Appendix D. By comparison of the performance, it is seen that the friction damper with negative stiffness and the viscous damper with negative stiffness are generally more efficient than the pure viscous damper.

The performance indices for the wind-exited benchmark problem are shown in Table 6.3. J_1 is calculated based on maximum value of Rms of some selective floor accelerations and it is clearly visible that maximum floor Rms acceleration are reduced for viscous with negative stiffness (VDNS) compared to pure viscous damping (VD) but somehow in friction damping with negative stiffness (FDNS) control strategy, there is no significant change in Rms acceleration value. But in both the cases, the performance index is lower than the pure viscous controller. J_2 is formulated based on average of selective floor acceleration. There is significant change in performance index when the negative stiffness is added with VD and it is further reduced in FDNS control strategy. J_3 is evaluated based on the top floor displacement and from performance comparision. It is visible that top floor displacement is significantly decreased in VDNS model and also the performance index is more reduced in FDNS case. J_4 is formulated based on the average of RMS values of displacements of some selective floors. From the comparision chart, it is visible that negative stiffness can significantly decrease the index value and FDNS control law performs better than other two semi-active controller. J_5 and J_6 are based on constraints in actuator capacity and average

TABLE 6.3: Evaluation Criteria for Controllers

Load	Criteria	VD	VDNS	FDNS	LQG
wind	J_1	0.63	0.54	0.54	0.38
	J_2	0.76	0.66	0.64	0.43
	J_3	0.96	0.93	0.88	0.71
	J_4	0.90	0.85	0.81	0.67
	J_5	0.55	0.41	0.41	0.14
	J_6 kN	32.55	31.21	27.4	59.9
	J_7	0.69	0.61	0.53	0.31
	J_8	0.82	0.77	0.75	0.44
	J_9	0.94	0.93	0.82	0.75
	J_{10}	0.85	0.82	0.81	0.65
	J_{11}	0.25	0.19	0.21	0.03
	J_{12} kN m/s	332.75	324.54	298.11	601.1

power respectively which are also very important for damper or actuator selection. The performance indices are significantly decreasing for the case of VDNS and even more in FDNS controller. J_7 is constructed based on maximum peak response of the acceleration values of some selective floors and J_8 is formulated based on average peak values of acceleration in some selective floors. FDNS control strategy is also showing better performance in comparision chart for both the cases. J_9 and J_{10} are formulated based on peak value of the top floor and average peak value of some selective floor respectively. VDNS is performing better

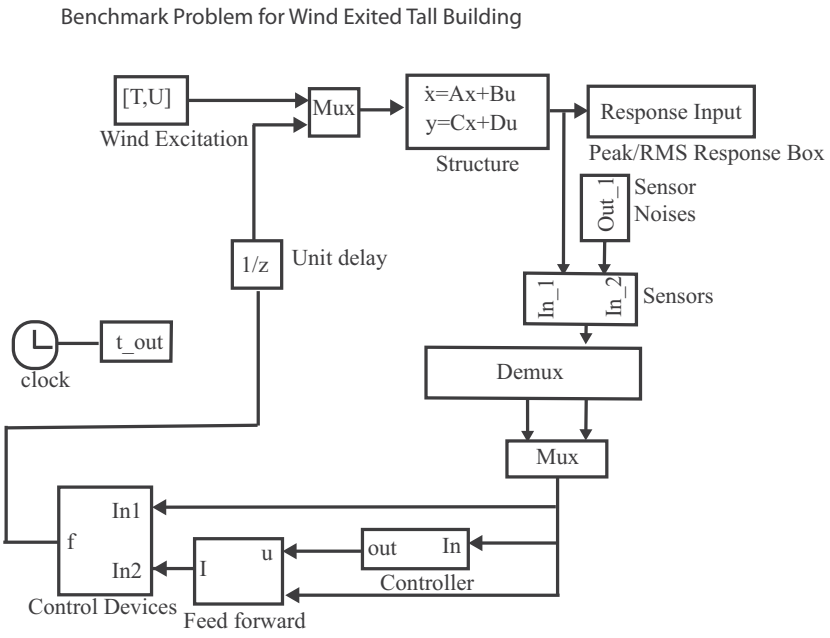

FIGURE 6.10: Modified block diagram for wind-benchmark problem

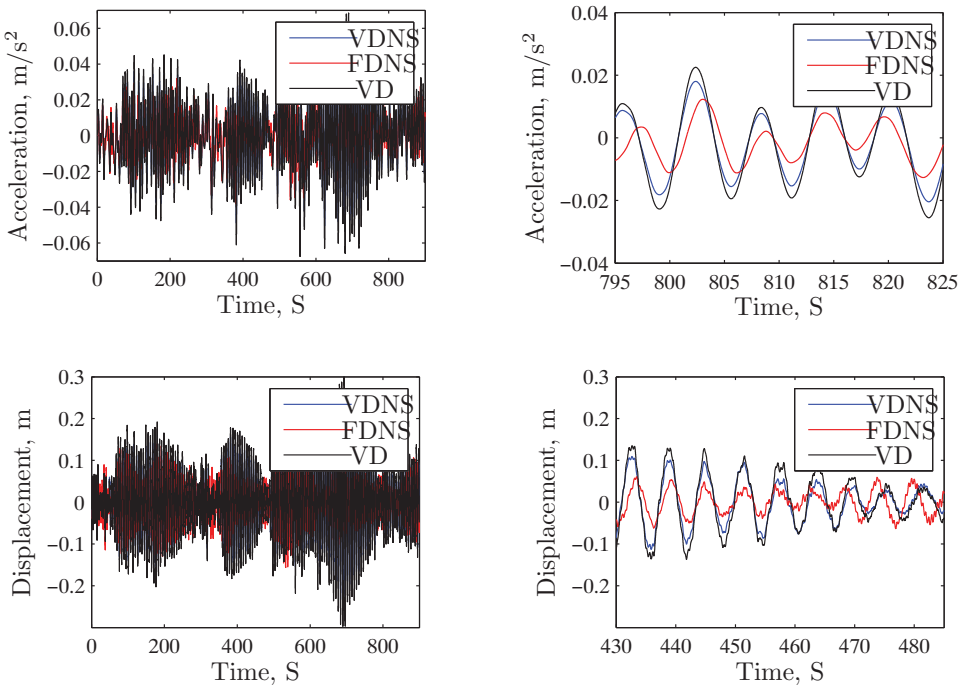

FIGURE 6.11: Top floor acceleration (a,b), Top floor displacement (c,d)

than the pure viscous control strategy. FDNS control strategy also reduce the performance indices even more than VDNS. J_{11} and J_{12} are constructed based on actuator capacity and power and this two performance indices are also important for suitable damper selection. For both the performance indices, negative stiffness plays significant role. Friction damping with negative stiffness (FDNS) and viscous damping with negative stiffness (VDNS) are performing better than the pure viscous damping (VD). All the controller performances are compared with active LQG controller performance which is used in the benchmark problem as sample controller. Somehow the semi-active controllers are not able to reach the performance obtained from active LQG control. The top floor displacement and the top floor acceleration in time domain are shown in Figure 6.11.

From the time domain analysis of both the displacement and the acceleration, it is visible that the the viscous damping with negative stiffness and friction damping with negative stiffness perform better than the pure viscous damping strategy. This benchmark study also demonstrated the influence of negative stiffness in control strategy for vibration reduction problem.

6.4 Summary

The benchmark problem for a base-isolated building structure and wind-exited tall building are demonstrated and some semi-active control strategies are implemented on both the benchmark structure. The force evaluated from the controller is used to emulate the desired current to get the actual force for a large-scale MR damper from inverse MR model. The negative stiffness has significant contribution in terms of vibration reduction. The performance of the semi-active control strategies are also quite satisfactory in benchmark problems.

Chapter 7

Conclusions

This thesis presents the modelling of a rotary type MR damper from the measurement data and compares several semi-active control strategies by simulations and experiments. In the first part, neural network based models of the forward and the inverse behaviour of a rotary MR damper using measurement data have been evaluated. Three signification actions have been taken to prepare the data sets for neural network architecture: filtering with low-pass filter in order to remove high-frequency signal parts, removing offset values and finally downsampling from higher frequency to lower frequency for easy handling of bulk amount data. A sub-optimal neural network architecture is developed to model the forward and inverse dynamics of the MR damper. Both models are verified with independent measurement data. It is demonstrated that a proper combination of number of previous values of the input states and the number of hidden layers and neurons gives the best numerical fit. It is also shown that if velocity estimation is possible from displacement or acceleration, then velocity is only enough to use as model input, while adding displacement and acceleration as model input will not improve the modelling error significantly. This sub-optimal procedure is faster and simpler and also effective in closed loop simulations. Another significant contribution to the inverse modelling of MR dampers is the proposal of the absolute values of damper velocity and damper force as input to the neural network with damper current as output. It seems that this simple modification improves the force tracking, as it limits the generation of negative values of the damper current predicted by the neural network. In the validation results, the forward neural network model is able to estimate the force with high accuracy at different constant current input and also quite accurately for sinusoidal current input. It is also illustrated that the neural network model is comparatively better than the often used Bouc-Wen model to capture in particular the non-linearities in the forward dynamics of the damper. The inverse model is also showing minimum modeling error in the current prediction. But at sinusoidal current level, the inverse model has better accuracy than at constant level.

In the second part of the thesis a five-mass shear frame structure has been modelled using an experimental analysis. The stiffness of the model has been determined from the mode shapes, which are constructed from the frequency transfer functions obtained by the test data. The damping matrix has been determined from the estimated damping ratio through free decay tests, and from the corresponding frequency response the resonance frequencies are determined. The validation of the model shows quite satisfactory accuracy, and this model can be sued for the calibration of the control strategies.

In the third part of the thesis, several semi-active control strategies are developed and applied to the shear frame structure by a rotary type MR damper. The applied control laws are pure viscous damping, viscous damping with negative stiffness, semi-active friction damping with negative stiffness and a neural network based model reference control. The inverse neural model is used to track the desired control force. Since the neural network output, i.e. the desired MR damper current, is very sensitive to measurement noise in the measured damper velocity input, the neural network output is fed through a low-pass filter. Also the so-called Kinematic Kalman Filter (KKF) is used to estimate the velocity by combining measured displacement and acceleration data in an effective way. The actual MR damper force is spiky

due to small modeling errors in the inverse model, but the control forces are still tracked fairly accurately, except when the desired force is smaller than the residual force at 0 A of the MR damper. The advantage of using the neural network model is the ability to model the inverse MR damper behaviour directly in order to track the desired force with sufficient accuracy without feedback from a force sensor. The performances of the structural building with harmonic base excitation are compared for different types of control strategies and it is shown that friction damping with negative stiffness gives better performance compared to the other methods. In general it is clearly observed that the inclusion of negative stiffness significantly decreases the structural response and thus improves the damping efficiency.

In the last part of the thesis, some of the above-mentioned control strategies are applied to two benchmark problems. The benchmark problem for a seismically excited base-isolated structure is used for implementing control strategies with negative stiffness, and it is demonstrated that the inclusion of negative stiffness is significantly reducing the overall damping of the structure. The second benchmark problem concerns the wind excitation of a tall building, and it is in the present thesis used to investigate the performance of the various control strategies for more stationary type loading conditions. The results are also significantly improving when negative stiffness is included in the control law. Based on the results for the benchmark problems it is observed that the application of negative stiffness improves the general damping efficiency for both the transient earthquake loading and the stationary random wind excitation.

Bibliography

[1] S.K. Rasouli, M. Yahyai, Control of response of structures with passive and active tuned mass dampers, *The Structural Design of Tall Buildings*, 11 (2002) 1–14.

[2] K.M. Choi, H.J. Jung, H.J. Lee, S.W. Cho, Seismic protection of base-isolated building with nonlinear isolation system using smart passive control strategy, *Structural Control and Health Monitoring*, 15 (2008) 785–796.

[3] C.C. Chang, T.Y. Yang, Control of building using active tuned mass dampers, *Journal of Engineering Mechanics*, 121 (1995) 355–366.

[4] A. Preumont, *Vibration Control of Active Structures, An Introduction*, second ed., Kluwer Academic Publishers, Dordrecht, 2002.

[5] J. Zhang, P. Roschke, Active control of a tall structure excited by wind, *Journal of Wind Engineering and Industrial Aerodynamics*, 83 (1999) 209–223.

[6] Z.X. De, C.D. Zheng, Active vibration control of nonlinear benchmark building, *Journal of Applied Mathematics and Mechanics*, 28 (2007) 785–796.

[7] S.L. Djajakesukma, B. Samali, H. Nguyen, Study of a semi-active stiffness damper under various earthquake inputs, *Earthquake Engineering and Structural Dynamics*, 31 (2002) 1757–1776.

[8] S. Nagarajaiah, E. Sonmez, Structures with semi-active variable stiffness single/multiple tuned mass dampers, *Journal of Structural Engineering*, 133 (2007) 67–77.

[9] B.F. Spencer, S. Nagarajaiah, State of the art of structural control, *Journal of Structural Engineering*, 129 (2003) 845–856.

[10] L.M. Jansen, S.J. Dyke, Semi-active control strategies for MR dampers: a comparative study, *Journal of Engineering Mechanics*, 126 (2000) 795–803.

[11] B.F. Spencer, S.J. Dyke, M.K. Sain, J.D. Carlson, Phenomenological model for magnetorheological dampers, *Journal of Engineering Mechanics*, 123 (1997) 230–238.

[12] S.J. Dyke, B.F. Spencer, M.K. Sain, J.D. Carlson, An experimental study of MR dampers for seismic protection, *Smart Materials and Structures*, 7 (1998) 693–703.

[13] T.G. Yang, B.F. Spencer, H.J. Jung, J.D. Carlson, Dynamic modeling of large-scale magnetorheological damper systems for civil engineering applications, *Journal of Engineering Mechanics*, 130 (2001) 1107–1114.

[14] S.J. Dyke, B.F. Spencer, M.K. Sain, J.D. Carlson, Modeling and control of magnetorheological dampers for seismic response, *Smart Material and Structures*, 5 (1996) 565–575.

[15] W.Q. Zhu, M. Luo, L. Dong, Semi-active control of wind exited building structures using MR/ER dampers, *Probabilistic Engineering Mechanics*, 19 (2004) 279–285.

[16] H. Iemura, M.H. Pradono, Passive and semi-active seismic response control of a cable-stayed bridge, *Journal of Structural Control*, 9 (2002) 189–204.

[17] C.L. Ng, Y.L. Xu, Semi-active control of a building complex with variable friction dampers, *Journal of Engineering Structures*, 29 (2007) 1209–1225.

[18] J.A. Inaudi, Modulated Homogeneous Friction: A Semi-active Damping Strategy, *Earthquake Engineering and Structural Dynamics*, 26 (1997) 361–367.

[19] J.N. Yang, J.C. Wu, A.K. Agarwal, Sliding mode control for nonlinear and hysteretic structures, *Journal of Engineering Mechanics*, 121 (1995) 1330–1339.

[20] J.C. Wu, J.N. Yang, Modified sliding mode control for wind-exited benchmark problem, *Journal of Engineering Mechanics*, 130 (2004) 499–504.

[21] Z.D. Xu, Y.P. Shen, Y.Q. Guo, Semi-active control of structures incorporated with magnetorheological dampers using neural networks, *Smart Materials and Structures*, 12 (2003) 80–87.

[22] H.C. Cho, M.S. Fadali, M.S. Siidi, K.S. Lee, Neural network active control of structures with earthquake excitation, *International Journal of Control, Automation and Systems*, 3 (2005) 202–210.

[23] K.A. Bani-Hani, M.A. Sheban, Semi-active neuro-control for base-isolation system using magnetorheological (MR) dampers, *Earthquake Engineering and Structural Dynamics*, 35 (2006) 1119–1144.

[24] S. Suresh, S. Narasimhan, S. Nagarajaiah, Direct adaptive neural controller for the active control of earthquake-exited nonlinear base-isolated buildings, *Structural Control and Health Monitoring*, (2011) DOI: 10.1002/stc.437.

[25] H. Du, N. Zhang, Model-based fuzzy control for buildings installed with magneto-rheological dampers, *Journal of Intelligent Material Systems and Structures*, 20 (2009) 1091–1105.

[26] K.K. Bidokhti, H. Moharrami, A. Fayezi, Semi-active fuzzy control for fuzzy control for seismic response reduction of building frames using SHD dampers, *Structural Control and Health Monitoring*, (2011) DOI: 10.1002/stc.441.

[27] X. Jiang, H. Adeli, Neuro-genetic algorithm for non-linear active control of structures, *International Journal for Numerical Methods in Engineering*, 75 (2008) 770–786.

[28] K.C. Schurter, P.N. Roschke, Neuro-fuzzy control of structures using acceleration feedback, *Smart Materials and Structures*, 10 (2001) 770–779.

[29] J.A. Main, S. Krenk, Efficiency and tuning of viscous dampers on discrete systems, *Journal of Sound and Vibration*, 286 (2005) 97–122.

[30] C. Boston, F. Weber, L. Guzzella, Optimal semi-active damping of cables: evolutionary algorithms and closed-form solutions, *Smart Materials and Structures*, 18 (2009) 055006(9pp).

[31] H. Iemura, M.H. Pradono, Simple algorithm for semi-active seismic response control of cable stayed bridges, *Earthquake Engineering and Structural Dynamics*, 34 (2005) 409–423.

[32] H. Iemura, A. Igarashi, M.H. Pradono, A. Kalantari, Negative stiffness friction damping for seismically isolated structures, *Structural Control and Health Monitoring*, 13 (2006) 775–791.

[33] H. Iemura, M.H. Pradono, Advances in the development of pseudo-negative-stiffness dampers for seismic response control, *Structural Control and Health Monitoring*, 16 (2009) 784–799.

[34] H. Li, M. Liu, J. Ou, Negative stiffness characteristics of active and semi-active control systems for stay cables, *Structural Control and Health Monitoring*, 15 (2008) 120–142.

[35] J. Høgsberg, The role of negative stiffness in semi-active control of magneto-rheological dampers, *Structural Control and Health Monitoring*, 18 (2011) 289–304.

[36] F. Weber, C. Boston, Clipped viscous damping with negative stiffness for semi-active cable damping, *Smart Materials and Structures*, 20 (2011) 045007(13pp).

[37] F. Weber, C. Boston, M. Maślanka, An adaptive tuned mass damper based on the emulation of positive and negative stiffness with an MR damper, *Smart Materials and Structures*, 20 (2011) 015012(11pp).

[38] S. Narasimhan, S. Nagarajaiah, E.A. Johnson, H.P. Gavin, Smart base-isolated benchmark building. Part I: problem definition, *Structural Control and Health Monitoring*, 13 (2006) 573–588.

[39] S. Nagarajaiah, S. Narasimhan, Smart base-isolated benchmark building. Part II: phase I sample controllers for linear isolation systems, *Structural Control and Health Monitoring*, 13 (2006) 589–604.

[40] J.N. Yang, A.K. Agrawal, B. Samali, J.C. Wu, Benchmark problem for response control of wind-exited tall buildings, *Journal of Engineering Mechanics*, 130 (2004) 437–446.

[41] B. Samali, K. Kwok, G. Wood, J.N. Yang, Wind tunnel tests for wind-exited benchmark building, *Journal of Engineering Mechanics*, 130 (2004) 447–450.

[42] R.E. Christenson, B.F. Spencer, E. Johnson, Experimental verification of smart cable damping, *Journal of Engineering Mechanics*, 132 (2006) 268–278.

[43] H. Li, M. Liu, X. Guan, J. Ou, Vibration control of stay cables of the Shandong Binzhou yellow river highway bridge using magnetorheological dampers, *Journal of Bridge Engineering*, 12 (2007) 401–409.

[44] V.A. Neelakantan, G.N. Washington, Vibration control of structural systems using MR dampers and a modified sliding mode control technique, *Journal of Intelligent Material Systems and Structures*, 19 (2008) 211–224.

[45] W.J. Wu, C.S. Cai, Cable vibration control with a semi-active MR damper - numerical simulation and experimental verification, *Structural Engineering and Mechanics*, 34 (2010) 611–623.

[46] M. Maslanka, B. Sapinski, J. Snamina, Experimental study of vibration control of a cable with an attached MR damper, *Journal of Theoretical and Applied Mechanics*, 45 (2007) 893–917.

[47] F. Weber, H. Distl, G. Feltrin, M. Motavalli, Cycle energy control of magnetorheological dampers on cables, *Smart Materials and Structures*, 18 (2009) 055005(16pp).

[48] C. Boston, F. Weber, L. Guzzella, Force tracking with an MR damper, *Journal of Dynamic Systems, Measurement and Control*, (under review).

[49] G. Yang, B.F. Spencer, H.J. Jung, J.D. Carlson, Dynamic modeling of large-scale magnetorheological damper systems for civil engineering applications, *Journal of Engineering Mechanics*, 130 (2004) 1107–1114.

[50] A. Dominguez, R. Sedaghati, I. Stiharu, A new dynamic hysteresis model for magnetorheological dampers, *Smart Material and Structures*, 15 (2006) 1179–1189.

[51] F. Ikhouane, S. Dyke, Modeling and identification of a shear mode magnetorheological damper, *Smart Material and Structures*, 16 (2007) 605–616.

[52] N.M. Wereley, J.U. Cho, Y.T. Choi, S.B. Choi, Magnetorheological dampers in shear mode, *Smart Materials and Structures*, 17 (2008) 015022(11pp).

[53] Z.P. Shulman, E.V. Korobko, M.L. Levin, A.E. Binshtok, V.A. Bilyk, Y.G. Yanovsky, Energy dissipation in electrorheological damping devices, *Journal of Intelligent Material Systems and Structures*, 17 (2006) 315–320.

[54] R. Jiménez, I.L. Alvarez, LuGre friction model for a magnetorheological damper, *Structural Control and Health Monitoring*, 12 (2005) 91–116.

[55] F. Yang, R. Sedaghati, E. Esmailzadeh, Development of LuGre friction model for large scale magnetorheological fluid dampers, *Journal of Intelligent Material Systems and Structures*, 20 (2009) 923–937.

[56] C. Boston, F. Weber, L. Guzzella, Modeling of a disc-type magnetorheological damper, *Smart Materials and Structures*, 19 (2010) 045005(12pp).

[57] I. Sahin, T. Engin, S. Cesmeci, Comparison of some existing parametric models for magnetorheological fluid dampers, *Smart material and Structure*, 19 (2010) 035012(11pp).

[58] D.H. Wang, W.H. Liao, Magnetorheological fluid dampers: a review of parametric modelling, *Smart Materials and Structures*, 20 (2011) 023001(34pp).

[59] N.D. Sims, N.J. Holmes, R. Stanway, An unified modeling and model updating procedure for electrorheological and magnetorheological vibration dampers, *Smart Materials and Structures*, 13 (2004) 100-121.

[60] F. Weber, F. Feltrin, H. Distl, Detailed analysis and modeling of MR dampers at zero current, *Structural Engineering Mechanics*, 30 (2008) 787–790.

[61] H.J. Jung, B.F. Spencer, I.N. Lee, Control of seismically excited cable-stayed bridge employing magnetorheological fluid dampers, *Journal of Structural Engineering*, 129 (2003) 873–883.

[62] N.M. Kwok, Q.P. Ha, T.H. Nguyen, J. Li, B. Samali, A novel hysteretic model for magnetorheological fluid dampers and parameter identification using particle swarm optimization, *Sensors and Actuators A*, 132 (2006) 441–451.

[63] M. Ye, X. Wang, Parameter estimation of the Bouc-Wen hysteresis model using particle swarm optimization, *Smart Materials and Structures*, 16 (2007) 2341–2349.

[64] X. Xiaomin, S. Qing, Z. Ling, Z. Bin, Parameter estimation and its sensitivity analysis of the MR damper hysteresis model using a modified genetic algorithm, *Journal of Intelligent Material Systems and Structures*, 20 (2009) 2089–2100.

[65] J. Won, M. Sunwoo, Fuzzy modelling approach to magnetorheological dampers: forward and inverse model, *Journal of Systems and Control Engineering*, 20 (2003) 1055–1065.

[66] C. Chang, P. Roschke, Neural network modeling of a magnetorheological damper, *Journal of Intelligent Material Systems and Structures*, 9 (1998) 755–764.

[67] C. Chang, L. Zhou, Neural Network emulation of inverse dynamics for a magnetorheological damper, *Journal of Structural Engineering*, 128 (2002) 231–239.

[68] D.H. Wang, W.H. Liao, Modeling and control of magnetorheological fluid dampers using neural networks, *Smart Materials and Structures*, 14 (2005) 111–126.

[69] P. Xia, An inverse model of MR damper using optimal neural network and system identification, *Journal of Sound and Vibration*, 266 (2003) 1009–1023.

[70] T. Tse, C. Chang, Shear-mode rotary magnetorheological damper for small-scale structural control experiments, *Journal of Structural Engineering*, 130 (2004) 904–910.

[71] H. Lee, H. Jung, S. Cho, I. Lee, An experimental study of semi-active modal neurocontrol scheme using MR damper for building structure, *Journal of Intelligent Material Systems and Structures*, 19 (2008) 1005–1015.

[72] H. Metered, P. Bonello, S.O. Oyadiji, The experimental identification of magnetorheological dampers and evaluation of their controllers, *Mechanical Systems and Signal Processing*, 24 (2009) 976–994.

[73] F.J. Soeiro, L.T. Stutz, R.A. Tenenbaum, A.J. Neto, Stochastic and hybrid methods for the identification in the Bouc-Wen model for magneto-rheological dampers, *Journal of Physics: conference series*, 135 (2008) 012093.

[74] L. Tsoukalas, R. Uhrig, *Fuzzy and Neural Approaches in Engineering*, Wiley, 1997.

[75] J.W. Hines, L. Tsoukalas, L.A. Zadeh, R. Uhrig, *Fuzzy and Neural Approaches in Engineering: Supplement: MATLAB*, Wiley, 2005.

[76] H.J. Jung, J.E. Jang, K.M. Choi, H.J. Lee, Optimal design of viscous dampers for multi-mode vibration control of bridge cables, *Smart Structures and Systems*, 4 (2008) 697–710.

[77] F. Weber, G. Feltrin, M. Motavalli, Passive damping of cable with MR dampers, *Journal of Materials and Structures*, 38 (2005) 568–577.

[78] S.B. Kim, C.B. Yun, B.F. Spencer, Vibration control of wind-excited tall buildings using sliding model fuzzy control, *Journal of Engineering Mechanics*, 130 (2004) 505–510.

[79] G.P.Cai, J.H. Huang, F. Sun, C. Wang, Modified sliding-mode bang-bang control for seismically excited linear structures, *Erathquake Engineering and Structural Dynamics*, 29 (2000) 1647–1657.

[80] A.I. Dounis, R.E. King, Optimum fuzzy sliding mode semi-active control of structures subjected to earthquakes, *Journal of Intelligent and Fuzzy Systems*, 14 (2003) 37–47.

[81] R. Guclu, Sliding mode and PID control of a structural system against earthquake, *Mathematical and Computer Modelling*, 44 (2006) 210–217.

[82] S.J. Moon, L.A. Bergman, P.G. Voulgaris, Sliding mode control of cable-stayed bridge subjected to seismic excitation, *Journal of Engineering Mechanics*, 129 (2003) 71–78.

[83] K.C. Lu, C.H. Loh, J.N. Yang, P.Y. Lin, Decentralized sliding mode control of a building using MR dampers, *Smart Materials and Structures*, 17 (2008) 055006(15pp).

[84] W.L. He, A.K. Agarwal, J.N. Yang, Novel Semi-active Friction Controller for Linear Structures against Earthquakes, *Journal of Structural Engineering*, 129 (2003) 941–950.

[85] N. Aguirre, F. Ikhouane, J. Rodellar, R. Christenson, Parametric identification of the Dahl Model for large scale MR dampers, *Structural Control and Health Monitoring*, (2011) DOI: 10.1002/stc.434.

[86] Z.D. Xu, Y.Q. Guo, Neuro-fuzzy control strategy for earthquake-exited nonlinear magnetorheological structures, *Soil Dynamics and Earthquake Engineering*, 28 (2008) 717–727.

[87] Z.Q. Gu, S.L. Oyadiji, Application of MR damper in structural control using ANFIS method, *Computers and Structures*, 86 (2008) 427–436.

[88] D.H. Kim, S.N. Seo, I.W. Lee, Optimal neuro-controller for nonlinear benchmark structure, *Journal of Engineering Mechanics*, 130 (2004) 424–429.

[89] H.S. Kim, P.N. Roschke, GA-fuzzy control of smart base isolated benchmark building using supervisory control technique, *Advances in Engineering Software*, 38 (2007) 453–465.

[90] S.F. Ali, A. Ramaswamy, Optimal fuzzy logic control for MDOF structural systems using evolutionary algorithms, *Engineering Applications of Artificial Intelligence*, 22 (2009) 407–419.

[91] G. Yan, L.L. Zhou, Integrated fuzzy logic and genetic algorithms for multi-objective control of structures using MR dampers, *Journal of Sound and Vibration*, 296 (2006) 368–382.

[92] S.F. Ali, A. Ramaswamy, GA-optimized FLC-driven semi-active control for phase-II smart nonlinear base-isolated benchmark building, *Structural Control and Health Monitoring*, 15 (2008) 797–820.

[93] A.K. Karamodin, H.H. Kazemi, Semi-active control of structures using neuro-predictive algorithm for MR dampers, *Structural Control and Health Monitoring*, 278 (2008) 1002–1020.

[94] A.S. Ahlawat, A. Ramaswamy, Multi-objective optimal fuzzy logic control system for response control of wind-exited tall buildings, *Journal of Engineering Mechanics*, 130 (2004) 524–530.

[95] S.F. Ali, A. Ramaswamy, Hybrid structural control using magnetorheological dampers for base isolated structures, *Smart Materials and Structures*, 18 (2009) 055011 (16pp).

[96] J.R. Høgsberg, S. Krenk, Linear control strategies for damping of flexible structures, *Journal of Sound and Vibration*, 293 (2006) 59–77.

[97] J. Ou, H. Li, Analysis of capability for semi-active or passive damping systems to achieve the performance of active control systems, *Structural Control and Health Monitoring*, 17 (2010) 778–794.

[98] S. Jeon, M. Tomizika, Kinematic Kalman Filter (KKF) for robot end-effector sensing, *Journal of Dynamic Systems, Measurement and Control*, 131 (2009) 021010 (8 pages).

[99] S. Qing, Z. Ling, Z. Jinxiong, S. Qingxuan, Experimental study of the semi-active control of building structures using the shaking table, *Earthquake Engineering and Structural Dynamics*, 32 (2003) 2353–2376.

[100] J.C. Ramallo, E.A. Johnson, B.F. Spencer, Smart Base Isolation Systems, *Journal of Engineering Mechanics*, 128 (2002) 1088 (12 pages).

[101] F. Pozo, J. Rodellar, L. Acho, Acceleration feedback control of hysteretic base-isolated structures: application to a benchmark Case, *17th World Congress on Automatic Control*, 2526–2531, July 6-11, Seoul, Korea, 2008.

[102] F. Pozo, L. Acho, J. Rodellar, J.M. Rossell, A velocity-based seismic control for base-isolated structures, *American Control Conference*, 3908–3913, June 10-12, St. Louis, MO, USA, 2009.

[103] H.J. Jung, K.M. Choi, B.F. Spencer, I.W. Lee, Application of some semi-active control algorithms to a smart base-isolated building employing MR dampers, *Structural Control and Health Monitoring*, 13 (2006) 693–704.

[104] A. Sharma, R.S. Jangid, Seismic response of base-isolated benchmark building with variable sliding isolators, *Journal of Earthquake Engineering*, 14 (2010) 1063–1091.

[105] H. Yoshioka, J.C. Ramallo, Smart base isolation strategies employing magnetorheological dampers, *Journal of Engineering Mechanics*, 128 (2002) 540–551.

[106] S. Nagarajaiah, S. Narasimhan, Seismic control of smart base isolated buildings with new semi-active variable damper, *Earthquake Engineering and Structural Dynamics*, 36 (2007) 729–749.

[107] H.J. Lee, G. Yang, H.J. Jung, B.F. Spencer, I.W. Lee, Semi active neuro control of base-isolated benchmark structure, *Structural Control and Health Monitoring*, 13 (2005) 682–692.

[108] J.C. Wu, J.N. Yang, W.E. Schmitendorf, Reduced-order $H\infty$ and LQR control for wind-exited tall buildings, *Engineering Structures*, 20 (1998) 222–236.

[109] G. Mei, A. Kareem, J.C. Kantor, Model predictive control of wind-exited building: benchmark study, *Journal of Engineering Mechanics*, 130 (2004) 459–465.

[110] K.D. Pham, G. Jin, M.K. Sain, B.F. Spencer, S.R. Liberty, Generalized linear quadratic gaussian techniques for the wind benchmark problem, *Journal of Engineering Mechanics*, 130 (2004) 466–470.

[111] B. Erkus, E.A. Johnson, Smart base-isolated benchmark building Part III: A simple controller for bilinear isolation, *Structural Control and Health Monitoring*, 13 (2006) 605–625.

Appendix A

Base-Isolated Benchmark Model

Base-isolated buildings are designed such that the superstructure remains elastic. The superstructure is modelled by a linear elastic system. The base-isolation consists of 92 linear isolation bearings. All bearings are designed as linear elastic rubber bearings so that a fully linear isolation system is constructed. The details of linear and non-linear base-isolated benchmark building models are discussed in [39, 111]. Here linear base-isolation is considered.

The dynamics of an uncontrolled benchmark building with linear rubber bearings will be described. A structural model of the base-isolated building is presented together with a detailed elaboration of the mass, damping and stiffness matrix and the force vector. The equation of motion of the uncontrolled linear base-isolated building is formulated combining the superstructure model consisting of an eight-floor structure above the base (24 DOF) and the base with linear isolation bearing (3 DOF).

The superstructure is linear and the slabs are all assumed to be rigid. The response of each floor is characterised by three main degrees of freedom located at the centre of mass (COM): two horizontal in the longitudinal and transverse axis directions and one rotational about the vertical axis. This gives a (24 DOF finite element model. The superstructure equation of motion can be written as

$$\mathbf{M}_s\ddot{\mathbf{x}}_s + \mathbf{C}_s\dot{\mathbf{x}}_s + \mathbf{K}_s\mathbf{x}_s = -\mathbf{M}_s\mathbf{R}_1\ddot{\mathbf{x}}_b \tag{A.1}$$

where $\mathbf{R}_1 = \begin{bmatrix} \mathbf{I}_{3\times3} \\ . \\ . \\ \mathbf{I}_{3\times3} \end{bmatrix}_{24\times3}$

$\mathbf{M}_s$, $\mathbf{C}_s$ and $\mathbf{K}_s$ are the 24×24 respectively. $\mathbf{x}_s$ is the displacement of the superstructure with respect to the base, $\dot{\mathbf{x}}_s$ is the velocity, $\ddot{\mathbf{x}}_s$ is the acceleration and $\dot{\mathbf{x}}_b$ is the absolute acceleration of the base. The dots denote differentiation with respect to time. $\mathbf{R}_1$ is a transformation matrix used to distribute the earthquake acceleration effect to all floors. Absolute values and values with respect to the ground and the base, are depicted in Figure A.1. The index g refers to the ground and b refers to the base.

The displacement of the superstructure with respect to the base is described by the 24×24 vector $\mathbf{x}_s = [x_8, y_8, \theta_8, ..., x_1, y_1, \theta_1]^{\mathrm{T}}$ where x_i, y_i, θ_i are the displacement in the horizontal x and y direction and the rotational respectively. The absolute displacement of the base, x_b can be expressed as the sum of the displacement of the base with respect to the ground and the absolute acceleration of the ground.

$$\mathbf{x}_b = \mathbf{x}_b^g + \mathbf{R}_3\mathbf{x}_g \quad , \quad \mathbf{R}_3 = \begin{bmatrix} 1 & 0 \\ 0 & 1 \\ 0 & 0 \end{bmatrix} \tag{A.2}$$

$\mathbf{R}_3$ is denoted the transformation coefficient matrix and the displacement of the base with respect to the ground is given by the 3×1 vector $\mathbf{x}_b^g = [x_b^g, y_b^g, \theta_b^g]^{\mathrm{T}}$. By using the same

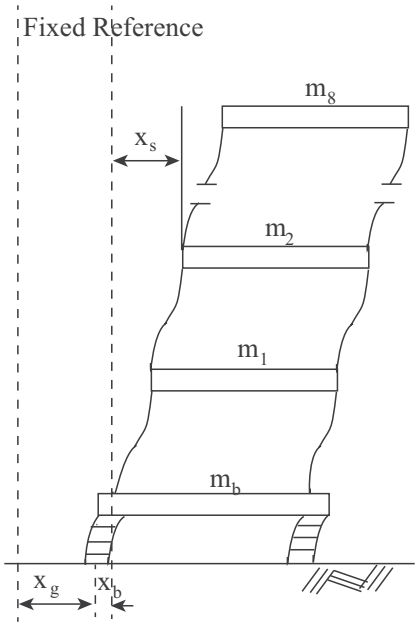

FIGURE A.1: The displacement coordinates used to formulate the equations of motion.

principle as(A.2) on the acceleration and inserting this in(A.2), the equation of motion is modified as

$$\mathbf{M}_s\ddot{\mathbf{x}}_s + \mathbf{C}_s\dot{\mathbf{x}}_s + \mathbf{K}_s\mathbf{x}_s = -\mathbf{M}_s\mathbf{R}_1\left(\ddot{\mathbf{x}}_b^g + \mathbf{R}_3\ddot{\mathbf{x}}_g\right) \tag{A.3}$$

where $\mathbf{M}_s$, $\mathbf{C}_s$ and $\mathbf{K}_s$ are the mass, damping and stiffness matrices of the superstructure respectively. $\mathbf{M}_s$ is given as a diagonal matrix containing the mass in the two horizontal directions and the rotational mass for each of the eight floors.

$$\mathbf{M}_s = \begin{bmatrix} m_8^x & & & & & & & \\ & m_8^y & & & & & & \\ & & m_8^\theta & & & & & \\ & & & \ddots & & & & \\ & & & & \ddots & & & \\ & & & & & m_1^\theta & & \\ & & & & & & m_1^\theta & \\ & & & & & & & m_1^\theta \end{bmatrix}_{24\times 24} \tag{A.4}$$

The resonance frequency is determined from an eigenvalue problem

$$(\mathbf{K}_s - \omega_{0s}^2\mathbf{M}_s)\mathbf{u}_{0s} = 0 \tag{A.5}$$

The equation of motion for the base is given by

$$\mathbf{M}_b\ddot{\mathbf{x}}_b + \mathbf{C}_b\dot{\mathbf{x}}_b + \mathbf{K}_b\mathbf{x}_b + \mathbf{Q}_s = -\mathbf{M}_b\mathbf{R}_3\ddot{\mathbf{x}}_g \tag{A.6}$$

where $x_b = [x_b, y_b, \theta_b]^{\mathrm{T}}$ describes the displacement of the base with respect to the ground. $\mathbf{M}_b$, $\mathbf{C}_b$ and $\mathbf{K}_b$ are the (3×3) mass, damping and stiffness matrices of the base respectively. $\mathbf{Q}_s$ is the superstructure shear force given by

$$\mathbf{Q}_s = \mathbf{R}_1^{\mathrm{T}}\mathbf{M}_s(\ddot{\mathbf{x}}_s + \mathbf{R}_1\ddot{\mathbf{x}}_b) \tag{A.7}$$

By substituting (A.7), together with the expression for the absolute base acceleration, into (A.6), it gives

$$\mathbf{M}_b\ddot{\mathbf{x}}_b + \mathbf{C}_b\dot{\mathbf{x}}_b + \mathbf{K}_b\mathbf{x}_b + \mathbf{R}_1^{\mathsf{T}}\mathbf{M}_s\left(\ddot{\mathbf{x}}_s + \mathbf{R}_1(\ddot{\mathbf{x}}_b^g + \mathbf{R}_3\ddot{\mathbf{x}}_g)\right) = -\mathbf{M}_b\mathbf{R}_3\ddot{\mathbf{x}}_g \tag{A.8}$$

M_b is given as a diagonal matrix containing the mass in the two horizontal direction and the rotational mass of the base

$$\mathbf{M}_b = \begin{bmatrix} m_b^x & & \\ & m_b^y & \\ & & m_b^\theta \end{bmatrix} \tag{A.9}$$

The masses are given in [39] for constructing model.

The damping matrix for the base is constructed based on the rubber damping parameter $c_{\texttt{rub}}$ given in benchmark problem [39]. The damping for one bearing can be formulated as

$$\mathbf{C}_i^{bear} = \begin{bmatrix} c_{rub}^x & & \\ & c_{rub}^y & \\ & & . \end{bmatrix} \tag{A.10}$$

where i is the number of isolation bearing. The rubber has the same damping in both x and y direction so $c_{rub}^x = c_{rub}^y = c_{rub}$. This yields a total diagonal damping matrix for the base-isolation system

$$\mathbf{C}^{bear} = \begin{bmatrix} \mathbf{C}_1^{bear} & & & \\ & . & & \\ & & . & \\ & & & \mathbf{C}_n^{bear} \end{bmatrix} \tag{A.11}$$

where $n = 92$ is the number of isolation bearings.

The damping matrix for the isolation system is transformed with respect to the center of mass. The final damping matrix for the base becomes

$$\mathbf{C}^b = \mathbf{R}_2^{bear}\mathbf{C}^{bear}(\mathbf{R}_2^{bear})^{\mathsf{T}} \tag{A.12}$$

where the transformation matrix $\mathbf{R}_2^{bear}$ is given by

$$\mathbf{R}_2^{bear} = \begin{bmatrix} \mathbf{r}_1^{bear} & . & . & . & \mathbf{r}_n^{bear} \end{bmatrix} \quad , \quad \mathbf{r}_i^{bear} = \begin{bmatrix} 1 & 0 & 0 \\ 0 & 1 & 0 \\ -y_i^{bear} & x_i^{bear} & 1 \end{bmatrix} \tag{A.13}$$

The stiffness matrix for the base is based on the rubber stiffness k_{rubb} given in [39]. The final stiffness matrix will be constructed in a similar way to the damping matrix. The stiffness for one bearing can be formulated as

$$\mathbf{K}_i^{bear} = \begin{bmatrix} k_{rub}^x & & \\ & k_{rub}^y & \\ & & . \end{bmatrix} \tag{A.14}$$

The rubber has the same stiffness in both x and y direction so $k_{rub}^x = k_{rub}^y = k_{rub}$. This yields a total diagonal stiffness matrix for the base-isolation system

$$\mathbf{K}^{bear} = \begin{bmatrix} \mathbf{K}_1^{bear} & & & \\ & . & & \\ & & . & \\ & & & \mathbf{K}_n^{bear} \end{bmatrix} \tag{A.15}$$

The stiffness matrix is transformed with respect to the center of the mass. The final stiffness matrix for the base becomes

$$\mathbf{K}^b = \mathbf{R}_2^{bear}\mathbf{K}^{bear}(\mathbf{R}_2^{bear})^{\mathsf{T}} \tag{A.16}$$

The motion of the entire building is expresses as a combination os super structure and base. Combining the (A.1) and (A.6) the total structural model is constructed and expressed as below

$$\mathbf{M}\ddot{\mathbf{x}} + \mathbf{C}\dot{\mathbf{x}} + \mathbf{K}\mathbf{x} = \mathbf{S}\ddot{\mathbf{x}}_g \tag{A.17}$$

where the displacement $\mathbf{x}$ is described by a (27×1) vector. The displacements of the superstructure is represented with respect to the base and the displacements of the base is represented with respect to the ground.

$$\mathbf{x} = \begin{bmatrix} \mathbf{x}_s \\ \mathbf{x}_b \end{bmatrix} \tag{A.18}$$

The mass, damping, stiffness and load matrices are constructed as

$$\begin{aligned} \mathbf{M} &= \begin{bmatrix} \mathbf{M}_s & \mathbf{M}_s\mathbf{R}_1 \\ \mathbf{R}_i^{\mathsf{T}}\mathbf{M}_s & \mathbf{M}_b + \mathbf{R}_1^{\mathsf{T}}\mathbf{M}_s\mathbf{R}_1 \end{bmatrix} & \mathbf{C} &= \begin{bmatrix} \mathbf{C}_s & 0 \\ 0 & \mathbf{C}_b \end{bmatrix} \\ \mathbf{K} &= \begin{bmatrix} \mathbf{K}_s & 0 \\ 0 & \mathbf{K}_b \end{bmatrix} & \mathbf{S} &= \begin{bmatrix} -\mathbf{M}_s\mathbf{R}_1\mathbf{R}_3 \\ -(\mathbf{M}_b + \mathbf{R}_1^{\mathsf{T}}\mathbf{M}_s\mathbf{R}_1)\mathbf{R}_3 \end{bmatrix} \end{aligned} \tag{A.19}$$

Appendix B

Evaluation Criteria For Base-Isolated Benchmark Building

To evaluate the performance of the base-isolated benchmark building and to compare the results with different kinds of control strategies, 9 evaluation criteria, J-values, are presented in [38]. A detailed description of the evaluation criteria is given below. The symbol u describes results obtained from the uncontrolled structure. Considering the indices, j=device number, f=floor number: 1,...,8 and b represents the base. Regarding the variables and t = time: $0 \leq t \leq T$ (T = 30s). Q equals to the shear force and F equals to the controller force. $J3, J4, J5$ are representing deviation in base displacements, inter-floor drifts and superstructure floor accelerations. x_b is the displacement of the base with respect to the ground. Δx is the inter-storey drift and $\ddot{x}$ is the absolute acceleration of the superstructure. The root-mean-square (RMS) response quantities indicate if the peak value obtained for the given response is representative, or if the general response lies a lot lower than this. The objective is to minimize these RMS values. σ indicates that it is an RMS value and the subscript indicates whether it is displacement or acceleration. Another performance index $J9$ measures the energy dissipated by the control devices as a percentage of the input excitation energy. An increase in $J9$ means that energy is dissipated by use of the controller, i.e. damping is induced. $\dot{x}_j$ is the velocity of the jth device with respect to the ground and $\dot{x}_g$ is the velocity of the ground. $\| \ . \ \|$ is vector magnitude incorporating NS and EW components. $\langle . \rangle$ is inner product.

The evaluation criteria are denoted by performance indices which are constructed by the controlled quantity divided by the uncontrolled quantity and are given below

- Peak base shear (isolation-level) in the controlled structure normalised by the corresponding shear in the uncontrolled structure

  $J_1 = \frac{max_t \|Q_b(t)\|}{max_t \|Q_b^u(t)\|}$

- Peak structure shear (at first storey level) in the controlled structure normalised by the corresponding shear in the uncontrolled structure

  $J_2 = \frac{max_t \|Q_1(t)\|}{max_t \|Q_1^u(t)\|}$

- Peak base displacement or isolator deformation in the controlled structure normalised by the corresponding displacement in the uncontrolled structure

  $J_3 = \frac{max_{t,i} \|\mathbf{x}_b(t)\|}{max_{t,i} \|\mathbf{x}_b^u(t)\|}$

- Peak inter-storey drift in the controlled structure normalised by the corresponding inter-storey drift in the uncontrolled structure

  $J_4 = \frac{max_{t,f} \|\Delta \mathbf{x}_f(t)\|}{max_{t,f} \|\Delta \mathbf{x}_f^u(t)\|}$

- Peak absolute floor acceleration in the controlled structure normalised by the corresponding acceleration in the uncontrolled structure

  $J_5 = \frac{max_{t,f} \|\ddot{\mathbf{x}}_f(t)\|}{max_{t,f} \|\ddot{\mathbf{x}}_f^u(t)\|}$

- Peak force generated by all control devices normalised by the peak base shear in the controlled structure
  $J_6 = \frac{max_t \|\sum_j F_j(t)\|}{max_t \|Q_b(t)\|}$
- RMS base displacement in the controlled structure normalised by the corresponding RMS base displacement in the uncontrolled structure
  $J_7 = \frac{max_i \|\sigma_{x_b}(t)\|}{max_i \|\sigma_{x_b^u}(t)\|}$
- RMS absolute floor acceleration in the controlled structure normalised by the corresponding RMS acceleration in the uncontrolled structure
  $J_8 = \frac{max_f \|\sigma_{\ddot{x}}(t)\|}{max_f \|\sigma_{\ddot{x}^u}(t)\|}$
- Total energy absorbed by all control devices normalised by energy input into the controlled structure
  $J_9 = \frac{\sum_j [\int_0^T F_j(t)\dot{x}_j(t)dt]}{\int_0^T \langle Q_b(t)\dot{x}_g(t)\rangle dt}$

Appendix C

Wind-Excited Benchmark Model

The building considered for wind-excited benchmark problem is a 76-floor tall building. The detailed structural model is given in [40]. The equation of motion for the controlled building structure model subjected to wind excitation can be expressed as

$$\mathbf{M}\ddot{\mathbf{x}} + \mathbf{C}\dot{\mathbf{x}} + \mathbf{K}\mathbf{x} + \mathbf{H}u = \mathbf{G}\mathbf{W} \tag{C.1}$$

where $x = [x_1, x_2, ..., x_{76}]^T$ is displacement vector. x_i represents the displacement of the ith floor. $\mathbf{M}$, $\mathbf{C}$ and $\mathbf{K}$ are (76×76) mass, damping and stiffness matrices, u is control force, $\mathbf{W}$ is wind excitation vector with dimension 76, $\mathbf{H}$ is control influence vector, and $\mathbf{G}$ is excitation influence matrix.

The state order reduction model is implemented to derive the low order model model from (C.1). In the reduced order model, eigenvalues and eigenvectors of selected modes of the full-order system are preserved. The 76 DOF model is reduced to a 23 DOF system by retaining first 46 complex modes of the full order system. The reduced order state equation is expressed by

$$\dot{\mathbf{x}} = \mathbf{A}\mathbf{x} + \mathbf{B}u + \mathbf{E}\mathbf{W} \tag{C.2}$$

in which $\mathbf{x} = [\bar{\mathbf{x}}, \dot{\bar{\mathbf{x}}}]^T$ is 46-dimensional deduced order state vector and $\bar{\mathbf{x}} = [x_3, x_6, x_{10}, x_{13}, x_{16}, x_{20}, x_{23}, x_{26}, x_{30}, x_{33}, x_{36}, x_{40}, x_{43}, x_{46}, x_{50}, x_{53}, x_{56}, x_{60}, x_{63}, x_{66}, x_{70}, x_{73}, x_{76}]$. $\mathbf{A}$ is (46×46) system matrix, $\mathbf{B}$ is (46×1)location vector and $\mathbf{E}$ is (46×76) matrix.

The controlled output vector $\mathbf{z}$ and the measured output vector $\mathbf{y}$ in the output equation of the state model in (C.2) are expressed as

$$\mathbf{z} = \mathbf{C}_z\mathbf{x} + \mathbf{D}_z u + \mathbf{F}_z\mathbf{W} \tag{C.3}$$

$$\mathbf{y} = \mathbf{C}_y\mathbf{x} + \mathbf{D}_y u + \mathbf{F}_y\mathbf{W} + \mathbf{v} \tag{C.4}$$

in which $\mathbf{z} = [x_1, x_{30}, x_{50}, x_{55}, x_{60}, x_{65}, x_{70}, x_{75}, x_{76}, \dot{x}_1, \dot{x}_{30}, \dot{x}_{50}, \dot{x}_{55}, \dot{x}_{60}, \dot{x}_{65}, \dot{x}_{70}, \dot{x}_{75}, \dot{x}_{76}, \ddot{x}_1, \ddot{x}_{30}, \ddot{x}_{50}, \ddot{x}_{55}, \ddot{x}_{60}, \ddot{x}_{65}, \ddot{x}_{70}, \ddot{x}_{75}, \ddot{x}_{76}]^T$ which is a (27×1) vector of regulated response and $\mathbf{y} = [\dot{x}_1, \dot{x}_{30}, \dot{x}_{50}, \dot{x}_{55}, \dot{x}_{60}, \dot{x}_{65}, \dot{x}_{70}, \dot{x}_{75}, \dot{x}_{76}, \ddot{x}_1, \ddot{x}_{30}, \ddot{x}_{50}, \ddot{x}_{55}, \ddot{x}_{60}, \ddot{x}_{65}, \ddot{x}_{70}, \ddot{x}_{75}, \ddot{x}_{76}]^T$ which is a (18×1) vector of measured response from the sensors. $\mathbf{v}$ is noise vector. $\mathbf{C}_z$, $\mathbf{D}_z$, $\mathbf{F}_z$, $\mathbf{C}_y$, $\mathbf{D}_y$, $\mathbf{F}_y$ have appropriate dimension based on model order.

Appendix D

Evaluation Criteria For Wind-Excited Benchmark Building

To evaluate the performance of the wind-excited benchmark building and compare the results with several control strategies, 12 evaluation criteria, J-values, are presented by Yang et al. [40]. A detailed description of the evaluation criteria is discussed below. The symbol σ describes the rms value of the corresponding measurement. Considering the indices, i represents floor number: 1,..., 76, p represents peak value, u represents uncontrolled case and d represents the actuator. Here x_i, $\dot{x}_i$ and $\ddot{x}_i$ represent the displacement, velocity and the acceleration of ith floor respectively. From the time history of the structural response, the peak response values and the rms values are evaluated.

The evaluation criteria is denoted by the performance indices which are constructed by the controlled quantity divided by the uncontrolled quantity and is given below

- The first evaluation criterion of the controller is evaluated based on its ability to reduce the maximum floor rms acceleration with compared to rms value of the 75th floor acceleration.

  $J_1 = \frac{max(\sigma_{\ddot{x}1},\sigma_{\ddot{x}30},\sigma_{\ddot{x}50},\sigma_{\ddot{x}55},\sigma_{\ddot{x}60},\sigma_{\ddot{x}65},\sigma_{\ddot{x}70},\sigma_{\ddot{x}75})}{\sigma_{\ddot{x}75u}}$

  where $\sigma_{\ddot{x}i}$ is the RMS acceleration of the ith floor and $\sigma_{\ddot{x}75u}$ is the RMS acceleration of the 75th floor without controller. For evaluating this criterion only up to 75th floor acceleration values are considered. 76th floor is top floor and unoccupied and thats why only displacement of that floor is important but acceleration is not considered.

- The second criterion is evaluated based on the average performance of acceleration for some selected floors above the 49th floor.

  $J_2 = \frac{1}{6}\sum_i(\frac{\sigma_{\ddot{x}i}}{\sigma_{\ddot{x}iu}})$

  for $i = 50, 55, 60, 65, 70, 75$ and $\sigma_{\ddot{x}iu}$ is RMS acceleration of the ith floor without control.

- The third criteria is evaluated based on the ability of the controller to reduce the top floor displacements. After normalization, the criteria is expressed as

  $J_3 = \frac{\sigma_{x76}}{\sigma_{x76u}}$

- The fourth evaluation criteria is also reduction of some selective floor displacement above 49th floor, i.e.,

  $J_4 = \frac{1}{7}\sum_i \frac{\sigma_{xi}}{\sigma_{xiu}}$

  for $i = 50, 55, 60, 65, 70, 75, 76$

- The fifth criteria is based on actuator capacity constraints which is given in [40]. If σ_{xm} is RMS actuator displacement then the non dimensionalized actuator stroke can be represented as

  $J_5 = \frac{\sigma_{xm}}{\sigma_{x76u}}$

- The sixth criteria is based on the average power from actuator and represented as $J_6 = \{\frac{1}{T}\int_0^T [\dot{x}_m(t)u(t)]^2 dt\}^{1/2}$

  in which $\dot{x}_m$ is actuator velocity and T is the total time of integration.

- The seventh criteria is based on peak response quantity. The non-dimensional performance criteria is given as

  $J_7 = \frac{max(\ddot{x}_{p1},\ddot{x}_{p30},\ddot{x}_{p50},\ddot{x}_{p55},\ddot{x}_{p60},\ddot{x}_{p65},\ddot{x}_{p70},\ddot{x}_{p75})}{\ddot{x}_{p75}}$

- The eighth criterion is the average peak value of acceleration for selected floors above 49th floor, i.e.,

  $J_8 = \frac{1}{6}\sum_i(\frac{\ddot{x}_{pi}}{\ddot{x}_{piu}})$

  for $i = 50, 55, 60, 65, 70$ and 75.

  where $\ddot{x}_{pi}$ and $\ddot{x}_{piu}$ are the peak accelerations of the ith floor with and without controller.

- The ninth criteria is evaluated based on the ability of the controller to reduce the peak value of the top floor displacement. After normalization, the criteria is expressed as

  $J_9 = \frac{x_{p76}}{x_{p76u}}$

- The tenth criterion is the average peak value of displacement for selected floors above 49th floor, i.e.,

  $J_{10} = \frac{1}{7}\sum_i(\frac{x_{pi}}{x_{piu}})$

  for $i = 50, 55, 60, 65, 70, 75$ and 76.

  where x_{pi} and x_{piu} are the peak displacement of the ith floor with and without controller.

- The eleventh and twelfth criterions are based on constrains of the actuator capacity in terms of actuator strokes and actuator power respectively

  $J_{11} = \frac{x_{pm}}{x_{p76u}}$;

  $J_{12} = P_{max} = max|\dot{x}_m(t)u(t)|$

  where x_{pm} is peak stroke of actuator and P_{max} is the peak control power.

Appendix E

LQG Control Design: Sample Controller In Benchmark Problems

Linear Quadratic Gaussian(LQG) Control is one of the most useful optimal control techniques. LQG is used in base-isolated as well as wind-excited benchmark problems as a sample controller [39, 40]. The detailed description about formation of LQG controller is depicted by Yang et al. [40] and also given as below. The LQG controller is used as a sample controller for comparing with the proposed control design methodologies in benchmark problems. A brief discussion on LQG control design based on articles [14, 40, 111] is given below

The system model for LQG controller can be full-order or reduced-order based on benchmark problem. The reduced-order system model is derived from the full-order system model. The standard LQG controller used in benchmark problem is shown in Figure E.1.

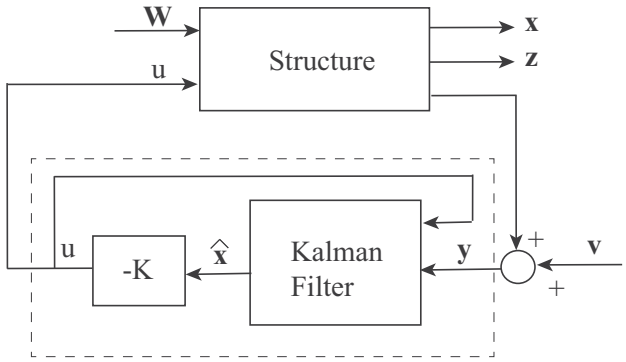

Figure E.1: LQG Controller.

The system model is written as

$$\dot{\mathbf{x}} = \mathbf{A}\mathbf{x} + \mathbf{B}\mathbf{u} + \mathbf{E}\mathbf{W} \tag{E.1}$$

The controlled output equation and the output measurement equation are expressed as

$$\mathbf{z} = \mathbf{C}_z\mathbf{x} + \mathbf{D}_z\mathbf{u} + \mathbf{F}_z\mathbf{W} \tag{E.2}$$

$$\mathbf{y} = \mathbf{C}_y\mathbf{x} + \mathbf{D}_y\mathbf{u} + \mathbf{F}_y\mathbf{W} + \mathbf{v} \tag{E.3}$$

where $\mathbf{x}$ is a n-dimensional state vector consists of displacements and velocities at different floor location, $\mathbf{z}$ is controlled output vector, $\mathbf{y}$ is the measured output vector. $\mathbf{A}, \mathbf{B}, \mathbf{E}$ are system matrices. $\mathbf{C}_z, \mathbf{D}_z, \mathbf{F}_z, \mathbf{C}_y, \mathbf{D}_y, \mathbf{F}_y$ are output matrices having appropriate dimensions. $\mathbf{W}$ is the external excitation and $\mathbf{v}$ is the measurement noise which are constructed by uncorrelated Gaussian white noise vectors.

A LQG controller is constructed by minimising a cost function that weights the regulated outputs and the control forces is given as

$$J = \lim_{\tau\to\infty} \frac{1}{\tau} E\left[\int_0^\tau (\mathbf{z}_a^T\mathbf{Q}\mathbf{z}_a + \mathbf{u}^T\mathbf{R}\mathbf{u})dt\right] \tag{E.4}$$

where $\mathbf{z}_a = \mathbf{z} - \mathbf{F}_z\mathbf{W} = \mathbf{C}_z\mathbf{x} + \mathbf{D}_z\mathbf{u}$, $\mathbf{Q}$ is a diagonal matrix that weights the regulated outputs and $\mathbf{R}$ is an identity matrix that weights the control forces. For the linear system,the separation principle for LQG method allows the control and estimation problems to be considered separately. The control law for the LQG is obtained as

$$\mathbf{u} = -\mathbf{K}\hat{\mathbf{x}} \tag{E.5}$$

$\mathbf{K}$ is obtained from

$$\mathbf{K} = -\bar{\mathbf{R}}^{-1}(\mathbf{B}^T\mathbf{P} + \mathbf{S}^T) \tag{E.6}$$

in which $\mathbf{P}$ is the solution of the Riccati equation

$$\mathbf{P}\bar{\mathbf{A}} + \bar{\mathbf{A}}^T\mathbf{P} - \mathbf{P}\mathbf{B}\bar{\mathbf{R}}^{-1}\mathbf{B}^T\mathbf{P} + \bar{\mathbf{Q}} - \bar{\mathbf{S}}\bar{\mathbf{R}}^{-1}\bar{\mathbf{S}}^T = 0 \tag{E.7}$$

where $\bar{\mathbf{Q}} = \mathbf{C}_z^T\mathbf{Q}\mathbf{C}_z$, $\bar{\mathbf{R}} = \mathbf{D}^T{}_z\mathbf{Q}\mathbf{D}_z + \mathbf{R}$, $\bar{\mathbf{S}} = \mathbf{C}_z^T\mathbf{Q}\mathbf{D}_z$ and $\bar{\mathbf{A}} = \mathbf{A} - \mathbf{B}\bar{\mathbf{R}}^{-1}\mathbf{S}^T$. Calculation of $\mathbf{K}$ is performed using MATLAB control toolbox functions *lqry* .

The LQG controller in (E.5) is based on the state feedback $\mathbf{x}$, which can be estimated from Kalman-Bucy Filter which acts as an observer. The estimated state is denoted by $\hat{\mathbf{x}}$. The Kalman filter is expressed as

$$\dot{\hat{\mathbf{x}}} = \mathbf{A}\hat{\mathbf{x}} + \mathbf{B}\mathbf{u} + \mathbf{L}(\mathbf{y} - \mathbf{C}_y\hat{\mathbf{x}} - \mathbf{D}_y\mathbf{u}) \tag{E.8}$$

in which the Kalman gain matrix $\mathbf{L}$ is calculated from

$$\mathbf{L} = (\mathbf{P}_k\mathbf{C}_y{}^T + \mathbf{S}_k)\mathbf{R}_k{}^{-1} \tag{E.9}$$

where $\mathbf{P}_k$ is obtained from the solution of the Riccati equation

$$\mathbf{P}_k\hat{\mathbf{A}} + \hat{\mathbf{A}}^T\mathbf{P}_k - \mathbf{P}_k\mathbf{C}_y{}^T\mathbf{R}_k^{-1}\mathbf{C}_y\mathbf{P}_k + \mathbf{Q}_k - \mathbf{S}_k\mathbf{R}_k^{-1}\mathbf{S}_k = 0 \tag{E.10}$$

where

$$\hat{\mathbf{A}} = \mathbf{A}^T - \mathbf{C}_y^T\mathbf{R}_k^{-1}\mathbf{S}_k^T \tag{E.11}$$

$\mathbf{Q}_k$ and $\mathbf{R}_k$ are autopower spectral density function of two vectors $\mathbf{EW}$ and $\mathbf{F}_y\mathbf{W} + \mathbf{v}$, respectively. $\mathbf{S}_k$ is the cross-power spectral density function of two vectors $\mathbf{EW}$ and $\mathbf{F}_y\mathbf{W}+\mathbf{v}$.

$$\mathbf{Q}_k = \mathbf{E}\mathbf{S}_w\mathbf{E}^T;\ \mathbf{S}_k = \mathbf{E}\mathbf{S}_w\mathbf{F}_y^T;\ \mathbf{R}_k = \mathbf{S}_v + \mathbf{F}_y\mathbf{S}_w\mathbf{F}_y^T \tag{E.12}$$

where $\mathbf{S}_w$ and $\mathbf{S}_v$ are power spectral density matrices of the white noise $\mathbf{W}$ and $\mathbf{v}$ respectively. The Kalman estimator gain $\mathbf{L}$ is calculated using MATLAB control toolbox function *lqew*.

P1

(Journal paper)

Experimental calibration of forward and inverse neural networks for rotary type magnetorheological damper

Submitted
2011

Experimental calibration of forward and inverse neural networks for rotary type magnetorheological damper

S. Bhowmik [a 1, 2], F. Weber * [2] and J. Høgsberg [b 1]

[1] *Department of Mechanical Engineering, Technical University of Denmark, Lyngby 2800, Denmark*

[2] *Empa, Swiss Federal Laboratories for Materials Science and Technology, Structural Engineering Research Laboratory, Ueberlandstrasse 129, CH-8600 Duebendorf, Switzerland*

Abstract. This paper presents a systematic design and training procedure for the feed-forward back-propagation neural network (NN) modelling of both forward and inverse behaviour of a rotary magnetorheological (MR) damper based on experimental data. For the forward damper model, with damper force as output, an optimization procedure demonstrates accurate training of the NN architecture with only current and velocity as input states. For the inverse damper model, with current as output, the absolute value of velocity and force are used as input states to avoid negative current spikes when tracking a desired damper force. The forward and inverse damper models are trained and validated experimentally, combining a limited number of harmonic displacement records, and constant and half-sinusoidal current records. In general the validation shows accurate results for both forward and inverse damper models, where the observed modelling errors for the inverse model can be related to knocking effects in the measured force due to the bearing plays between hydraulic piston and MR damper rod. Finally, the validated models are used to emulate pure viscous damping. Comparison of numerical and experimental results demonstrates good agreement in the post-yield region of the MR damper, while the main error of the inverse NN occurs in the pre-yield region where the inverse NN overestimates the current to track the desired viscous force.

Keywords: experimental validation, inverse MR damper model, rotary MR damper, neural network.

* Corresponding author, Dr. Mech. Eng., E-mail: felix.weber@empa.ch
a Ph.D. student E-mail: subho@mek.dtu.dk
b Professor, Ph.D. E-mail: jhg@mek.dtu.dk

1. Introduction

Magnetorheological (MR) dampers used for controlled damping of structural vibrations have received considerable attention during the last decades because they offer the possibility to adapt their semi-active force in real-time to the structural vibrations (Christenson et al 2006, Li et al 2007, Neelakantan and Washington 2008, Wu and Cai 2010). MR dampers are suitable for mitigation of vibrations in large civil engineering structures because they combine large control force ranges, low power requirements, fast response time and fail safe performance (Spencer and Nagarajaiah 2003).

Basically, rotary type magnetorheological (MR) dampers consist of a housing including the MR fluid and the rotating part of the disc. The MR fluid is a suspension of oil with magnetizable particles with average diameter of 5 μm and some additives. The particles and the ferromagnetic parts of the housing and disc are magnetized by the magnetic field that is produced by two coils which are installed within the housing on both sides of the disc. The magnetized particles built chains and thereby stick to the disc and housing (Weber and Boston 2011a). When the disc starts to rotate the particle chains are initially stretched before they start to slide relative to the surfaces of the disc and/or the housing. The particle chains may also brake, whereby rupture between particles occurs. The phase where particle chains are elastically stretched is commonly denoted as the pre-yield region of the MR fluid, while the sliding phase is called the post-yield region. The particle chains start to slide when the dry friction force between particles or between particle chains and disc or between particle chains and housing is balanced by the elastic force due to elongation of the particle chains (Weber and Boston 2011a). Since this sticking depends strongly on the magnetization of the MR fluid, and thereby on the MR damper current, the post-yield force of the MR damper typically exhibits a strong current dependency. Because the superposed viscous force is usually rather small and the MR fluid viscosity depends only slightly on the coil current, the applied current primarily controls the friction force of the MR damper, while the viscous force component is mainly governed by the rotating speed of the disc and the inherent viscosity of the MR fluid (Weber et al 2011). In order to be able to control the total MR damper force relative to a desired control force, the coil current must be modulated so that the control force tracking error is acceptable. Due to the non-linear behavior of the MR damper force, i.e. the non-linear relation between current and sticking force and the non-linear dependency of the MR fluid viscosity on current, force

tracking with force feedback only may fail to track the desired force accurately. Therefore, model-based feed forward control schemes are needed to solve the force tracking task with sufficient accuracy (Weber et al 2011, Weber and Boston 2011b). Such approaches can then later be extended by a force feedback in order to further decrease the remaining force tracking error.

MR dampers are either operated at zero or constant current, which are called passive-off or passive-on strategies (Weber et al 2005), or they are controlled in real-time within a particular feedback loop (Maslanka et al 2007, Weber et al 2009). In the latter case the structural response is typically measured at damper position and the MR damper current is controlled in real-time to obtain minimum tracking error with respect to a desired control force. The force tracking task is usually solved by a model-based feed forward control scheme, simply to avoid costly force sensors (Maslanka et al 2007, Weber et al 2009). The input states of the feed forward controller may be the damper displacement, velocity, acceleration, or any combination of these states, and the desired control force, while the output state is the desired MR damper current. In practice the desired current is realized by a current driver, which compensates for the coil impedance dynamics of the MR damper. Therefore, an inverse MR damper model is required that estimates the desired damper current based on a limited number of the above mentioned input states. This model is usually referred to as an inverse MR damper model (Tse and Chang 2004, Yang et al 2004, Dominguez et al 2006, Weber et al 2011, Weber and Boston 2011a, Weber and Boston 2011b) because it predicts the controllable damper current, while the classic forward models predict the damper force.

Many parametric and non-parametric forward models for classic cylindrical type MR dampers have been presented in the literature. Some of the prominent parametric approaches are the Bouc-Wen model, which captures both the pre- and post-yield regions (Yang et al 2004, Dominguez et al 2006), the Bingham model which basically represents current dependent friction (Ikhouane and Dyke 2007), the Dahl model which describes an elasto-plastic material behaviour with supplemental viscous effects (Shulman et al 2006) and the LuGre approach that models the MR fluid particle chains as brushes with sticking and sliding against the damper housing (Jiménez and Alvarez-Icaza 2005, Yang et al 2009, Boston et al 2010). These models have also been extended by additional stiffness, viscous and mass elements to account for the accumulator behaviour, the current dependent viscous force and the inertia of the damper piston and other accelerated

parts (Sahin et al 2010). The parameters for minimum model error are typically obtained from the test data directly (Sims et al 2004, Weber et al 2008) or by a numerical optimization tool (Ye and Wang 2007). Once calibrated, these parametric approaches can be used as observers to solve the force tracking problem without feedback from a force sensor (Maslanka et al 2007, Weber et al 2011, Weber and Boston 2011).

Non-parametric models are mainly based on fitted polynomials (Weber et al 2009), genetic algorithms (Xiaomin et al 2009), fuzzy logic (Tsoukalas and Uhrig 1997, Won and Sunwoo 2003), neural networks (NN) (Chang and Roschke 1998, Xia 2003, Chang and Zhou 2002, Wang and Liao 2005, Lee et al 2008, Metered et al 2009) or hybrid approaches (Soeiro et al 2008). As demonstrated in Chang and Roschke (1998) the NN approach is able to model the forward MR damper behaviour fairly accurate. Most of the NNs are trained with simulated input-output data, usually generated by the Bouc-Wen model, as e.g. in Wang and Liao (2005). Only few NN have been trained with experimental data (Metered et al 2009), containing system noise and knocking effects due to bearing tolerances. This makes the training of the network much more difficult, and appropriate filtering of the training data during post processing can be very crucial for the NN performance. The NN architecture is usually found by a trial and error method, and the resulting NN architecture is therefore not necessarily optimal with respect to the minimization of the modelling error.

The present investigation provides a systematic approach to the design and calibration of NNs for both the forward and inverse behaviour of a rotary type MR damper based on experimentally measured training data. It is shown that only force, velocity and current, with necessary previous states, are sufficient for the construction of effective NN architectures. For the NN based inverse modelling of the MR damper the absolute value of velocity and damper force are used as input training data. This modification by the absolute value in the training data input has a major influence on the proper estimation of the current because the current is always positive, irrespective of the sign of the training inputs. Moreover, the MR damper behaviour is measured at constant and half-sinusoidal current, where the half-sinusoidal current tests are performed because they generate training data very similar to the current records associated with damping of structures excited at resonance. The experimental data is filtered so that potential noise is minimised and any offset values are removed. The paper describes a semi-systematic approach for the calibration of the NN architecture based on the minimization of the associated modelling error. The architecture of the NNs for

both the forward and the inverse MR damper models are presented and validated with measurement data independent of the training data. Good accuracy is generally reported, and the validated inverse and forward models are subsequently used in numerical simulations, where pure viscous damping is reproduced real-time.

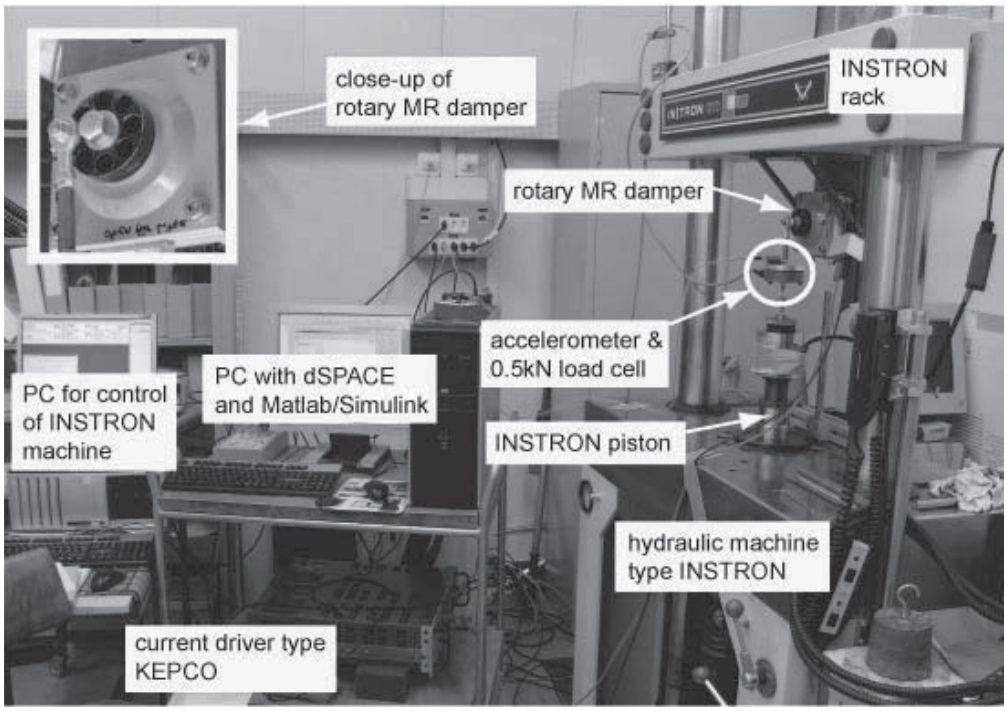

Figure 1. Experimental set-up with rotary MR damper in hydraulic test machine.

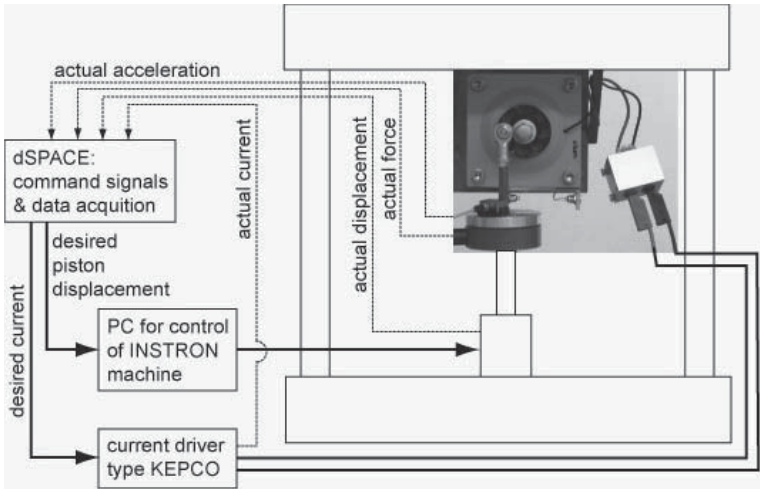

Figure 2. Schematic of test set-up.

2. Experimental data

Section 2.1 introduces the experimental test set-up used to obtain the MR damper response data used for training of the NN, while the necessary post-processing of the measured time histories is described in section 2.2.

2.1. Experimental set-up

The MR damper under consideration is a rotary type MR damper with a maximum current of 4 A. The damper is shown in Fig. 1 and further details on the damper characteristics can be found in Weber et al (2008) and Boston et al (2010). At constant current the damper behaves almost as a friction damper, with only a small velocity dependency. The apparent friction force level is approximately 30 N at 0 A and 300 N at 4 A. Details concerning the behaviour of the rotary type MR damper have been explained in the previous section. The training and the validation data are obtained from forced displacement tests using a hydraulic testing machine of type INSTRON, see Fig. 1. The desired piston displacement is defined in Matlab®, processed real time by a dSPACE® DS1104 R&D controller board and finally send as a command signal directly to the INSTRON PC unit. A flow diagram of the experimental setup is shown in Fig. 2. The actual displacement is captured directly as output from the INSTRON machine and acquired by the dSPACE® system at 1000 Hz sampling frequency. The desired MR damper current is also defined in Matlab/dSPACE®, and tracked real time by a KEPCO current driver. The actual damper current is measured by the KEPCO amplifier and acquired by the dSPACE® system. The MR damper force is measured by a 500 N load cell, and the acceleration of the piston is also measured for verification and potential later use in connection with training or validation. Furthermore, acceleration is suitable for detection of the knocking effects due to the finite bearing tolerances of 0.01-0.02 mm of the joints of the damper rod. A summary of the tests conducted is provided in Table 1. Each test is performed twice: The first set is used as training data, while the second completely independent set is used to validate the NN models. Tests 1-10 are performed at constant current, while tests 11-19 are conducted with half-sinusoidal current. As seen in Table 1 the desired displacement is pure sinusoidal, combining amplitudes of 5 mm and 10 mm, and frequencies from 0.5 Hz to 2.2 Hz.

Table 1. Measurement data for training of NN and model validation.

set for trai-ning	set for vali-dation	desired displacement	desired current
1a	1b	sin, 5 mm, [0.5, 1.0, 1.27, 1.8, 2.2] Hz	0 A
2a	2b	sin, 5 mm, [0.5, 1.0, 1.27, 1.8, 2.2] Hz	1 A
3a	3b	sin, 5 mm, [0.5, 1.0, 1.27, 1.8, 2.2] Hz	2 A
4a	4b	sin, 5 mm, [0.5, 1.0, 1.27, 1.8, 2.2] Hz	3 A
5a	5b	sin, 5 mm, [0.5, 1.0, 1.27, 1.8, 2.2] Hz	4 A
6a	6b	sin, 10 mm, [0.5, 1.0, 1.27, 1.8, 2.2] Hz	0 A
7a	7b	sin, 10 mm, [0.5, 1.0, 1.27, 1.8, 2.2] Hz	1 A
8a	8b	sin, 10 mm, [0.5, 1.0, 1.27, 1.8, 2.2] Hz	2 A
9a	9b	sin, 10 mm, [0.5, 1.0, 1.27, 1.8, 2.2] Hz	3 A
10ae	10b	sin, 10 mm, [0.5, 1.0, 1.27, 1.8, 2.2] Hz	4 A
11a	11b	sin, 5 mm, [0.5, 1.0, 1.27, 1.8, 2.2] Hz	half-sin, 0 A, [0.5, 1.0, 1.27, 1.8, 2.2] Hz
12a	12b	sin, 5 mm, [0.5, 1.0, 1.27, 1.8, 2.2] Hz	half-sin, 1 A, [0.5, 1.0, 1.27, 1.8, 2.2] Hz
13a	13b	sin, 5 mm, [0.5, 1.0, 1.27, 1.8, 2.2] Hz	half-sin, 2 A, [0.5, 1.0, 1.27, 1.8, 2.2] Hz
14a	14b	sin, 5 mm, [0.5, 1.0, 1.27, 1.8, 2.2] Hz	half-sin, 3 A, [0.5, 1.0, 1.27, 1.8, 2.2] Hz
15a	15b	sin, 5 mm, [0.5, 1.0, 1.27, 1.8, 2.2] Hz	half-sin, 4 A, [0.5, 1.0, 1.27, 1.8, 2.2] Hz
16a	16b	sin, 10 mm, [0.5, 1.0, 1.27, 1.8, 2.2] Hz	half-sin, 1 A, [0.5, 1.0, 1.27, 1.8, 2.2] Hz
17a	17b	sin, 10 mm, [0.5, 1.0, 1.27, 1.8, 2.2] Hz	half-sin, 2 A, [0.5, 1.0, 1.27, 1.8, 2.2] Hz
18a	18b	sin, 10 mm, [0.5, 1.0, 1.27, 1.8, 2.2] Hz	half-sin, 3 A, [0.5, 1.0, 1.27, 1.8, 2.2] Hz
19a	19b	sin, 10 mm, [0.5, 1.0, 1.27, 1.8, 2.2] Hz	half-sin, 4 A, [0.5, 1.0, 1.27, 1.8, 2.2] Hz

2.2. Post processing of experimental data

Initially, the measurement data is post-processed by a low pass filter in order to avoid that the NN is trained by high frequency signal components, e.g. noise and knocking effects, which are typically of no interest. The applied low pass filter has the following properties:

- Digital Butterworth low pass filter.
- Filter order 2.
- Cut-off frequency 100 Hz.

Any offset in the displacement, acceleration and force signals are removed by simply balancing positive and negative maxima during steady state conditions. The effect of the filtering of displacement, acceleration,

damper current and damper force is shown in Fig. 3. As seen in Figs. 3(a,c) the high-frequency dithers in the displacement and damper current are effectively removed by the filter, and the main task is basically to avoid a too significant change in the phase and reduction in the peak values. The acceleration is very sensitive to the various sources of noise, and the influence of the filter therefore becomes very evident in Fig. 3(b). Fig. 3(d) shows the damper force, where the main modification is the removal of the offset level. Note that the constant force level at zero crossing is due to the previously mentioned bearing tolerance. The effect is mainly visible in the acceleration signal, which is also shown in Fig. 3(d).

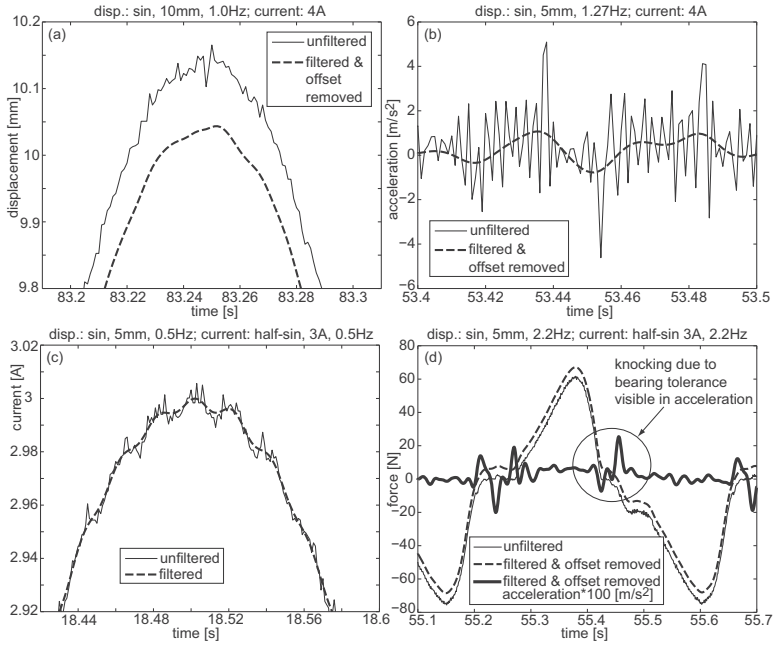

Figure 3. Filtering of measurement data.

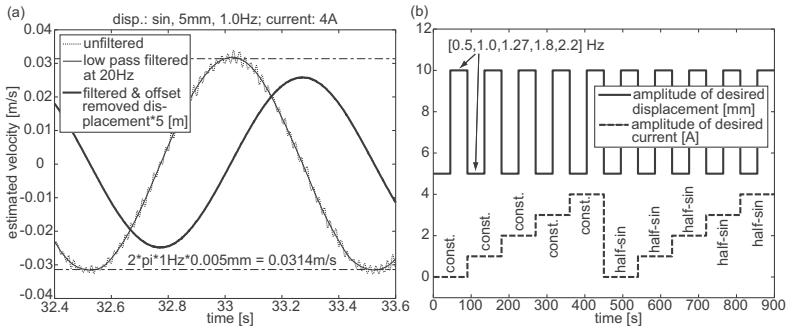

Figure 4. Estimated velocity (a) and training data time history (b).

The training of the NN also requires the damper velocity $\dot{x}$, which is not directly measured. It is instead estimated at each time instant k by numerical differentiation of the displacement x as

$$\dot{x}(k) = \left(\frac{x(k) - x(k-1)}{t(k) - t(k-1)} \right) \text{ with initial condition } \dot{x}(1) = 0 . \quad (1)$$

The inherent noise resulting from the numerical differentiation is subsequently removed by the following low pass filter:

- Digital Butterworth low pass filter.
- Filter order 2.
- Cut-off frequency 20 Hz.

Fig. 4(a) shows the velocity record obtained by differentiation of the sinusoidal displacement with amplitude 5 mm and frequency 1 Hz. The amplitude of the velocity is 31 mm/s, which agrees well with the analytical value of $2\pi(1\,\text{Hz})(5\,\text{mm}) = 31.4\,\text{mm/s}$. The figure also shows the corresponding displacement, and it is observed that the phase shift between displacement and velocity is the expected one quarter of a period. Fig. 4(a) therefore indicates that the method in Eq. (1) leads to a velocity signal with correct amplitude and phase compared to the associated displacement. After the signal post processing, 10 steady state cycles of the data sets 1-19 in Table 1 are isolated and then connected after each other to get individual continuous time histories for displacement, velocity, acceleration, current and force, respectively. Fig. 4(b) shows the combination system for the generation of the resulting time histories used for training of the NN. It should be noted that the sets are always connected at zero crossings of the displacement. To have a reasonably limited amount of data for the training of the NN the time histories are finally down sampled from 1000 Hz to 200 Hz.

3. Modelling

This section concerns the modelling of the NN, with section 3.1 describing the optimization of the NN architecture and sections 3.2 and 3.3 presenting the NN models used to model both the forward and the inverse MR damper characteristics.

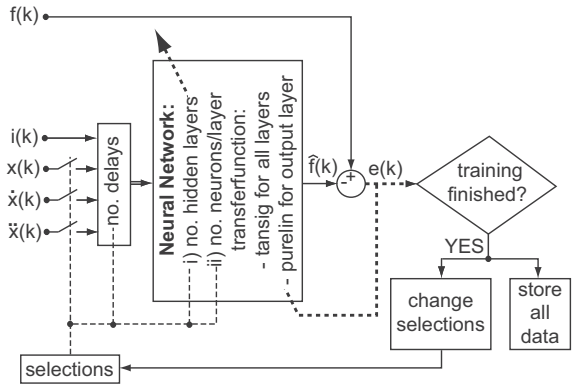

Figure 5. Procedure to find suboptimal NN architecture.

3.1. NN architecture

The modelling of a given system using the NN tool requires basically three steps: (a) measurement of the input and output states of the system under consideration, (b) choosing the architecture of the particular NN and (c) training the chosen architecture with the measurement data. The NN architecture is characterized by:

- What states are used as input.
- How many previous values of the input states are used.
- The number of hidden layers and neurons per layer.
- The transfer function of each layer.

Because of the large variety of modelling parameters, the trial and error method is often applied to find an NN architecture with acceptable modelling errors. Using the trial and error approach the training yields the best parameters for the chosen NN architecture, but not necessarily the best NN architecture with the best parameters. In the present work, a semi-systematic approach is used to obtain a near optimal NN architecture. The procedure is illustrated schematically in Fig. 5. A number of NN are trained to model the forward MR damper behaviour with the current records and one, or several, of the time histories for displacement, velocity and acceleration as input states. The number of previous states, the number of hidden layers and neurons are also varied. For all hidden layers the tangent sigmoid function is chosen as transfer function, while the linear transfer function is chosen for the output layer. All trained NN candidates are determined by the Levenberg-Marquardt optimization method, using the $error(k)$ between the target force

$f(k)$ and the estimated force $\hat{f}(k)$ by back propagation. When the training is finished, the individual NN architecture is stored and a new NN architecture is trained for different input properties. After all possible combinations of input data have been used for training of the NN architecture, the particular NN architecture with the smallest modelling error is identified as the best NN architecture, and stored for subsequent analyses. This systematic optimization strategy shows the following trends:

1. Velocity and damper current are mandatory input states. This is also confirmed by the large number of parametric MR damper models that are based on velocity and current as input states (Dominguez et al 2004, Maslanka et al 2007, Aguirre et al 2010, Weber et al 2011, Weber and Boston 2011b).
2. Using acceleration as additional input seems to increase the noise in the estimated force without improving the model accuracy.
3. Using displacement as additional input does not decrease the modelling error. This can be explained by the fact that the velocity is determined from displacement by Eq. (1) and because the rotary MR damper has no accumulator and therefore no significant stiffness component.
4. Using both displacement and acceleration as additional input has no influence on the modelling error.
5. It seems that including three previous values, two hidden layers and six neurons per hidden layer provides a suitable compromise between modelling error and computational effort.

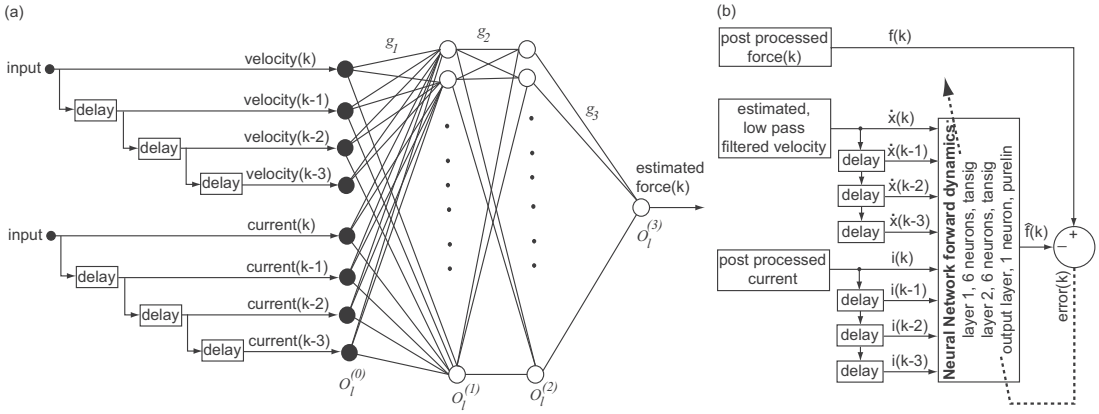

Figure 6. NN architecture of forward MR damper model and its training.

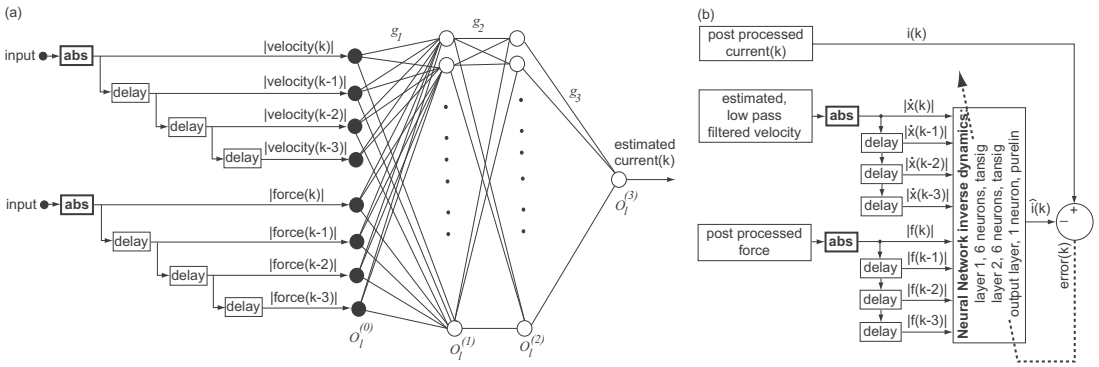

Figure 7. NN architecture of inverse MR damper model and its training.

3.2. Forward damper model

The NN architecture that is found to minimize the error of the forward MR damper model is based on velocity and damper current as input states, three previous values and two hidden layers of six neurons each. The architecture of the forward NN is shown in Fig. 6. The transfer function $g^{(j)}$ of the neurons of the two hidden layers are selected as a tangent sigmoid function, while the transfer function of the single output layer, i.e. layer 3, is selected as a linear function. If $N^{(j)}$ is the number of neurons in the j^{th} layer then $N^{(3)}=1$, since the output layer has only a single signal output. Let $O_l^{(0)}$ be the $R\times 1$ column vector comprising the signal inputs to the 1st hidden layer. In the present case $R=8$ because of the two input variables: velocity and current, both with a current state value and three previous values. The subscript l denotes the individual neurons of the particular layer. Let $O_l^{(j)}$ be the $N^{(j)}\times 1$ vector comprising the signal outputs of the j^{th} layer, which means that the output layer is represented by $O_l^{(3)}$. For the two hidden layers and the single output layer the output is computed as

$$O_l^{(j)} = g^{(j)}(w_l^{(j)} O_l^{(j-1)} + b_l^{(j)}), \quad j=1,2,3\ , \tag{2}$$

where $g^{(j)}$ is the tangent sigmoid function for the hidden connections with $j=1,2$, while it is the linear function for the output connection with $j=3$. The vector $w_l^{(j)}$ contains the weights of the neural connections, while $b_l^{(j)}$ is the bias vector of the j^{th} layer, which is zero in the present application. Each of the transfer functions operates on the respective element of the vector argument. Thus, the estimation of the damper force by the NN can be expressed as

$$\hat{f}(k) = NN\begin{bmatrix} \dot{x}(k) & \dot{x}(k-1) & \dot{x}(k-2) & \dot{x}(k-3) \\ i(k) & i(k-1) & i(k-2) & i(k-3) \end{bmatrix} \tag{3}$$

where $NN[...]$ represents the computation by the neural network. For feed forward neural network based forward dynamics modeling, the network output is $\hat{f}(k) = O_l^{(3)}$ whereby $\hat{f}(k)$ is the predicted force from the forward MR model at current time state *k*. The target of the forward neural network model is

$$T_l = f(k) \tag{4}$$

where $f(k)$ is the desired force, or in this case the measured force data, at current time state *k*. The network training was performed using the MATLAB® function *trainlm*. The network has been trained with the input-output data sets obtained from the experiments summarized in Table 1. For training of small-to-medium size networks, the Levenberg-Marquardt algorithm (LM) is fairly efficient. The performance index used for the training of the feed forward neural network is the sum of squares of the difference e_l between the desired target T_l and the actual network output $O_l^{(3)}$,

$$V(\mathbf{Z}) = \sum_{l=1}^{I} e_l^2 = \sum_{l=1}^{I} (T_l - O_l^{(3)})^2 \ , \tag{5}$$

where $\mathbf{Z}$ is a vector containing all network weights and bias values to be optimized, while q is the length of the data set. The LM algorithm updates the parameters based on minimization of the performance index V.

3.3. Inverse damper model

Fig. 7 shows the corresponding NN for the inverse damper model with velocity and damper force as input states, and desired damper current as the single output. In order to estimate the MR damper current $\hat{i}(k)$, the NN for the inverse model uses the actual and three previous values of the two input states,

$$\hat{i}(k) = NN\begin{bmatrix} |\dot{x}(k)| & |\dot{x}(k-1)| & |\dot{x}(k-2)| & |\dot{x}(k-3)| \\ |f(k)| & |f(k-1)| & |f(k-2)| & |f(k-3)| \end{bmatrix} . \tag{6}$$

For the feed forward neural network based inverse dynamics modeling of the MR damper, the network output is $\hat{i}(k) = O_l^{(3)}$ where $\hat{i}(k)$ is the predicted current from the inverse MR model. The target of the inverse neural model,

$$T_l = i(k) \tag{7}$$

is the desired damper current $i(k)$, which in this case is the experimentally measured data. The structure of the NN architecture is similar to that of the forward model. However, the output current can only take on positive values, irrespective of the sign of velocity and/or force. Therefore, the NN architecture for the inverse damper model is trained using the absolute values of the two input states. This approach helps to avoid negative spikes in the estimated current when tracking a desired damper force.

4. Model validation

The model validation is carried out for independent and experimentally determined time records. Sections 4.1 and 4.2 consider the NNs of the forward and inverse damper model, respectively, while section 4.3 demonstrates that the presented NNs are able to emulate pure viscous damping.

4.1. Forward model

The forward MR damper model is validated using the validation data sets 1b-19b listed in Table 1. Due to the large amount of validation data, the measured and simulated force displacement trajectories are compared for some selected tests. The selection is made such that the comparison considers all displacement amplitudes, frequencies and damper currents. Figs. 8 and 9 show the result for combinations of constant current values at different displacement amplitudes and driving frequencies. As seen from the figures the NN model is fairly accurate in predicting the forward dynamics of the MR damper. Figs. 10 and 11 show the results for half-sinusoidal current at different amplitudes and frequencies. As can be observed from these figures, the forward MR damper model is able to predict the main characteristics of the MR damper under consideration with fairly good accuracy. The strong current dependent yield force is captured well, the slope of the pre-yield region is estimated very accurately in all cases and the force response due to the aggregation and radial migration of particles (Boston et al 2010, Weber and Boston 2011b), which is visible by the rather slow force increase after the damper rod turns its direction, is also predicted satisfactorily. It is evident that all of the major damper characteristics are predicted significantly better for the half-sinusoidal current in Figs. 10 and 11 than for the constant current case in Figs. 8 and 9.

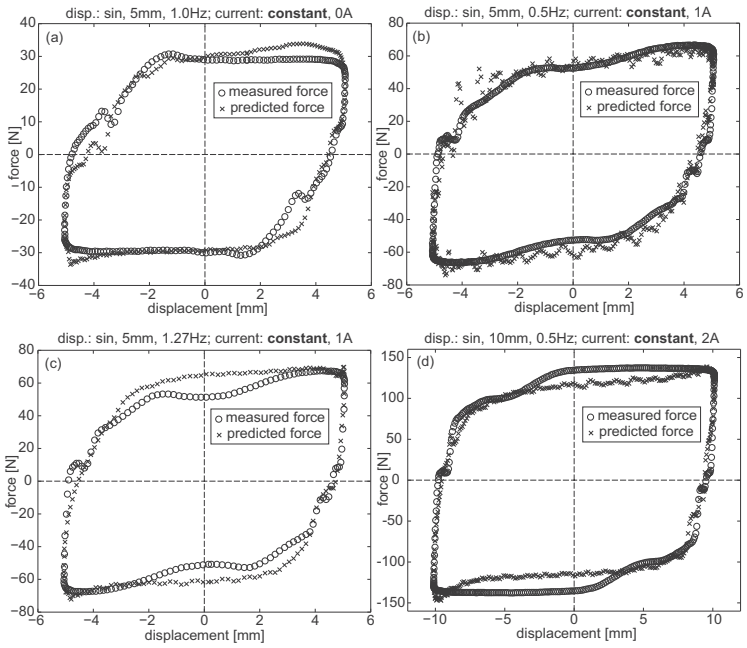

Figure 8. Validation of forward MR damper model for constant current of 0 A (a), 1 A (b, c) and 2 A (d) and different displacement amplitudes and frequencies.

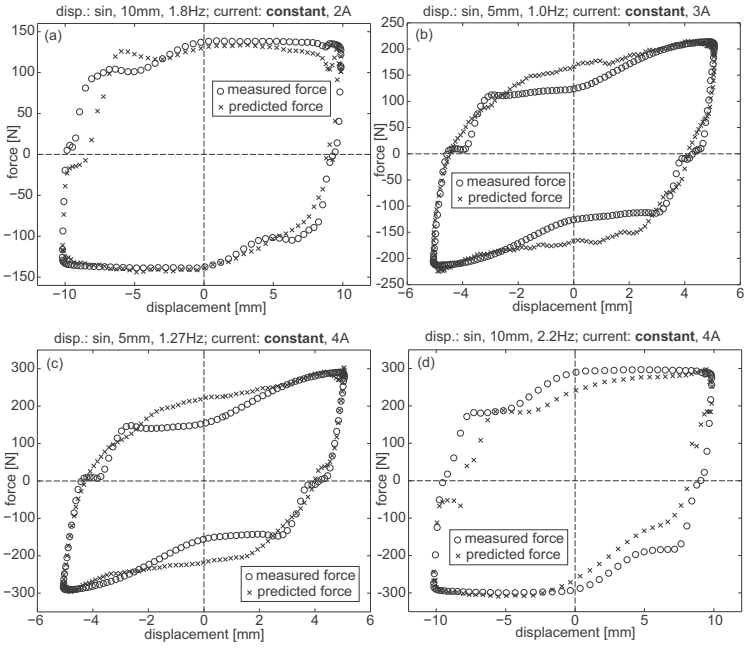

Figure 9. Validation of forward MR damper model for constant current of 2 A (a), 3 A (b) and 4 A (c, d) and different displacement amplitudes and frequencies.

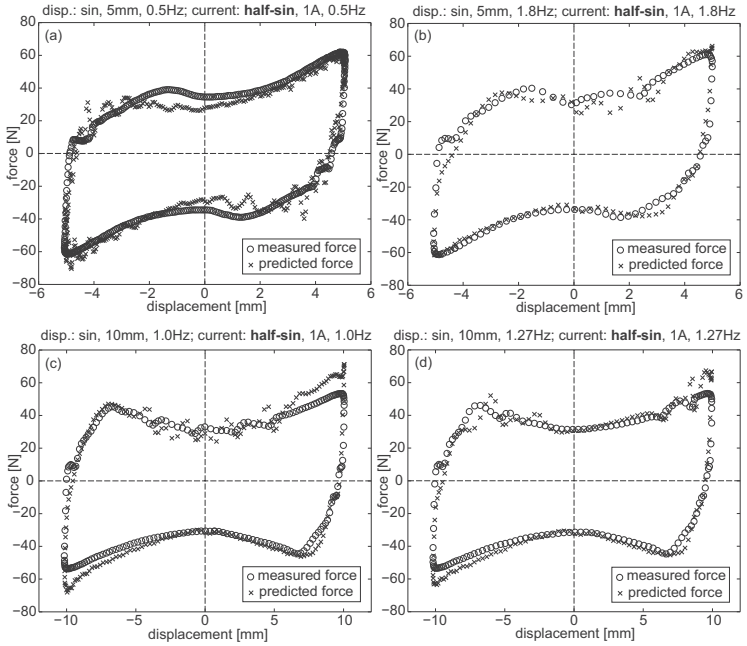

Figure 10. Validation of forward MR damper model for half- sinusoidal current at 1 A and different displacement amplitudes and frequencies.

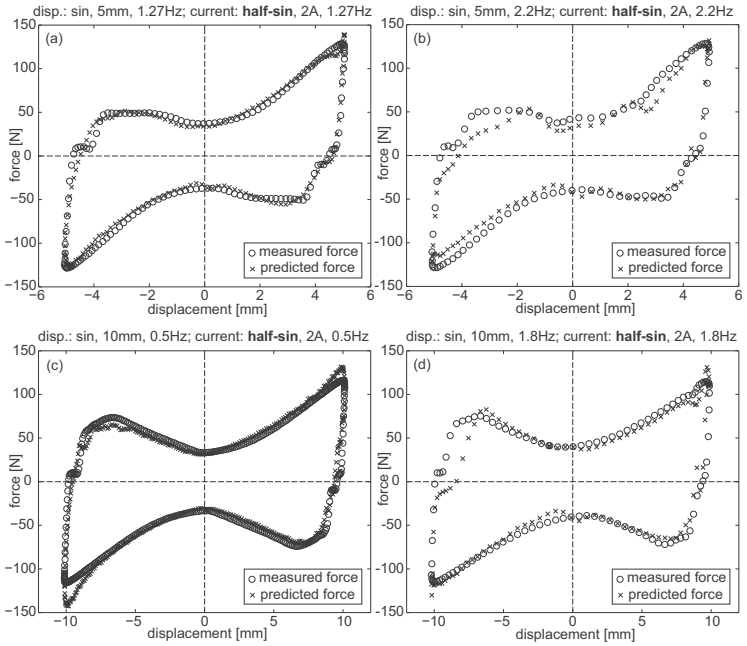

Figure 11. Validation of forward MR damper model for half-sinusoidal current at 2 A and different displacement amplitudes and frequencies.

4.2. Inverse model

The inverse MR damper model is also validated using the validation data sets 1b-19b in Table 1. The results for constant current, two different displacement amplitudes and four different displacement frequencies are shown in Figs. 12(a,b). The estimated current shows significant local spikes that might arise because the NN architecture has also been trained with half-sinusoidal current data or from the bearing plays of the damper rod joints at zero-crossing of the velocity. Although the bearing plays are on the order of 0.02 mm or less, force knocking effects cannot be avoided when the piston of the hydraulic machine turns its direction and thereby the damper force and velocity undergo zero-crossings. This hypothesis is partly verified by the fact that the spikes show the same frequency characteristics as the applied displacement. Similar results have also been reported in Wang and Liao (2005) and Metered et al (2009). This fact might indicate that the NN is fairly sensitive to high frequency signal inputs and has only little low pass behaviour. In contrast to the prediction of constant current, the prediction of the half-sinusoidal current is fairly accurate for different displacement amplitudes, frequencies and current amplitudes as shown in Figs. 12(c,d), 13 and 14. However, also this model validation test shows current spikes and therefore local modelling errors at each half period. Since these spikes occur later than the current maximum, which means after the hydraulic piston has turned its direction, the current spikes cannot result from the force knocking effects at zero velocity crossing, but may instead result from the Stribeck effect, which occurs at the transition between the pre- and post-yield regions. Despite the apparent modelling error due to the spikes of the estimated current, these spikes are rather small compared to e.g. the validation results presented in Wang and Liao (2005).

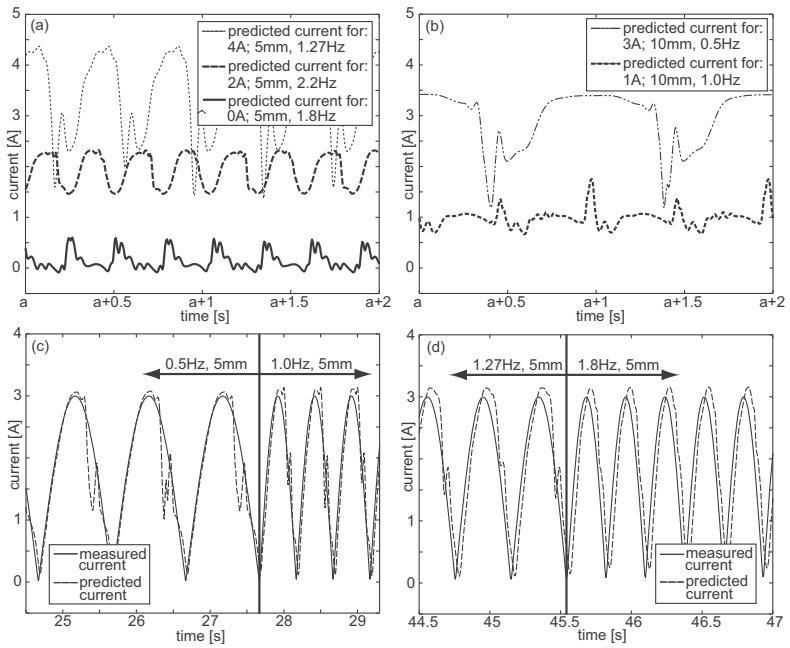

Figure 12. Validation of inverse MR damper model for constant current (a, b) and half-sinusoidal current at 3 A (c, d).

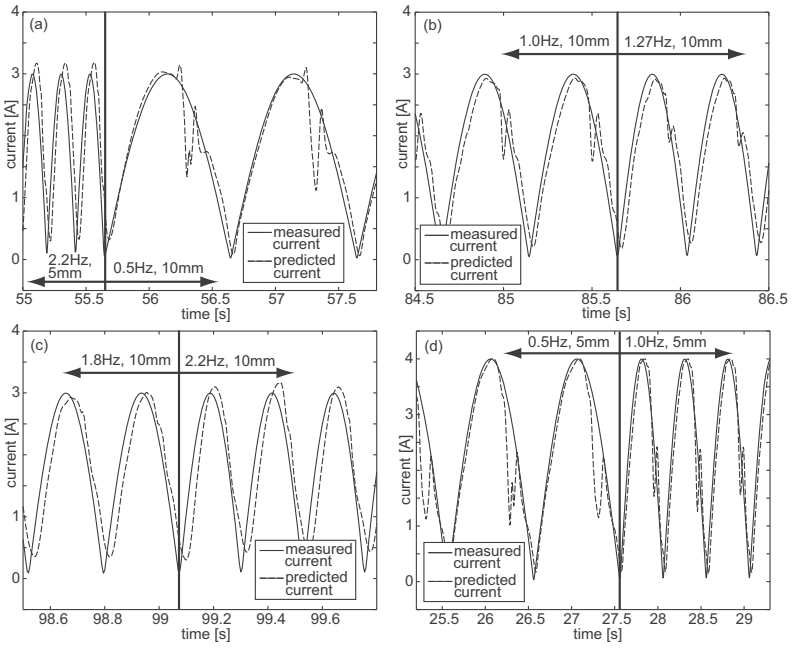

Figure 13. Validation of inverse MR damper model for half- sinusoidal current at 3 A (a-c) and 4 A (d).

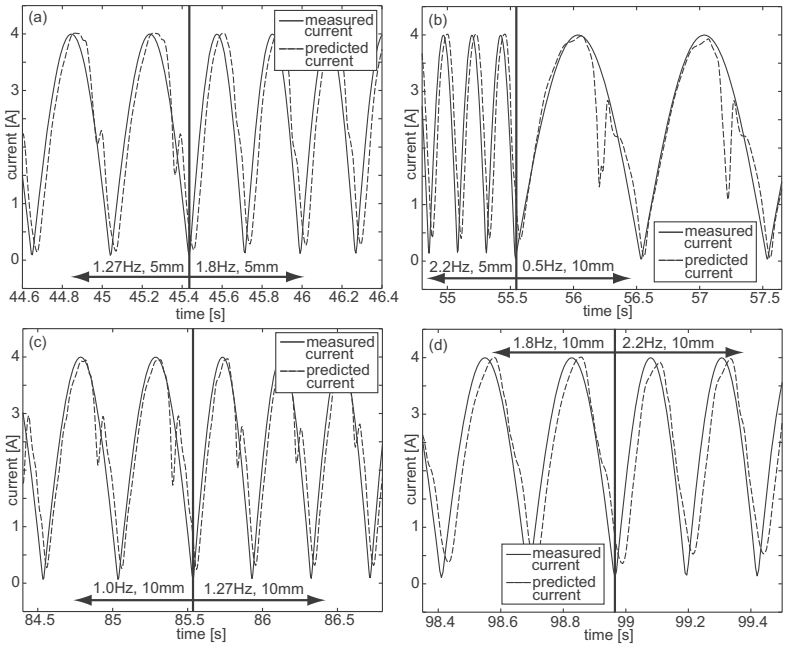

Figure 14. Validation of inverse MR damper model for half- sinusoidal current at 4 A (a-d).

4.3. Emulation of viscous damping using validated models

In this section the forward and inverse models are used to demonstrate how accurate pure viscous damping can be emulated by the rotary MR damper of the present study. Fig. 15(a) shows the flow chart of this simulation. The velocity of the MR damper is assumed to be pure sinusoidal. This is a reasonable assumption for damping of lightly damped structures, where the structural response is typically dominated by resonance at the frequency of the critical vibration mode and with a slowly varying amplitude envelope. The desired control force is the product of velocity and the viscous coefficient c. The damper velocity and the desired control force are used as the input states for the inverse MR damper model, which then estimates the corresponding damper current that is applied to the MR damper in order to generate a pure viscous force. This force is estimated using the forward MR damper model. If the NN for the inverse and the forward MR damper model are sufficiently accurate the simulated damper force should be comparable to the corresponding pure viscous damper force. The simulation results are shown in Figs. 15(b-d). The simulated current in Figs. 15(b) exhibits two significant spikes on top of the approximately half-sinusoidal time history. The first spike should not occur because the desired force decreases to zero. Hence, zero current

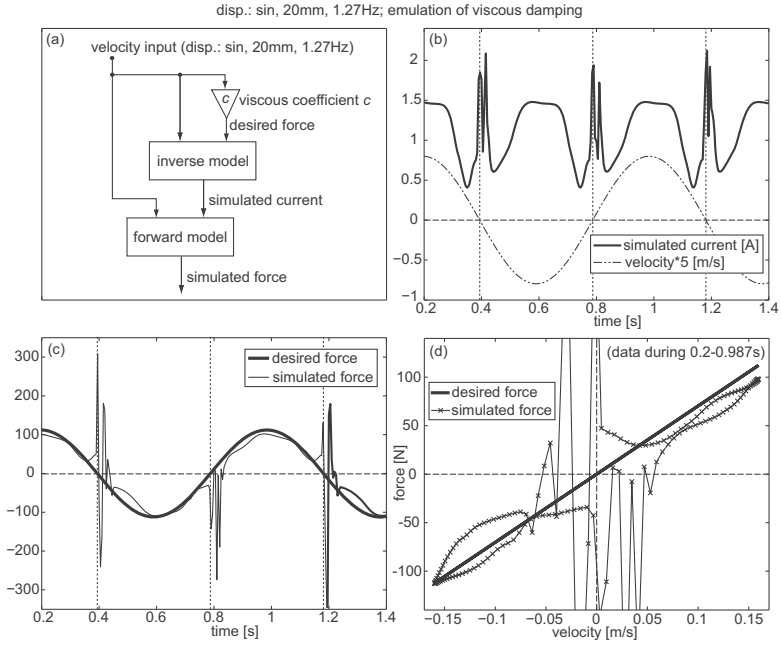

Figure 15. Simulated emulation of viscous damping: Flow chart (a), simulated MR damper current (b) and simulated MR damper force (c, d).

would be the best choice to track the desired viscous force as precise as possible. The second current spike occurs when the MR fluid is operated within the pre-yield region. This spike is therefore needed because the actual MR damper force at 0 A within the pre-yield region is smaller than the desired viscous force that increases rapidly at displacement extremes due to the elliptic force displacement trajectory of viscous damping (Maslanka et al 2007). When the MR fluid is operated in the post-yield region, the current shows approximately a half-sinusoidal behaviour because of the pure sinusoidal behaviour of the desired force, see Fig. 15(c). The main discrepancies are mainly due to the non-linear relation between yield force and current and the force response, arising because of the inherent migration and aggregation of the particles in the MR fluid (Weber et al 2008, Boston et al 2010). Despite the mediocre estimate of the current at zero velocity and the slightly overestimated current during the pre-yield region, the time history of the damper force in Fig. 15(c) and the force velocity trajectory in Fig. 15(d) demonstrate that pure viscous damping is in fact tracked fairly accurate at velocities larger than 0.05 m/s. The obtained results indicate that the NNs have

difficulties to accurately estimating the behaviour of the MR damper in the pre-yield region, which produces current spikes and thereby significant force tracking errors at small velocities. However, effective structural damping is mainly governed by the energy dissipation at large velocities, why these low-velocity current spikes are only of minor importance for most practical applications.

5. Summary and Conclusions

This paper describes the feed forward back propagation neural network based modelling of the forward and the inverse behaviour of a rotary MR damper using experimentally measured data for both training and validation. The measured data has been low pass filtered in order to remove high frequency signal parts that might have significant influence on the performance of the NN. The measured data comprising two displacement amplitudes, five frequencies and both constant and half-sinusoidal current has been combined to get a single sequential time history and afterwards down-sampled from 1000 Hz to 200 Hz to optimize the training of the NN architecture. An optimization procedure has been presented to identify the NN architecture that minimizes the error of the forward model. For training the procedure has been tested with combinations of measured displacement, velocity, acceleration and damper current as input states. Furthermore, the number of previous values of the input states and the number of hidden layers and neurons have been altered to obtain the best numerical fit. To limit the computational time of this numerical optimization, the transfer functions for the hidden and output layers were fixed to the tangent sigmoid function and the linear function, respectively. The present procedure demonstrates that the modelling error is not decreased significantly:

- if displacement and acceleration are taken as inputs in addition to velocity, and
- if substantially more than three past values of the inputs are taken into account, and
- if substantially more than two hidden layers of more than six neurons are considered.

The same NN architecture has also been used to model the inverse MR damper behaviour. In this case the damper current is the output, while the absolute values of damper force and velocity are used as input states. The introduction of the absolute values as the input to the NN minimizes the possibility of negative spikes in the estimated damper current when e.g. tracking a desired viscous force.

The trained forward and inverse MR damper models have been validated with measurement data that is independent of the training data at different displacement amplitudes and frequencies. The validation data comprises test records at two displacement amplitudes, five frequencies and both constant and half-sinusoidal damper current signals. The validation shows that the forward model is able to predict the MR damper force with high accuracy. Especially the force response due to the migration and aggregation of the MR fluid particles is captured well, and the slope of the force displacement trajectory in the pre-yield region is predicted accurately. The validation of the inverse MR damper model shows two particular characteristics. When the measurement data has been obtained from constant current, the predicted current records contain significant spikes with the same frequency as the damper displacement. This might therefore result from force knocking effects at displacement extremes due to the inherent bearing plays between the damper rod and the hydraulic machine, which are of the order of 0.02 mm. For these tests, only the mean value of the predicted current is accurate. In contrast, the prediction based on the half-sinusoidal current turns out to give more accurate results for all amplitudes and frequencies used in the tests. Nevertheless, also this validation shows current spikes which do not occur at the time of displacement extremes, but later. This indicates that these spikes are forced by the Stribeck effect, which occurs between the pre- and post-yield regions.

The validated forward and inverse MR damper models are finally used to simulate the emulation of viscous damping. The simulation shows that the inverse model overestimates the current in the vicinity of zero velocity, i.e. in the pre-yield region, while the output current is quite accurate within the post-yield region. As a result, the force tracking error is fairly large at small damper velocities, but considerably smaller at velocities where the MR damper is not operated in the pre-yield region.

This investigation shows that the NN technique can be used to model the inverse MR damper behaviour and thereby effectively solve the force tracking task with sufficiently small force tracking error.

Acknowledgement

The work is supported via the research grant *Damping of Flexible Structures by Smart Control of Semi Active devices* by the Danish Council of Research and Innovation. The authors also gratefully acknowledge the use of the testing facilities as well as the technical assistance of Empa, Swiss Federal Laboratories for

Materials Science and Technology, Dübendorf, Switzerland, and the technical support of the industrial partner Maurer Söhne GmbH & Co. KG, Munich, Germany.

References

Aguirre, N., Ikhouane, F., Rodellar, J., Wagg. D.J. and Neild, S.A. (2010), "Viscous and Dahl model for MR dampers characterization: A Real time hybrid test (RTHT) validation", *Proceedings of the 14th European Conference on Earthquake Engineering*, August 30 - September 03, 2010, Ohrid, Republic of Macedonia.

Boston, C., Weber, F. and Guzzella, L. (2010), "Modeling of a disk-type magnetorheological damper", *Smart Mater. Struct.,* **19** 045005.

Chang, C. and Roschke, P. (1998), "Neural network modeling of a magnetorheological damper", *Journal of Intelligent Material Systems and Structures*, **9**, 755-64.

Chang, C. and Zhou, L. (2002), "Neural network emulation of inverse dynamics for a magnetorheological damper", *Journal of Structural Engineering*, **128**, 231-9.

Christenson, R.E., Spencer, Jr.B.F. and Johnson, E.A. (2006), "Experimental verification of smart cable damping", *Journal of Engineering Mechanics*, **132**(3), 268-78.

Dominguez, A., Sedaghati, R. and Stiharu, I. (2004), "Modelling the hysteresis phenomenon of magnetorheological dampers", *Smart Mater. Struct.*, **13**, 1351-61.

Dominguez, A., Sedaghati, R. and Stiharu, I. (2006), "A new dynamic hysteresis model for magnetorheological dampers", *Smart Mater. Struct.*, **15**, 1179-89.

Ikhouane, F. and Dyke, S. (2007), "Modeling and identification of a shear mode magnetorheological damper", *Smart Mater. Struct.*, **16**, 605-16.

Jiménez, R. and Alvarez-Icaza, L. (2005), "LuGre friction model for a magnetorheological damper", *Journal of Structural Control and Health Monitoring*, **12**, 91-116.

Lee, H., Jung, H., Cho, S. and Lee, I. (2008), "An experimental study of semiactive modal neuro-control scheme using MR damper for building structure", *Journal of Intelligent material Systems and Structures*, **19**, 1005-15.

Li, H., Liu, M., Li, J., Guan, X. and Ou, J. (2007), "Vibration control of stay cables of the Shandong Binzhou yellow river highway bridge using magnetorheological fluid dampers", *Journal of Bridge Engineering*, **12**(4), 401-9.

Maslanka, M., Sapinski, B. and Snamina, J. (2007), "Experimental study of vibration control of a cable with an attached MR damper", *Journal of Theoretical and Applied Mechanics*, **45**(4), 893-917.

Metered, H., Bonello, P. and Oyadiji, S.O. (2009), "The experimental identification of magnetorheological dampers and evaluation of their controllers", *Journal of Mechanical Systems and Signal Processing*, **24**, 976-94.

Neelakantan, V.A. and Washington, G.N. (2008), "Vibration control of structural systems using MR dampers and a 'modified' sliding mode control technique", *Journal of Intelligent Material Systems and Structures*, **19**(2), 211-24.

Sahin, I., Engin, T. and Cesmeci, S. (2010), "Comparison of some existing parametric models for magnetorheological fluid dampers", *Smart Mater. Struct.*, **19**, 035012 (11pp).

Shulman, Z.P., Korobko, E.V., Levin, M.L. et al. (2006), "Energy dissipation in electrorheological damping devices", *Journal of Intelligent Material Systems and Structures*, **17**(4), 315-20.

Sims, N.D., Holmes, N.J. and Stanway, R. (2004), "A unified modelling and model updating procedure for electrorheological and magnetorheological vibration dampers", *Smart Mater. Struct.*, **13**(1), 100-21.

Soeiro, F.J., Stutz, L.T., Tenenbaum, R.A. and Neto, A.J. (2008), "Stochastic and hybrid methods for the identification in the Bouc-Wen model for magneto-rheological dampers", *Journal of Physics: conference series*, **135**, 012093.

Spencer, Jr.B.F. and Nagarajaiah, S. (2003), "State of the art of structural control", *Journal of Structural Engineering*, **129**(8), 845-56.

Tse, T. and Chang, C. (2004), "Shear-mode rotary magnetorheological damper for small-scale structural control experiments", *Journal of Structural Engineering*, **130**, 904-10.

Tsoukalas, L. and Uhrig, R. (1997), *Fuzzy and Neural Approaches in Engineering,* John Wiley & Sons Inc.

Wang, D.H. and Liao, W.H. (2005), "Modeling and control of magnetorheological fluid dampers using neural networks", *Smart Mater. Struct.*, **14**, 111-26.

Weber, F., Feltrin, F. and Distl, H. (2008), "Detailed analysis and modeling of MR dampers at zero current", *Structural Engineering Mechanics*, **30**, 787-90.

Weber, F. and Boston, C. (2011a), "Measured tracking of negative stiffness with MR damper", *Proceedings of the 5th ECCOMAS Thematic Conference on Smart Structures and Materials*, Saarbrücken / Germany, on July 6 - 8, 2011, on CD.

Weber, F., Boston, C. and Maslanka, M. (2011), "Adaptive TMD based on the emulation of positive and negative stiffness with MR damper", *Smart Mater. Struct*., **20**, 015012 (11pp).

Weber, F. and Boston, C. (2011b), "Clipped viscous damping with negative stiffness for semi-active cable damping", *Smart Mater. Struct.*, **20**, 045007 (13pp).

Weber, F., Feltrin, G. and Motavalli, M. (2005), "Passive damping of cables with MR dampers", *Journal of Materials and Structures*, **38**(279), 568-77.

Weber, F., Distl, H., Feltrin, G. and Motavalli, M. (2009), "Cycle energy control of MR dampers on cables", *Smart Mater. Struct.*, **18**(1), 015005.

Won, J. and Sunwoo, M. (2003), "Fuzzy modelling approach to magnetorheological dampers: forward and inverse model", *Journal of Systems and Control Engineering*, **20**, 1055-65.

Wu, W.J. and Cai, C.S. (2010), "Cable vibration control with a semiactive MR damper - numerical simulation and experimental verification", *Structural Engineering and Mechanics*, **34**(5), 611-23.

Xia, P. (2003), "An inverse model of MR damper using optimal neural network and system identification", *Journal of Sound and Vibration*, **266**, 1009-23.

Xiaomin, X., Qing, S., Ling, Z. and Bin, Z. (2009), "Parameter estimation and its sensitivity analysis of the MR damper hysteresis model using a modified genetic algorithm", *Journal of Intelligent Material Systems and Structures*, **20**(17), 2089-100.

Yang, G., Spencer, Jr.B.F., Jung, H.-J. and Carlson, J.D. (2004), "Dynamic modeling of large-scale magneto-rheological damper systems for civil engineering applications", *Journal of Engineering Mechanics*, **130**(9), 1107-14.

Yang, F., Sedaghati, R. and Esmailzadeh, E. (2009), "Development of LuGre friction model for large-scale magneto-rheological fluid damper", *Journal of Intelligent Material Systems and Structures*, **1** doi: 10.1177/1045389X08099660.

Ye, M. and Wang, X. (2007), "Parameter estimation of the Bouc-Wen hysteresis model using particle swarm optimization", *Smart Mater. Struct.*, **16**, 2341-49.

P2

(Journal paper)

Design and experimental verification of semi-active control with negative stiffness for MR dampers

Submitted
2011

Design and experimental verification of semi-active control with negative stiffness for MR dampers

F Weber[1,#], **S Bhowmik**[1,2] and **J Høgsberg**[2]

(1) Empa, Swiss Federal Laboratories for Materials Science and Technology, Structural Engineering Research Laboratory, Ueberlandstrasse 129, CH-8600 Duebendorf, Switzerland
E-mail: felix.weber@empa.ch

(2) Department of Mechanical Engineering, Technical University of Denmark, Lyngby 2800, Denmark
E-mail: s.bhowmik@mek.dtu.dk, jhg@mek.dtu.dk

(#) Author to whom any correspondence should be addressed.

Abstract

For external damping of flexible structures the introduction of negative damper stiffness in the damper force locally increases the deformation of the structure at damper position and thereby the energy dissipation in the external damper. For a suitable design of the negative stiffness and the damping forces this concept may improve the damping of the structure. The present paper considers both a linear control model, with a viscous term and a negative stiffness term, and a non-linear model composed of friction and negative stiffness. Expressions are derived for the calibration of these control models. However, the introduction of negative stiffness may produce active parts in the desired damper force, and in semi-active control these parts are typically clipped. The linear control model requires the clipping independent of the viscous and negative stiffness terms which may lead to a reduction in the attainable damping and an increase in high frequency noise in the structure. In contrast, the non-linear model does not need to be clipped if the friction force level is controlled in proportion to the damper displacement amplitude and balances the maximum negative stiffness force. The performances of both control strategies are verified by experiments, where a magnetorheological damper acts on a five storey shear frame structure. The tests show that negative damper stiffness can enhance the structural damping significantly compared to pure viscous damping. Due to the clipping, the linear model leads to smaller structural damping than theoretically expected and to additional high frequency components in the structure. In contrast, the non-linear model, which does not need to be clipped for proper choice of friction and stiffness, almost generates the theoretically expected structural damping and the high frequency components introduced by the non-linear friction force by the controlled magnetorheological damper are limited.

1. Introduction

Magneto-rheological (MR) dampers are commonly used for controlled vibration mitigation of civil engineering structures because they are fail safe and reliable due to their dissipative nature and residual force level at 0 A, and because proper semi-active control combines the advantages of active and passive damping, see e.g. [1]. For damping of stay cables the potential associated with controlled MR dampers has been investigated by simulation, laboratory and field tests in several research projects. A general overview can be found in the references [2-10]. Similarly, the vibration reduction of civil engineering structures -- such as buildings, bridges and models of these structures – by controlled MR dampers has been simulated and/or tested experimentally in [11-26]. Also, controlled MR dampers have been installed in tuned mass dampers [27-29] or in tuned masses [30, 31] in order to make these otherwise passive devices adaptive. Many different clipped active, semi-active and passive control laws have been tested and verified for MR dampers. Among these the so-called clipped optimal control schemes are presented in e.g. [2-4, 7], the clipped viscous

model with negative stiffness is investigated in e.g. [9], various semi-active algorithms have been proposed in [32, 33] and simple passive approaches such as controlled viscous damping, controlled friction damping and controlled energy dissipation have been proposed and analysed in [5], [2, 16, 34] and [8], respectively. For model-based control of semi-active dampers the real-time tracking of the desired damper force can be solved in different ways. The Heaviside step function – or on/off – approach requires the measuring of the actual MR damper force, as described in e.g. [35]. The force tracking can also be based on the inversion of sufficiently simple mathematical models, as for example the Bingham plasticity model [5, 9, 11]. Alternatively, more detailed and validated models can be used as observers, which has been demonstrated in [36-38] for the LuGre friction model. A mapping approach based on tests of the MR damper connected to a cable is presented in [8], neural network based force tracking approaches have been developed in [39-43] and also fuzzy logic [44] and other methods [45] have been adopted to capture the inverse dynamics of an MR damper.

In recent years, the structural damping due to the emulation of a negative stiffness force besides the damping force in the MR damper has been investigated in several research projects [4, 9, 32, 33, 46-49]. As described in [9], larger structural damping is achieved because the negative stiffness force increases the motion in the damper, which leads to an increase in energy dissipation per cycle in the damper when compared to for instance a pure viscous damper [51]. It has also been shown in [4, 9, 49] that clipped optimal control of a cable with a semi-active damper results in approximately the same control force behaviour as for simple clipped viscous damping with negative stiffness.

The aim of the present paper is to demonstrate and experimentally verify the influence of negative stiffness in the semi-active control of an MR damper. The tracking of the desired damper force by the MR damper is provided by a validated neural network with absolute values of damper velocity and desired damper force as network input, and the desired MR damper current as the output. Details on the training and validation of the neural network can be found in [39]. The benchmark damper model is the pure viscous damper, while the control laws of interest in the present study are the linear model with a viscous term and a negative stiffness term and the non-linear model with a friction term and a negative stiffness term. The non-linear approach has been introduced in [32, 33]. Based on a free approximate vibration analysis theoretical estimates are derived for the damper calibration associated with maximum modal damping ratio of the targeted vibration form. It is found by the theoretical results that a substantial increase in damping performance can be expected for the ideal linear control model. However, in a linear model negative stiffness produces active control forces, which must be clipped or truncated in a semi-active control environment. It is illustrated by simulations and experiments that this clipped linear model with negative stiffness improves the damping performance compared to the pure viscous damper. However, it is also indicated that the clipping yields a significant reduction in the performance compared to the theoretical predictions. On the other hand the friction force level and the negative stiffness component of the non-linear model are balanced so that in steady-state harmonic conditions clipping is avoided. Furthermore, the friction force level of the non-linear control model is adaptively changed according to the collocated response amplitude. This secures effective damping of the structure. Simulations and in particular experiments show that this non-linear model is not affected as much by clipping as the linear model, and it more or less provides the performance predicted by the theory. This shows that, although clipping of linear active control methods lead to improved semi-active damping compared to passive methods, the formulation of non-linear control strategies, which take the inherent properties of the MR damper into account, result in robust and effective damping of the flexible structure.

The outline of the paper is as follows. In Section 2 the general results for free vibrations of the structure with a local damper are reviewed. The details on this approach are presented in e.g. [50, 51]. These results are applied in Section 3 to derive the calibration of the various control strategies based on maximization of the modal damping ratio for the targeted vibration mode. These results show that the non-linear control results in an attainable damping ratio that is twice the value of pure viscous damping, while the linear control method with negative stiffness potentially leads to a very significant increase in modal damping. The performance of the control strategies is investigated in Section 4 by simulations and experiments, where a rotational MR damper is operating on a shear frame model structure. The experiments show that due to heavy clipping of the present linear model with negative stiffness the predicted efficiency is significantly reduced, while the performance of the adaptively controlled non-linear model is more or less maintained.

Section 4 also gives an overview of practical aspects related to the experiments, while the construction and validation of the numerical model for the shear frame structure is presented in Appendix A.

2. Damping of Structures

The discretized equations of motion for a flexible structure can be written in the classic matrix form

$$\mathbf{M}\ddot{\mathbf{x}} + \mathbf{C}\dot{\mathbf{x}} + \mathbf{K}\mathbf{x} = -\mathbf{v}f + \mathbf{f}_{ext} \tag{1}$$

where $\mathbf{x}$ contains the degrees of freedom, $\mathbf{M}$ is the mass matrix, $\mathbf{C}$ is the structural damping matrix and $\mathbf{K}$ is the stiffness matrix. The external damping is provided by the single damper force f, where the connectivity vector $\mathbf{v}$ represent the point of action of the damper force on the structure. The external loading is governed by the vector function $\mathbf{f}_{ext}$. The minus on the damper force implies that f in the theoretical derivations is considered as an internal force.

The calibration of the various semi-active control strategies presented in Section 3 is based on the maximization of the damping ratio of the targeted vibration mode. An explicit estimate of the modal damping ratio can be determined following the system reduction technique in [50, 51]. The characteristics of the system are governed by the free vibrations without structural damping. In the frequency domain the equation of motion (1) can be written as

$$\left(-\omega^2\mathbf{M} + \mathbf{K}\right)\bar{\mathbf{x}} = -\mathbf{v}\bar{f} \tag{2}$$

where $\bar{\mathbf{x}}$ and $\bar{f}$ are the frequency amplitudes of the response vector and damper force, respectively. In the frequency domain formulation it is convenient to formulate the damper forces as

$$\bar{f} = H(\omega)\bar{x} \tag{3}$$

introducing the frequency dependent damper function $H(\omega)$. The damper format is collocated, which means that the damper force is proportional to the energetically conjugate damper displacement, given in terms of the connectivity vector by $\bar{x} = \mathbf{v}^T\bar{\mathbf{x}}$. The frequency function in (3) is in general complex valued,

$$H(\omega) = \mathrm{Re}\left[H(\omega)\right] + i\,\mathrm{Im}\left[H(\omega)\right] \tag{4}$$

where i is the imaginary unit. The real value represents the stiffness component in phase with displacement, while the imaginary part represents the damping component out-of-phase with displacement and thereby in phase with velocity.

As demonstrated in [50] the modal response of the structure with the damper acting on the structure can be effectively represented by the two-component representation,

$$\bar{\mathbf{x}} = \mathbf{u}_0\bar{r}_0 + \mathbf{u}_\infty\bar{r}_\infty \tag{5}$$

where $\mathbf{u}_0$ is the vibration form of the target mode without the damper, while $\mathbf{u}_\infty$ is the corresponding vibration form with the damper link fully locked. The frequency amplitudes $\bar{r}_0$ and $\bar{r}_\infty$ represent the degrees of freedom of the two-dimensional subspace. The limiting vibration forms are illustrated in Fig. 1 for a five storey shear frame structure with the damper acting on the relative motion between the first floor and ground, see Fig. 1a. For this damper configuration the connectivity vector is $\mathbf{v} = [1,0,0,0,0]^T$.

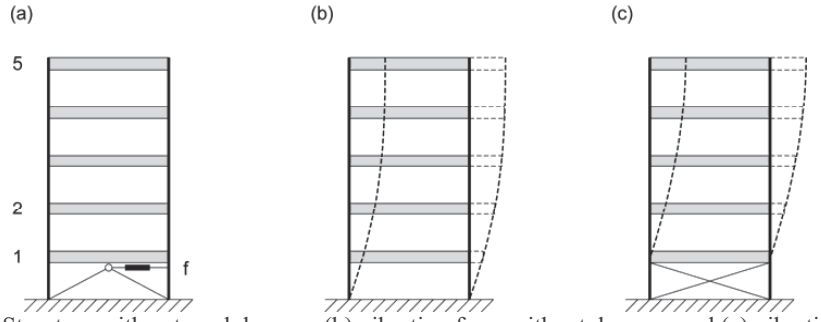

Figure 1. (a) Structure with external damper, (b) vibration form without damper, and (c) vibration form with damper link fully locked.

The two limiting vibration forms are governed by the eigenvalue problems derived from (2) when $H \to 0$ and $H \to \infty$, respectively. They are conveniently formulated as

$$\left(\mathbf{K} - \omega_0^2 \mathbf{M}\right)\mathbf{u}_0 = \mathbf{0} \qquad , \qquad \left(\mathbf{K}_\infty - \omega_\infty^2 \mathbf{M}\right)\mathbf{u}_\infty = \mathbf{0} \tag{6}$$

where the locked stiffness matrix is given as $\mathbf{K}_\infty = \lim_{g\to\infty}\left(\mathbf{K}_0 + g\,\mathbf{v}\mathbf{v}^T\right)$. In the following the vibration forms are normalized to unit modal mass, whereby the corresponding natural frequencies are determined directly from the corresponding modal stiffness as $\omega_0^2 = \mathbf{u}_0^T\mathbf{K}\mathbf{u}_0$ and $\omega_\infty^2 = \mathbf{u}_\infty^T\mathbf{K}_\infty\mathbf{u}_\infty$.

As demonstrated in e.g. [51] an approximate solution for the complex valued natural frequency ω can be obtained by projection of the equation of motion (2) on to the reduced subspace governed by the two-component representation in (5). The damping ratio $\zeta = \mathrm{Im}[\omega]/|\omega|$ represents the relative imaginary part of the complex natural frequency, and an explicit expression for the damping ratio of the target mode can be written as

$$\zeta \simeq \frac{\omega_\infty - \omega_0}{\omega_\infty + \omega_0}\,\frac{2\nu\,\mathrm{Im}\left[H(\omega_0)\right]}{\left(1+\nu\,\mathrm{Re}\left[H(\omega_0)\right]\right)^2 + \nu^2\,\mathrm{Im}\left[H(\omega_0)\right]^2} \tag{7}$$

where the magnitude of the natural frequency has been approximated by the mean value $|\omega| \simeq \left(\omega_0 + \omega_\infty\right)/2$. In (7) the damper function H is normalized by the parameter

$$\nu = \frac{\left(\mathbf{v}^T\mathbf{u}_0\right)^2}{\omega_\infty^2 - \omega_0^2} \tag{8}$$

The magnitude of the damper function H is in the following calibrated to provide maximum modal damping to the targeted mode. It follows from (7) that the attainable damping ratio depends on the particular relation between real and imaginary part of the damper function H. However, it is observed from (7) that a reduction in the damper stiffness (real part) implies a potential increase in the damping ratio. For linear control strategies the application of negative stiffness requires active control forces, while for semi-active control these active parts are simply clipped. In Section 4 it is demonstrated that with an adaptive control scheme, formulated specifically for an MR type damper, the clipping can be avoided and apparent negative stiffness will effectively improve the damping performance. The calibration with respect to maximum damping ratio is presented for the various control strategies in Section 3.

3. Calibration of control strategies

The present paper investigates and verifies several strategies for the control of the semi-active MR damper presented in Section 4.1 and [36]. For each of the following control strategies the calibration of the corresponding gain parameter is obtained by maximization of the damping ratio in (7) for the targeted vibration mode. Initially, the classic linear control format is considered, where a viscous and a stiffness term are simply added. Since this is a linear model the expression in (7) is directly applicable. Afterwards, the combination of pure friction and negative stiffness is considered. This is a non-linear model and an equivalent transfer function H_{eq} is derived and substituted into (7).

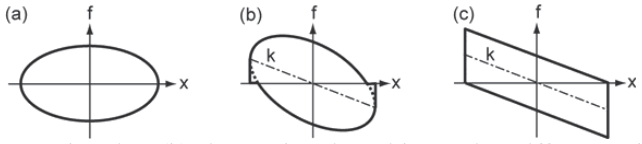

Figure 2. (a) Pure viscous damping, (b) viscous damping with negative stiffness, and (c) friction damping with negative stiffness.

3.1. Linear control model

A simple linear control strategy is composed of a viscous term with viscous parameter c and a stiffness term with stiffness k. This case is illustrated in terms of steady-state hysteresis loops in Fig. 2a,b, where the influence of negative stiffness results in a negative inclination of the ellipse, as indicated in Fig. 2c. In the time domain the damper force is given as

$$f = k\,x + c\,\dot{x} \tag{9}$$

while in the frequency domain it can be written as

$$\overline{f} = \left(i\omega c + k\right)\overline{x}\ . \tag{10}$$

Hereby the real and imaginary parts of the damper function are

$$\mathrm{Re}\left[H\right] = k \qquad , \qquad \mathrm{Im}\left[H\right] = \omega c \tag{11}$$

and substitution of the real and imaginary part into (7) gives

$$\zeta \simeq \frac{\omega_\infty - \omega_0}{\omega_\infty + \omega_0}\frac{2\nu\omega_0 c}{\left(1+\nu k\right)^2 + \left(\nu\omega_0 c\right)^2}\ . \tag{12}$$

The damper stiffness k is considered as a system parameter, while the viscous parameter c is the control gain. Thus, the viscous parameter which corresponds to maximum modal damping follows from $d\zeta / dc = 0$, which gives

$$c_{\max} = \frac{1}{\nu\omega_0} + \frac{k}{\omega_0} = \frac{\omega_\infty^2 - \omega_0^2}{\left(\mathbf{v}^T\mathbf{u}_0\right)^2} + \frac{k}{\omega_0}\ . \tag{13}$$

The subscript *max* simply indicates that the above result for the viscous parameter is derived based on maximum of the modal damping ratio. The solution for pure viscous damping is given by the first term in (13), which is recovered for $k = 0$. Thus, the influence of the apparent damper stiffness on the calibration of the viscous parameter appears in the form of an additive term. The attainable damping can be estimated by substitution of (13) into (12),

$$\zeta_{\max} \simeq \frac{\omega_\infty - \omega_0}{\omega_\infty + \omega_0}\frac{1}{1+\nu k}\ . \tag{14}$$

It is seen from this expression that a decrease in damper stiffness increases the estimated attainable modal damping. In linear damping or control the pure viscous model represents the most effective passive format, while in active control negative stiffness components might increase the effective damping of the targeted vibration mode. In semi-active control of an MR damper the active parts of the desired damper force associated with $k < 0$ must be clipped, whereby the derivations above are compromised. This is illustrated in Fig. 2b, where clipping leads to deviations from the inclined elliptical shape. The larger the magnitude of the negative stiffness, the larger then amount of clipping. However, as demonstrated by both simulations and experiments in Section 4 a reduction in stiffness actually results in a reduction of the structural response.

3.2. Non-linear control model

The non-linear model considered in the present paper is illustrated in Fig.2d, and corresponds to the superposition of a friction component and a negative stiffness component. As demonstrated by means of an evolutionary algorithm in [32] this model is optimal with respect to maximum modal damping for a taut cable. Similar findings are reported in [47] based on results obtained by LQR control. In the following an explicit expression is presented for the calibration of this model. In steady-state conditions with constant amplitude X it is convenient to formulate the damper force as

$$f = sign\left(\dot{x}\right)\alpha X + k\,x \tag{15}$$

where $\alpha > 0$ determines the friction force level at reversal ($\dot{x} = 0$), while the stiffness $k < 0$ represents the inclination of the force-displacement trajectory between reversals. As indicated in the previous section efficiency increases with reduced stiffness, while a pure dissipative model in (15) requires that $\alpha \geq |k|$. Thus, a suitable level of the friction force is obtained by the limit $k = -\alpha$. With this definition the force level at reversal is $\pm 2\alpha X$, and the balance between friction and negative stiffness implies that clipping of active forces is avoided in steady-state conditions. The calibration based on maximization of the damping ratio requires a linear model, or in this case an equivalent linear model. This can be written as

$$f = k_{eq}\,x + c_{eq}\dot{x} \tag{16}$$

where the equivalent stiffness k_{eq} and the equivalent viscous parameter c_{eq} are determined by averaging over a full vibration period when assuming pure sinusoidal motion, see e.g. [46]. The averaging procedure leads to

$$c_{eq} = \frac{4\alpha}{\pi\,\omega} \qquad , \qquad k_{eq} = -\alpha \tag{17}$$

whereby the equivalent viscous parameter secures the correct energy dissipation while the equivalent stiffness recovers the mean inclination of the hysteresis loop in Fig. 2d. In terms of the damper function the equivalent real and imaginary parts are

$$\mathrm{Re}\left[H(\omega)\right]_{eq} = -\alpha \qquad , \qquad \mathrm{Im}\left[H(\omega)\right]_{eq} = \omega c_{eq} = \alpha\frac{4}{\pi} \tag{18}$$

and substitution into the expression for the damping ratio in (7) gives

$$\zeta \simeq \frac{\omega_\infty - \omega_0}{\omega_\infty + \omega_0}\frac{2\nu\alpha\left(4/\pi\right)}{\left(1-\nu\alpha\right)^2 + \left(\nu\alpha\right)^2\left(4/\pi\right)^2}\ . \tag{19}$$

The calibration of α is obtained by the condition $d\zeta / d\alpha = 0$ which yields

$$\alpha_{\max} = \frac{1}{\nu\sqrt{1+\left(4/\pi\right)^2}} \simeq 0.62\frac{\omega_\infty^2 - \omega_0^2}{\left(\mathbf{v}^T\mathbf{u}_0\right)^2}\ . \tag{20}$$

Note that this result corresponds to the condition $\nu|H|=1$, which has been derived in [51] for linear control strategies with a single proportional gain parameter. Substitution into the expression for the damping ratio in (19) gives

$$\zeta_{\max} \simeq \frac{\omega_\infty - \omega_0}{\omega_\infty + \omega_0} \frac{4/\pi}{\sqrt{1+(4/\pi)^2}-1} \simeq 2.06 \frac{\omega_\infty - \omega_0}{\omega_\infty + \omega_0} \ . \tag{21}$$

This approximate result indicates that the attainable damping obtained the present non-linear control strategy is about twice the damping level from the pure viscous model given in (14) for $k=0$.

4. Experimental verification

The performance of the various control strategies presented in the previous section are in this section applied on a simple five storey shear frame structure by a rotary type MR damper. The properties of the experimental setup are initially described. The real-time tracking of the desired damper force is provided by a neural network and the aspects related to the implementation are briefly discussed. The results based on both simulations and experiments are finally presented.

4.1. Shear frame with MR damper

The experimental setup is shown in the photo in Fig. 3 and the schematic drawing in Fig. 4. A five storey shear frame structure is mounted on a shaking table, which is driven by a Schenk hydraulic cylinder. An MR damper is fixed to the shaking table and the MR damper rod applies the semi-active control force to the first mass of the 5 DOF system. Thus, the MR damper operates on the relative motion of the first floor, which corresponds to the damper configuration shown in Fig. 1 with connectivity vector $\mathbf{v}=[1,0,0,0,0]^T$. The MR damper under consideration is of the rotational type, with approximately 22 N residual force at 0 A and 300 N at the maximum current of 4 A. Details about the properties of the MR damper can be found in [36].

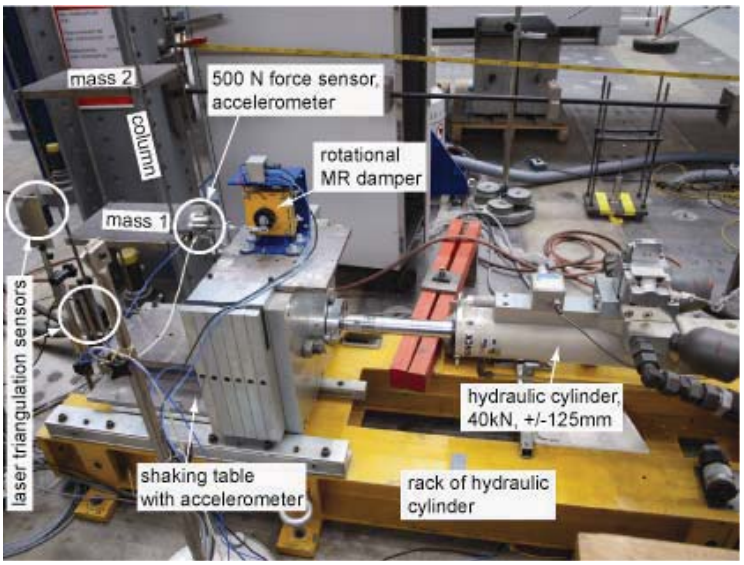

Figure 3. Shear frame structure on shaking table with MR damper acting on first floor.

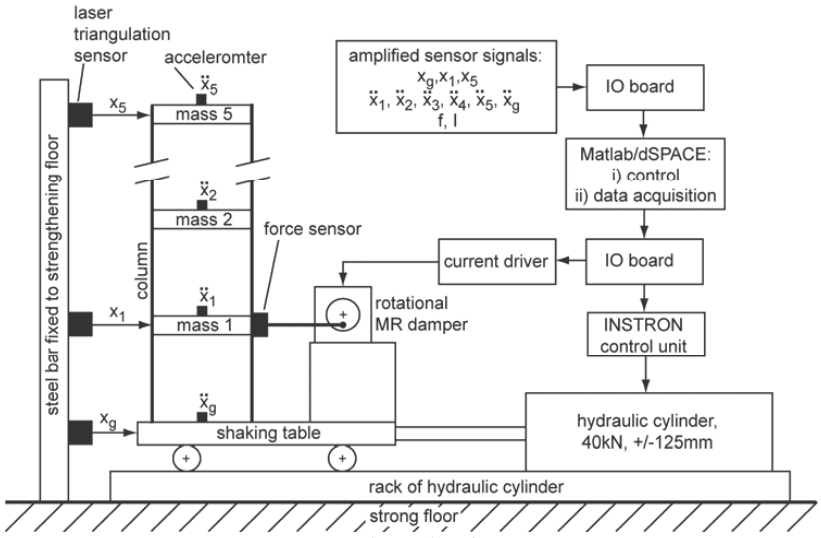

Figure 4. Schematic of test setup.

The accelerations of all five structure masses and the ground acceleration are recorded by accelerometers from PCB. Furthermore, the absolute displacement of the shaking table, the first floor and the fifth floor are recorded by laser distance sensors from Micro-Epsilon. Hereby, the acceleration and displacement of the MR damper motion can be obtained in real-time as the difference between the first floor acceleration and displacement and the acceleration and displacement of the shaking table, respectively. The control strategies require real-time estimation of the damper velocity. This is obtained via the measured relative displacement and acceleration through a Kinematic Kalman Filter (KKF), which is explained in detail in [52]. Finally, a force sensor is installed between the MR damper rod and the first floor plate in order to measure the damper force real-time. This force signal is used to determine the tracking error of the implemented control strategies.

The control of the MR damper is programmed and implemented in Matlab/dSPACE®, which is also used for the data acquisition. The real-time loop implemented for both the experimental and the numerical analysis is shown in Fig. 7, where the bottom part shows the control implementation. The output of this control algorithm is the desired damper force at a sampling frequency of 500 Hz. The desired current is converted into a command voltage, which is passed through the IO board to the KEPCO current driver, which provides a negligible tracking error of the desired MR damper current. The Matlab/Simulink® file of the controller is simultaneously used to compute the command voltage for the INSTRON control unit, which controls the motion of the hydraulic cylinder. In the simulations the response of the shear frame structure is determined by integration of the equation of motion in (1), where the MR damper force is governed by a Bouc-Wen type model. In Fig. 7 these elements are contained in the upper right part of the diagram.

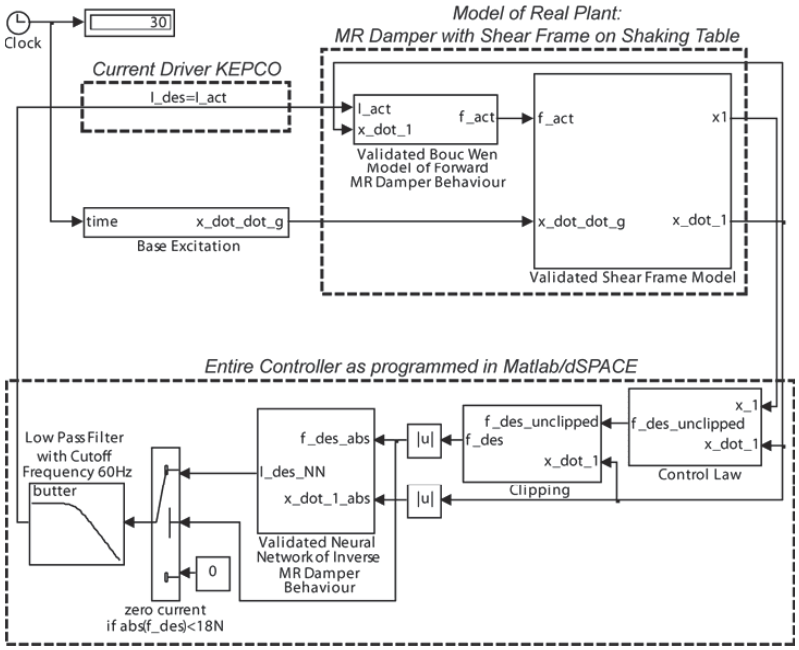

Figure 5. Real-time implementation of semi-active control in Matlab/dSPACE®.

4.2. Implementation of semi-active control

The semi-active control of the MR damper is contained in the bottom part of the diagram in Fig. 7. The input to the control part is the displacement and the velocity of the damper. In the experiments the displacement is directly measured, while the velocity is determined by the KKF. The box "Control Law" computes the desired damper force by (9) for the linear models and (15) for the non-linear model. In (15) the amplitude X is simply the magnitude of the most recent minimum or maximum in the damper displacement response. Thus, (15) is implemented as an adaptive scheme, which has been used in e.g. [34,46,53] for control of friction and MR type dampers.

The desired control is then passed on to the "Clipping" box, where any non-dissipative force components are simply removed. The logic is

$$f_{des} = \begin{cases} f_{des} & : \quad f_{des}\,\dot{x} \geq 0 \\ 0 & : \quad f_{des}\,\dot{x} < 0 \end{cases} \tag{22}$$

whereby any non-dissipative forces are set to zero.

The absolute values of the desired damper force and the damper velocity are passed on to the force tracking box, which is denoted "Validated Neural Network of Inverse MR Damper Behaviour" in Fig. 7. The model-based force tracking without feedback from a force sensor is in this case based on an inverse neural network model of the MR damper. The input to the neural network is the absolute value of the damper velocity $|\dot{x}|$ and the absolute value of the desired damper force $|f_{des}|$. The output of the neural network is the associated desired MR damper current I_{des}. The input-output relation of the neural network (NN) is modelled by the following architecture, where details can be found in [39],

$$I_{des}(j) = NN\begin{bmatrix} |\dot{x}(j)| & |\dot{x}(j-1)| & |\dot{x}(j-2)| & |\dot{x}(j-3)| \\ |f_{des}(j)| & |f_{des}(j-1)| & |f_{des}(j-2)| & |f_{des}(j-3)| \end{bmatrix}. \tag{23}$$

It is seen that the present values at time step j and values at only three previous time steps are needed for sufficiently accurate tracking of the desired damper current. The neural network approach in (23) uses the absolute values of the relative velocity and the desired force to estimate the MR damper current because the output current must always be a positive quantity. And as demonstrated in [39] the use of the absolute values of the input signals reduces the possibility of negative output current and thereby undesirable spikes in the actual damper force. A systematic derivation of the neural network architecture (23), the associated training with real measurement data of the present MR damper and the model validation are described in greater detail in [39].

As seen in Fig. 7 the output current I_{des} from the inverse neural network model is passed through a switch, where the desired damper current is truncated, so that

$$I_{des} = \begin{cases} I_{des} & : \ |f_{des}| \geq f_{res} \\ 0 & : \ |f_{des}| < f_{res} \end{cases} \tag{24}$$

where a conservative choice of residual force is $f_{res} = 18\,\mathrm{N}$. This truncation reduces the control force tracking error from to the modelling errors in the neural network in (23) at small force levels. The truncated desired damper current in (24) is low-pass filtered before it leaves the control part in Fig. 7 and is passed on to the current driver. The low pass filter is a Butterworth filter with cut-off frequency at 60 Hz, which effectively reduces the noise level in the desired current signal. The controller runs at 200 Hz sampling frequency, which corresponds to the sampling rate used for training of the neural network. It should be noted that in the simulation zero current tracking error is assumed. This means that the Bouc-Wen model is controlled directly by I_{des}. In the experiments the KEPCO current driver is used to track the desired current, which is sufficiently accurate to at least guarantee negligible tracking errors so that $I_{act} \approx I_{des}$.

The shaking table is driven by the hydraulic cylinder and the acceleration record of the shaking table $\ddot{x}_g = \ddot{x}_g^{meas}$ is measured by an accelerometer. In the simulations this measured acceleration signal is then used as excitation in the equation of motion (1), whereby the load vector can be written as

$$\mathbf{f}_{ext} = -\mathbf{M}\mathbf{1}\ddot{x}_g \qquad , \qquad \mathbf{1} = \left[1,1,\ldots,1\right]^T \tag{25}$$

As in all experiments noise is an inherent problem which should be eliminated as much as possible. In the present experiments two main sources for noise are observed:

a) One source is the high frequency noise in the damper velocity, which is generated when the desired damper force moves from the region $f_{des} < f_{res}$, where it cannot be tracked, to the region $f_{des} \geq f_{res}$, where it can suddenly be tracked by the neural network. This transition involves a sudden release of the damper, which introduces high frequency parts in the velocity signal. Note that this source exists in both simulations and experiments.

b) Another source is the measurement noise, which only exists in the experimental data. The input to the neural network in (23) is the measured damper velocity $\dot{x}$ and the desired force f_{des}, which both include measurement noise and thereby evoke a noisy current I_{des}.

4.3. Calibration of control strategies

In the present paper three control strategies are investigated for the semi-active MR damper:

a) Pure Viscous Damping (VD) with $k = 0$.

b) Viscous damping with negative stiffness (VDNS) with $k < 0$.

c) Friction damping with negative stiffness (FDNS).

The first two linear models are given in (9), while the friction model with negative stiffness is determined by the expression in (15). It should of course be noted that all strategies are clipped and truncated according to the diagram in Fig. 7. Since negative stiffness in the linear model VDNS results in active force components, it is expected that this model is clipped extensively. The non-linear FDNS also contains a negative stiffness component. However, the friction term is adaptively scaled with respect to the response amplitude X, and the stiffness term is balanced by $\alpha = -k$. This means that clipping is effectively reduced by the non-linear control model. The model calibration of the shear frame structure is described in Appendix A, and based on the estimated mass and stiffness matrix the two limiting frequencies and the modal scaling parameter associated with the first vibration mode are determined as

$$\omega_0 = 8.0\,\text{rad/s} \quad , \quad \omega_\infty = 10.4\,\text{rad/s} \quad , \quad \nu = 1.54{\cdot}10^{-4}$$

For the pure VD model the damper parameter (13) and the estimated damping ratio (14) are obtained as

$$c_{\max} = 650\,\text{Nm/s} \quad , \quad \zeta_{\max} = 0.13$$

For the VDNS model with $k = -4.5\,\text{kN/m}$ the values are

$$c_{\max} = 590\,\text{Nm/s} \quad , \quad \zeta_{\max} = 0.43$$

It should be noted that the apparent stiffness of the bottom storey is approximately 9.5 kN/m, and the magnitude of the negative stiffness component corresponds to about half of this inter-storey stiffness. The negative stiffness results in a slight reduction of the viscous parameter, while the estimate of the damping ratio indicates a significant increase in damping. For the non-linear FDNS model in (15), which is composed of friction and negative stiffness, the damper parameter is determined by (20) and the corresponding estimate of the damping ratio is given in (21),

$$\alpha = 4\,\text{kN/m} \quad , \quad \zeta_{\max} = 0.27$$

It is observed that the value of α is of the same order of magnitude as the negative stiffness component used for VDNS. The estimated damping ratio by the non-linear control model is a factor two larger than for pure viscous damping, but not nearly as high as for the VDNS. However, as indicated by the experimental and numerical results presented in the following the clipping of the active parts of the linear VDNS leads to a significant deterioration of the expected performance and thus a change in the calibration. Because the non-linear FDNS is adaptively controlled proportional to the response amplitude the clipping is significantly reduced and the expected performance is almost recovered in the experiments, as demonstrated in the following sections.

4.4. Force tracking

The force tracking error is in this case illustrated for the pure VD in Fig. 6. The results are for a maximum force level of approximately 60 N, which is a typical value for the first mode of the present shear frame structure. Figures 6a,b show the force tracking and the corresponding current signal for the experiment, while Figs. 6c,d show the similar results for the simulations. It is seen that the force tracking error in the experiment is slightly larger than in the simulation, which is mainly due to measurement noise in the collocated velocity which generates a noisy current. Note that because the MR damper behaves as a low-pass filter the actual damper force is not as noisy as the damper current. By comparison with the simulations in Fig. 6c it is found that the noise level in the experimental record in Fig. 6a is acceptable. Both time histories show the regions of the residual force that constrains the force tracking. Within these regions zero current is applied in order to minimize the force tracking error.

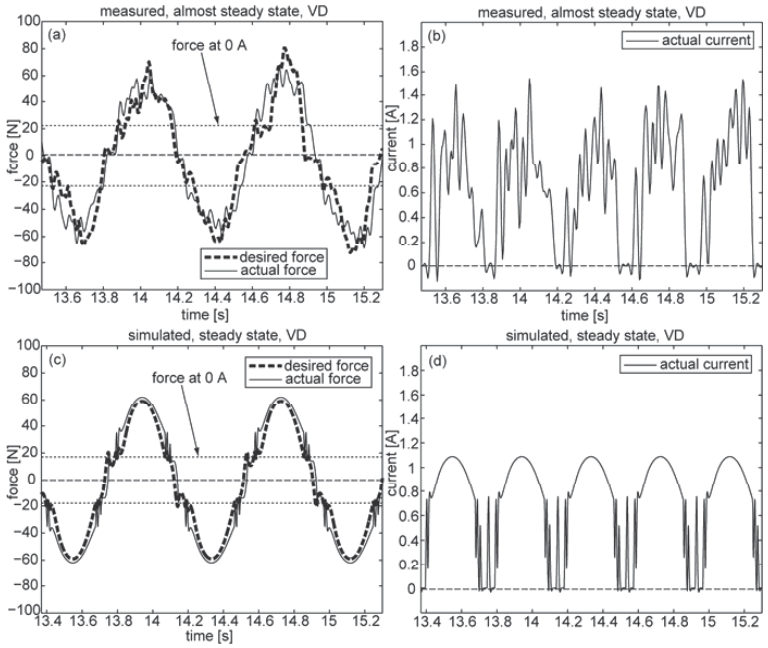

Figure 6. Measured (a,b) and simulated (c,d) force tracking of viscous damper force.

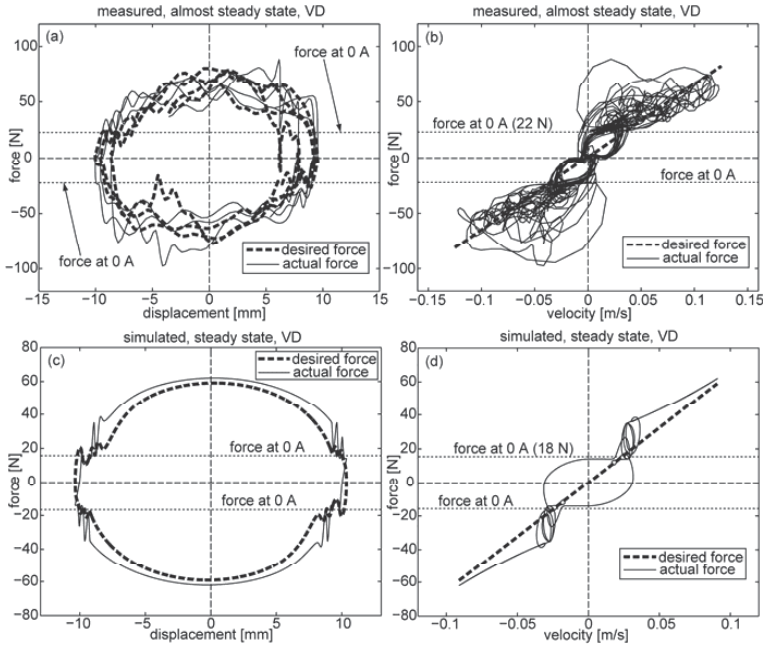

Figure 7. Measured (a,b) and simulated (c,d) force-displacement and force-velocity trajectories for pure VD.

4.5. Steady-state response

The performance of the control strategies for the rotational MR damper is assessed at steady-state and harmonic conditions and by free vibration decay. For the pure VD the force-displacement and force-velocity trajectories are shown in Fig. 7. It is seen that the force tracking is fairly accurate, where the main tracking

error is due to the residual force level at 0 A, where the MR damper basically operates as a friction damper. Thus, inside this region deviations from the ideal viscous ellipse are expected and observed. Furthermore, the level of experimental noise can be evaluated by comparison with Fig. 7c,d, which show the corresponding simulation results.

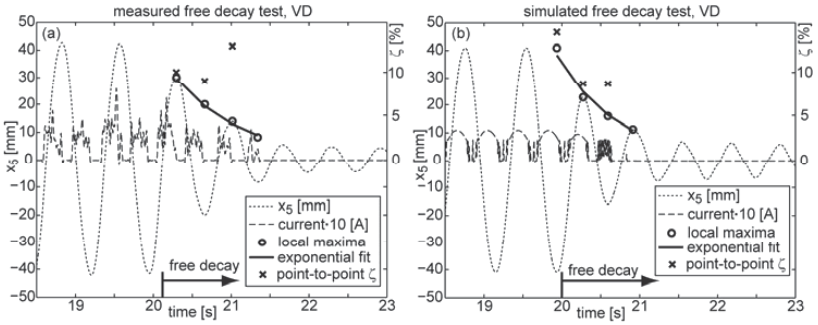

Figure 8. Steady-state response and free decay for pure VD.

Figure 8 shows the response of the top floor, where Fig. 8a is the experimental response and Fig. 8b is obtained by simulations. The amplitude and root-mean-square (*rms*) values are determined during steady-state conditions. As indicated in Fig. 8 the harmonic excitation by the shaking table is suddenly stopped and the free vibration decay provides an estimate of the damping ratio. Due to the fairly large damping the number of local peaks with non-zero MR damper current is quite limited. This means that the estimation of the damping ratio is quite difficult. The point-to-point estimate of the damping ratio by logarithmic decrement is shown by the crosses in Fig. 8, and an average value is used to generate the exponential fit also shown in the figure. The average damping ratio is given in Table 1, and for the VD it is 0.12, which is quite similar to the expected value of 0.13 determined in Section 4.3. Details on the estimation of the damping ratio can be found in [34]. The damper parameters presented in Table 1 are determined by trial-and-error, and represent the damper parameters that lead to the largest average damping ratio in the free vibration decay experiments. For the pure viscous damper the experimentally determined damper parameter agrees very well with the theoretical estimated determined in Section 4.3.

Table 1. Measured and simulated mean damping ratios and steady state responses.

	Control law calibration	VD c =650 Nm/s	Clipped VDNS c =250 Nm/s k =-4500 N/m	FDNS α =3000 N/m
measured	$\overline{\zeta}$ [%]	11.8	approx. 22	approx. 26
	$rms(x_5)$ [mm]	24.3	15.5	11.2
	$rms(x_1)$ [mm]	6.6	4.9	3.5
	$rms(\ddot{x}_5)$ [m/s^2]	1.81	1.25	1.02
	$rms(\ddot{x}_1)$ [m/s^2]	0.87	1.02	0.94
simulated	$\overline{\zeta}$ [%]	13.4	approx. 30	approx. 30
	$rms(x_5)$ [mm]	24.3 (*)	13.8	13.6
	$rms(x_1)$ [mm]	6.1	6.3	5.5
	$rms(\ddot{x}_5)$ [m/s^2]	1.60	0.98	1.16
	$rms(\ddot{x}_1)$ [m/s^2]	0.64	1.40	1.36

In addition to the mean damping ratio, the damping performance of the tested control concepts is also assessed by the root mean square of the steady state response at constant excitation amplitude and the resonance frequency of the first vibration mode. The *rms* is determined for the displacement of the first floor and the top floor. Furthermore, the *rms* values are computed for the associated acceleration records, where in particular the acceleration of the first floor relates to the high-frequency content in the damper force. Note that the undamped case is not reported, since the resonant response without the MR damper will lead to collapse of the shear frame structure. Thus, the pure VD represents the benchmark case for the two control models with negative stiffness.

Figure 9 shows the steady-state response and free vibration decay for VDNS. The results for the average damping ratio and *rms* are given in Table 1. By the trial and error procedure it has been found that due to the heavy clipping of the active parts of the damper force associated with the negative stiffness component the best viscous parameter is reduced from the theoretical value of $c_{\max} = 590\,\text{Nm/s}$ to $250\,\text{Nm/s}$. For this value the damping ratio is around $\overline{\zeta} = 0.2$, which is significantly smaller than the estimated value of more than 0.4. It is seen from the *rms* values that the introduction of negative stiffness improves the response reduction at both top and first floor. However, the increase in first floor acceleration indicates that the high-frequency content in the damper force also increased. This is furthermore verified by the curves in Fig. 9a, which show that the strong clipping at the points of reversal in the damper motion results in a very spiky damper response.

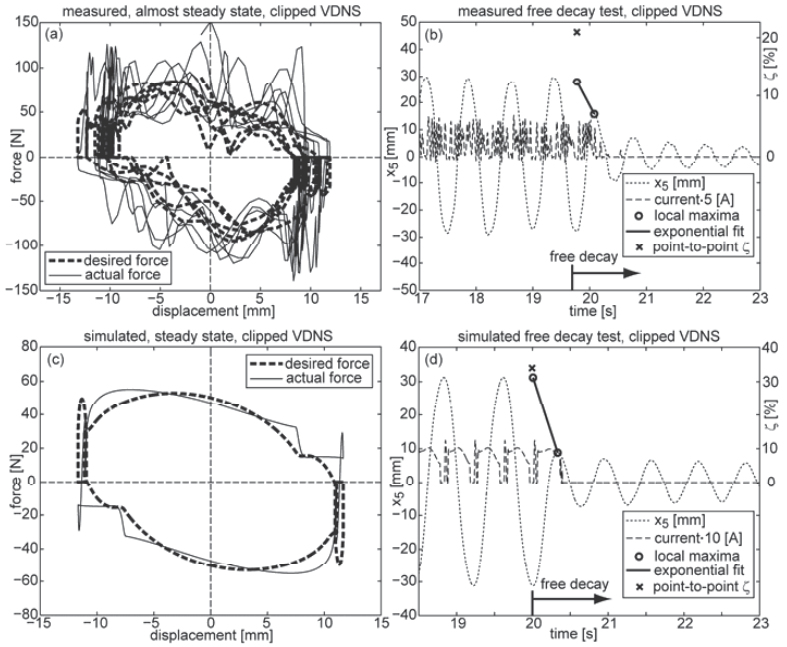

Figure 9. Steady-state response and free decay for clipped VDNS.

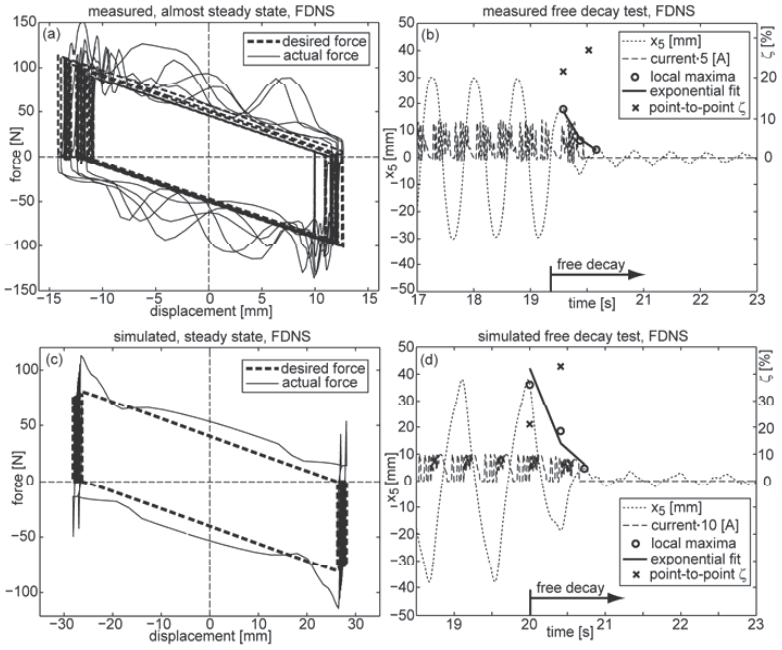

Figure 10. Steady-state response and free decay for FDNS.

Figure 10 shows the steady-state response and free vibration decay for the non-linear FDNS. It is seen that the tracking of the force-displacement trajectory in Fig. 10a is fairly good compared to the case of VDNS in Fig. 9a. As seen in Table 1 the actual damper value is $\alpha = 3000\,\mathrm{N/m}$, which is somewhat smaller than the estimated value of $4000\,\mathrm{N/m}$. The reason for that is that the attainable force level at 4 A of the MR damper is not large enough to realize the full potential of the FDNS for the present shear frame structure. And because the excitation level of the structure has been chosen so that the pure viscous damper is operating in the full force range, the damper parameter for the FDNS has simply been reduced to $\alpha = 3000\,\mathrm{N/m}$. However, the average damping ratio is approximately $\bar{\zeta} = 0.26$, which agrees well with the theoretical prediction of 0.27. This indicates that effective damping by semi-active devices, in this case an MR damper, requires control strategies that take the inherent characteristics of the particular damping device into account. In the present case the negative stiffness in (15) is balanced so that the damper force is zero at reversal, which is verified by the results shown in Figs. 10a,c. The *rms* values for the FDNS also show a significant reduction in the structural response, and the increase in the *rms* value of the first floor acceleration is significantly smaller compared to clipped VDNS and it is only slightly larger than the value for pure VD.

5. Conclusions

The present paper investigates the performance of semi-active control schemes with negative stiffness in connection with damping of flexible structures by an MR damper. The results and main conclusions are based on experimental results where a rotational type MR damper is operating on the first floor of a simple five storey shear frame model structure.

As discussed in the introduction the application of negative stiffness leads to an increase of the local motion over the damper, and combined with a proper calibration of the associated dissipative damper component this may result in improved energy dissipation and thereby structural damping. The increased motion at damper location might lead to an increase in local strains and stresses in the structure. However, as illustrated by the experiments performed in the paper the increase in damping, due to the introduction of negative damper stiffness, results in an overall reduction of the MR damper motion, which at least indicates

that for semi-active control the introduction of proper negative stiffness is beneficial for damping of flexible structures.

Two simple control models are considered for the MR damper: a linear model with a viscous term and a negative stiffness term, and a non-linear model with a friction term and a negative stiffness term. For the non-linear term the negative stiffness is balanced so that in harmonic steady-state conditions the damper force is entirely dissipative. In practice the force level of the friction force is scaled with the value of the most recent minimum or maximum in the damper displacement record. This adaptive procedure is fairly simple and also quite accurate in the case of resonant response, where the response amplitude is slowly varying. Both models are compared to the performance of the pure viscous damper model with vanishing damper stiffness.

The desired calibration and predicted damping ratio is based on the free vibration analysis of the structure in Section 2. The derived expression for the modal damping ratio indicates that the introduction of negative stiffness might lead to an increase in the damping ratio. This is verified by the experiments reported in Section 4. For the linear damper model a very large damping ratio is predicted by the theory when $\nu k \to -1$. However, for negative stiffness the linear model produces non-dissipative, and thereby active, control forces. In semi-active control these parts are typically clipped, which results in a deterioration of the theoretical findings. For small values of νk the influence of the negative stiffness is limited and the results for the pure viscous model are basically recovered, while for νk close to -1 the active parts dominate the damper force and clipping limits the performance of the damper. The best calibration is most certainly somewhere between these limits, and the present experiments apply $\nu k = -0.7$, which is a fairly large value. As observed during the experiments this value leads to a significant amount of clipping, and the best viscous parameter, found by simple trial-and-error, is less than half the value predicted by the theory. Furthermore, the damping performance determined by the free vibration decay tests is also significantly less than the theoretical estimate. This indicates that in connection with semi-active control care must be taken with respect to clipping of active parts when introducing negative stiffness in a linear damper model.

Since the friction part and the negative stiffness of the non-linear model have been properly balanced by $\alpha = -k$, the need for clipping in steady-state conditions is significantly reduced, and the calibration and corresponding damping performance of this model agree fairly well with the analytical results. In fact, the mayor discrepancy in the non-linear model seems to be due to the limited force level of the MR damper at 4 A, which implies that the desired damper force cannot be fully realized by the damper. In the experiments the actual value of α is therefore slightly reduced compared to the analytical estimate in Section 4.3. A modified version of the present non-linear model could be formulated to take this saturation into account, whereby the analytical calibration should agree better with the experimental results, obtained by trial and error. The formulation of such a modified damper model is definitely part of future work on the control of semi-active dampers.

The experiments and the experimental results are presented in Section 4, where it is explained how the control loop is implemented in Matlab/dSPACE®. A main issue in the control implementation is the real-time tracking of the desired control force. This is performed by a simple neural network, where the desired output current from the neural network is subsequently clipped to avoid non-dissipative forces, truncated to take care of the 0 A residual force and low-pass filtered to reduce the noise level. Despite these subsequent modifications of the neural network output the actual MR damper force is still rather spiky. Nevertheless, the measured structural damping agrees quite well with the simulated values. Thus, the neural network method represents an effective tool for the modelling of the inverse MR damper dynamics for real-time tracking of a desired damper force without feedback from a force sensor.

ACKNOWLEDGEMENTS

The work is supported by Empa, Swiss Federal Laboratories for Materials Science and Technology, Switzerland, by the research grant of the Danish Council of Research and Innovation, Denmark, and by the industrial partner Maurer Söhne GmbH & Co. KG, Germany.

6. Appendix A

The shear frame structure is shown in Fig1. 1 and 2, and in this appendix the procedure for the modelling of the structure is briefly described. The horizontal floor displacements represent the five degrees of freedom in $\mathbf{x} = \left[x_1, x_2, x_3, x_4, x_5 \right]^T$. The equation of motion is given (1), introducing the mass matrix $\mathbf{M}$, the damping matrix $\mathbf{C}$ and the stiffness matrix $\mathbf{K}$. These system matrices are determined by the following engineering type approach:

a) The mass matrix is assumed diagonal, where each component represents the weights of a single floor mass and four columns.

b) The shear frame is base excited (without MR damper) by a sine sweep, which determines the five natural frequencies and the corresponding mode shapes.

c) The free decay response of the five vibration modes estimates the modal damping ratios.

The diagonal elements of the mass matrix $\mathbf{M}$ are the sum of floor mass and column mass, which gives

$$\mathbf{M}(j, j) = m_{mass} + 4\, m_{column} = 5.95\,\mathrm{kg}$$

The natural frequencies and mode shapes are estimated from the base sine sweep of the structure. The response is recorded by the accelerometers on each floor and base, and Fig. A1a,c shows acceleration record for floors 1 and 4.

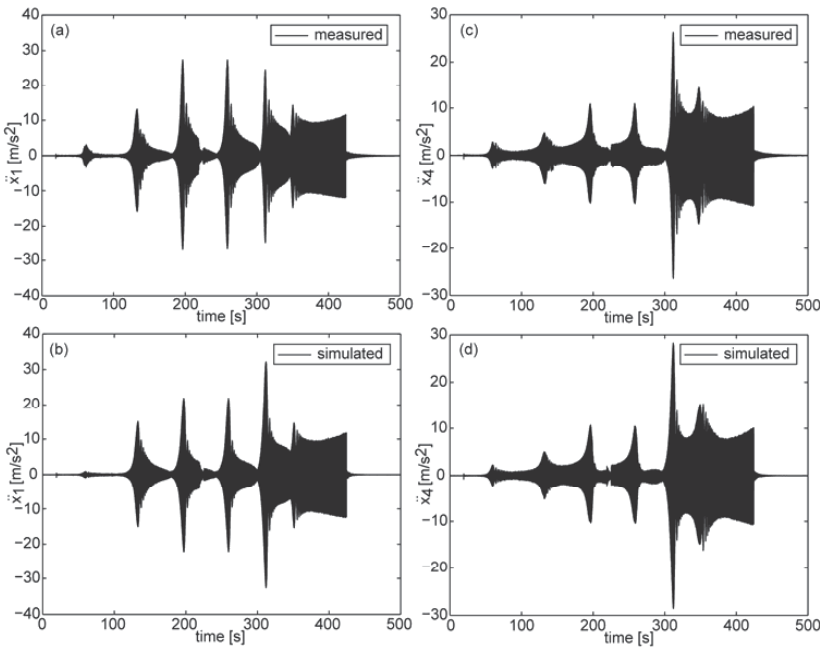

Figure A1. Acceleration record from base sine sweep: (a,c) experiments, (b,d) simulations.

From the sine sweep record and by the peaks in the associated power spectrum, Fig.A2, the experimental angular natural frequencies are determined as

$$\omega_1 = 8.0 \quad , \quad \omega_2 = 24.2 \quad , \quad \omega_3 = 38.4 \quad , \quad \omega_4 = 49.9 \quad , \quad \omega_5 = 58.3$$

all in rad/s.

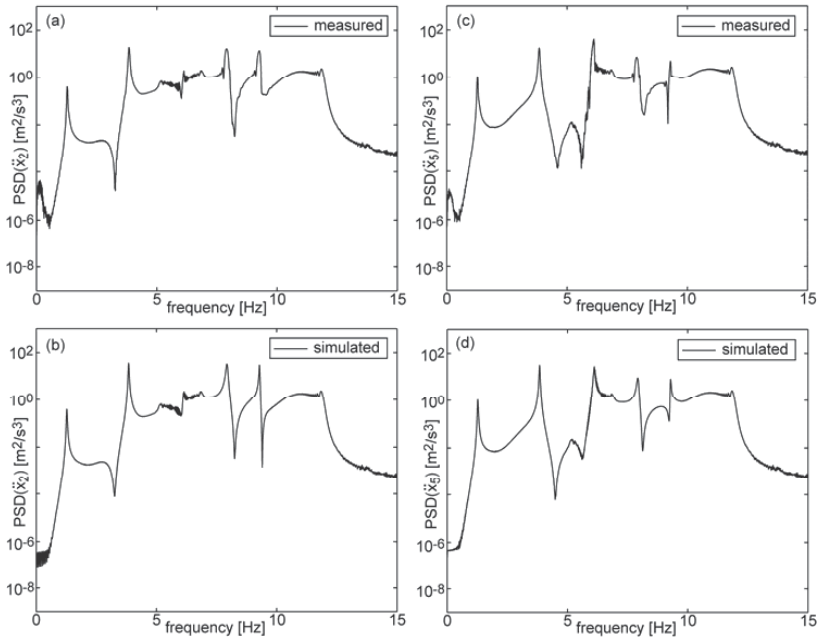

Figure A2. Power spectrum: (a,c) experiments, (b,d) simulations.

The associated vibration forms $\mathbf{u}_i$ are estimated from the measured transfer functions and by inspection of the correlation of the minima and maxima in the floor records. The estimated vibration forms are shown in Fig.A3a, and it is seen that they agree well with the analytical solution for the mode of an ideal shear frame structure

$$u_{i,j} = \sin\left(\pi i \frac{2j-1}{2n+1}\right) \tag{A1}$$

where i is the mode number, j is the floor number and n is the number of degrees of freedom. It is seen from Fig. A3a that the agreement between the estimated vibration forms and the analytical expressions is quite good. The measured mode shape vectors are collected in the matrix $\mathbf{U} = [\mathbf{u}_1 \ldots \mathbf{u}_n]$, whereby the modal mass matrix is determined as

$$\mathbf{M}_m = \mathbf{U}^T \mathbf{M} \mathbf{U} \tag{A2}$$

The associated diagonal modal stiffness matrix is determined by multiplication of the diagonal elements of the modal mass matrix with the square of the natural frequencies,

$$\mathbf{K}_m(j,j) = \omega_i^2 \, \mathbf{M}_m(j,j) \tag{A3}$$

The back transformation from modal to Cartesian coordinates gives the estimate of the stiffness matrix,

$$\mathbf{K} = \left(\mathbf{U}^T\right)^{-1} \mathbf{K}_m \left(\mathbf{U}\right)^{-1} . \tag{A4}$$

The stiffness matrix is symmetric but not necessary tri-diagonal, as for an ideal shear frame structure. However, it is found that the off tri-diagonal elements are small compared to the elements in the tri-diagonal band.

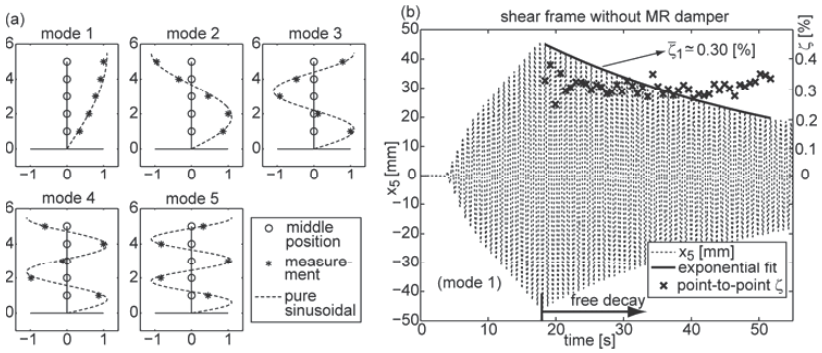

Figure A3. (a) Mode shapes and (b) free vibration decay of shear frame structure.

The modal damping is estimated by free vibration decay tests. Figure A3b shows the top floor displacement response when the structure is base excited at the natural frequency of the first mode. When the base excitation is stopped the structure performs free vibration decay in the particular vibration form. By point-to-point logarithmic decrement [34] the modal damping ratios are determined as

$$\zeta_1 = 0.0030 \quad , \quad \zeta_2 = 0.0024 \quad , \quad \zeta_3 = 0.0020 \quad , \quad \zeta_4 = 0.0015 \quad , \quad \zeta_5 = 0.0010$$

When using the estimated modal mass and modal stiffness matrices the diagonal elements of the modal damping matrix becomes

$$\mathbf{C}_m(j,j) = 2\,\zeta_j\,\sqrt{\mathbf{K}_m(j,j)\,\mathbf{M}_m(j,j)} \tag{A5}$$

where the off-diagonal elements are assumed to vanish. The damping matrix in Cartesian coordinates is determined as for the stiffness matrix in (A4). The natural frequencies and the damping ratios of the estimated model are determined by solving the damped eigenvalue problem associated with the homogeneous version of the equation of motion in (1). The natural frequencies are

$$\omega_1 = 8.0 \quad , \quad \omega_2 = 24.2 \quad , \quad \omega_3 = 38.4 \quad , \quad \omega_4 = 49.9 \quad , \quad \omega_5 = 58.3$$

while the modal damping ratios are

$$\zeta_1 = 0.0010 \quad , \quad \zeta_2 = 0.0040 \quad , \quad \zeta_3 = 0.0071 \quad , \quad \zeta_4 = 0.0055 \quad , \quad \zeta_5 = 0.0016$$

It is seen that good agreement is observed for the natural frequencies, while fairly large errors are observed for the modal damping. The sine sweep response is simulated based on the estimated system matrices, see Fig. A1b,d. Comparison with the experimental records indicates a deviation in the response magnitude, which follows from the errors in the damping. This is also observed for the power spectra in Fig. A2.

7. References

[1] Spencer Jr. B F and Nagarajaiah S, 2003, State of the Art of Structural Control, *Journal of Structural Engineering* **129**(8) 845-56.

[2] Christenson R E, Spencer Jr. B F and Johnson E A, 2006, Experimental Verification of Smart Cable Damping, *Journal of Engineering Mechanics* **132**(3) 268-78.

[3] Jung H J, Jang J E, Choi K M and Lee H J, 2008, MR fluid damper-based smart damping systems for long steel stay cable under wind load, *Smart Structures and Systems* **4**(5) 697-710.

[4] Li H, Liu M, Li J, Guan X and Ou J, 2007, Vibration control of stay cables of the Shandong Binzhou yellow river highway bridge using magnetorheological fluid dampers, *Journal of Bridge Engineering* **12**(4) 401-409.

[5] Maslanka M, Sapinski B and Snamina J, 2007, Experimental study of vibration control of a cable with an attached MR damper, *Journal of Theoretical and Applied Mechanics* **45**(4) 893-917.

[6] Weber F, Feltrin G and Motavalli M, 2005, Passive damping of cables with MR dampers, *Journal of Materials and Structures* **38**(279) 568-77.

[7] Weber F, Feltrin G and Motavalli M, 2005, Measured LQG Controlled Damping, *Smart Mater. Struct.* **14**(6) 1172-83.

[8] Weber F, Distl H, Feltrin G and Motavalli M, 2009, Cycle energy control of MR dampers on cables, *Smart Mater. Struct.* **18** 015005.

[9] Weber F and Boston C, Clipped viscous damping with negative stiffness for semi-active cable damping, *Smart Mater. Struct.* **20** (2011) 045007 (13pp).

[10] Wu W J and Cai C S, 2010, Cable vibration control with a semiactive MR damper-numerical simulation and experimental verification, *Structural Engineering and Mechanics* **34**(5) 611-23.

[11] Aguirre N, Ikhouane F, Rodellar J, Wagg D J and Neild S A, 2010, Viscous and Dahl model for MR dampers characterization: A Real time hybrid test (RTHT) validation *Proceedigns of the 14th European Conference on Earthquake Engineering*, August 30 - September 03, 2010, Ohrid, Republic of Macedonia.

[12] Cho S-W, Kim B-W, Jung H-J and Lee I-W, 2005, Implementation of Modal Control for Seismically Excited Structures using Magnetorheological Dampers, *Journal of Engineering Mechanics* **131**(2) 177-84.

[13] Choi K-M, Jung H-J, Lee H-J and Cho S-W, 2008, Seismic protection of base-isolated building with nonlinear isolation system using smart passive control strategy, *Structural Control and Health Monitoring* **15**(5) 785-96.

[14] Gattulli V, Lepidi M and Potenza F, 2009, Seismic protection of frame structures via semi-active control: modeling and implementation issues, *Earthquake Engineering and Engineering Vibration* **8**(4) 627-45.

[15] Gordaninejad F, Saiidi M, Hansen B C, Ericksen E O and Chang F-K 2002 Magneto-Rheological Fluid Dampers for Control of Bridges, *Journal of Intelligent Material Systems and Structures* **13**(2/3) 167-80.

[16] He W L, Agrawal A K and Yang J N, 2003, Novel Semiactive Friction Controller for Linear Structures against Earthquakes *Journal of Structural Engineering* **1291**(7) 941-50.

[17] Jung H-J, Spencer Jr. B F and Lee I-W, 2003, Control of Seismically Excited Cable-Stayed Bridge Employing Magnetorheological Fluid Dampers, *Journal of Structural Engineering* **129**(7) 873-83.

[18] Lee H J, Jung H J, Moon S J, Lee S K, Park E C and Min K W, 2010, Experimental Investigation of MR Damper-based Semiactive Control Algorithms for Full-scale Five-story Steel Frame Building, *Journal of Intelligent Material Systems and Structures* **21**(19) 1025-37.

[19] Lin Y Z and Christenson R, 2011, Real-Time Hybrid Test Validation of a MR Damper Controlled Building with Shake Table Tests, *Advances in Structural Engineering* **14**(1) 79-92.

[20] Lu K C, Loh C H, Yang J N and Lin P Y, 2008, Decentralized sliding mode control of a building using MR dampers, *Smart Mater. Struct.* **17**(5) 055006.

[21] Neelakantan V A and Washington G N, 2008, Vibration Control of Structural Systems using MR dampers and a 'Modified' Sliding Mode Control Technique, *Journal of Intelligent Material Systems and Structures* **19**(2) 211-24.

[22] Pradono M H, Iemura H, Igarashi A, Toyooka A and Kalantari A, 2009, Passively controlled MR damper in the benchmark structural control problem for seismically excited highway bridge, *Structural Control and Health Monitoring* 16(6) 626-38.

[23] Sun Q, Wu XH, Xue XM, Zhang L and Zhang L, 2010, Mechanics performance test of MR damper and its application in structural seismic response control, *International Journal of Applied Electromagnetics and Mechanics* **33**(3-4) 1493-1501.

[24] Yoshida O and Dyke S J, 2004, Seismic Control of a Nonlinear Benchmark Building Using Smart Dampers, *Journal of Engineering Mechanics* **130**(4) 386-92.

[25] Zapateiro M, Karimi H R, Luo N and Spencer B F, 2010, Real-time hybrid testing of semiactive control strategies for vibration reduction in a structure with MR damper, *Structural Control & Health Monitoring* **17**(4) 427-51.

[26] Zapateiro M, Karimi H R, Luo N S, Phillips B M and Spencer B F, 2009, Semiactive Backstepping Control for Vibration Reduction in a Structure with Magnetorheological Damper Subject to Seismic Motions, *Journal of Intelligent Material Systems and Structures* **20**(17) 2037-53.

[27] Cai C S, Wu W J and Araujo M, 2007, Cable Vibration Control with a TMD-MR Damper System: Experimental Exploration, *Journal of Structural Engineering* **133**(5) 629-37.

[28] Weber F, Boston C and Maślanka M, 201,1 Adaptive TMD based on the emulation of positive and negative stiffness with MR damper, *Smart Mater. Struct.* **20** (2011) 015012 (11pp).

[29] Wu W J and Cai C S, 2007, Theoretical exploration of a taut cable and a TMD system *Journal of Engineering Structures* **29** 962-72.

[30] Zemp R, de la Llera J C and Roschke P, 2011, Tall building vibration control using a TM-MR damper assembly: Experimental results and implementation, *Earthquake Engineering & Structural Dynamics* **40**(3) 257-71.

[31] Zemp R, de la Llera J C and Almazan JL, 2011, Tall building vibration control using a TM-MR damper assembly, *Earthquake Engineering & Structural Dynamics* **40**(3) 339-54.

[32] Boston C, Weber F and Guzzella L, 2009, Optimal semi-active damping of cables: evolutionary algorithms and closed-form solutions, *Smart Mater. Struct.* **18** 055006.

[33] Boston C, Weber F and Guzzella L, 2011, Optimal semi-active damping of cables with bending stiffness, *Smart Mater. Struct.* **20** 055005 (8pp).

[34] Weber F, Høgsberg J and Krenk S, 2010, Optimal tuning of amplitude proportional Coulomb friction damper for maximum cable damping, *Journal of Structural Engineering* **136**(2) 123-34.

[35] Dyke S J, Spencer Jr B F, Sain M K and Carlson J D, 1996, Modeling and control of magnetorheological dampers for seismic response reduction, *Smart Mater. Struct.* **5**(5) 565–75.

[36] Boston C, Weber F and Guzzella L, 2010, Modeling of a disk-type magnetorheological damper, *Smart Mater. Struct.* **19** 045005.

[37] Jiménez R and Alvarez-Icaza L, 2005, LuGre friction model for a magnetorheological damper, *Journal of Structural Control and Health Monitoring* **12** 91-116.

[38] Yang F, Sedaghati R and Esmailzadeh E, 2009, Development of LuGre Friction Model for Large-Scale Magneto-Rheological Fluid Damper, *Journal of Intelligent Material Systems and Structures* **1** doi: 10.1177/1045389X08099660.

[39] Bhowmik S, Weber F and Høgsberg J, 2011, Experimental calibration of forward and inverse neural networks for rotary type magnetorheological damper, *submitted for publication*.

[40] Karamodin A, Kazemi H, 2010, Semi-active control of structures using neuro-predictive algorithm for MR dampers, *Structural Control & Health Monitoring* **17**(3) 237-53.

[41] Sun W, Hu H and Weng J, 2006, Design, Testing and Modeling of a Magnetorheological Damper with Stepped Restoring Torque, *Journal of Intelligent Material Systems and Structures* **17**(4) 335-40.

[42] Wang D H and Liao W H, 2005, Modeling and control of magnetorheological fluid dampers using neural networks, *Journal of Smart Materials and Structures* **14** 111-26.

[43] Xia P, 2003, An inverse model of MR damper using optimal neural network and system identification, *Journal of Sound and Vibration* **266** 1009-23.

[44] Won J and Sunwoo M, 2003, Fuzzy modelling approach to magnetorheological dampers: forward and inverse model, *Journal of Systems and Control Engineering* **20** 1055-65.

[45] Tse T and Chang C, 2004, Shear-mode rotary magnetorheological damper for small-scale structural control experiments, *Journal of Structural Engineering* **130** 904-10.

[46] Høgsberg J, 2009, The role of negative stiffness in semi-active control of magneto-rheological dampers, *Struct. Control Health Monit.* DOI: 10.1002/stc.371.

[47] Iemura H and Pradono M H, 2009, Advances in the development of pseudo-negative-stiffness dampers for seismic response control, *Structural Control and Health Monitoring* **16**(7-8) 784-99.

[48] Li H, Liu M and Ou J P, 2008, Negative stiffness characteristics of active and semiactive control systems of stay cables, *Structural Control &Health Monitoring* **15**(2) 120-42.

[49] Ou J and Li H, 2010, Analysis of capability for semi-active or passive damping systems to achieve the performance of active control systems, *Structural Control and Health Monitoring* **17**(7) 778-94.

[50] Main J A and Krenk S, 2005, Efficiency and tuning of viscous dampers on discrete systems, *Journal of Sound and Vibration* **286**(1-2) 97-122.

[51] Høgsberg J R and Krenk S, 2006, Linear control strategies for damping of flexible structures, *Journal of Sound and Vibration* **293**(1-2) 59-77.

[52] Jeon S, Tomizuka M and Katou T, 2009, Kinematic Kalman Filter (KKF) for robot end-effector sensing, *Journal of Dynamic Systems, Measurement and Control* **131**(2) 021010 (8 pp).

[53] Weber F and Boston C, 2010, Energy Based Optimization of Viscous-Friction Dampers on Cables, *Smart Mater. Struct.* **19** 045025.

P3

(Conference paper)

Neural Network based semi-active control strategy for structural vibration mitigation with magnetorheological damper

Proceedings of the third ECCOMAS Thematic Conference on Computational Methods in Structural Dynamics and Earthquake Engineering
May 25–28, Corfu, Greece, 2010, 540–553

COMPDYN 2011
3rd ECCOMAS Thematic Conference on
Computational Methods in Structural Dynamics and Earthquake Engineering
M. Papadrakakis, M. Fragiadakis, V. Plevris (eds.)
Corfu, Greece, 25–28 May 2011

NEURAL NETWORK BASED SEMI-ACTIVE CONTROL STRATEGY FOR STRUCTURAL VIBRATION MITIGATION WITH MAGNETORHEOLOGICAL DAMPER

SUBRATA BHOWMIK

Department of Mechanical Engineering, Technical University of Denmark
403 Nils Koppens Allé, Lyngby, Denmark 2800
e-mail: subho@mek.dtu.dk

Keywords: Magnetorheological damper, neural network, semi-active control.

Abstract. *This paper presents a neural network based semi-active control method for a rotary type magnetorheological (MR) damper. The characteristics of the MR damper are described by the classic Bouc-Wen model, and the performance of the proposed control method is evaluated in terms of a base exited shear frame structure. As demonstrated in the literature effective damping of flexible structures is obtained by a suitable combination of pure friction and negative damper stiffness. This damper model is rate-independent and fully described by the desired shape of the hysteresis loops or force-displacement trajectories. The proposed neural network controller is therefore trained based on data derived from these desired force-displacement curves, where the optimal relation between friction force level and response amplitude is determined explicitly by simply maximizing the damping ratio of the targeted vibration mode of the structure. The neural network control is then developed to reproduce the desired force based on damper displacement and velocity as network input, and it is therefore referred to as an amplitude dependent model reference control method. An inverse model of the MR damper is needed to determine the damper current based on the derived optimal damper force. For that reason an inverse MR damper model is also designed based on the neural network identification of the particular rotary MR damper. The performance of the proposed controller is compared to that of an optimal pure viscous damper. The top floor displacement and acceleration of the base excited shear frame structure are selected as the performance parameters of this comparison. It is found by the simulations that the proposed control design yields a reduction in the structural response compared to the viscous case.*

1 INTRODUCTION

As large scale structures become increasingly slender and flexible the magnitude of dynamic response due to loading from wind, traffic and even earthquakes may increase beyond the acceptable level. Thus, the need for additional external damping is pronounced, where in particular the concept of semi-active control has received a great amount of attraction during the most recent decades. The Magnetorheological (MR) damper is one of the most popular types of semi-active devices. It is inherently dissipative and thereby stable, and it behaves roughly as a friction damper, where the friction force level can be altered real-time by simply changing the applied damper current. Thus, the MR damper is a cost effective device that combines some of the adaptability of active control with the low power requirements and reliability of pure passive dampers.

The main challenges arising in connection with the use of most semi active damping devices lies in the development of effective control laws, and in the subsequent digital and real-time implementation. Most control strategies for semi-active structural control fall into two main categories. The first one consists of control strategies that require accurate mathematical formulation for the plant model. Examples in this category are the H2/LQG, H_∞ and the sliding mode control, where any active parts are simple clipped. Conversely, the second category contains control strategies that do not require an accurate mathematical model of the plant. Neural network and fuzzy control fall into this category. Several neural network based control strategies [1-3], neuro-fuzzy network based strategies [4,5] or neuro-predictive control methods [6] have been developed for different control aspects of MR dampers. The advantage of neural network based methods is that they mainly excel in the handling of uncertainties in nonlinear applications, which makes them suitable for both modeling and control of the inherently nonlinear MR damper.

It has been demonstrated in [7,8] that for semi-active control of flexible structures the combination of pure friction and a negative stiffness component yields very effective damping of structural vibrations. Therefore, this paper considers the development of a model reference neural network, which will track the desired hysteresis behavior of an ideal friction damper with negative stiffness. The proposed controller performance is compared with performance of an optimal viscous damper, and for the response of a simple shear frame structure subjected to harmonic base excitation the good performance of the proposed method is verified.

2 STRUCTURAL MODEL AND MR DAMPER PROPERTIES

The performance of the semi-active control strategies for the MR damper is in this paper assessed by the harmonic response of a base excited five-storey shear frame structure. The MR damper is collocated at the first floor of the shear frame, where the measuring data is collected. To apply the semi-active control strategy on the MR damper, an inverse model of the damper is needed to predict the damper current associated with the desired MR damper force. The equation of motion of the shear frame structure with MR damper and inverse MR damper model are discussed in the following sub-sections.

2.1 Equation of motion

In dynamic analysis of flexible structures the structural model is typically modeled by finite elements or determined by experimental modal analysis, whereby the equation of motion can be written in the form

$$\mathbf{M}_c\ddot{\mathbf{x}} + \mathbf{C}_c\dot{\mathbf{x}} + \mathbf{K}_c\mathbf{x} = -\boldsymbol{\lambda} f + \mathbf{M}_c\,\mathbf{I}\left(-\ddot{x}_g\right) \tag{1}$$

where $\mathbf{M}_c$, $\mathbf{C}_c$ and $\mathbf{K}_c$ are the mass, damping and stiffness matrices in Cartesian coordinates, $\mathbf{x}$ is the displacement vector containing the displacements of the five concentrated masses, the dot represents the time derivative, f is the force of the external MR damper, $\boldsymbol{\lambda} = [1,0,0,0,0]^T$ is the connectivity vector that applies the semi-active force f to the first mass, $\mathbf{I} = [1,1,1,1,1]^T$ is the unity vector and $\ddot{x}_g$ is the ground acceleration. The schematic illustration of the shear frame structure with rotational MR damper is shown in Fig. 1.

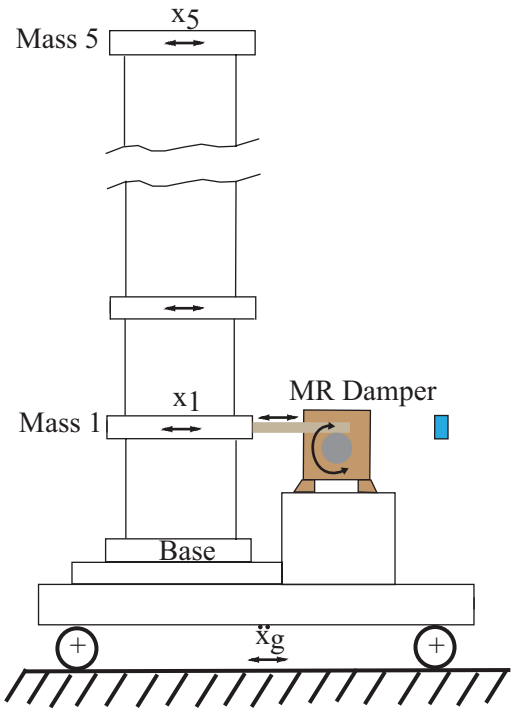

Figure 1: Shear Frame Structure with MR damper

2.2 MR damper model

The rotational MR damper is modeled using the classical Bouc-Wen hysteresis model. The parameters of the model have been calibrated by experiments, where the damper has been driven harmonically in a testing machine at various frequency-amplitude combinations. The modified Bouc-Wen model by Spencer et al. [9] was formulated for the cylindrical type MR damper. In the present case this model is slightly simplified, mainly because the cylindrical damper concept has no need for an accumulator chamber, which for the many cylindrical type dampers introduce an additional stiffness component. Figure 2 shows the close up of the rotary type damper at the Swiss Federal Laboratory of Material Science and Research (EMPA) and the schematic diagram of the classical Bouc-Wen model. For more information on the characteristics and modeling of the rotary MR damper please see Boston et al. [10].

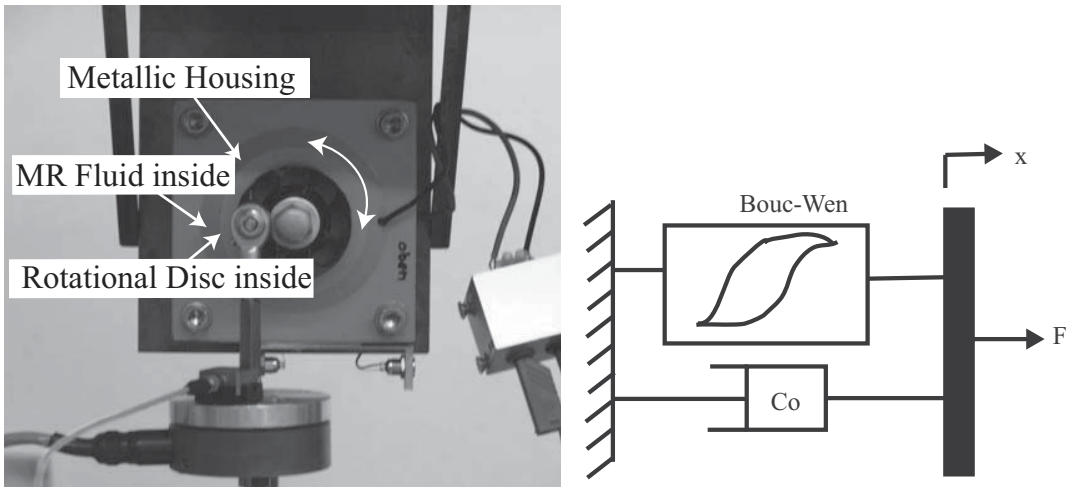

Figure 2: Rotational MR Damper and Bouc-Wen damper model

The governing equations for the damper force *f* predicted by the classical Bouc-Wen model can be written as follows:

$$f = \left(\alpha z + c_0 \dot{x}\right) \tag{2}$$

where the hysteresis effect follows from the evolutionary variable *z* controlled by the Bouc-Wen equation

$$\dot{z} = -\gamma \left|\dot{x}\right| z \left|z\right|^{n-1} - \beta(\dot{x}) \left|z\right|^{n} + A(\dot{x}) \tag{3}$$

The gain parameters on the hysteresis effect and the viscous effect are in the present case described by cubic and linear functions of the applied current, respectively:

$$\alpha = \alpha_a + \alpha_b u + \alpha_c u^2 + \alpha_d u^3 \quad , \quad c_0 = c_{0a} + c_{0b} u \tag{4}$$

The applied current *u* is described with a time delay relative to the desired current *I* by the following first order filter:

$$\dot{u} = -\eta(u - i) \tag{5}$$

The estimated parameters of the simplified Bouc-Wen model for the rotational MR damper are given in Table. 1.

MR Damper Parameters			
α_a	4.038	η	100
α_b	1.984	γ	410
α_c	7.901	β	410
α_d	-0.704	A	1000
c_{0a}	10	c_{0b}	100

Table 1: Parameters for Bouc-Wen Model

Typical force-displacement and force-velocity hysteresis loops for the rotational MR damper are shown in Fig. 3. It is seen that the MR damper behaves approximately as a friction damper, where the friction force level can be altered by changing the applied damper current. The opening of the force-velocity loops indicates some pre-yield stiffness.

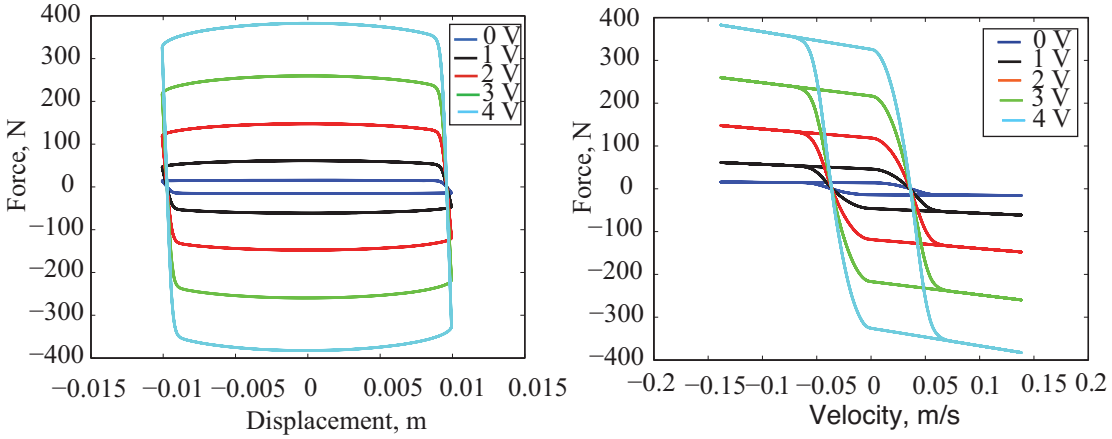

Figure 3: Force Displacement /Velocity hysteresis loops.

2.3 Inverse MR damper

The inverse model modeling for rotary MR damper is a quite complicated task due to high nonlinearity in MR damper dynamics. This work can be done by using parametric [10] such as Evolutionary Algorithm and also non-parametric system identification methods such as neural network identification approach [11, 12]. The inverse MR damper behavior is modeled to solve the force tracking task by MR damper in closed loop cycle. The training and validation data are generated by dynamic tests of the MR damper mounted on a hydraulic testing machine. The inverse modeling training data are absolute velocity and absolute force and the current is the target. This approach has been chosen because current is always positive and thereby leads to a small modeling error independently of the sign of velocity. The inverse model of the MR damper is verified with totally independent set of input-output data. The model validation is thoroughly described in Bhowmik et al [14].

The inverse MR damper behaviour, i.e. the input states at time instant k are the damper velocity $\dot{x}_1(k)$ and desired control force $f_{des}(k)$ and the output state is current $I(k)$, is modelled by a neural network with the following architecture

$$I(k) = NN\begin{bmatrix} |\dot{x}_1(k)| & |\dot{x}_1(k-1)| & |\dot{x}_1(k-2)| & |\dot{x}_1(k-3)| \\ |f_{des}(k)| & |f_{des}(k-1)| & |f_{des}(k-2)| & |f_{des}(k-3)| \end{bmatrix} \tag{6}$$

The neural network based inverse MR damper model is used to solve the force tracking task.

3 CONTROL STRATEGIES

The present paper describes a neural network based model reference control strategy for the prediction of the desired force to control structural vibrations. To evaluate the performance of the proposed model reference controller, the optimal pure viscous damper force is also applied to the structure.

For linear damper models the characteristics of the damper are conveniently formulated in the frequency domain as

$$f(\omega) = gH(\omega)x \tag{7}$$

where g is the control gain and $H(\omega)$ is the associated frequency dependent transfer function.

The effective damping of the structure is evaluated in terms of its modal damping ratio, where the presence of the external damper generates a non-proportional damping with corresponding complex valued natural frequencies and mode shapes. The analysis of the damper modal vibrations is described by the two-component system reduction technique introduced by Main and Krenk [13]. In that formulation the response of the structure is represented by a linear combination of the two limiting mode shapes for the structure without damper $\mathbf{u}_0$ and for the structure with the damper fully locked $\mathbf{u}_\infty$, respectively. The linear combination can then be written as:

$$\mathbf{x} = \mathbf{u}_0 \mathrm{r}_0 + \mathbf{u}_\infty \mathrm{r}_\infty \tag{8}$$

The first term represents the classical undamped case, while the second term introduces the local effect of the damper described in terms of its ability to lock the structure at its location. The undamped mode shape is governed by the classical generalized eigenvalue problem

$$\left(\mathbf{K} - \omega_0^2 \mathbf{M}\right)\mathbf{u}_0 = \mathbf{0} \tag{9}$$

A similar eigenvalue problem exists for the case where the damper link is fully locked, defining ω_∞ and $\mathbf{u}_\infty$. The locked mode shape $\mathbf{u}_\infty$ is by construction orthogonal to the connectivity vector which yields the identity $\boldsymbol{\lambda}^{\mathrm{T}}\mathbf{u}_\infty = 0$.

The two-component representation reduces the full dimensional problem to a two-dimensional problem, where the associated characteristic equation can be solved explicitly, providing expressions for the complex valued natural frequency and the corresponding modal damping ratio. Optimal calibration of the damper model is based on the maximization of the damping ratio. For the general damper format in (7) it is demonstrated in [14] that the optimal gain can be determined by the expression:

$$g_{opt} = \frac{1}{|H|}\frac{\left(\omega_\infty^2 - \omega_0^2\right)}{u_0^2} \tag{10}$$

where u_0 is the amplitude of the undamped mode shape at damper location. This expression is in the following used to calibrate the control strategies.

3.1 Viscous damping strategy

The prototype damper model is the pure viscous model. For this model the damper force is directly proportional to the collocated velocity of the damper motion,

$$f = c\dot{x} \tag{11}$$

where c is the viscous parameter. When compared with the linear frequency representation of the damper force in Eq. 7, the damper transfer function for the viscous damper is

$$H(\omega) = i\omega \simeq i\omega_0 \tag{12}$$

while the gain value is

$$g = c \tag{13}$$

Substitution of (12) and (13) into (10) gives the following expression for the optimal viscous parameter:

$$c_{opt} \approx \frac{2\left(\omega_{\infty} - \omega_0\right)}{u_0^2} \tag{14}$$

where $\omega_{\infty} + \omega_0 \approx 2\omega_0$

The optimal viscous damper is without stiffness and is therefore a suitable benchmark example for damper models with negative stiffness.

3.2 Proposed Neural network based model reference control strategy

The proposed controller is developed based on a neural network model identification technique, where the neural network model is trained by a reference damper model. In this paper, the characteristics of the damper model are described by the desired shape of the hysteresis loop, which combines an amplitude dependent friction damper with a negative stiffness component. The optimal shape of this hysteresis loop has originally been identified and verified by Boston et al. [7]. The hysteresis loop is based on the assumption of pure harmonic displacement and velocity, which is used as the input to the proposed neural model, while the damper force based on the desired hysteresis loop is used as the output of the neural controller. The optimal shape of the force-displacement trajectory is shown in fig. 4.

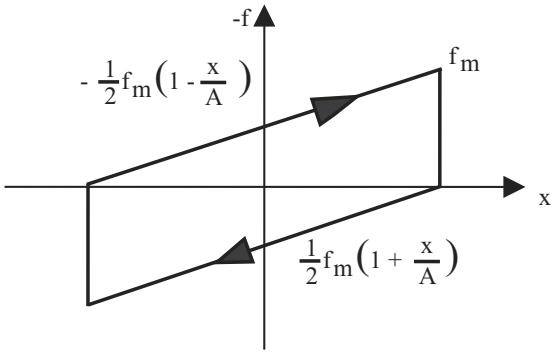

Figure 4: Force-Displacement Hysteresis model for Friction Damper with negative stiffness

The hysteresis model is inherently nonlinear, whereas the calibration formulation in (10) requires a linear damper model. Thus, an equivalent linear model is assumed to contain a viscous and a stiffness component,

$$f = c\dot{x} + kx \tag{15}$$

If x is a sinusoidal signal, the parameters of the linear equivalent model in (15) can be determined by equivalence over a full vibration period, see [14]. The yields the following equivalent linear model for the hysteresis loop in Fig. 4:

$$f = \frac{2f_m}{\pi\omega A}\dot{x} - \frac{f_m}{2A}x \tag{16}$$

where A is the amplitude of the damper displacement, k is negative stiffness and f_m is maximum force of the hysteresis loop. In frequency domain the model is expressed as

$$f = \frac{f_m}{A}\left(-\frac{1}{2} + i\frac{2}{\pi}\right)x \tag{17}$$

Comparison with the frequency representation in Eq. 7 gives the following expression for the transfer function of the linear equivalent hysteretic damper model:

$$H(\omega) = \left(-\frac{1}{2} + i\frac{2}{\pi} \right) \tag{18}$$

and the corresponding gain value:

$$g = \frac{f_{\mathrm{m}}}{A} \tag{19}$$

From Eq.10 the optimal value of g is determined as

$$g_{opt} = 1.24 \frac{\left(\omega_{\infty}^2 - \omega_0^2 \right)}{u_0^2} \tag{20}$$

The optimal value f_m is determined as

$$f_{\mathrm{m}} = g_{opt} A \tag{21}$$

where A is the amplitude of the displacement.

In this paper, a four-layer feed forward neural network is adopted which consists of one input, two hidden layers and a single output layer. The displacement and velocity with current state and five preceding values are taken as input and force at current state is output in the proposed neural network. The neural network controller is trained with training data generated at different amplitudes and at different frequencies of both the displacement response and the corresponding force data from the optimal friction model. The trained model is verified with independent data set and subsequently used in a closed loop implementation. The training algorithm used in the feed forward back propagation neural network is the Levenberg-Marquardt (LM) algorithm based on a least-square curve fitting.

4 NUMERICAL EXAMPLES

To evaluate the effectiveness of the proposed control strategy for the structural vibration mitigation with rotary MR damper, two numerical examples are considered. The first one is based on pure viscous damping strategy and the second one is our proposed neural network based model reference control (NN-MRC). Both the examples are discussed below

4.1 Viscous Damper

The viscous damping strategy using MR damper in closed loop is simulated for five storied shear frame structure with harmonic base excitation. The force-velocity and force-displacement hysteresis plots of the damper force and desired force from control law are compared for optimal viscous damping strategy and the result is quite satisfactory. The force tracking task by MR damper is quite well. From fig. 3, it is visible that MR damper has a force limit at zero current. For that reason it is not possible for MR damper to follow the desired force below the force limit at zero current. Here for this damper, force limit is 24 N.

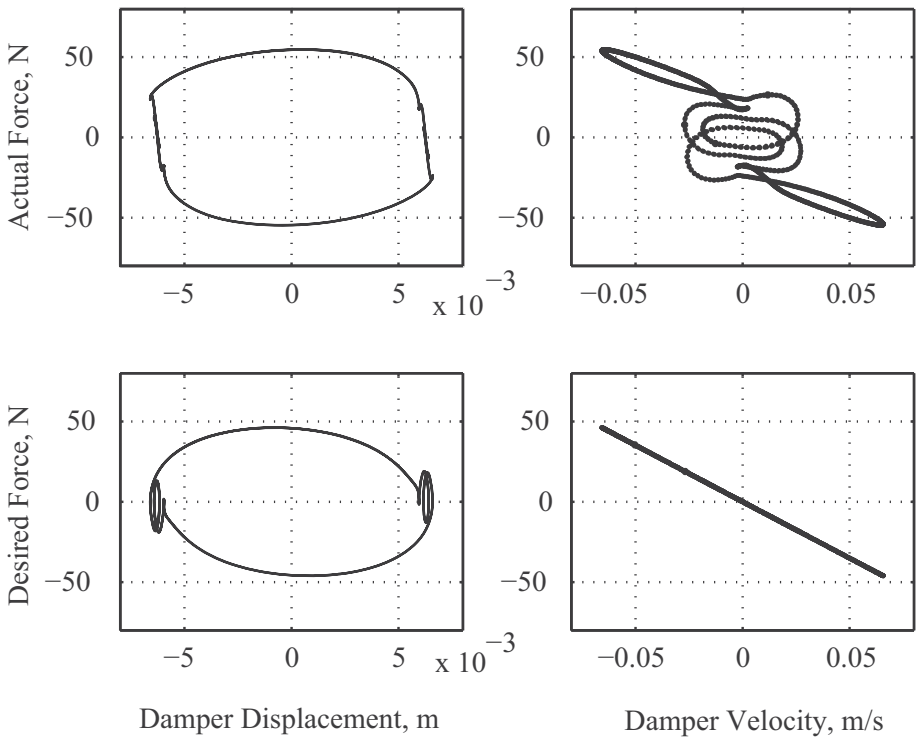

Figure 5: Force-Displacement and Force Velocity hysteresis diagram for viscous damper

The top floor displacement and damper displacement are shown in fig. 6.

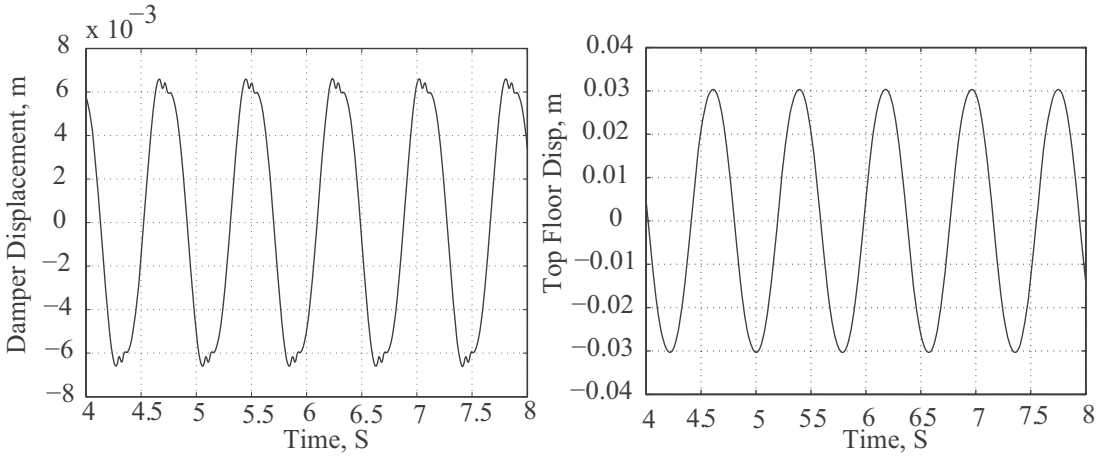

Figure 6: Time history of damper and top floor displacement for viscous damper

The viscous damping strategy is also applied directly on structure without MR damper and compared the change in performance.

4.2 Model Reference Neural Controller

The proposed neural control strategy is applied for structural vibration reduction based on harmonic base excitation using MR damper in closed loop simulation. The Time history of damper displacement and top floor displacement are shown below.

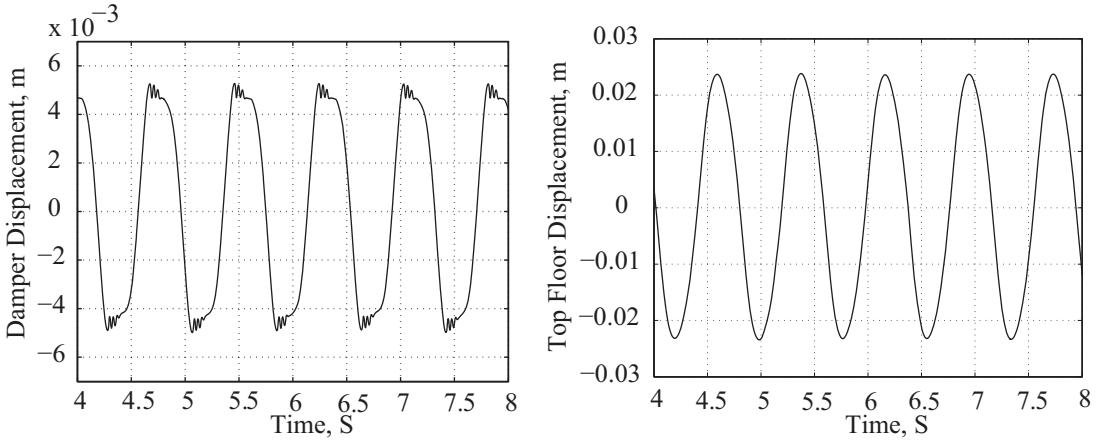

Figure 7: Force-Displacement and Force Velocity hysteresis diagram for neural controller

The hysteresis plots for force-displacement and force-velocity trajectories are shown in fig.8.

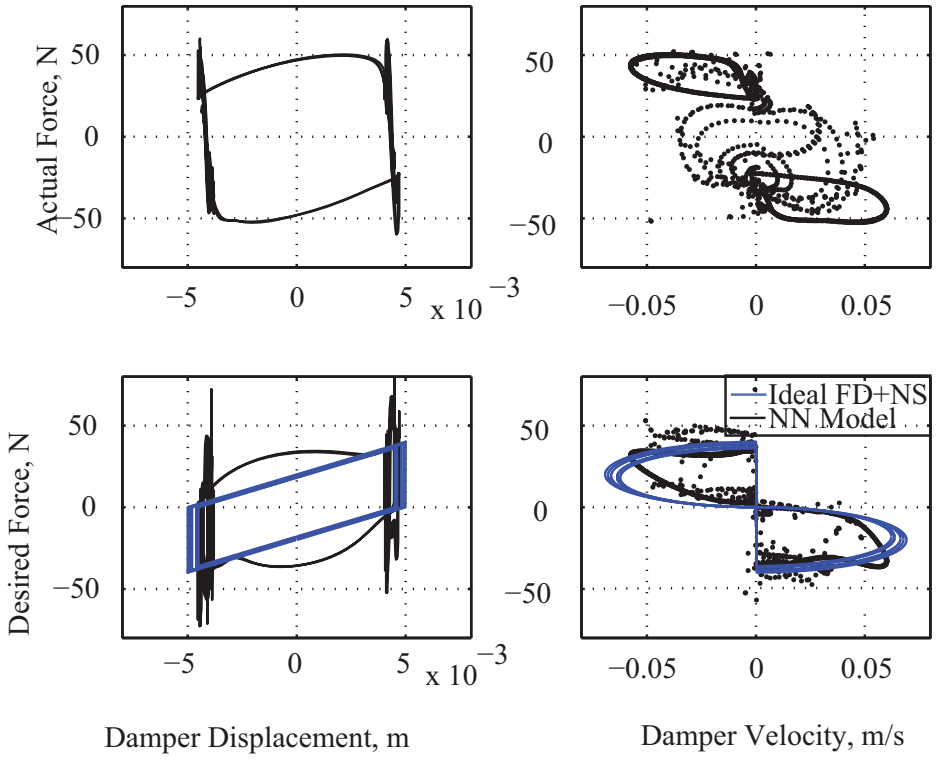

Figure 8: Time history of damper and top floor displacement for neural controller

The schematic diagram for the closed loop simulation is shown below

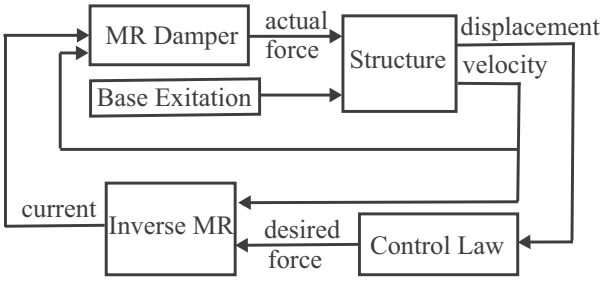

Figure 9: Schematic diagram for closed loop simulation

Force from an optimal friction damper with negative stiffness are calculated by analytical method and compared with the desired force prediction from neural network. Desired force from neural controller and the analytical force have some deviation because the slope of the desired force is not linear due to change in the motion of the damper. The damper displacement is slightly changed from pure sinusoidal due to some spiky effect in current output from inverse MR damper model. The current from inverse MR damper model is shown in fig. 10

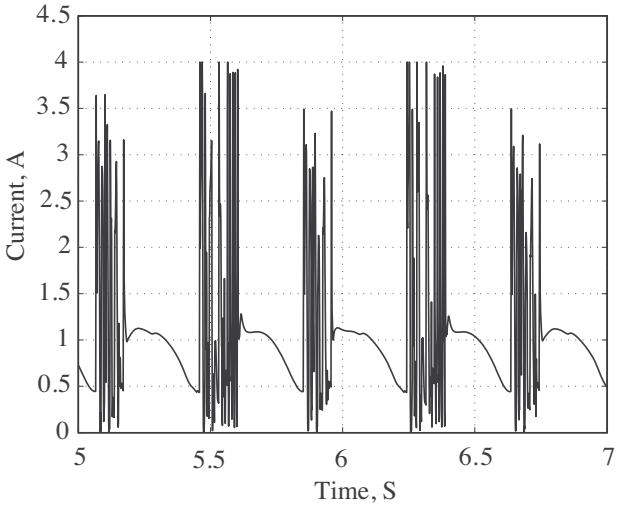

Figure 10: Time history of current from inverse MR model

The force-displacement and force-velocity diagram are shown in Fig. 8. The diagrams are quite satisfactory with compared with identical one. There is some deviation in the force prediction due to non-sinusoidal behaviour of the structural response. This is mainly due to some spiky current prediction by inverse MR model but overall the force tracking is quite satisfactory.

	Passive Viscous	Viscous with MR damper	NN-MRC
RMS(x_1^{max})	0.0091 m	0.0066 mm	0.0044 mm
RMS(x_5^{max})	0.036 m	0.030 m	0.024 m
RMS(a_1^{max})	0.64 m/s^2	0.81 m/s^2	0.80 m/s^2
RMS(a_5^{max})	2.02 m/s^2	1.81 m/s^2	1.76m/s^2

Table 1: Performance Parameters

5 CONCLUSIONS

In the closed loop simulation, two neural network models are used. One is for force tracking which is an inverse MR damper model and another is used for tracking reference damper model which is following hysteresis force-displacement behaviour for optimal friction damper with negative stiffness. RMS of the peak displacement and peak acceleration of each cycle for top floor and damper location are taken as performance parameters. From the performance parameters chart, it is clearly visible that proposed control method can reduce around 35% in damper displacement and 30% in top floor displacement. The damper displacement for viscous damping strategy with and without MR damper has deviation due to limitation MR damper force realization at zero current when MR damper is attached. The response of the top floor using semi active neural controller gives is quite satisfactory with compared to pure viscous damping. There is also significant improvement in acceleration term and but the acceleration contains some noise. The major advantage of the proposed controller is it is inherritently modeled with amplitude dependency and the inherent time-delay problem which is an important drawback of model based control can be solved in neural based control. In general, a neural network is trained under certain condition which can be used in a slightly modified but similar nature of the training state. The important feature of neural network is that it can handle nonlinearity so well that it can apply to nonlinear structural control also based on linearly trained neural model. This is the reason why neural network is used in this paper for structural control. The numerical study revealed that proposed neural based model reference controller can track the desired hysteresis behaviour of optimal friction damper with negative stiffness satisfactorily and the performance is better than optimal viscous damper.

ACKNOWLEDGEMENT

This research is financially supported by the Danish Agency for Science, Innovation and Research. The major part of the work has been done at Swiss Federal laboratory for Material Science and Research, Switzerland with collaboration with Dr. Felix Weber. These supports are gratefully acknowledged.

REFERENCES

[1] Z.D. Xu, Y.P. Shen, Y. Q. Guo, Semi-active control of structures incorporated with magnetorheological dampers using neural network. *Smart materials and Structure*, **12**, 80-87, 2003.

[2] K.A. Bani-Hami, M.A. Sheban, Semi-active neuro-control for base-isolation system using magnetorheological (MR) dampers. *Earthquake Engineering and Structural Dynamics*, **35**, 1119-1144, 2006.

[3] D.H. Kim, S.N. Seo, I. W. Lee, Optimal neurocontroller for nonlinear benchmark structure. *Journal of Engineering Mechanics*, **130**, 424-429, 2004.

[4] Z.Q. Gu, S.O. Oyadiji, Application of MR damper in structural control using ANFIS method. *Computers and Structures*, **86**, 427-436, 2008.

[5] Z.D. Xu, Y. Q. Guo, Neuro-fuzzy control strategy for earthquake-exited nonlinear magnetorheological structures. *Soil Dynamics and Earthquake Engineering*, **28**, 717-727, 2008.

[6] A.K. Karamodin, M.H. Kazemi, Semi-active control of structures using neuro-predictive algorithm for MR dampers. *Structural Control and Health Monitoring,* **DOI: 10.1002/stc.278**, 2008.

[7] C. Boston, F. Weber, L. Guzzella, Optimal semi-active damping of cables: evolutionary algorithms and closed-form solutions, *Smart Material and Structures*, **18**, 055006 (9 pp), 2009

[8] H. Iemura, M.H. Pradono, Advances in the development of pseudo-negative-stiffness dampers for seismic response control, *Structural Control & Health Monitoring*, **16**, 784-799, 2009

[9] B.F. Spencer, S.J. Dyke, M.K. Sain, J.D. Carlson, Phenomenological model for magnetorheological dampers. *Journal of Engineering Mechanics*, **123**, 230-238, 1997.

[10] C. Boston, F. Weber, L. Guzzella, Modeling of a disc-type magnetorheological damper, *Smart Material and Structures*, **19**, 045005 (12 pp), 2010

[11] H. Metered, P. Bonello, S. Oyadiji, The experimental identification of magnetorheological dampers and evaluation of their controllers, *Mechanical Systems and Signal Processing*, **24**, 976-994, 2010

[12] S.Bhowmik, J. Høgsberg, F. Weber, Neural Network Modeling of forward and inverse behaviour of rotary MR damper. 23*rd* *Nordic Seminar on Computation Mechanics (NSCM23),* Stockholm, Sweden, October 14-15, 2010.

[13] J.A. Main, S. Krenk, Efficiency and tuning of viscous dampers on discrete systems, *Journal of Sound and vibration,* **286,** 97-122, 2005

[14] J. Høgsberg, Modeling of Dampers and Damping in Structures, *PhD Thesis*, Technical University of Denmark, 2005

P4

(Conference paper)

Semi-active control of magnetorheological dampers with negative stiffness

Proceedings of the fourth ECCOMAS Thematic Conference on Smart Structures and Materials
July 13–15, Porto, Portugal, 2009, 581–590

Semi-active Control of Magneto-Rheological Dampers with Negative Stiffness

Subrata Bhowmik
Department of Mechanical Engineering, Technical University of Denmark, Lyngby, Denmark

Jan Høgsberg
Department of Mechanical Engineering, Technical University of Denmark, Lyngby, Denmark

ABSTRACT: Effective damping of large and flexible structures by semi-active dampers relies greatly on the control strategy applied, which should combine the robustness of passive devices and the increased damping performance often available from active control. For structural control the Magneto-rheological (MR) damper is among the most popular and promising devices due to its low power requirement, high dynamic range, high force capacity and robustness. The objective of this paper is to formulate semi -active feedback control methods based on simple linear damper models, which lead to increased damping performance by introduction of apparent negative damper stiffness. The design of the control strategy aims at maximizing the damping ratio of the critical mode of the structure. Explicit solutions for the complex valued natural frequency of the damped structure and the associated damping ratio are obtained by the two-component system reduction technique, which shows that a potential increase in damping is associated with a similar reduction of stiffness, or even with the introduction of negative stiffness. For linear control strategies negative stiffness can only be realized by active control, which is limited by stability. In the present paper it is realized by having the MR damper force track the simple pure viscous damper model with vanishing stiffness and the Kelvin model with negative stiffness. The applied voltage of the MR damper should be controlled in such a way that the desired control force is followed sufficiently accurate. This is done by letting the desired force be the input to an inverse Bingham model, which provides the corresponding desired voltage level of the MR damper. Numerical simulations are conducted to demonstrate the performance of the proposed semi-active control strategy with apparent negative stiffness.

1 INTRODUCTION

Survival of structures from excessive vibration due to uncontrollable events—environmental and otherwise—is of great importance, where vibration control of large flexible structures, such as building or bridges, is installed primarily to reduce transverse deflections and/or accelerations. Some success toward this goal has been reported in the use of actively controlled devices like for instance active mass dampers. However, relatively large power requirement is a primary drawback for this type of structural control. On the other hand, variable or semi-active damping devices exhibit relatively low power demands and show performance abilities similar to those of active control schemes (Dyke 1996). In the category of semi-active control, simple variable damping devices such as magneto-rheological (MR) damper, have received great attention in the civil engineering community. The MR damper is typically produced in cylindrical form filled with an MR fluid and surrounded by one or more electromagnetic coils. The fluid contains very small magnetically polarizable particles that allow the properties of the fluid to change almost instantaneously according to the strength of the applied magnetic field. A detailed description of MR dampers can be found in Spencer (1997) or Yang et al. (2001). The application of MR dam-

pers to the control of vibration has been applied for mitigation of wind and seismic effects on tall buildings by e.g. Zhang and Roschke (1999) or Jansen and Dyke (1999). An important benefit of an MR damper is its capacity to operate from a remote power source, like a battery or a solar panel, thus increasing its viability during destructive environmental events.

Because of the increasing research in and development of new semi-active devices, the associated formulation of suitable control algorithms is of great importance. Two decades ago Yang et al. (1986) proposed new optimal control algorithms for structural control using standard quadratic performance and Ricccati equation to generate appropriate force. Within the framework related to linear quadratic Gaussian, H_2 or H_∞ control a number of promising approaches have been presented and have lead to the development and implementation of e.g. sliding mode control algorithms. Lately, soft computing techniques, for instance based on fuzzy logic theory, have received some attention. However, the efficiency of these techniques is still to be demonstrated.

In the present paper two main objectives are considered. Initially a framework for design of external dampers is presented. This is based on the maximization of the damping ratio of a critical vibration form and it follows the two-component reduction technique presented by Main and Krenk (2005). This analysis provides expressions for the modal damping ratio, which indicates that effective damping can be obtained by imposing apparent negative stiffness. Expressions for optimal tuning of the simple pure viscous damper model and the Kelvin model with negative stiffness are presented. The second step of the paper considers the realization of the desired control force, where the applied voltage is obtained in terms of the desired control force by a simple inverse Bingham plasticity model. A numerical study is presented where the performance of the introduced semi-active control schemes are evaluated based on the response of a 10 story shear frame structure exposed to the El Centro earthquake.

2 MODELING OF MAGNETO-RHEOLOGICAL DAMPER

The response of MR fluids results from the polarization induced in suspended particles by application of an external magnetic field. The interaction between the resulting induced dipoles causes the particles to form columnar structure, parallel to the applied field. These chain-like structures restrict the motion of the fluid, thereby increasing the viscous characteristic suspension. Spencer et al (1997) presented a phenomenological model to analyze the behavior of a small scale version of a Magneto- rheological (MR) damper. The model is an augmented version of the classic Bouc-Wen hysteresis model, and it appears to be representative over a large frequency and amplitude range. A schematic diagram of the modified Bouc-wen model is presented in Fig. 1.

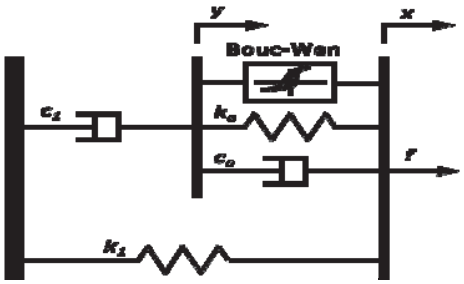

Fig.1. Modified Bouc-wen Model

The equation governing the force f predicted by the modified Bouc-Wen model is as follows:

$$f = c_1 \dot{y} + k_1 (x - x_0) \tag{1}$$

where the energy dissipation is introduced via the filter

$$\dot{y} = \frac{1}{(c_0 + c_1)}\left[\alpha z + c_0 \dot{x} + k_0 (x - y)\right] \tag{2}$$

and the hysteresis effect follows from the evolutionary variable z governed by the Bouc-Wen equation

$$\dot{z} = -\gamma |\dot{x} - \dot{y}| z |z|^{n-1} - \beta (\dot{x} - \dot{y}) |z|^n + A(\dot{x} - \dot{y}) \tag{3}$$

The following model parameters are typically represented as linear functions of the applied voltage:

$$\alpha = \alpha_a + \alpha_b u \quad , \quad c_1 = c_{1a} + c_{1b} u \quad , \quad c_0 = c_{0a} + c_{0b} u \tag{4}$$

where the applied voltage u is described with a time delay relative to the desired voltage v

$$\dot{u} = -\eta (u - v) \tag{5}$$

Representing the dynamics involved in reaching rheological equilibrium and in driving the electromagnet in the MR damper, a total of fourteen model parameters are to characterize the MR damper using experimental data and e.g. a constrained nonlinear optimization algorithm. Taking displacement, velocity and voltage as input, the model can determine the damper force quite accurately. But due to the nonlinearities of the model its inverse is non-trivial. Therefore, the simple Bingham plasticity model

$$f = \left[f_a + f_b v\right] sign\left[\dot{x}\right] + \left[c_a + c_b v\right] \dot{x} \tag{6}$$

is used to obtain the voltage based on a desired control force, which is derived in the following. Governing parameters for a 1000 kN MR damper for both the Bingham and the modified Bouc-Wen model are given in [2]. These parameters are presented in table 1. It should be noted that the saturation voltage level is around 10 V and that the maximum damper stroke is 0.08 m.

3 DAMPING OF FLEXIBLE STRUCTURES

In dynamic analysis of flexible structures the structural model is typically modeled by finite elements, whereby the equation of motion can be written in the well known form

$$\mathbf{M}\ddot{\mathbf{q}} + \mathbf{C}\dot{\mathbf{q}} + \mathbf{K}\mathbf{q} = \mathbf{f}_e - \mathbf{w} f(t) \tag{7}$$

where the vector $\mathbf{q}$ contains the generalized displacements and a dot denotes time differentiation, and $\mathbf{K}$, $\mathbf{C}$ and $\mathbf{M}$ are the structural stiffness, damping and mass matrix respectively. The external load is represented by the vector process $\mathbf{f}_e$. Finally, a single damper is acting on the structure, where f represents the damper force and $\mathbf{w}$ is the connectivity vector describing the location of the damper. In a collocated setting the displacement of the damper is $x = \mathbf{w}^T \mathbf{q}$. The characteristics of the damper are conveniently formulated in the frequency domain as

$$f(\omega) = H(\omega) x \tag{8}$$

Where H is the frequency dependent transfer function which also contains any damper gain.

The effective damping of the structure is evaluated in terms of its modal damping, where the presence of the external damper generates non-proportional damping with complex valued natural frequencies and mode shape. The two-component system reduction technique by Main and Krenk [3] describes the response as a linear combination of two limiting mode shapes for the structure without damper $\mathbf{u}_0$ and for the structure with the damper fully locked $\mathbf{u}_\infty$, respectively.

$$\mathbf{q} = \mathbf{u}_0 \mathrm{r}_0 + \mathbf{u}_\infty \mathrm{r}_\infty \tag{9}$$

Bingham Model							
f_a	100.0 kN	f_b	75.0 kN/V	c_a	81.0 kN s/m	c_b	90.0 kN s/m/V
Modified Bouc-Wen							
α_a	46.2 kN/m	α_b	41.2 kN/m/V	c_{0a}	110.0 kNs/m	c_{0b}	114.3 kNs/m/V
c_{1a}	8359.2kNs/m	c_{1b}	7482.9 kNs/m/V	k_0	0.002 kN/m	k_1	0.0097 kN/m
x_0	0.18 m	η	100 s^{-1}	γ	164.0 m^{-2}	β	164.0 m^{-2}
A	1107.2	n	2				

Table1: MR damper parameters

The first term represents the classical undamped case, while the second term introduces the local effect of the damper described in terms of its ability to lock the structure at its location. The undamped mode shape is governed by the classical eigenvalue problem

$$\left(\mathbf{K}-\omega_0^2\mathbf{M}\right)\mathbf{u}_0=\mathbf{0} \tag{10}$$

A smaller eigenvalue problem exists for the case where the damper link is fully locked, defining ω_∞ and $\mathbf{u}_\infty$. The locked mode shape $\mathbf{u}_\infty$ is by construction orthogonal to the connectivity vector which yields the identity $\mathbf{w}^T\mathbf{u}_\infty=0$. Both limiting mode shapes are real-valued and conveniently normalized to unit modal mass,

$$\mathbf{u}_0^T\mathbf{M}\mathbf{u}_0=1 \quad , \quad \mathbf{u}_\infty^T\mathbf{M}\mathbf{u}_\infty=1 \tag{11}$$

Consequently, the limiting natural frequencies are given in terms of the modal stiffness,

$$\mathbf{u}_0^T\mathbf{K}\mathbf{u}_0=\omega_0^2 \quad , \quad \mathbf{u}_\infty^T\mathbf{K}\mathbf{u}_\infty=\omega_\infty^2 \tag{12}$$

The limiting mode shapes and natural frequencies are all real-valued and may be derived directly from the associated generalized eigenvalue problems.

The equations of motion can be described in the reduced two-dimensional subspace by substitution of (9) into (7) followed by pre-multiplication by the limiting mode-shapes, see e.g. Høgsberg and Krenk (2006, 2007). In the frequency domain the reduced system of equations can be written in the following homogeneous form when free vibrations are considered

$$\begin{bmatrix} \omega_0^2-\omega^2+u_0^2H & \kappa(\omega_0^2-\omega^2) \\ \kappa(\omega_0^2-\omega^2) & \omega_\infty^2-\omega^2 \end{bmatrix}\begin{bmatrix} r_0 \\ r_\infty \end{bmatrix}=\begin{bmatrix} 0 \\ 0 \end{bmatrix} \tag{13}$$

The amplitude of the mode shape at damper location is $u_0=\mathbf{w}^T\mathbf{u}_0$ and $\kappa=\mathbf{u}_\infty^T\mathbf{M}\mathbf{u}_0$ represents the coupling between the two limiting mode shapes. Free vibrations require a singular matrix which yields a characteristic equation in ω in e.g. Main and Krenk (2005). This characteristic equation can be re-written in an explicit, given solution when assuming that the coupling parameter $\kappa\simeq 1$. This solution is conveniently expressed in terms of the change in natural frequency $\Delta\omega=\omega-\omega_0$ and $\Delta\omega_\infty=\omega_\infty-\omega_0$ relative to the undamped case, whereby it appears in the following compact form

$$\frac{\Delta\omega}{\Delta\omega_\infty}\simeq\frac{\mu H}{1+\mu H} \tag{14}$$

In this expression the modal flexibility parameter is given as

$$\mu=\frac{u_0^2}{\omega_\infty^2-\omega_0^2}\simeq\frac{u_0^2}{2\omega_0\Delta\omega_\infty} \tag{15}$$

The modal damping ratio is determined as the relative imaginary part of the complex valued natural frequency: $\zeta=\mathrm{Im}\left[\Delta\omega_\infty\right]/\left|\omega\right|$. In the case of response dominated by resonance the magnitude of the structural is approximately inverse proportional to the damping ratio of the

dominant mode. Thus, a rational and load independent basis for optimal tuning is the maximization of the modal damping ratio ζ with respect to the damper gain. If the approximation $|\omega| \simeq \omega_0$ is introduced the damping ratio can be written as

$$\zeta \simeq \frac{\Delta\omega_\infty}{\omega_0} \frac{\mu \operatorname{Im}\left[H(\omega_0)\right]}{\left(1+\mu \operatorname{Re}[H(\omega_0)]\right)^2 + \left(\mu \operatorname{Im}\left[H(\omega_0)\right]\right)^2} \tag{16}$$

It is seen from this expression that the stiffness of the damper $\operatorname{Re}[H(\omega_0)]$ appears in the denominator of (16). It is therefore observed that a potential increase in the damping ratio is associated with a corresponding reduction of damper stiffness. And as demonstrated in Krenk and Høgsberg (2006) the application of *negative* stiffness improves the damping efficiency for resonant response conditions. In the present paper simple damper models are considered in the following, with emphasis on the design of models with negative stiffness and the application in a semi-active control setting. The optimal tuning of the damper is based on maximization of the damping ratio, which follows from having the variation $\delta\zeta = 0$.

4 SAMPLE DAMPER MODELS

4.1 *Pure Viscous Damper*

The prototype damper model is the pure viscous model. For this model the damper force is directly proportional to the collocated velocity of the damper motion,

$$f = c\mathbf{w}^T\dot{\mathbf{q}} \tag{17}$$

where c is the viscous parameter.
This means that the damper transfer function is given as

$$H(\omega) = ic\omega \simeq ic\omega_0 \tag{18}$$

where the frequency in the transfer function is approximated by the undamped frequency. Substitution into (16) followed maximization of the damping ratio gives the following expression for the optimal viscous parameter

$$c_{opt} = \frac{2\Delta\omega_\infty}{u_0^2} \tag{19}$$

The optimal viscous damper has vanishing stiffness and is therefore a suitable case of reference for damper models with negative stiffness.

4.2 *Kelvin Model*

The general format of a Kelvin type model has both frequency dependent stiffness and viscous components. However, in the present formulation it is assumed that the governing parameters are constant, whereby the damper force can be written as

$$f = \mathbf{w}^T\left[k_d\mathbf{q} + c\dot{\mathbf{q}}\right] \tag{20}$$

It is assumed that the stiffness is given and that c is the gain value of the model. The transfer function can be written as

$$H(\omega) = k_d + ic\omega \tag{21}$$

Substitution into (16) gives the damping ratio and maximization of the damping ratio with respect to c leads to the following expression for the optimal viscous parameter of the Kelvin model.

$$c_{opt} = \frac{2\Delta\omega_\infty}{u_0^2} + \frac{k_d}{\omega_0} \tag{22}$$

where the second term introduces the correction due to damper stiffness.

5 CONTROL STRATEGIES

In the present section a control strategy is presented which operates the semi-active MR damper similar to the optimally tuned simple viscous damper and the viscous damper with constant stiffness contribution (Kelvin model). The efficiency of the proposed control strategies depends in the first place on the proper tuning of the simple damper models, which is given in (19) and (22) and subsequently on the ability of the MR damper to track the desired optimal control force.

The following steps outline the design procedure used for the design of the proposed control scheme:

1. Formulate a MR damper model, which should be as detailed and accurate as possible since it represents the actual damper attached to the structure. Therefore, the modified Bouc-Wen model is applied in the present setting.
2. Design of an inverse model of the MR damper, which is used to predict the desired voltage based on the known optimal damper force. This model should be simple so that it can be inverted and therefore the Bingham plasticity model is used.
3. The optimal control force, which is input to the inverse MR model, is computed by (17) for the viscous damper and (20) for the Kelvin model. The corresponding optimal damper gains are given in (19) and (22), respectively.
4. The voltage is determined by the inverse MR damper model. If negative voltage is desired zero volts are chosen instead. Also a maximum voltage level of 10 volts is enforced.

A schematic block diagram of the overall system is shown in Fig. 2.

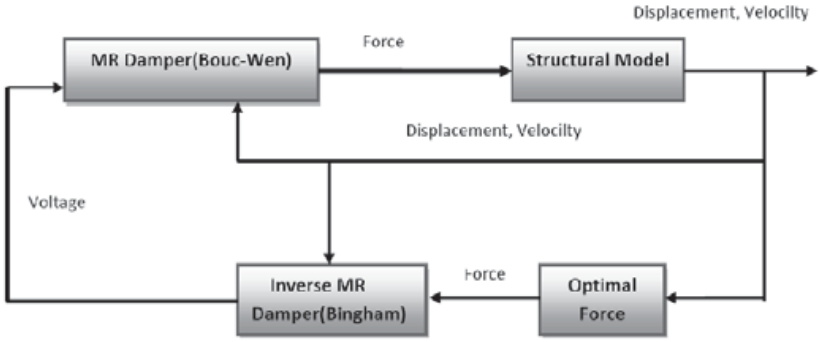

Fig. 2. Block diagram of the semi-active control strategy

6 SIMULATIONS

The efficiency of the semi-active control strategy is assessed for a 10 storied building. The MR damper acts between ground and first floor of the shear frame structure. The governing equation of motion is given in (1), where the mass and stiffness matrix and the connectivity vector are given as

$$\mathbf{M} = m\begin{bmatrix} 1 & & & \\ & 1 & & \\ & & \ddots & \\ & & & 1 \end{bmatrix}, \quad \mathbf{K} = k\begin{bmatrix} 2 & -1 & & \\ -1 & 2 & & \\ & & \ddots & \\ & & & \begin{matrix} \ddots & -1 \\ -1 & 1 \end{matrix} \end{bmatrix}, \quad \mathbf{w} = \begin{bmatrix} 1 \\ 0 \\ \vdots \\ 0 \end{bmatrix}$$

where the concentrated floor mass m and the intersory stiffness k are chosen so that the lowest

natural frequency is $\omega_{01} = 2\pi = 6.28$. In the present case m = 5000 and k = 1.5.10^7. The applied loading is the El Centro earthquake and simulations are conducted using the Simulink toolbox in Matlab.

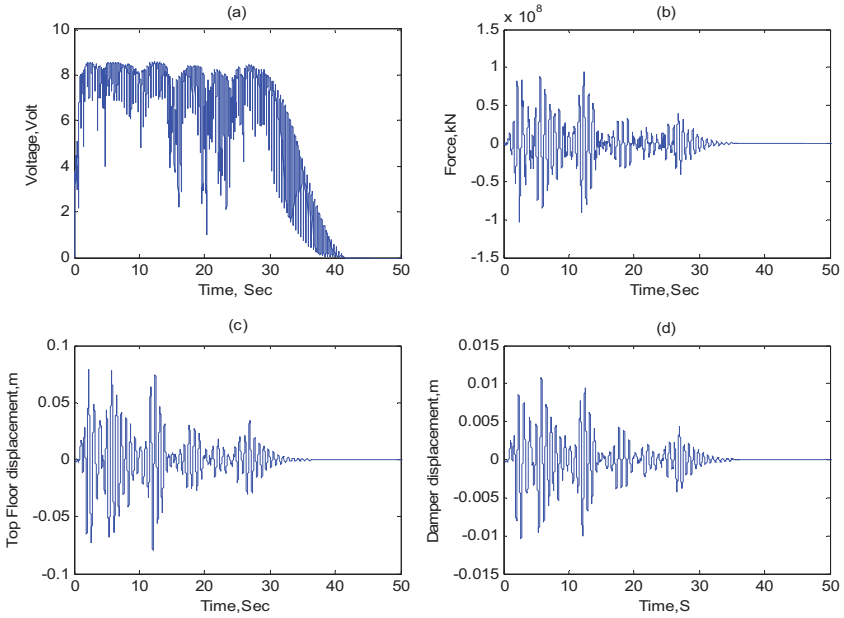

Fig.3. Voltage, force, top floor displacement and damper displacement diagrams for pure viscous

Initially the optimal viscous model is used to generate the desired control force, which is passed on to the inverse MR damper model. Figure 3 shows the applied voltage, the MR damper force, the displacement of the top floor and displacement of the damper. A detailed plot of the response is shown in Fig. 4. It is seen that the force-velocity curve in Fig. 4a is practically

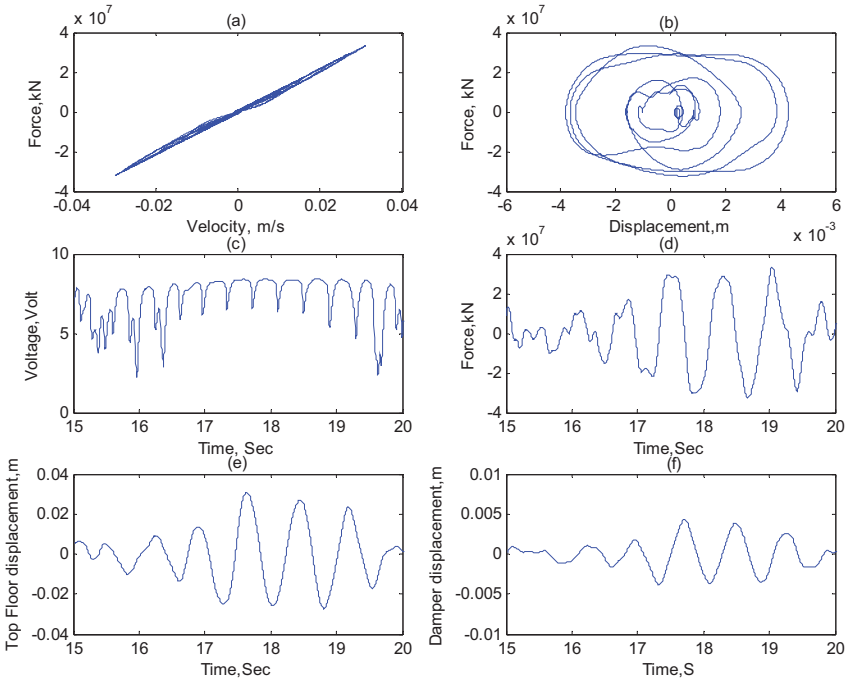

Fig.4. Response diagrams for Pure Viscous

straight line and that the force-displacement curve in Fig. 4b is an ellipse, indicating that the present control is able to capture the characteristics of the pure viscous damper. In Fig. 4c the applied voltage is shown, which over a half period is almost constant if the response is sufficiently sinusoidal.

Similar simulations are conducted for the Kelvin model with negative stiffness. For the shear frame structure the limit of negative stiffness is $k_d = -k$, which corresponds to the case where the negative stiffness of the damper has cancelled the structural stiffness between ground and first floor. In the present case two situations are investigated: $k_d = -0.3\,k$ and $k_d = -0.7\,k$. The results of the simulations are plotted in Fig. 5 and 6.

When comparing the first two figures in Fig. 4, 5 and 6 it is seen that introduction of negative stiffness yields an opening of the force-velocity curves and an inclination of the hysteresis loops in the force-displacement diagram. Thus, the semi-active control scheme is able to capture the desired effect of the viscous component and, in particular, the negative stiffness component. Whereas the voltage in Fig. 4c for the pure viscous damper is almost constant over a half vibration period it is seen in Figs. 4c and 5c that the negative stiffness component in the Kelvin model is realized by the semi-active control through a decreasing voltage over a half period. The response magnitude is assessed in terms of performance indices J1, J2, J3 and J4:

$$J1 = \frac{\max_i \left|x_i(t)\right|}{\max_i \left|x_i^{uc}(t)\right|} \qquad J2 = \frac{\max_i \left|\ddot{x}_i(t)\right|}{\max_i \left|\ddot{x}_i^{uc}(t)\right|}$$

$$J3 = \frac{\max_i (RMS(x_i))}{\max_i (RMS(x_i^{uc}(t)))} \qquad J4 = \frac{\max_i (RMS(\ddot{x}_i))}{\max_i (RMS(\ddot{x}_i^{uc}(t)))} \tag{23}$$

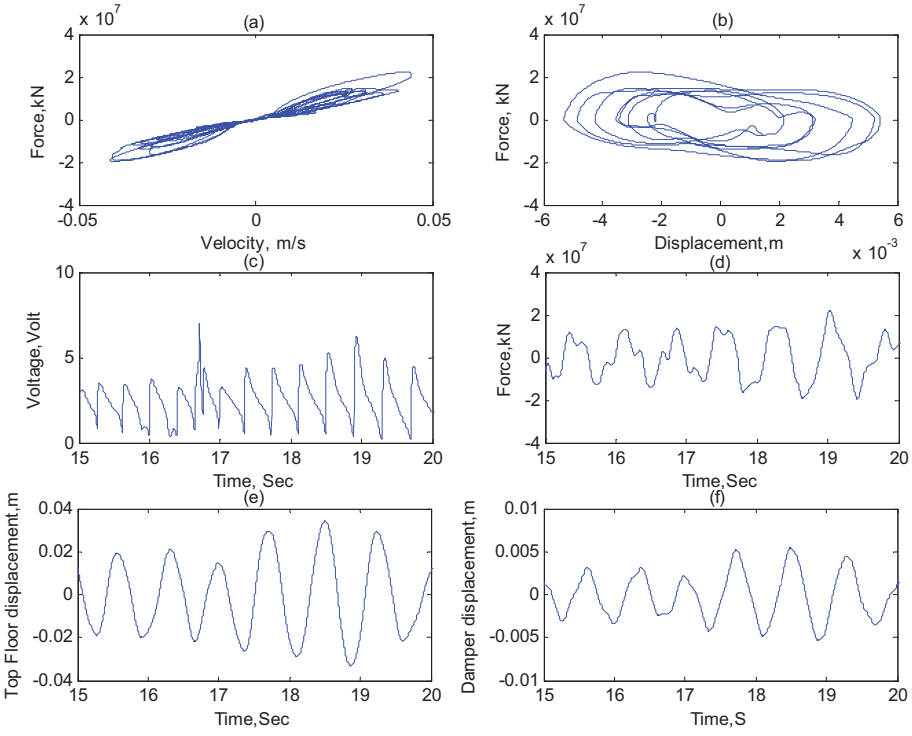

Fig. 5. Response diagrams for Kelvin Model ($k_d = -0.3k$)

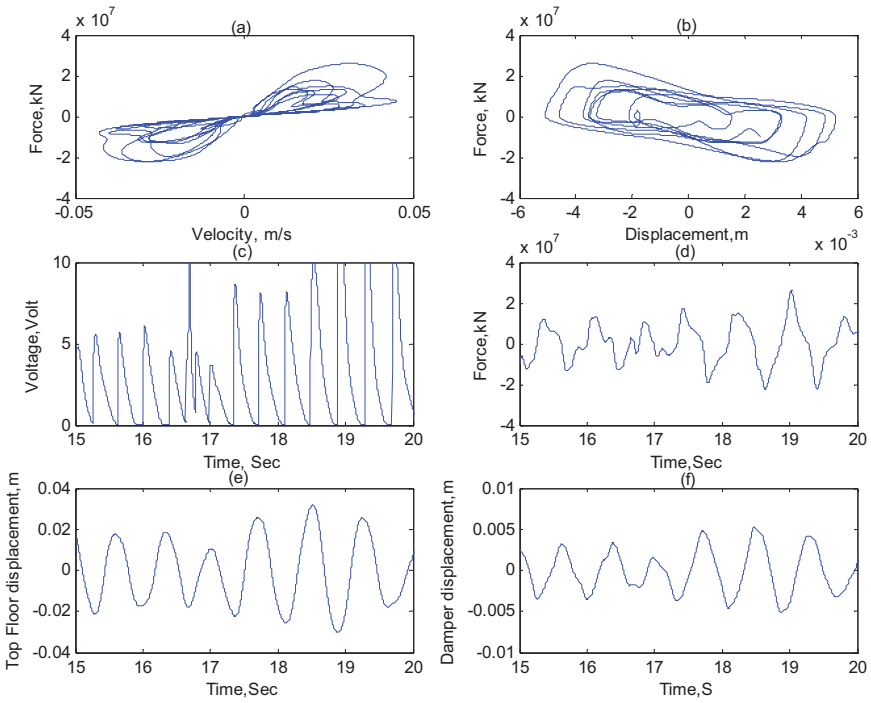

Fig.6. Response diagrams for Kelvin Model ($k_d = -0.7k$)

where superscript *uc* indicates the undamped case. The values of the J1-J4 are given in Table 2 for the three damper models. It is found that all three damper models introduce a significant response reduction compared to the undamped case. The influence of negative stiffness is moderate compared to the viscous case and the increase in negative stiffness from $k_d = -0.3\,k$ to $k_d = -0.7\,k$ is without significant impact. It was found that the voltage generated from inverse damper in some case was quite noisy. Therefore a simple first order filter has been implemented to improve the signal quality of the voltage (Yang 2001)

$$\dot{u}_{fil} + \lambda u_{fil} = \lambda u \tag{24}$$

where u_{des} is the desired force and u is the actual force generated from inverse MR damper model. Here λ is chosen as 31.4 inspired by Yang (2001).

System Model	J1	J2	J3	J4
Pure Viscous	0.6995	0.9526	0.7154	0.6789
Kelvin with negative stiffness ($k_d = -0.3k$)	0.6745	0.9332	0.6909	0.6645
Kelvin with negative stiffness($k_d = -0.7k$)	0.6574	0.9310	0.6799	0.6615

Table2: Performance Analysis

7 CONCLUSION

The semi-active control strategies for MR damper for getting optimal performance for pure viscous and Kelvin models are investigated above. The optimal force is found for both the cases from Modal analysis. Then this optimal force is used to get desired voltage for MR damper from inverse MR damper. The voltage, force, displacement diagrams are compared for both the case with increasing negative stiffness. From the results it is clearly shown that negative stiffness has

significant influence on reduction of displacements and as well as on acceleration. The voltage requirement is reduced with the increase of negative stiffness. Force-displacement diagram is elliptical and changing its inclination angle with the increase of negative stiffness.
For this case earthquake excitation data are used but wind load excitation remains for future work.

Acknowledgements

This work has been supported by the Danish Agency for Science, Technology and Innovation via the project 645-06-0371 “Damping of Flexible structures by smart control of semi active devices”.

8 REFERENCE

1. J.R. Høgsberg, S. Krenk, Linear Control strategies for damping of flexible structures, *Journal of Sound and Vibration*, Vol. 293 (2006) 59-77
2. G. Yang, B.F. Spencer, H.J. Jung, J.D. Carlson, Dynamic Modeling of large-scale magnetorheological damper systems for civil engineering applications, *Journal of Engineering Mechanics*, Vol. 130 (2001), No. 9, 1107-1114
3. J.A. Main, S. Krenk, Efficiency and tuning of viscous dampers on discrete systems, *Journal of Sound and Vibration*, 286 (2005) 97-122
4. J.R. Høgsberg, S. Krenk, System Reduction and Damping of Flexible Structures, *Proceedings of ECCOMAS Conference on Computational Methods in Structural Dynamics and Earthquake Engineering*, (2007)
5. C.L. Ng, Y.L. Xu, Semi-active control of a building complex with variable friction dampers, *Journal of Engineering Structures*,Vol.29 (2007) 1209-1225
6. S.J. Dyke, B.F. Spencer, M.K. Sain, J.D. Carlson, An experimental study of MR dampers for seismic protection, *Smart Materials and Structures*, Vol. 7(1998) 693-703
7. C.C. Chang, P. Roshke, Neural network modeling of a magneto rheological damper, *Journal of Intelligent Material Systems and Structure*, Vol.9 (1999) 755-764
8. L.M. Jansen, S.J. Dyke, Semi-active control strategies for MR dampers: comparative study, *Journal of Engineering Mechanics*, ASCE. Vol.126 (1999) 795-803
9. C.C. Chang, T.Y. Yang, Control of Building Using Active Tuned Mass Dampers, *Journal of Engineering Mechanics,* Vol.121 N.3 (1995) 355-366

P5

(Conference paper)

Neural Network modeling of forward and inverse behavior of rotary MR damper

Proceedings of the Twenty Third Nordic Seminar on Computational Mechanics
October 21–22, Stockholm, Sweden, 2010, 169–172

23rd Nordic Seminar on Computational Mechanics
NSCM-23
A. Eriksson and G. Tibert (Eds)

NEURAL NETWORK MODELING OF FORWARD AND INVERSE BEHAVIOR OF ROTARY MR DAMPER

NSCM-23

SUBRATA BHOWMIK[*,†], JAN HØGSBERG[*] AND FELIX WEBER[†]

[*]Section of Coastal, Maritime and Structural Engineering
Department of Mechanical Engineering
Technical University of Denmark
Nils Koppels Allé 403, 2800 Lyngby, Denmark
E-mail: subho@mek.dtu.dk, jhg@mek.dtu.dk

[†]Structural Engineering Laboratory
Swiss Federal Laboratories for Materials Science and Research (EMPA)
Ueberlandstrasse 129, 8600 Duebendorf, Switzerland
Email: felix.weber@empa.ch

Key words: Magneto rheological (MR) damper, neural network.

Summary. This paper describes the modeling of a rotary MR damper applying the feed-forward back propagation neural network method. The forward and inverse MR damper behavior are modeled to estimate the force and to solve the force tracking task in real-time. The training and validation data are generated by dynamic tests of the MR damper mounted on a hydraulic testing machine. The training data for the forward model are velocity and current whereby the force is the target. The inverse modeling training data are absolute velocity and absolute force and the current is the target. This new approach is chosen because current is always positive and thereby leads to a small modeling error independently of the sign of velocity. The validation demonstrates that the proposed neural network approach can reliably represent both the forward and inverse dynamic characteristics of the rotary type MR damper.

1 INTRODUCTION

Magneto-rheological (MR) dampers have received considerable attention within the last decades mainly because of their design simplicity, low power requirements, large force range and robustness. Typically, a rotary type MR damper consists of a rotating disk which is enclosed in a rectangular metallic housing filled with the MR fluid. The MR fluid housed within the rotary type MR damper is operated in shear mode. The dissipative torque produced is transformed into a translational force through the crank shaft mechanism.
The most common models to describe the dynamic behavior of MR dampers are the Bouc–Wen model [1], the LuGre friction model [2] and the Dahl model [3]. These modeling approaches are fairly complicated due to the high degree of nonlinearities in the system under consideration. From a computational point of view the nonparametric neural network technique is very versatile in connection with most types of nonlinear problems [4].

Therefore, this paper applies this method to model the dynamic behavior of the rotary MR damper.

2 EXPERIMENTAL SET-UP

The experimental test set up and its schematic diagram are shown in Fig. 1. The dSPACE is used to output the desired displacement going to the INSTRON controller, to output the desired current going to the current driver KEPCO and to acquire the measured states such as MR damper force, acceleration of the crank-shaft, actual displacement and current. Sinusoidal and triangular displacements with different frequencies from 0.5 Hz to 2.2 Hz are applied. Triangular displacements are used in order to perform tests at constant damper velocity. Constant and half-sinusoidal currents with different frequencies from 0.5 Hz to 2.2 Hz are also applied. The current of the MR damper under consideration is limited to 4 A and the maximum displacement amplitude is constraint to 10 mm due to the crank-shaft mechanism. The measured data is filtered to remove measurement noise and offsets in order to get the training data for the neural networks.

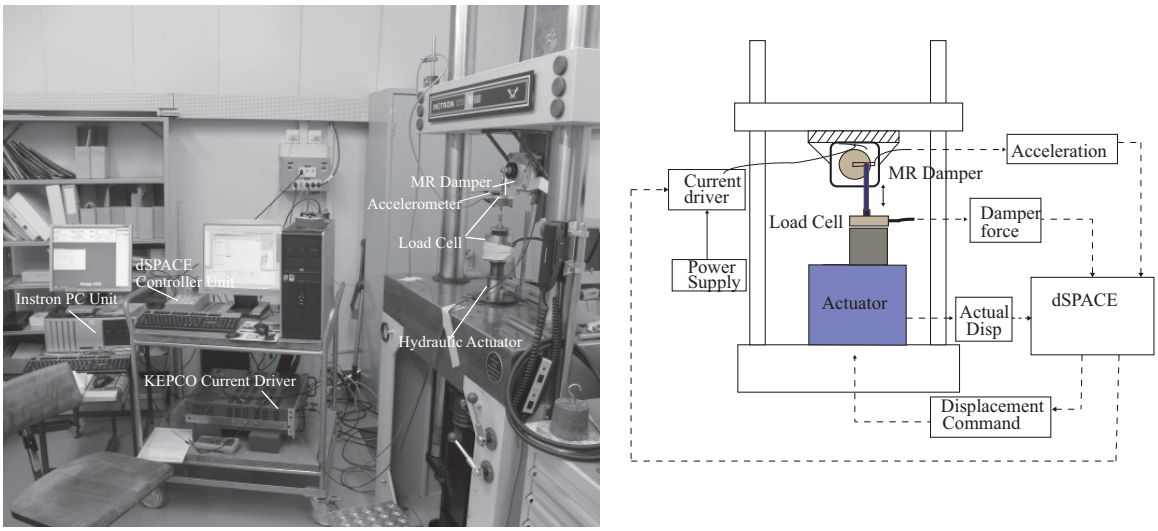

Figure 1. Experimental set-up and its schematic view

3 NEURAL NETWORK MODELING

Feed forward neural network (FFNN) is capable of modeling any nonlinear behaviour with acceptable accuracy. One data set is use as training data and another as validation set.

3.1 Forward MR damper modeling using FFNN

The identification methodology for the modeling of the forward dynamics of MR damper using the FFNN approach is illustrated in Fig. 2. The input states are current and velocity and their associated delay values. The velocity is required due to its significant influence on the hysteretic behavior of the MR damper. It is derived by numerical differentiation of the measured displacement. The noise resulting from the differentiation is removed by additional low pass filtering. The difference between modeled and measured MR damper force, i.e. the

error(k), is used to adjust the weights and the biases of the neural network model until a defined modeling error is reached. The feed forward neural network includes 2 hidden layers with 12 neurons in the first layer and 6 neurons in the second. The output layer includes one neuron and is chosen for input-output comparison. The numbers of layers and neurons have been found by trial and error. The transfer functions of the neurons of the two hidden layers are selected as tangent sigmoid function and the transfer function of the output layer is selected as linear function. The training algorithm is based on the Levenberg-Marquardt algorithm. The detailed mathematics of the neural network method is described well in [5].

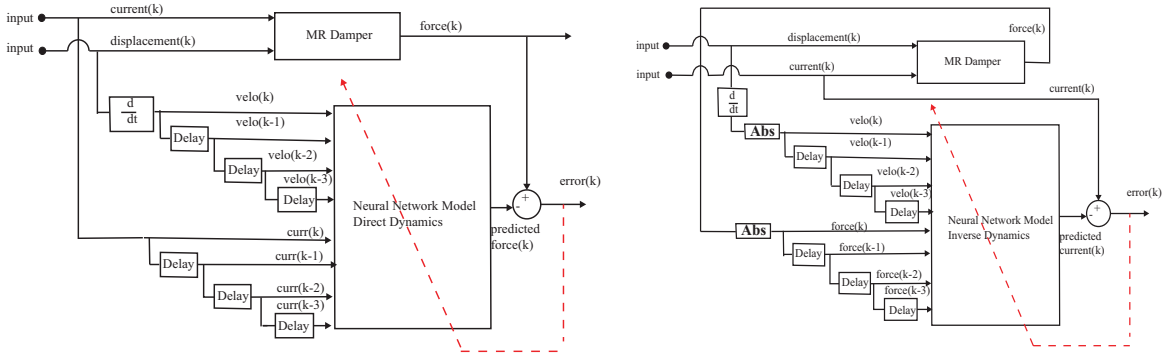

Figure 2. Forward and inverse neural network modeling of MR damper

3.2 Inverse MR damper modeling using FFNN

The architecture of the inverse model using the FFNN method is also shown in Fig. 2. The number of hidden layers and their transfer functions are chosen as before but the number of neurons in both hidden layers is 6. The significant change compared to the forward modeling is that the absolute values of velocity and force are used to train the neural network to get the estimated current because current is always positive. This new approach leads to small modeling error and the modeling error does not depend on the sign of velocity and direction of damper displacement, respectively.

4 MODEL VALIDATION AND DISCUSSION

The validations of both the forward and inverse MR damper models are shown in Fig. 3. The error of the forward model is depicted by comparing the measured and estimated forces resulting from 2 A and sinusoidal displacement (0.5 Hz, 4 mm). The modeling error of the inverse neural network approach is shown for the case of half-sinusoidal current input (0.5 Hz) and sinusoidal displacement (0.5 Hz, 6 mm). The inverse neural network is tested by a half-sinusoidal current because this is quite close to the current time history that is expected when emulating linear viscous damping except that the current spike during the pre-yield region is missing. The validation of the forward model shows an acceptably small error. The current estimated by the inverse MR damper model shows spikes that result from spikes in the measured displacement and force due to bearing plays between crank-shaft and INSTRON piston. Although these spikes have been partially removed by the filters to derive the training data, the estimated current is still spiky. The simple approach of filtering the estimated current cancels the spikes but leads to a still acceptably small time delay of approximately 0.05 s.

5 CONCLUSIONS

This investigation employed the back propagation feed forward neural network method to model the forward and inverse dynamics of an MR damper. The training data was taken on a prototype rotary MR damper that was connected to a hydraulic machine imposing sinusoidal and triangular displacements and constant and half sinusoidal current time histories. The goal of the forward MR damper model was to capture accurately the behavior of the MR damper behavior whereas the inverse MR damper model will later be used for the control force tracking when the MR damper will be connected to a shear frame. The novelty in the proposed neural network when modeling the inverse MR damper behavior is that the absolute values of velocity and force are used to estimate the damper current since current is always positive. The validations of both the forward and inverse MR damper models show that the applied neural network approaches capture the main MR damper dynamics with acceptable accuracy. However, the preliminary results demonstrate that the modeling accuracies can still be improved by further optimization of the filters that are used to process the measurement data to derive the training data for the neural network training.

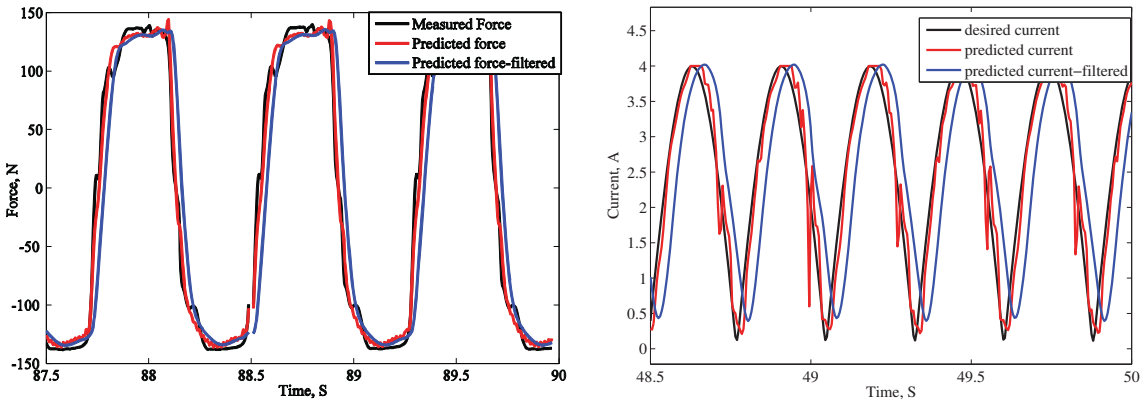

Figure 3. Validation of forward and inverse neural network models

REFERENCES

[1] T. Tse, C. Chang, Shear-Mode Rotary Magnetorheological Damper for Small-Scale Structural Control Experiments, *Journal of Structural Engineering*, 130 (2004) 904-910.

[2] C. Boston, F. Weber, L.Guzzella, Modeling of a disc-type magnetorheological damper, *Smart Mater. and Struct.*, 19 (2010) 045005 (12pp).

[3] F. Ikhouane, S. Dyke, Modeling and identification of a shear mode magneto rheological damper, *Smart Mater. and Struct.*, 16 (2007) 605-616.

[4] H. Metered, P. Bonello, S. Oyadiji, The experimental identification of magnetorheological dampers and evaluation of their controllers, *Mechanical Systems and signal Processing*, 24 (2010) 976-994.

[5] C. Chang, L. Zhou, Neural Network Emulation of Inverse Dynamics for a Magneto rheological Damper, *Journal of Structural Engineering*, 128 (2002) 231-239.

DTU Mechanical Engineering
Section of Coastal, Maritime and Structural Engineering
Technical University of Denmark

Nils Koppels Allé, Bld. 403
DK-2800 Kgs. Lyngby
Denmark
Phone (+45) 4525 1360
Fax (+45) 4588 4325
www.mek.dtu.dk
ISBN: 978-87-90416-70-6

DCAMM
Danish Center for Applied Mathematics and Mechanics

Nils Koppels Allé, Bld. 404
DK-2800 Kgs. Lyngby
Denmark
Phone (+45) 4525 4250
Fax (+45) 4593 1475
www.dcamm.dk
ISSN: 0903-1685